UNIVERSITÉ CATHOLIQUE DE LOUVAIN
ECOLE POLYTECHNIQUE DE LOUVAIN
INSTITUT DE MÉCANIQUE, MATÉRIAUX ET GÉNIE CIVIL

DISCONTINUOUS FINITE ELEMENT METHODS FOR TWO- AND THREE-DIMENSIONAL MARINE FLOWS

DOCTORAL DISSERTATION PRESENTED BY

RICHARD COMBLEN

IN PARTIAL FULLFILLMENT OF THE REQUIREMENTS
FOR THE DEGREE OF
DOCTOR IN APPLIED SCIENCES

THESIS COMMITTEE:

Prof. Vincent Legat, Université catholique de Louvain (Advisor)
Prof. Eric Deleersnijder, Université catholique de Louvain
Prof. Gérard Degrez, Université libre de Bruxelles
Prof. Jean-François Remacle, Université catholique de Louvain
Prof. Eric Delhez, Université de Liège
Prof. Emmanuel Hanert, Université catholique de Louvain
Prof. Matthew D. Piggott, Imperial College, London
Prof. Grégoire Winckelmans, Université catholique de Louvain (Chairman)

Louvain-la-Neuve, September 2010

Avant toute choses, j'ai de nombreux remerciements à adresser.

Durant la dernière année de mon cursus d'ingénieur, j'ai eu la chance de réaliser un mémoire sous la direction de Vincent Legat, en proche collaboration avec Laurent White. Laurent, Vincent, vous m'avez donné le goût de la recherche, et si cette thèse à commencé, c'est grâce à vous.

Durant ces quatres années, Vincent Legat a été le promoteur de ce travail. Avec sa légendaire bonne humeur, Vincent a rythmé toutes les étapes de cette thèse. Il a toujours été présent, et en particulier quand il le fallait. Merci pour tout, pour ces séances de correction d'articles en duo, pour le dynamisme communicatif que tu transmets à tout tes chercheurs.

Même si sur papier, Vincent est mon promoteur officiel, dans la pratique, il est largement secondé par Eric Deleersnijder et Jean-François Remacle. Eric, ta passion pour la recherche est totale. Merci pour ton entêtement à me faire publier, pour les échanges divers et souvent passionants qui m'ont permis de découvrir de nombreuses choses, des marches aléatoires à la percée de Sedan. Jean-François, merci pour la qualité de tes conseils, pour le sérieux que tu mets dans tout ce que tu fais. Et au plaisir d'écouter ton prochain concert. Enfin, merci à vous trois pour la gestion de cette équipe de recherche. Vous avez recruté ces chercheurs qui sont devenu pour moi des amis.

J'ai eu la chance de m'intégrer au sein d'une équipe de recherche, composée de gens particulièrement sympathiques et accueillants. Laurent, merci pour tout. Olivier, Olivier et Sylvain, c'était un vrai plaisir de partager vos bureaux. Jonathan, merci pour toutes ces journées à deux devant le PC, j'ai appris énormément avec toi. Sam, ma messagerie instantanée te sera toujours ouverte. Sébastien, c'est toujours un plaisir de travailler avec toi. Paul-Emile, merci pour tout, et surtout pour cette super semaine au Canada. Benjamin, Sam, Sébastien et Tuomas, bonne chance pour la suite...

Et puis tous les autres, merci à Brieux, pour toutes ces questions compliquées sur Petrov et Galerkin, auxquelles tu as toujours su apporter la bonne réponse. Merci à Laurence pour ces séances de mécanique des fluides en duo. Merci à Maxime, tu étais le meilleur voisin, et le meilleur adversaire aux échecs. Finalement, merci à tous ces habitants du batiment Euler, qui m'ont permi de réaliser une thèse dans un environnement convivial et sympathique.

Enfin, merci à Véronique. Ces quatres années de thèse, c'est quatre année de bonheur passées à tes côtés.

Pour conclure, un grand merci à tous les membres de mon jury, pour le sérieux avec lequel ils ont considéré ce travail.

Ce travail a été financé par le F.R.S-FNRS par le biais du mandat d'aspirant qui m'a été accordé. Qu'il en soit remercié.

CONTENTS

CHAPTER 1

INTRODUCTION

The oceans play a crucial role in the Earth system. They cover over two thirds of the Earth surface. They act as a thermal flywheel, thanks to the high specific heat of water compared to air. The thermohaline circulation, though slow, carries a huge amount of heat from the equator to the poles, homogenizing the atmosphere temperature around the globe. Further, the marine waters are a reservoir for many chemical species, and especially carbon dioxide. The carbon dioxide dissolves within the surface waters, where it is used by plankton for photosynthesis. This organic material eventually falls toward the sea bottom, and the carbon dioxide has therefore been captured. For all those reasons, and many more, it is mandatory for scientists to gain a deep knowledge of the ocean system, to understand the causes for the present status of the system, and to be able to predict its future behavior.

The need for numerical modeling

The oceans are a complex dynamical system. An wide spectrum of phenomena appears together in space and time, ranging from millimeters and seconds scales, to thousands of kilometers and hundreds of years scales. Furthermore, unlike fluid dynamics problems common to the engineer, it can hardly be reproduced in the laboratory.

The interesting timescales for climate studies are at least dozens of years. In situ and satellite observations can provide an insight into past events, but cannot help for prediction. Numerical models are the only predictive tools. Further, they allow to consider various scenarii.

This thesis deals with numerical methods, used to build softwares that can be used by oceanographers to model the behavior of the ocean system. Indeed, we stand at the frontier between applied mathematics and geosciences. Without applied mathematics, we cannot develop efficient software useful for oceanographers, but without a sufficient knowledge of the ins and outs of physical oceanography, we can develop something efficient but useless to oceanographers.

Structured grid methods in ocean modeling

The seminal paper of Bryan (1969) is usually considered as the starting point of numerical oceanography. This first large scale ocean model was developed at the Geophysical Fluid Dynamics Laboratory, Princeton, in the late sixties. It was based on finite differences on structured longitude-latitude grids, with layers of equal depth. Most of the mainstream ocean models can be seen as evolutions of Bryan's model. These evolutions are of three kind.

First, the numerical methods have evolved. For instance, vertical coordinate systems have been generalized (Bleck, 1978), shaved cells (Adcroft et al., 1997) allow to represent more accurately the sea-bottom topography, and monotonic advection schemes are available (Thuburn, 1996), that prevent nonphysical extrema of the solution.

Second, the subgrid-scale phenomena parameterizations have dramatically progressed. For instance, sophisticated turbulence models have been designed (Mellor and Yamada, 1982; Pacanowski and Philander, 1981), providing a much better mixing behavior. Further, isopycnal diffusion (Redi, 1982) and Gent-McWilliams stirring (Gent and McWilliams, 1990; Gent et al., 1995) provide effective parameterizations of unresolved mesoscale eddies. Moreover, a nonlinear equation of state enables nonlinear effects due to linear mixing, such as cabbeling and thermobaricity (Griffies, 2004).

Third, the resolved set of equations has evolved, as now free-surface movements are taken into account. Free-surface models handle much more easily the water fluxes at the sea surface (Blumberg and Mellor, 1987; Killworth et al., 1991). Implicit free-surface models provide a consistent coupling of two- and three-dimensional models (Dukowicz and Smith, 1994; Marshall et al., 1997), even if split-explicit is still resorted to in most models. Review and perspectives of numerical ocean modeling can be found in Griffies et al. (2000) and Griffies et al. (2009).

Within the wide range of numerical tools for solving partial differential equations in rectangular domains, finite difference methods on structured grids are the fastest, considering discretizations of the same order providing solutions with the same accuracy. This follows naturally the structured nature of the discretization, that enables efficient computation of the discrete terms, using the same stencil in the whole computational domain. This explains why for convective problems, finite difference models can use explicit time discretization, while we cannot afford such a time discretization for the same problem using unstructured finite elements. It is commonly thought that, for the same problem and the same resolution, an unstructured finite element model is one order of magnitude slower than a finite difference model (even if recent progress tends to reduce this gap).

However, finite difference models cannot be applied to all problems. They have intrinsic constraints, that are both their advantages and their drawbacks:

- The grid is structured, enabling fast computation of spatial operators, but preventing flexible variation of resolution.

- The grid is built upon the isolines of the parameters of the surface parameterization, for instance longitude and latitude. To obtain a resolution close to uniform, the parametrization must be either stretched (see for instance the grid used with the NEMO project) or split into different surfaces, such as for the cubed sphere (Adcroft et al., 2004). Parameterizations such as the stereographic projection cannot be used because of the too large variations of the metric.

- If the boundaries are aligned with the coordinate system, the finite difference solution can be highly accurate. If it is not the case, boundaries are represented as staircases, and the global accuracy of the scheme is decreased to first order, unless immersed boundary methods are resorted to (Mittal and Iaccarino, 2005; Griffith and Peskin, 2005), that allow to recover second order accuracy if implemented with care.

These drawbacks are inherent to structured grid methods. To circumvent them, we must resort to unstructured meshes.

Unstructured mesh methods for fluid flows

Finite volume methods are extremely popular in computational fluid mechanics. Indeed, these methods are well suited for advection dominated flows, as the fluxes computation takes into account the characteristic structure of the equations. Further, they allow to use unstructured meshes. However, using such methods, it is difficult to build a high order solution on unstructured grids. Indeed, to increase the accuracy, finite volume methods need information from the neighboring cells, and the higher order the discretization, the more neighbors needed (Toro, 1997, Section 13.4). Reconstructing a high order solution based on neighbors is complicated due to the unstructured nature of the mesh, unless block structured approaches such as the spectral volume method are used (Wang, 2002; Wang and Liu, 2002, 2004; Wang et al., 2004; Liu et al., 2006; Sun et al., 2006), that can be compared to discontinuous Galerkin methods (Zhang and Shu, 2005).

Finite element methods were first designed for elliptic problems, such as the Poisson equation or elasticity problems. Finite element methods are based on a functional formalism. The fields are discretized and the exact operators are applied onto these discrete fields. If such a method is used as it for advection dominated flows, strong oscillations spoil the solution. Indeed, the standard Galerkin method does not take into account the characteristic structure of the equations. To solve this issue, stabilized methods have been introduced, such as Petrov-Galerkin (Brooks and Hughes, 1982; Hughes and Mallet, 1986), in which test functions are upwinded, mimicking finite volume methods.

Discontinuous Galerkin finite element methods are increasingly popular for advection dominated flows. Indeed, they allows to keep to best from both finite element and finite volume methods. From the finite element point of view, they can be seen as edge-stabilized methods. From the finite volume point of view, they can be seen as high order finite volume with local embedded Galerkin reconstruction. As finite element methods, they allow for high order polynomial interpolation. From finite volume, they keep the interface fluxes that handles naturally hyperbolic phenomena.

Development of unstructured mesh ocean models

State of the art ocean general circulation models are tremendously complex. They involve many datasets, forcings, and coupling with a sea-ice model and/or an atmosphere model. Numerous parameterizations are used to model the effects of small scale turbulence, mesoscale eddies, unresolved straits, bottom friction, convective adjustment, and many more. All these tools have been added progressively in softwares based on the historical finite difference hydrodynamical kernel. However, it is impossible to modify these

models step by step to use a finite element hydrodynamical kernel on unstructured grids. Therefore, we must start at the beginning, and write models from scratch.

Starting from a white page does not mean forgetting forty years of numerical ocean modeling, but rather to develop a new model while rethinking all the key choices made by ocean modelers the past four decades.

Three research groups are working on similar projects, aiming at large scale ocean models using finite element methods on unstructured grids, resulting in a friendly competition:

- ICOM[1] (Imperial College Ocean Model) is developed at Imperial College, London, based on Fluidity, a home made finite element software for fluid flows. Mesh adaptivity is a key feature of this non-hydrostatic model.

- FEOM (Finite Element Ocean Model) is developed at the Alfred Wegener Institute for Polar Research, Bremerhaven in Germany. This model is the closest to practical large scale application, using robust numerical methods.

- SLIM[2] (Second-generation Louvain-la-Neuve Ice-ocean Model) is developed in Louvain-la-Neuve, Belgium, and my work fits within this project.

Several other groups are developing unstructured grid models for coastal and estuarine problems, using finite volumes (Chen et al., 2003; Fringer et al., 2006; Ham et al., 2005; Casulli and Zanolli, 2000), finite elements (Walters, 2006; Le Bars et al., 2010) or discontinuous Galerkin methods (Aizinger and Dawson, 2002; Dawson and Aizinger, 2005; Kubatko et al., 2006; Aizinger and Dawson, 2007).

The first step to build an unstructured mesh ocean model is to generate a mesh. For the model to benefit from the unstructured nature of the grid, we must be able to make meshes that have the right resolution at the right place, and represent accurately the coastlines. Sébastien Legrand worked on mesh generation for ocean modeling, on the sphere (Legrand et al., 2000), using complex length scale fields on complex domains (Legrand et al., 2006), and using anisotropy to capture complex features (Legrand et al., 2007). At Imperial College, Gerard Gorman developed mesh generation methods constrained by accuracy criterion on coastlines and bathymetry (Gorman et al., 2006, 2007). More recently, coastline approximation algorithms have been designed and incorporated into the open source software Gmsh[3] (Geuzaine and Remacle, 2009). Combined with the stereographic projection, it allows the user to build easily a mesh for his zone of interest (Lambrechts et al., 2008).

The next stage is to choose the three-dimensional structure of the mesh. ICOM relies on completely unstructured meshes made of tetrahedra (Piggott et al., 2008). Such a choice, while being the most flexible, does not take into account the specificity of the vertical direction in ocean flows: it is the axis along which gravity occurs and, in hydrostatic models, the equations are not the same for the horizontal and vertical momentum conservation.

For SLIM, the choice of prismatic elements has been made from the beginning (White et al., 2008a,b). These are built by extrusion of a surface two-dimensional mesh (see Fig-

[1] `http://amcg.ese.ic.ac.uk/index.php?title=ICOM`

[2] `http://www.climate.be/slim`

[3] `http://www.geuz.org/gmsh`

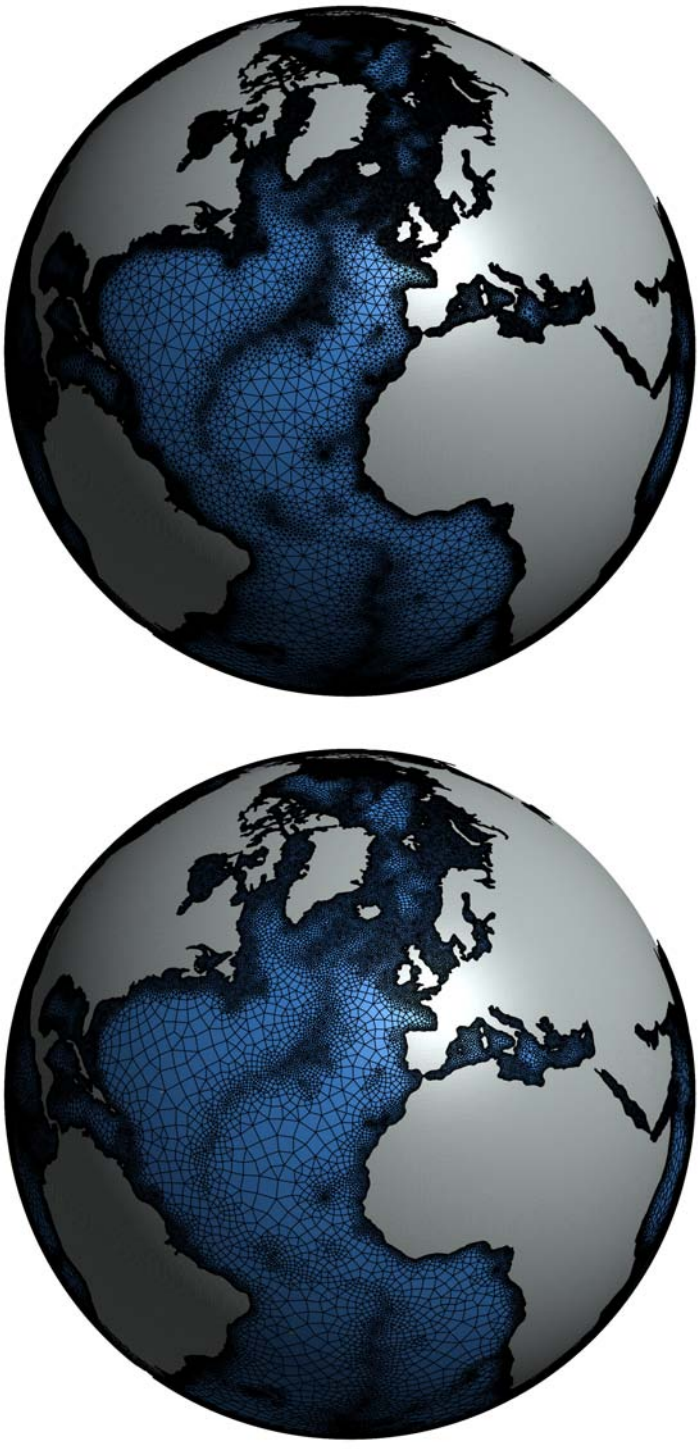

Figure 1.1: Illustrative meshes of the world ocean, made of triangles only (top), and made of both triangles and quadrilaterals (bottom). These meshes have been generated using Gmsh (Geuzaine and Remacle, 2009) using the same edge-length field, thanks to the tools developed by Lambrechts et al. (2008).

ure 1.2). Such vertically aligned elements allow for a natural treatment of the hydrostatic pressure.

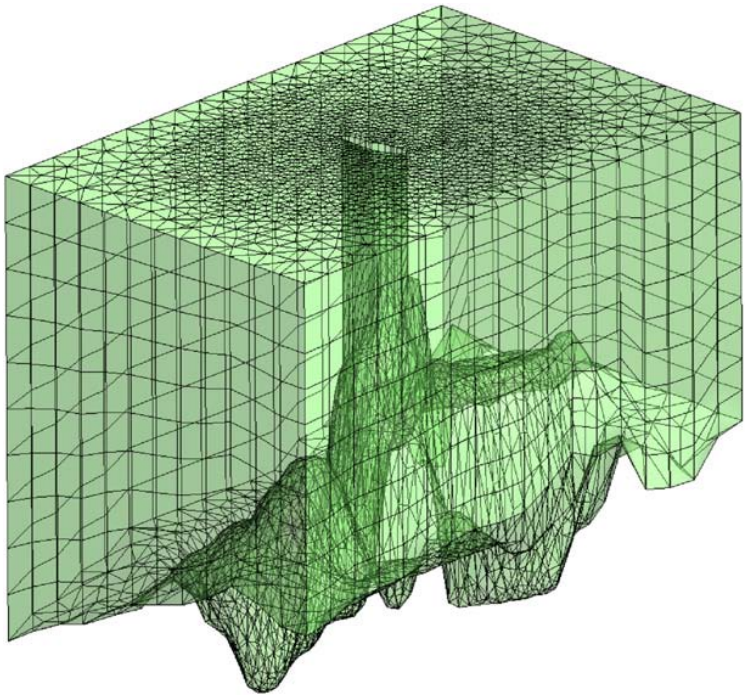

Figure 1.2: Three-dimensional mesh used to model the flow around the Rattray Island, Great Barrier Reef, Australia. Picture from Blaise et al. (2007).

During the development of FEOM, vertically structured meshes made of tetrahedra were first considered (Nechaev et al., 2003; Danilov et al., 2004, 2005), and now vertically structured meshes made of prismatic elements are used (Wang et al., 2008a,b).

Prismatic meshes can be extruded from two-dimensional triangular meshes, quadrilateral meshes, or mixed meshes made of triangles and quadrilaterals. In this thesis, we will use only meshes made of triangles, or prisms with a triangular basis for three-dimensional modeling. However, in a newer version of SLIM, we will be able to use mixed meshes. Illustrations of triangular and mixed meshes of the world ocean are found in Figure 1.1.

ICOM relies on a stabilized finite element formulation for the Navier-Stokes equations Ford et al. (2004b) using linear shape functions on tetrahedra. FEOM is now available with two versions (Danilov et al., 2008): a stabilized $P_1 - P_1$ formulation, and a mixed $P_1^{NC} - P_1$ formulation based on Hanert et al. (2005).

Motivations

We aim at the development of a three-dimensional model for large scale marine flows. This model will use meshes that are horizontally unstructured and vertically structured. We consider finite element methods based on discontinuous or partly discontinuous shape functions.

The two-dimensional equations for the vertically averaged dynamics of the ocean are the shallow water equations. An accurate discretization of this set of equations is therefore a prerequisite to the development of a three-dimensional model. Finite element methods for the shallow water equations are of two kind: naturally stable formulations, and stabilized formulations. Le Roux et al. (1998) presented a review of possible solution to obtain a stable finite element formulation for large scale flows. Among the proposed finite element pairs, the $P_1^{NC} - P_1$ pair, using non-conforming linear elements for velocities and continuous linear elements for sea-surface elevation, was the most promising. Hanert et al. (2005) proposed a complete description of a scheme based on this element pair. However, it appears that this scheme is unstable in the inviscid limit. **The first objective of this thesis was to obtain a stable formulation for the shallow water equations, for all range of parameters relevant to large scale oceanography**.

Geophysical flows develop at the surface of Earth, and this surface is not flat. Representing the surface of the sphere with a single two-dimensional frame of reference leads to singularities at poles, where the metric terms are ill-defined. In finite difference discretizations, the computational grid is intrinsically linked to the parameterization of the surface hosting the flow. It is not the case anymore using finite elements. When the regularity constraint on the surface representation is relaxed, several new algorithms can be designed. **The second objective of this thesis was to develop a suitable algorithm for the model to operate in spherical geometry.**

White et al. (2008a,b) presented the first version of the three-dimensional SLIM. This version was based on the $P_1^{NC} - P_1$ pair of elements, and did not include baroclinic effects, i.e. effects of density gradient on momentum. Indeed, baroclinicity induces a significant increase in the possible complexity of the flow. For barotropic flows, the only hyperbolic phenomena are surface gravity waves and advection. For baroclinic flows, internal wave dynamics appears. Barotropic large-scale geophysical flows are always subcritical, while internal waves can break. **The third, most important objective of the thesis, was to develop a three-dimensional baroclinic model.** On the one hand, an accurate spatial discretization must be deduced. On the other hand, an efficient time discretization must be performed.

Outline of the thesis

This manuscript is built as the collection of four papers written in the course of this thesis, reproduced here as four chapters.

In Chapter 2, we study a finite element formulation for the shallow water equations where a stabilization is induced using a Riemann solver for the interface terms. This formulation is used with five finite element pairs. The benefits and drawbacks of each solution are compared on a set of idealized benchmark triggering the main limit cases that appear in large scale oceanography.

In Chapter 3, we detail a new algorithm to solve vectorial system of equations on arbitrary curved surfaces, and validate this approach using standard benchmarks for the shallow water equations on the sphere. The main idea of this algorithm is to define a Cartesian frame of reference for each vectorial degree of freedom, and for each geometrical entity where finite element integrals are computed. This approach induces no modification in the discrete finite element formulation, all the metric terms are embedded in transfer operators used to switch between frames of reference. A similar approach using

local frames of reference has been designed by Bernard et al. (2009), enabling optimal convergence for high order discretizations.

In Chapter 4, we detail the spatial discretization of the baroclinic model that we have developed. This model is based on discontinuous Galerkin finite elements, taking into account the characteristic structure of the equations related to internal waves.

In Chapter 5, we detail the temporal discretization of this model. The range of propagation speeds is so wide for large scale oceanography that if we are interested in the slow dynamics, we cannot solve the fast dynamics explicitly. In this Chapter, we present a solution based on a mode-splitting approach, where the fast dynamics is solved implicitly while the slow dynamics is solved explicitly, using implicit-explicit (IMEX) methods.

Chapter 6 provides concluding remarks and perspectives for the future of the model.

Supporting publications

R. Comblen, S. Legrand, E. Deleersnijder, and V. Legat. A finite element method for solving the shallow water equations on the sphere. *Ocean Modelling*, 28:12–23, 2009. doi: 10.1016/j.ocemod.2008.05.004.

R. Comblen, J. Lambrechts, J.-F. Remacle, and V. Legat. Practical evaluation of five part-discontinuous finite element pairs for the non-conservative shallow water equations. *International Journal for Numerical Methods in Fluids*, 73:701–724, 2010. doi: 10.1002/fld.2094.

S. Blaise, **R. Comblen**, V. Legat, J.-F. Remacle, E. Deleersnijder, and J. Lambrechts. A discontinuous finite element baroclinic marine model on unstructured prismatic meshes. Part I: space discretization. *Ocean Dynamics (submitted)*, 2010.

R. Comblen, S. Blaise, V. Legat, J.-F. Remacle, E. Deleersnijder, and J. Lambrechts. A discontinuous finite element baroclinic marine model on unstructured prismatic meshes. Part II: implicit/explicit time discretization. *Ocean Dynamics (submitted)*, 2010.

O. Gourgue, **R. Comblen**, J. Lambrechts, T. K. V. Legat, and E. Deleersnijder. A flux-limiting wetting-drying method for finite-element shallow-water models, with application to the Scheldt Estuary. *Advances in Water Resources*, 32:1726–1739, 2009. doi: 10.1016/j.advwatres.2009.09.005.

S. Blaise, B. de Brye, A. de Brauwere, E. Deleersnijder, E. J. M. Delhez, and **R. Comblen**. Capturing the residence time boundary layer - application to the Scheldt Estuary. *Ocean Dynamics (in press)*, 2010. doi: 10.1007/s10236-010-0272-8.

B. de Brye, A. de Brauwere, O. Gourgue, T. Kärnä, J. Lambrechts, **R. Comblen**, and E. Deleersnijder. A finite-element, multi-scale model of the Scheldt tributaries, river, estuary and ROFI. *Coastal Engineering*, 57:850–863, 2010. doi: 10.1016/j.coastaleng.2010.04.001.

T. Kärnä, B. de Brye, O. Gourgue, J. Lambrechts, **R. Comblen**, V. Legat, and E. Deleersnijder. A fully implicit wetting-drying method for DG-FEM shallow water model. *Computer Methods in Applied Mechanics and Engineering (in press)*, 2010. doi: 10.1016/j.cma.2010.07.001.

A. de Brauwere, F. D. Ridder, O. Gourgue, J. Lambrechts, **R. Comblen**, R. Pintelon, J. Passerat, P. Servais, M. Elskens, W. Baeyens, T. Kärnä, B. de Brye, and E. Deleersnijder. Design of a sampling stategy to optimally calibrate a reactive transport model: Exploring the potential for Escherichia coli in the Scheldt Estuary. *Environmental Modelling & Software*, 24:969–981, 2009.
doi: 10.1016/j.envsoft.2009.02.004.

J. Lambrechts, **R. Comblen**, V. Legat, C. Geuzaine, and J.-F. Remacle. Multiscale mesh generation on the sphere. *Ocean Dynamics*, 58(5):461–473, 2008.
doi: 10.1007/s10236-008-0148-3.

P.-E. Bernard, J.-F. Remacle, **R. Comblen**, V. Legat, and K. Hillewaert. High-order discontinuous Galerkin schemes on general 2d manifolds applied to the shallow water equations. *Journal of Computational Physics*, 228:6514–6535, 2009.
doi: 10.1016/j.jcp.2009.05.046.

CHAPTER 2

COMPARISON OF FINITE ELEMENT PAIRS FOR THE SHALLOW-WATER EQUATIONS

This Chapter reproduces an updated version of the following paper, first submitted on 28 November 2008:

R. Comblen, J. Lambrechts, J.-F. Remacle, and V. Legat. Practical evaluation of five part-discontinuous finite element pairs for the non-conservative shallow water equations. *International Journal for Numerical Methods in Fluids*, 73:701–724, 2010.
doi: 10.1002/fld.2094.

Abstract

This paper provides a comparison of five finite element pairs for the shallow water equations. We consider continuous, discontinuous and partially discontinuous finite element formulations that are supposed to provide second order spatial accuracy. All of them rely on the same weak formulation, using a Riemann solver to evaluate interface integrals. We define several asymptotic limit cases of the shallow water equations within their space of parameters. The idea is to develop a comparison of these numerical schemes in several relevant regimes of the subcritical shallow water flow. Finally, a new pair, using non-conforming linear elements for both velocities and elevation (P_1^{NC}-P_1^{NC}), is presented, giving optimal rates of convergence in all test cases. The P_1^{NC}-P_1 and P_1^{DG}-P_1 mixed formulations lack of convergence for inviscid flows. The P_1^{DG}-P_2 pair is more expensive but provides accurate results for all benchmarks. The P_1^{DG}-P_1^{DG} provides an efficient option, except for inviscid Coriolis-dominated flows, where a small lack of convergence is observed.

2.1 Introduction

The shallow water equations are a classical model used in a wide area of physics and engineering. They govern flows in estuaries, enable modeling of dam-breaks, floods and tides, and are a key building block for ocean modeling as well as atmosphere modeling. Different numerical methods have been designed for the shallow water equations. Finite volumes are very popular for small scale applications as well as atmosphere modeling, whereas ocean models are mainly based on finite difference methods (Mesinger and Arakawa, 1976), as described for instance in the book Griffies (2004). In the finite element framework, major contributions have been developed with both discontinuous and continuous elements.

The Discontinuous Galerkin (DG) method focuses growing interest since the late nineties, and gives accurate results for hyperbolic conservation laws. Basically, it consists in a volume term built as in all finite element methods, and an interface term built as in finite volume methods. High order shape functions can be easily incorporated and at the interfaces, an efficient upwind flux calculation can be performed to tackle the treatment of wave phenomena. Thanks to the absence of continuity constrain on the inter-element boundaries, h-adaptivity (Hartmann and Houston, 2002; Bernard et al., 2007) and p-adaptivity (Burbeau and Sagaut, 2005) can be easily implemented. Efficient slope and flux limiters enable positive and shock-capturing versions of the scheme (Cockburn and Shu, 1998b; Chevaugeon et al., 2005; Remacle et al., 2006). For atmosphere modeling, the high order capabilities of this scheme are really attractive (Nair et al., 2005; Giraldo, 2006), and the increasing use of DG follows the trend to replace spectral transform methods with local ones. Coastal modeling also benefits from this method (Aizinger and Dawson, 2002; Kubatko et al., 2006; Bernard et al., 2008a), and high Froude number flows are accurately captured by this kind of schemes (Schwanenberg and Harms, 2004; Remacle et al., 2006). However, the implementation of elliptic dissipative terms requires some specific modifications, as reviewed in Arnold et al. (2002). The local-DG method (LDG) and the interior penalty method (IP) are among the most popular solutions. LDG introduces a mixed formulation for velocities and stress and can be difficult to handle with an implicit time-stepping (Cockburn and Shu, 1998a), while IP requires the introduction of a penalty parameter that worsens the conditioning of the discrete spatial operator (Riviere, 2008).

Continuous linear finite elements are compelling as they provide high geometric flexibility, they are supposed to be much more accurate than first order methods, and have fewer degrees of freedom than linear discontinuous Galerkin methods. Further, they naturally handle elliptic operators used as subgrid scale models. Several choices can be made between stable mixed methods, and stabilized methods. Stabilized methods were first designed for scalar advection-diffusion equation, where the standard Galerkin method gives oscillating result when the mesh Peclet number is too large (Donea and Huerta, 2003). For shallow water models, Bova and Carey (1996); Hauke (1998); Ribeiro et al. (2001); Hauke (2002) use a symmetric formulation that is stabilized with Petrov-Galerkin approach.

In this paper, we do not analyze stabilized continuous finite elements methods, we choose to use naturally stable finite elements. Furthermore, to develop a fair comparison with all stabilized continuous formulations, it would require a very systematic analysis that is out of the scope of this paper.

The search for an efficient mixed formulation for the shallow water equations without explicit stabilization is described in a series of papers (Le Roux et al., 1998; Le Roux et al., 2000; Le Roux, 2001; Hanert et al., 2005; Le Roux et al., 2005; Le Roux, 2005; Hanert et al., 2008). The favorite candidate is the $P_1^{NC} - P_1$ pair, namely linear non-conforming P_1^{NC} for the velocities, and linear conforming P_1 for the elevation. This pair was first presented by Hua and Thomasset (1984) within the framework of two-layer models. The idea is simple: try to mimic the staggering of variables used in finite difference schemes in the finite element framework. Le Roux et al. (1998) provide a seminal review paper on mixed methods for finite element shallow water and initiated several works on the $P_1^{NC} - P_1$ mixed element pair. Further, this pair has been shown to be free of spurious elevation modes (Le Roux et al., 2005), and it has been tested with both Eulerian and Lagrangian discretizations of advection terms (Hanert et al., 2005). In the inviscid limit, the semi-Lagrangian discretization of Hanert et al. (2005) exhibits a strong noise in the velocity field, which needs to be filtered out. The Eulerian formulation described in this paper appears to avoid this noise, due to the stabilizing effect of the upwind scheme on advection terms. The analysis of dispersion and dissipation properties is performed by Le Roux (2005) where a semi-analytical dispersion relation is derived on structured grids. Dissipation and dispersion relations are computed numerically on unstructured grids by Bernard et al. (2008b). It appears that the $P_1^{NC} - P_1$ pair works really well on structured grids, but is suboptimal on unstructured grids, in terms of accuracy (Hanert et al., 2008) and in terms of dispersion. Recently, a new mixed element, $P_1^{DG} - P_2$, has been presented. Such an element exhibits stability and good rates of convergence for the Stokes problem and the wave equation (Cotter et al., 2009a) and has been proven to be LBB stable (Cotter et al., 2009b).

Within its space of parameters, the shallow water system has several asymptotic limit cases. In the steady viscous limit, the well-known Stokes system is found. The linear non-rotating and inviscid shallow water equations reduce to a wave equation. When the Coriolis force is the leading term, we observe a geostrophic equilibrium. An almost optimal finite element method is known for each of those problems. The Stokes problem is a saddle-point problem, and the finite element formulation needs to satisfy the LBB condition, which for Galerkin formulations leads to choose a larger discrete space for velocities than for elevation, for instance P_2-P_1. The velocities and elevation have a symmetric role in the wave equation, so using the same space for both fields is the natural solution. In the geostrophic limit, the space for velocities is the gradient of the space for elevation, and a pair like P_1^{DG}-P_2^{DG} appears to be best suited. Of course, in real life applications, those different regimes are mixed, and a formulation at least stable in all ranges of parameters is sought. Our typical domain of application is estuarine, coastal and ocean modeling. Therefore, we do not put the focus on supercritical flows, where shocks require specific handling, while we are aware that this regime is of crucial importance for smaller scale applications.

In this paper, we focus on numerical schemes where the stabilizing strategies are only applied on the interface terms. It must be noted that it would be also possible to add stabilizing terms in the surface terms as it is usual in continuous stabilized formulations. In general, continuous stabilizing terms correspond to adding diffusion with a coefficient depending on the element size, in a more or less consistent manner. For discontinuous methods, the interfaces integrals are estimated with an upwind bias introducing the right amount of dissipation to keep the scheme stable. We provide here a comparison between different finite element pairs that all rely on the same weak formulation: $P_1^{DG} - P_1^{DG}$,

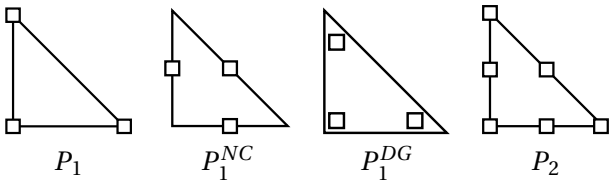

Figure 2.1: Sketch of the different finite elements used.

$P_1^{NC} - P_1^{NC}$, $P_1^{NC} - P_1$, $P_1^{DG} - P_1$ and $P_1^{DG} - P_2$. A sketch of those elements is given in Figure 2.1.

The outline of this paper is the following: Section 2.2 explains the methodology followed to derive all the formulations in the framework of one-dimensional linear shallow-water equations, Section 2.3 details the formulation for the five finite element pairs considered, and finally, we assess the qualities and drawbacks of each formulation in Section 2.4.

2.2 One-dimensional illustration of key concepts

In this section, the main concepts used in this paper are illustrated for the one-dimensional wave equation, which is the simplest idealization of the shallow water equations. The one-dimensional wave equation reads:

$$\frac{\partial^2 \eta}{\partial t^2} = g h \frac{\partial^2 \eta}{\partial x^2}, \tag{2.1}$$

and is equivalent to the following system of equations, known as the linearized inviscid shallow water equations in a non-rotating framework:

$$\frac{\partial \eta}{\partial t} + h\frac{\partial u}{\partial x} = 0, \tag{2.2}$$

$$\frac{\partial u}{\partial t} + g\frac{\partial \eta}{\partial x} = 0, \tag{2.3}$$

where u is the depth-averaged velocity, η the free surface elevation, h the depth at rest and g the gravitational acceleration.

We analyze the selection of mixed continuous or discontinuous spaces and the design of a suitable Riemann solver. In particular, three different finite element pairs are considered:

- $P_1 - P_1$ elements, for velocity and elevation, respectively.
- $P_1^{DG} - P_1^{DG}$ elements, the one-dimensional equivalent to the $P_1^{DG} - P_1^{DG}$ two-dimensional pair and the closest to the $P_1^{NC} - P_1^{NC}$ pair.
- $P_1^{DG} - P_1$ elements, which is the closest to two-dimensional $P_1^{NC} - P_1$ and $P_1^{DG} - P_1$.

All mixed methods rely on the same weak formulation:

$$< \frac{\partial \eta}{\partial t}\hat{\eta} > + < h\frac{\partial u}{\partial x}\hat{\eta} > = 0, \tag{2.4}$$

$$< \frac{\partial u}{\partial t}\hat{u} > + < g\frac{\partial \eta}{\partial x}\hat{u} > = 0, \tag{2.5}$$

with < > denoting the integral over Ω, and $\hat{\eta}$ and $\hat{u}$ the test functions. This domain Ω is then discretized into a mesh or a collection of non-overlapping elements Ω_e. Equations (2.4-2.5) can be expressed as a sum of the integrals on each element:

$$\sum_e \left(< \frac{\partial \eta}{\partial t} \hat{\eta} >_{\Omega_e} + < h \frac{\partial u}{\partial x} \hat{\eta} >_{\Omega_e} \right) = 0, \tag{2.6}$$

$$\sum_e \left(< \frac{\partial u}{\partial t} \hat{u} >_{\Omega_e} + < g \frac{\partial \eta}{\partial x} \hat{u} >_{\Omega_e} \right) = 0. \tag{2.7}$$

Finally, in order to incorporate the local Neumann boundary condition, we integrate the gradient terms by part:

$$\sum_e \left(< \frac{\partial \eta}{\partial t} \hat{\eta} >_{\Omega_e} + h u^* \hat{\eta} \Big|_{\partial \Omega_e} - < h u \frac{\partial \hat{\eta}}{\partial x} >_{\Omega_e} \right) = 0, \tag{2.8}$$

$$\sum_e \left(< \frac{\partial u}{\partial t} \hat{u} >_{\Omega_e} + g \eta^* \hat{u} \Big|_{\partial \Omega_e} - < g \eta \frac{\partial \hat{u}}{\partial x} >_{\Omega_e} \right) = 0, \tag{2.9}$$

where $f\Big|_{\partial \Omega_e}$ denotes the difference between f at the right end of the element and f at the left end. The values of the fields at both ends of each interval are denoted with a star superscript, because they need to be uniquely defined for both neighboring elements of the interface. The way to define u^* and η^* is the key ingredient to obtain a stable and accurate numerical formulation. Along interior interfaces, for continuous test functions, the boundary integral on the one element is canceled out by the boundary integral on the other element, but it is not the case for discontinuous test functions.

Riemann solver

To derive consistent values of fluxes u^* and η^* at the interface, relying on the characteristic structure of the equations, it is usual to introduce Riemann solver for numerical methods. Riemann solvers are a solution to deduce consistent values of fluxes. It allows to add just enough numerical dissipation to keep the scheme stable. For a scalar advection equation, using the upwind value at the interface introduces the right amount of dissipation that prevents the oscillations of the numerical solution. The Riemann solvers can be viewed as the generalization of the upwinding technique for systems of equations.

In matrix notation, the shallow water system of equations (2.2-2.3) reads:

$$\begin{pmatrix} \eta_{,t} \\ u_{,t} \end{pmatrix} + \underbrace{\begin{pmatrix} 0 & h \\ g & 0 \end{pmatrix}}_{A} \begin{pmatrix} \eta_{,x} \\ u_{,x} \end{pmatrix} = \begin{pmatrix} 0 \\ 0 \end{pmatrix}. \tag{2.10}$$

Let us now perform a change of variable such that the matrix A becomes diagonal. We then obtain the shallow water equations in terms of the characteristic variables:

$$\begin{pmatrix} U \\ V \end{pmatrix} = R^{-1} \begin{pmatrix} \eta \\ u \end{pmatrix} = \begin{pmatrix} \frac{\eta}{2} + \sqrt{\frac{h}{g}} \frac{u}{2} \\ \frac{\eta}{2} - \sqrt{\frac{h}{g}} \frac{u}{2} \end{pmatrix}, \tag{2.11}$$

where R is the matrix whose columns are the eigenvectors of A:

$$R = \begin{pmatrix} 1 & 1 \\ \sqrt{g/h} & -\sqrt{g/h} \end{pmatrix}. \tag{2.12}$$

The system in terms of the characteristic variables corresponds to two uncoupled advection equations:

$$\begin{pmatrix} U_{,t} \\ V_{,t} \end{pmatrix} + \begin{pmatrix} \sqrt{gh} & 0 \\ 0 & -\sqrt{gh} \end{pmatrix} \begin{pmatrix} U_{,x} \\ V_{,x} \end{pmatrix} = \begin{pmatrix} 0 \\ 0 \end{pmatrix}. \tag{2.13}$$

We define the $*$ variables using the upwind value, that depends on the sign of the eigenvalue:

$$U^* = U^L, \quad V^* = V^R, \tag{2.14}$$

where the L and R superscript denote values taken at the left and right side of the interface, respectively. Expressing the original variables in terms of the characteristic ones, we get:

$$\eta = U + V, \quad u = \sqrt{\frac{g}{h}}(U - V), \tag{2.15}$$

and we derive the classical well-known expressions:

$$\eta^* = U^L + V^R = \{\eta\} + \sqrt{\frac{h}{g}}[u], \quad u^* = \sqrt{\frac{g}{h}}(U^L - V^R) = \{u\} + \sqrt{\frac{g}{h}}[\eta], \tag{2.16}$$

with $\{a\} = \frac{a^L + a^R}{2}$ the mean and $[a] = \frac{a^L - a^R}{2}$ the half jump.

The same methodology can be applied to the hybrid continuous/discontinuous finite element pair. The interface terms in the elevation equation disappear due to the continuity of the test functions, as corresponding equal contributions are added at a node by the two elements surrounding the interface. If η is continuous, (2.16) degenerates to:

$$\eta^* = \eta + \sqrt{\frac{h}{g}}[u], \quad u^* = \{u\}. \tag{2.17}$$

To assess the quality of this formulation with the three finite element pairs, we have performed a convergence analysis on a wave problem with periodic boundary conditions (Figure 2.2). We observe second order accuracy for each discretization. The optimal rate of convergence observed with the hybrid discretization $P_1^{DG} - P_1$ shows that using a mixed discontinuous-continuous pair of elements is not a priori a bad idea, even if the number of degrees of freedom is different, and so the symmetry of the discretization is broken.

2.3 Two-dimensional discretization of the shallow water equations

Let us now consider the complete shallow water equations including inertia terms, Coriolis effects, viscous terms, and both wind and bottom stresses. It is usual to distinct two classical formulations, when deriving a numerical scheme. On the one hand, the conservative formulation in terms of the total depth H and the transport $H\boldsymbol{u}$ reads:

$$\frac{\partial H}{\partial t} + \nabla \cdot \big(H\boldsymbol{u}\big) = 0, \tag{2.18}$$

$$\frac{\partial H\boldsymbol{u}}{\partial t} + \nabla \cdot \big(H\boldsymbol{u}\boldsymbol{u}\big) + f\boldsymbol{k} \times \big(H\boldsymbol{u}\big) + gH\nabla\big(H - h\big) = \nabla \cdot \Big(H\nu\big(\nabla \boldsymbol{u}\big)\Big) + \frac{\boldsymbol{\tau}^s + \boldsymbol{\tau}^b}{\rho}, \tag{2.19}$$

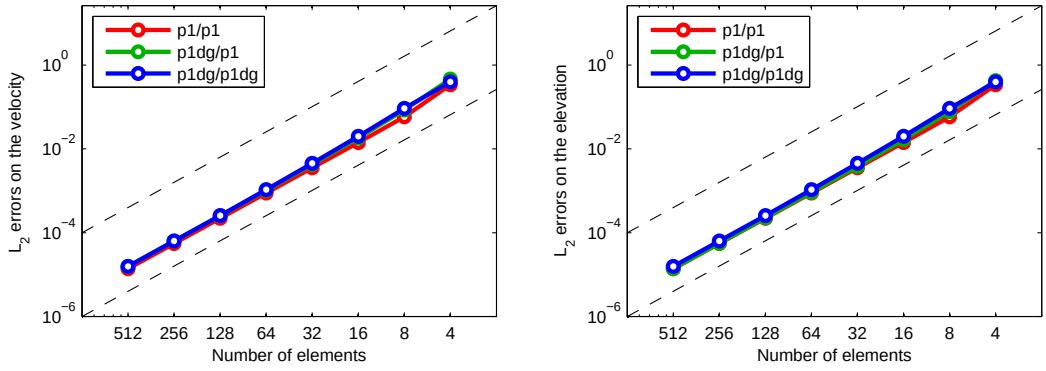

Figure 2.2: Convergence analysis for the wave equation with periodic boundary conditions. Second order convergence is observed on both fields for three mixed linear continuous/discontinuous discretizations.

with h the depth at rest, f is the Coriolis factor, $\boldsymbol{k}$ the vertical unit vector, $\boldsymbol{\tau}^s$ and $\boldsymbol{\tau}^b$ the surface and bottom stresses, ρ the density and ν the eddy viscosity. On the other hand, the non-conservative formulation in terms of free-surface elevation η (with $H = h + \eta$) and velocity $\boldsymbol{u}$ reads:

$$\frac{\partial \eta}{\partial t} + \nabla \cdot \Big((h+\eta)\ \boldsymbol{u} \Big) = 0, \tag{2.20}$$

$$\frac{\partial \boldsymbol{u}}{\partial t} + \boldsymbol{u} \cdot \big(\nabla \boldsymbol{u}\big) + f\boldsymbol{k} \times \boldsymbol{u} + g\nabla\eta = \frac{1}{H}\nabla \cdot \Big(H\nu\big(\nabla \boldsymbol{u}\big)\Big) + \frac{\boldsymbol{\tau}^s + \boldsymbol{\tau}^b}{\rho H}. \tag{2.21}$$

It is customary to use the conservative formulation when deriving finite difference schemes for the shallow water equations, in order to obtain a conservative numerical scheme. However, in a continuous framework, both formulation are strictly equivalent.

In this paper, we use the non-conservative form of the shallow water equations to derive the weak formulation, with a nonlinear approximate Riemann solver deduced from the conservative form of the same equations. This approach might appear exotic but it is motivated by the following facts. Firstly, it is natural to write a Riemann solver in terms of fluxes of quantities to be conserved. Secondly, it would be attractive to write a weak conservative formulation but in this case, the elevation gradient term has to be split in two parts, a flux term and a source term:

$$gH\nabla\big(H-h\big) = \frac{g\nabla\big(H^2-h^2\big)}{2} - g\big(H-h\big)\nabla h. \tag{2.22}$$

With discontinuous Galerkin methods, both terms are not treated in the same way. It has been shown that the scheme may exhibit nonphysical oscillations if the integration is not accurate enough (Bernard et al., 2008a). Therefore, a weak non-conservative formulation seems more efficient and robust in the considered numerical discretization.

Non-conservative weak formulation

The weak form of this non-conservative formulation reads:

$$\sum_e \left(< \frac{\partial \eta}{\partial t} \hat{\eta} >_{\Omega_e} + < \nabla \cdot \Big((h+\eta)\ \boldsymbol{u} \Big) \hat{\eta} >_{\Omega_e} \right) = 0 \,, \tag{2.23}$$

$$\begin{aligned} \sum_e \Big(& < \frac{\partial \boldsymbol{u}}{\partial t} \cdot \hat{\boldsymbol{u}} >_{\Omega_e} + < \boldsymbol{u} \cdot \big(\nabla \boldsymbol{u}\big) \cdot \hat{\boldsymbol{u}} >_{\Omega_e} + < f(\boldsymbol{k} \times \boldsymbol{u}) \cdot \hat{\boldsymbol{u}} >_{\Omega_e} + g < \big(\nabla \eta\big) \cdot \hat{\boldsymbol{u}} >_{\Omega_e} \Big) \\ & = \sum_e \left(< \frac{1}{H} \nabla \cdot \Big(H \nu \big(\nabla \boldsymbol{u}\big) \Big) \cdot \hat{\boldsymbol{u}} >_{\Omega_e} + < \frac{\boldsymbol{\tau}^s + \boldsymbol{\tau}^b}{\rho H} \cdot \hat{\boldsymbol{u}} >_{\Omega_e} \right). \end{aligned} \tag{2.24}$$

Again integrating by parts, we get:

$$\sum_e \left(< \frac{\partial \eta}{\partial t} \hat{\eta} >_{\Omega_e} + \ll (h+\eta^*) u_n^* \hat{\eta} \gg_{\partial \Omega_e} - < (h+\eta)\ \boldsymbol{u} \cdot \nabla \hat{\eta} >_{\Omega_e} \right) = 0 \,, \tag{2.25}$$

$$\begin{aligned} & \sum_e \Big(< \frac{\partial \boldsymbol{u}}{\partial t} \cdot \hat{\boldsymbol{u}} >_{\Omega_e} + \ll u_n^* \boldsymbol{u}^* \cdot \hat{\boldsymbol{u}} \gg_{\partial \Omega_e} - < \nabla \cdot \big(\boldsymbol{u} \hat{\boldsymbol{u}} \big) \cdot \boldsymbol{u} >_{\Omega_e} \\ & \qquad + < f(\boldsymbol{k} \times \boldsymbol{u}) \cdot \hat{\boldsymbol{u}} >_{\Omega_e} + g \ll \eta^* \hat{u}_n \gg_{\partial \Omega_e} - g < \eta \big(\nabla \cdot \hat{\boldsymbol{u}} \big) >_{\Omega_e} \Big) \\ = & \sum_e \Big(\ll \nu \Big\{ \frac{\partial \boldsymbol{u}}{\partial n} \Big\} \cdot \hat{\boldsymbol{u}} \gg_{\partial \Omega_e} - < \nu \big(\nabla \boldsymbol{u} \big) : \big(\nabla \hat{\boldsymbol{u}} \big) >_{\Omega_e} \\ & \qquad + < \nu \frac{1}{H} \big(\nabla H \big) \cdot \big(\nabla \boldsymbol{u} \big) \cdot \hat{\boldsymbol{u}} >_{\Omega_e} + < \frac{\boldsymbol{\tau}^s + \boldsymbol{\tau}^b}{\rho H} \cdot \hat{\boldsymbol{u}} >_{\Omega_e} \Big) . \end{aligned} \tag{2.26}$$

The vector quantities multiplied by the outward normal are denoted with a n subscript. Again, the variables used in the boundary integrals are doubled-valued, and are denoted with a star superscript. However, for the diffusive flux, it is natural to take the centered values denoted by $\{\ \ \}$, as diffusive phenomena are isotropic. As explained in the introduction, a specific treatment is needed to obtain a stable and accurate discretization of the diffusive term when using discontinuous elements for the velocities. We implement an incomplete interior penalty method (IIPG), following Riviere (2008). In this case, the following term is added in the right-hand side of equation (2.26):

$$\sum_e \Big(- \ll \nu \sigma \hat{\boldsymbol{u}} \cdot [\boldsymbol{u}] \gg_{\partial \Omega_e} \Big), \tag{2.27}$$

with σ a penalization parameter defined as:

$$\sigma = \frac{(p+1)(p+2)}{h}, \tag{2.28}$$

with h a typical length scale of the element, and p the polynomial order of the finite element space. This value of the penalization parameter has been proposed by Shahbazi (2005).

Approximate nonlinear Riemann solver

A Riemann solver cannot be applied on the non-conservative form of the equations, as they are not in flux form. To derive the Riemann solver, we use the conservative form (2.18-2.19) of the shallow water equations, where the dissipation, Coriolis and diffusion

terms are neglected. Considering u the velocity normal to the interface, and v the velocity tangent to the interface, the flux reads:

$$F = \begin{pmatrix} F_H \\ F_{Hu} \\ F_{Hv} \end{pmatrix} = \begin{pmatrix} Hu \\ Huu + \frac{g}{2}H^2 \\ Huv \end{pmatrix}. \tag{2.29}$$

The exact Riemann solver requires the resolution of a nonlinear problem at each integration point. It is usually preferred to use an approximate Riemann solver. In order to deduce such an approximate Riemann solver, the next step consists in linearizing the fluxes. The Jacobian matrix of the fluxes is:

$$J = \begin{pmatrix} 0 & 1 & 0 \\ -u^2 + gH & 2u & 0 \\ -uv & v & u \end{pmatrix}. \tag{2.30}$$

Finally, we use the Roe averages to obtain a approximate Jacobian matrix $J_{\text{linearized}}$, as in classical textbooks (LeVeque, 2002). This rule can be deduced easily from the Rankine-Hugoniot relation:

$$J_{\text{linearized}} \begin{pmatrix} [H] \\ [Hu] \\ [Hv] \end{pmatrix} = [F]. \tag{2.31}$$

As the first line of the Jacobian matrix is linear, the Rankine-Hugoniot relation leads to an underdetermined system. To obtain a unique solution of the system, we select the arithmetic mean for H, and we get the classical Roe averages:

$$H_{\text{Roe}} = \{H\}, \tag{2.32}$$

$$u_{\text{Roe}} = \frac{u_L\sqrt{H_L} + u_R\sqrt{H_R}}{\sqrt{H_L} + \sqrt{H_R}}, \tag{2.33}$$

$$v_{\text{Roe}} = \frac{v_L\sqrt{H_L} + v_R\sqrt{H_R}}{\sqrt{H_L} + \sqrt{H_R}}. \tag{2.34}$$

By substituting (H, u, v) by $(H_{\text{Roe}}, u_{\text{Roe}}, v_{\text{Roe}})$ in the Jacobian, the approximate Riemann values of the conservative variables can be deduced as the exact solution of the linearized problem, as shown in the illustrative one-dimensional wave equation. The values of the conservative and non-conservative variables at the interface are given by:

$$H^* = \{H\} + \frac{1}{\sqrt{gH_{\text{Roe}}}}\left([Hu] - u_{\text{Roe}}[H]\right), \tag{2.35}$$

$$(Hu)^* = \{Hu\} + \frac{1}{\sqrt{gH_{\text{Roe}}}}\left(u_{\text{Roe}}[Hu] - u_{\text{Roe}}^2[H]\right) + \sqrt{gH_{\text{Roe}}}[H], \tag{2.36}$$

$$(Hv)^* = (Hv)_{\text{upwind}} + v_{\text{Roe}}(\{H\} - H_{\text{upwind}}) + \frac{1}{\sqrt{gH_{\text{Roe}}}}\left(v_{\text{Roe}}[Hu] - u_{\text{Roe}}v_{\text{Roe}}[H]\right), \tag{2.37}$$

$$\eta^* = H^* - h, \tag{2.38}$$

$$u^* = \frac{(Hu)^*}{H^*}, \tag{2.39}$$

$$v^* = \frac{(Hv)^*}{H^*}. \tag{2.40}$$

2.4 Mesh refinement methodology

Description of the meshes

Convergence tests are carried out with a family of 25 meshes adapted to the reference solution of the flow except for both wave problems where uniform unstructured meshes are used. We use adapted meshes rather than uniform meshes, since some of the studied flows have western boundary layers that need to be sufficiently resolved to observe the asymptotic convergence of the schemes. Using uniform meshes would require many more elements to observe asymptotic behavior. Note that this is different from mesh adaptation in time, where the mesh is adapted to the numerically computed flow during the simulation, as in Bernard et al. (2007). The greatest eigenvalue of the elevation field's Hessian matrix is used as an a priori error estimator, since with linear elements, the error is dominated by the quadratic component of the solution. We define a reference edge length field δ as:

$$\delta(x,y) = \sqrt{\frac{\int_\Omega e(x',y')\,dx'dy'}{e(x,y)}}. \tag{2.41}$$

where $e(x,y)$ is the norm of the greatest eigenvalue of the Hessian matrix of the elevation field. The meshes are generated using Gmsh (Geuzaine and Remacle, 2009), where we use $h\delta$ as edge length field, with h a constant over the domain. The generated meshes have therefore about $1/(ah^2)$ elements, with $a \approx 0.8$ the typical area of a triangle whose edge have unit length. Such meshes are designed optimally for schemes giving second order accuracy, i.e. among all the meshes with such a number of elements, these meshes provide the best results. However, the mesh need not to be optimally adapted to observe the right convergence behavior. If it is suitably adapted, asymptotic convergence will occur with fewer elements. In Figure 2.3, we show the reference edge length field δ and five of the corresponding meshes for the nonlinear Munk testcase. The 9^{th} finest mesh of each family, made of about 2500 triangles, are shown in Figures 2.5 to 2.9. Reference solutions are obtained using highly accurate P_3^{DG}-P_2^{DG} scheme for Stokes problem and P_3^{DG}-P_3^{DG} scheme for all other problems, using the same discrete formulation and time-stepping algorithm on the finest mesh used for the convergence tests.

Description of the 8 testcases

In realistic applications, a process, i.e. advection, geostrophy, diffusion, etc..., can be the leading phenomena in some areas while being almost negligible in other areas for a single computation. Therefore, the limit cases including or not including this phenomenon have both to be solved accurately. Unfortunately, it is not the case for some schemes that would appear to be attractive otherwise.

Considering typical oceanic and coastal flows, we define a serie of testcases, with the corresponding relevant meshes, detailed in Figures 2.4, 2.5, 2.6, 2.7, 2.8 and 2.9. The objective is to compare fairly the proposed finite element pairs. Three limit flow states of the shallow water system, namely geostrophy, wave propagation and viscosity, are tested separately, and then the complexity of the problem is increased toward more realistic computations. Each flow develops in a square basin of 1000×1000 km.

Some of the testcases use a zonal wind stress, defined as:

$$\boldsymbol{\tau}^s = 0.1 \times \sin\left(\pi \frac{y}{L}\right) \boldsymbol{e}_x, \tag{2.42}$$

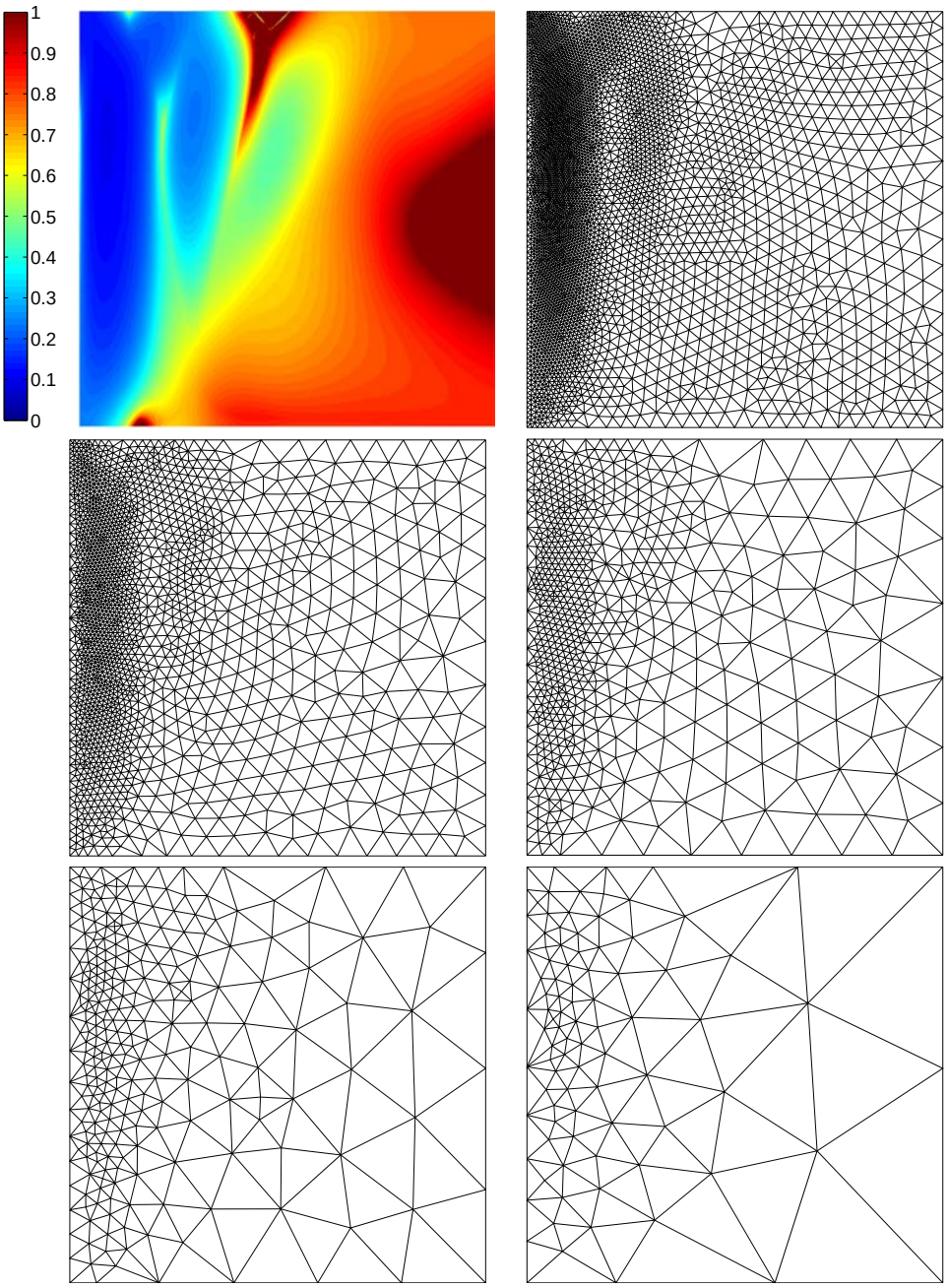

Figure 2.3: Sketch of the edge-length field δ and five corresponding meshes for the nonlinear Munk testcase.

	L $[m]$	H $[m]$	g $[ms^{-2}]$	f $[s^{-1}]$	β $[m^{-1}s^{-1}]$	γ $[s^{-1}]$	ν $[m^2s^{-1}]$	Nonlinear advection and free-surface terms	Wind stress
Unsteady wave	10^6	10^3	9.81	0	0	0	0	no	no
Steady wave	10^6	10^3	9.81	0	0	10^{-6}	0	no	yes
Stokes	10^6	10^3	9.81	0	0	0	10^4	no	yes
Geostrophic equilibrium	10^6	10^3	9.81	10^{-4}	0	0	0	no	no
Stommel gyre	10^6	10^3	9.81	10^{-4}	2×10^{-11}	10^{-6}	0	no	yes
Munk gyre	10^6	10^3	9.81	10^{-4}	2×10^{-11}	0	10^4	no	yes
Advective Stommel gyre	10^6	10^3	9.81	10^{-4}	2×10^{-11}	5×10^{-7}	0	yes	yes
Advective Munk gyre	10^6	10^3	9.81	10^{-4}	2×10^{-11}	0	3000	yes	yes

Table 2.1: Summary of physical parameters for each testcase.

inducing a clockwise circulation, and a linear dissipation term defined as:

$$\boldsymbol{\tau}^b = -\rho h \gamma \boldsymbol{u}. \tag{2.43}$$

For all the testcases, we use slipping coasts. Indeed, we do not consider problems with a viscous boundary layer. The testcases with viscosity need a second boundary condition, so we cancel out the normal flux of tangential velocity, and we compute the normal flux of normal velocity with the interior value of the velocity. Table 2.1 summarizes the physical parameters that define each testcase.

Wave equation

As a first testcase, we consider the linear wave equation:

$$\frac{\partial \eta}{\partial t} + \nabla \cdot \left(h\boldsymbol{u}\right) = 0, \tag{2.44}$$

$$\frac{\partial \boldsymbol{u}}{\partial t} + g\nabla\eta = 0. \tag{2.45}$$

It is the simplest approximation of the shallow water equations. Wave phenomena are the leading effects in small scale low Froude number flows. A Gaussian is given as initial condition for the elevation, and we observe the solution after one hour, so that the wave crest has covered more than 350 km. A fourth order explicit Runge-Kutta scheme is used to progress in time, with a time step corresponding to the CFL condition, ensuring that the solution is converged in time.

As the goal of this paper is to show which finite element pair may be unstable or exhibit a lack of convergence, a steady testcase is much tougher. Indeed, the spurious modes that can appear in a finite element discretization are fully excited in steady solution, while they appear progressively in a time dependent problem. We then simulate a steady flow where wind forcing is balanced by linear dissipation:

$$\nabla \cdot (h\boldsymbol{u}) = 0, \tag{2.46}$$

$$g\nabla\eta = \frac{\boldsymbol{\tau}^s}{\rho h} - \gamma u, \tag{2.47}$$

with $\gamma = 10^{-6}\ s^{-1}$.

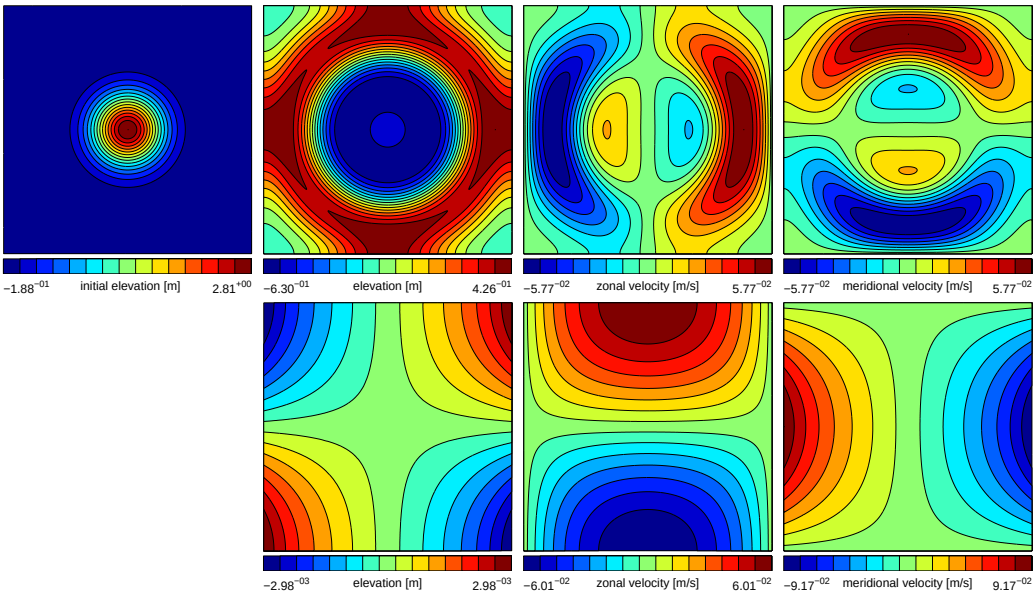

Figure 2.4: Sketch of the elevation and velocity fields for the unsteady (top, after one hour of physical time) and steady (bottom) wave testcases.

Stokes flow

The Stokes equations represent creeping flows, where inertial terms are negligible compared to viscous terms. This problem is difficult to solve numerically, because the incompressibility equation acts as a constrain on the velocity field. In order to obtain a mixed discrete formulation that defines a well-posed problem, it is mandatory to stabilize the discrete formulation or to define the mixed discretization space in such a way that the LBB condition is satisfied (Brezzi and Fortin, 1991). From a practical point of view, the discrete space for elevation/pressure must be small enough compared to the discrete space for velocities, in a usual mixed formulation. The wind forcing now balances the viscous dissipation:

$$\nabla \cdot (h\boldsymbol{u}) = 0, \tag{2.48}$$

$$g\nabla\eta = \frac{\boldsymbol{\tau}^s}{\rho h} + \nabla \cdot (\nu \nabla \boldsymbol{u}), \tag{2.49}$$

with $\nu = 10^4\ m^2 s^{-1}$.

Geostrophic equilibrium

Geophysical flows experience the Coriolis force, due to Earth rotation. It is one of the leading terms in the large scale shallow water equations. We test the ability of the different methods to maintain a linear geostrophic equilibrium, where the Coriolis force is in balance with the elevation gradient. As there is no dissipation, a good numerical scheme should maintain this equilibrium for a long time. The elevation field is a Gaussian bell of

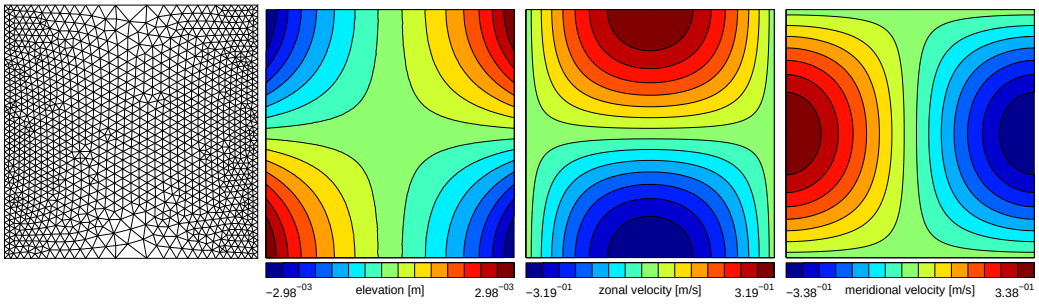

Figure 2.5: Typical mesh and sketch of the elevation and velocity fields for the Stokes testcase.

three meter height. Coriolis parameter f is $10^{-4}s^{-1}$ in the whole domain. A third-order implicit-explicit Runge-Kutta method is used to progress in time, with a time step corresponding to the CFL criterion on advection, the terms related to gravity waves being treated implicitly. The flow satisfies the following equations:

$$\frac{\partial \eta}{\partial t} + \nabla \cdot (h\boldsymbol{u}) = 0, \tag{2.50}$$

$$\frac{\partial \boldsymbol{u}}{\partial t} + f\boldsymbol{k} \times \boldsymbol{u} + g\nabla\eta = 0. \tag{2.51}$$

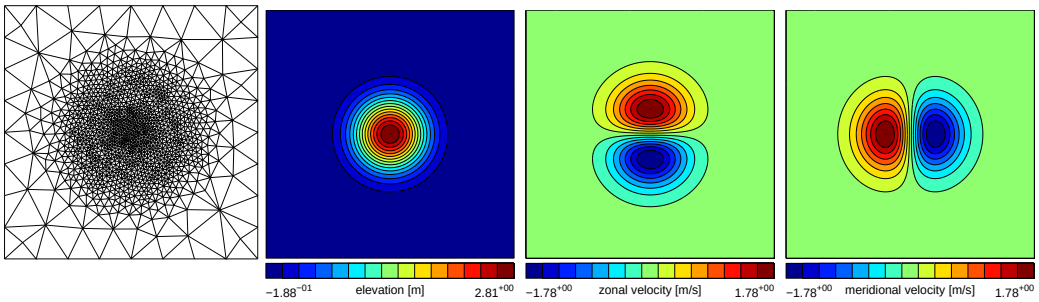

Figure 2.6: Typical mesh and sketch of the elevation and velocity fields for the geostrophic equilibrium testcase.

Stommel gyre

A time dependent problem may not exhibit all the troubles that can be generated by the discretization. The steady counterpart to the geostrophic equilibrium is the Stommel gyre (Pedlosky, 1987). The Coriolis effect is taken into account using the β-plane approximation, $f = f_0 + \beta y$, with $f_0 = 10^{-4}\ s^{-1}$ and $\beta = 2 \times 10^{-11}\ m^{-1}s^{-1}$, corresponding to a midlatitude domain in the northern hemisphere. The flow is forced by the wind stress defined at equation (2.42), that induces a clockwise circulation, while a linear dissipation with coefficient $\gamma = 10^{-6}\ s^{-1}$ balances the forcing. The variation of this Coriolis parameter induces Rossby waves that propagate westward and generate a strong boundary current. The flow satisfies the following equations:

$$\frac{\partial \eta}{\partial t} + \nabla \cdot (h\boldsymbol{u}) = 0, \tag{2.52}$$

$$\frac{\partial \boldsymbol{u}}{\partial t} + f\boldsymbol{k} \times \boldsymbol{u} + g\nabla\eta = \frac{\boldsymbol{\tau}^s}{\rho h} - \gamma \boldsymbol{u}. \tag{2.53}$$

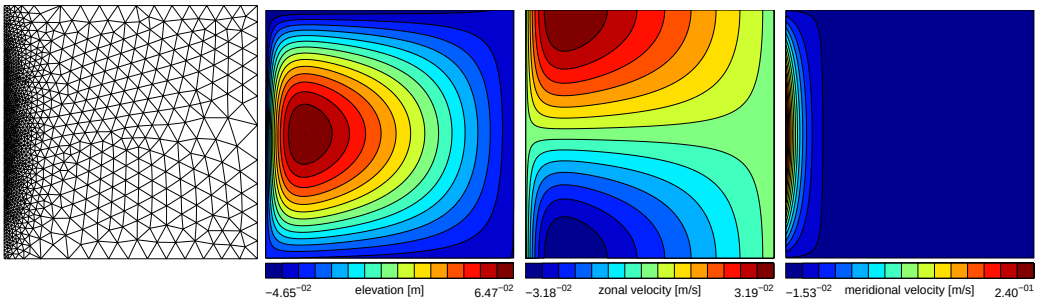

Figure 2.7: Typical mesh and sketch of the elevation and velocity fields for the Stommel gyre testcase.

Munk gyre

The Munk gyre testcase is similar to the Stommel one, the difference is that now the wind forcing is balanced by viscous dissipation rather than linear damping (Pedlosky, 1987). The viscosity parameter is constant in space and taken as $\nu = 10^4\ m^2 s^{-1}$. The flow satisfies the following equations:

$$\frac{\partial \eta}{\partial t} + \nabla \cdot (h\boldsymbol{u}) = 0, \tag{2.54}$$

$$\frac{\partial \boldsymbol{u}}{\partial t} + f\boldsymbol{k} \times \boldsymbol{u} + g\nabla\eta = \frac{\boldsymbol{\tau}^s}{\rho h} + \nabla \cdot (\nu \nabla \boldsymbol{u}). \tag{2.55}$$

This testcase is often the easiest to solve by all numerical schemes. The viscous terms are typical elliptic contributions removing most of the troubles that may pollute the inviscid solution.

Nonlinear problems

Finally, we incorporate the advection terms in both the Stommel and the Munk gyre problems. The first one is inviscid, satisfying the system:

$$\frac{\partial \eta}{\partial t} + \nabla \cdot \big((h+\eta)\boldsymbol{u}\big) = 0, \tag{2.56}$$

$$\frac{\partial \boldsymbol{u}}{\partial t} + \boldsymbol{u} \cdot \nabla \boldsymbol{u} + f\boldsymbol{k} \times \boldsymbol{u} + g\nabla\eta = \frac{\boldsymbol{\tau}^s}{\rho H} - \gamma \boldsymbol{u}, \tag{2.57}$$

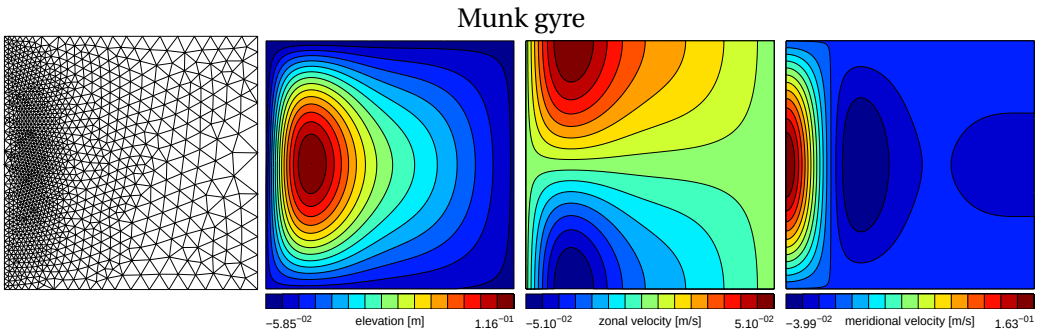

Figure 2.8: Typical mesh and sketch of the elevation and velocity fields for the Munk gyre testcase.

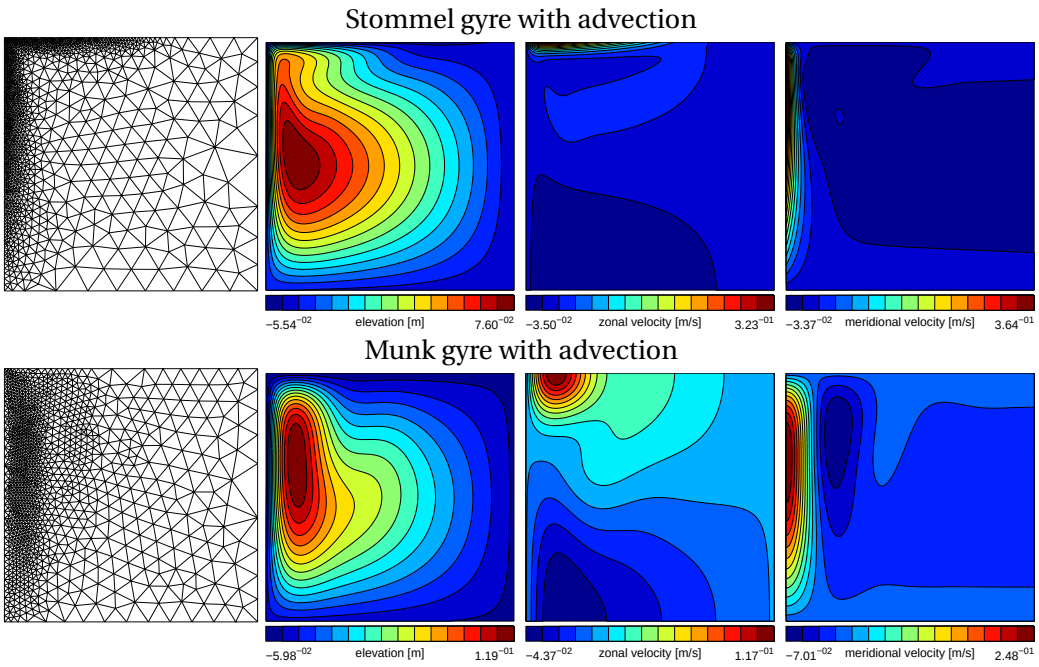

Figure 2.9: Typical meshes and sketch of the elevation and velocity fields for the nonlinear Stommel (top) and Munk (bottom) gyres.

with the same Coriolis factor as the two previous testcases, and a linear dissipation of coefficient $\gamma = 5 \times 10^{-7}$. The second one is viscous, with viscosity $\nu = 3000\ m^2 s^{-1}$:

$$\frac{\partial \eta}{\partial t} + \nabla \cdot \big((h+\eta)\boldsymbol{u}\big) = 0, \tag{2.58}$$

$$\frac{\partial \boldsymbol{u}}{\partial t} + \boldsymbol{u} \cdot \nabla \boldsymbol{u} + f\boldsymbol{k} \times \boldsymbol{u} + g\nabla\eta = \frac{\boldsymbol{\tau}^s}{\rho H} + \frac{1}{H}\nabla \cdot (H\nu\nabla\boldsymbol{u}). \tag{2.59}$$

The numerical handling of the advection term is not simple, and requires a suitable numerical strategy. However, some difficulties appearing in the problems without advection terms are sometimes solved by the diffusion introduced within the discretization of those advection terms.

2.5 Numerical results

To quantify the errors for all finite element pairs for each testcase, convergence studies are given in Figures 2.10 and 2.11. The left panels show the diagrams for the elevation field, while the right panels show the diagrams for velocities. The dots represent the values of the L_2 norm of the discretization error normalized by the range of the field. The slopes of the linear mean-square regression, representing the orders of accuracy, are given in the legends. To further quantify the optimality of the method, the error of the best solution that can be obtained in the sense of the L_2 norm is traced in continuous line. It is defined as the error in L_2 norm between the reference solution and the L_2 projection of this reference solution onto the finite element space defined with the current mesh.

A few conclusions may be drawn directly. The velocity fields of P_1^{NC}-P_1 and P_1^{DG}-P_1 pairs lack of convergence in the absence of viscosity. The P_1^{NC}-P_1 pair was known to have such a behavior (Hanert et al., 2008, 2005). This trouble is related to the wave component of the shallow water problem. The velocity field has too many degrees of freedom, and a velocity noise can develop with little influence on the elevation field. This noise component is bounded, as we still observe convergence at a reduced rate. The boundedness of the noise implies that the noise is not an eigenvector lying in the nullspace of the discrete operator, hence this noise was not shown by the study of Le Roux et al. (2005). This mode depends on the structure of the mesh. With structured meshes made of squares divided in half, optimal convergence is observed for both fields (Hanert et al., 2008). The same observation has been made for dispersion and dissipation properties, where analytical considerations on structured grids give promising results (Le Roux, 2005; Le Roux et al., 2007, 2008), while numerical analysis on unstructured grids exhibits disappointing results (Bernard et al., 2008b). Using structured meshes of squares divided in four where all triangles are not topologically identical, a relatively structured noise appears (see Figure 2.12). It is therefore possible to carry out spectral analysis as by Le Roux et al. (2007, 2008), to further characterize the behavior of this pair.

The $P_1^{DG} - P_2$ pair demonstrates its very good properties in the vast majority of the testcases. An optimal rate of convergence for velocities is observed in all the testcases, and furthermore the solution is always quite close to the optimal solution for this element (i.e. close to the solid line in the right panels of Figures 2.10 and 2.11). Optimal convergence rate for elevation is obtained for the time-dependent testcases, where initial condition was third order accurate, but also for the linear Stommel gyre. The latter can be explained as the functional spaces are optimally designed for geostrophy, as the gradient of the P_2 space exactly lies in the P_1^{DG} space. The nonlinearities seem to slightly deteriorate the accuracy of the solution to second order as the velocity and elevation fields are much more coupled.

For the Stokes flow, all the pairs exhibit second order accuracy for velocities, and a 1.5 order of convergence for elevations. Our discontinuous Galerkin method applied to the Stokes equations must be related to the one from Bassi et al. (2006) and Di Pietro (2007), where interface fluxes are deduced from an artificial incompressibility Riemann problem. The time-dependent shallow water equations do not exhibit a solenoidal constrain for the velocity field, but in the steady limit, we recover an incompressibility constrain. Therefore, we use the surface gravity wave speed $\sqrt{gh}$ where an arbitrary wave velocity c is used in Bassi et al. (2006). An additional difference is that the BRMPS method (referred as *Bassi et al. [13]* in the review Arnold et al. (2002)) is used to treat the diffusion terms,

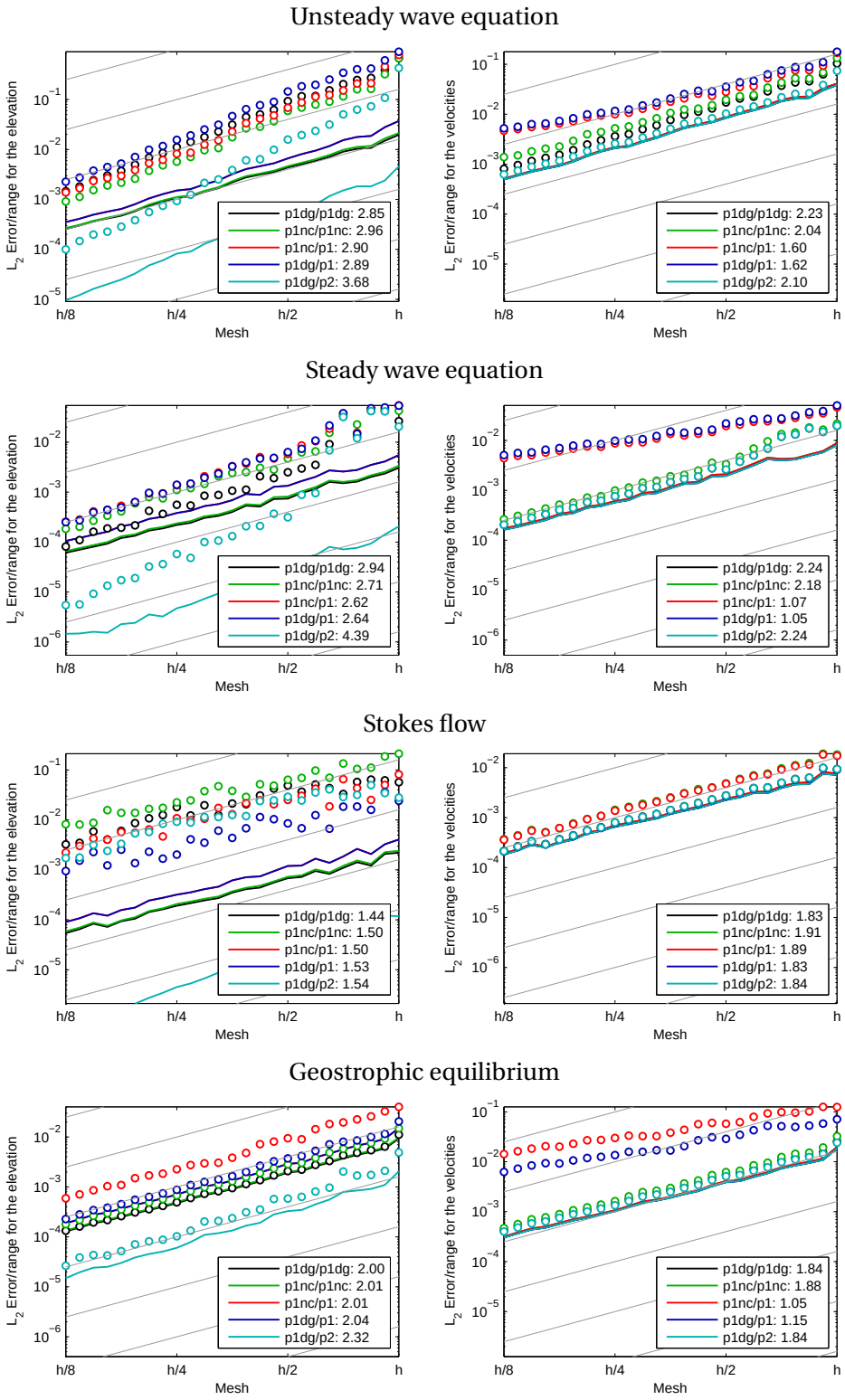

Figure 2.10: Convergence analysis. The circles denote the L_2 error, while continuous lines indicate the error of the L_2 projection of the reference solution onto the finite element space. The light gray lines indicates reference second order convergence. The errors are plotted against the ratio h between the edge length and the reference size field. The number of elements scales as h^2.

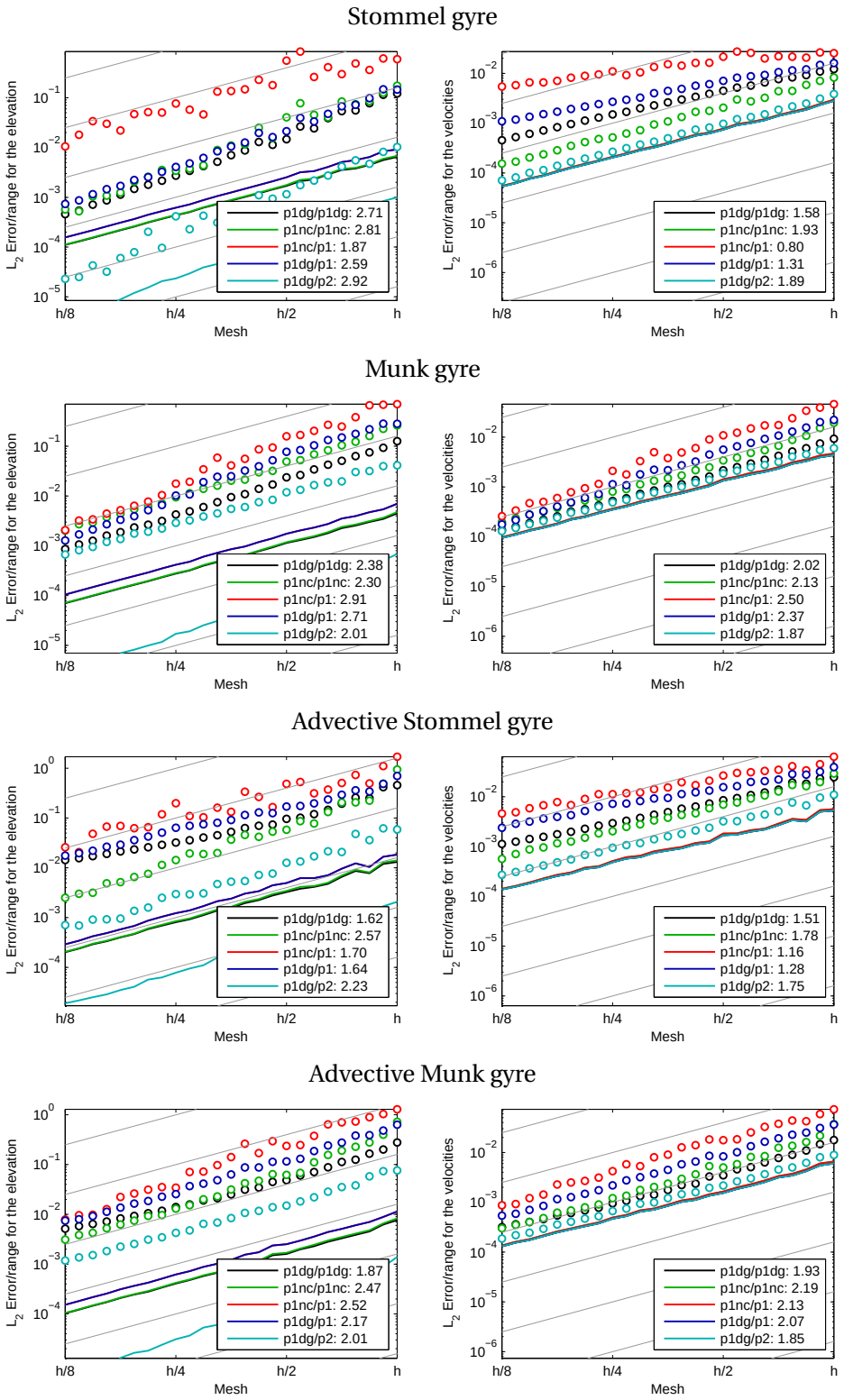

Figure 2.11: Convergence analysis. The circles denote the L_2 error, while continuous lines indicate the error of the L_2 projection of the reference solution onto the finite element space. The light gray lines indicates reference second order convergence. The errors are plotted against the ratio h between the edge length and the reference size field. The number of elements scales as h^2.

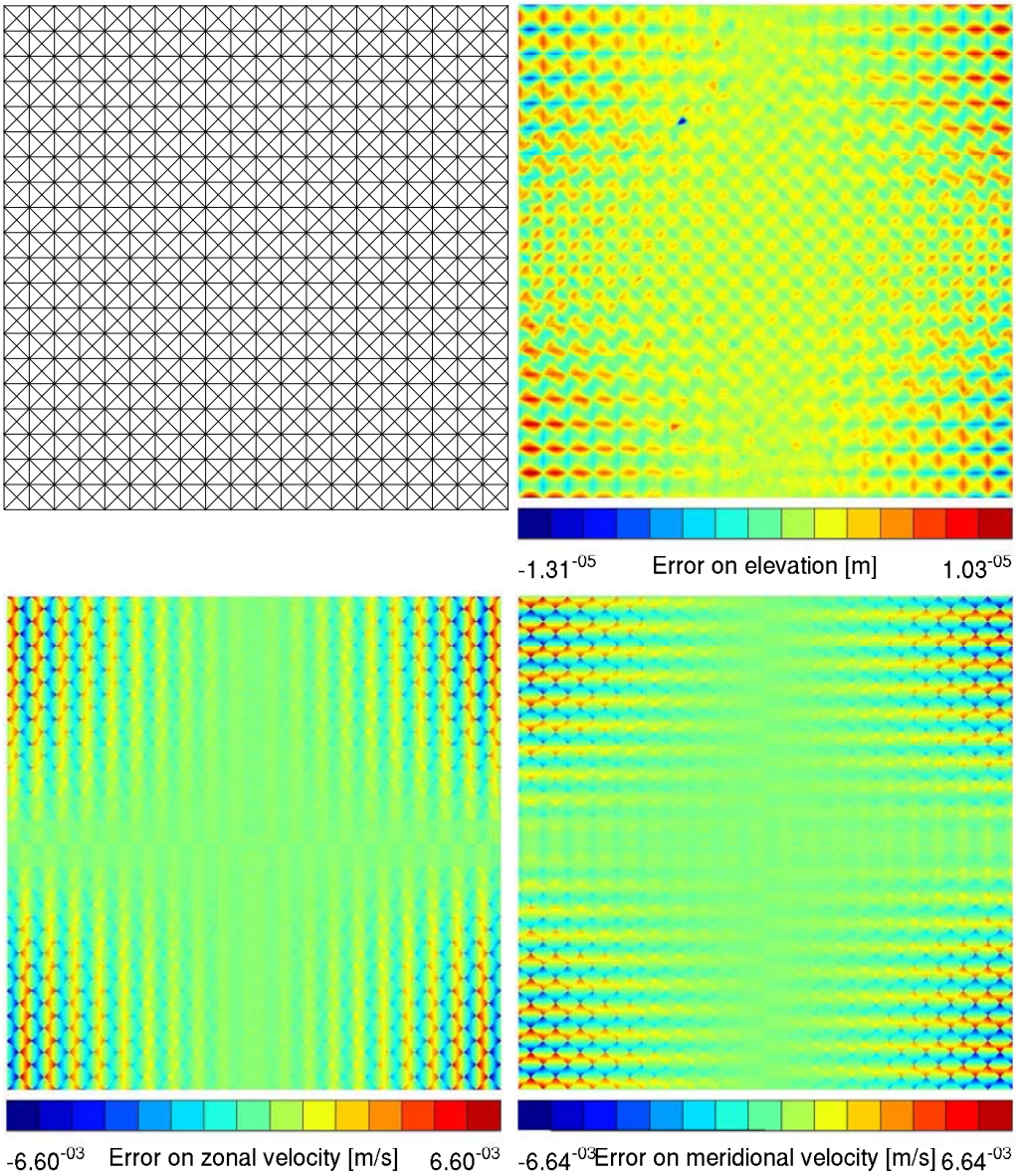

Figure 2.12: Sketch of the error for the steady wave problem, using P_1^{NC}-P_1 on the "Union Jack" mesh.

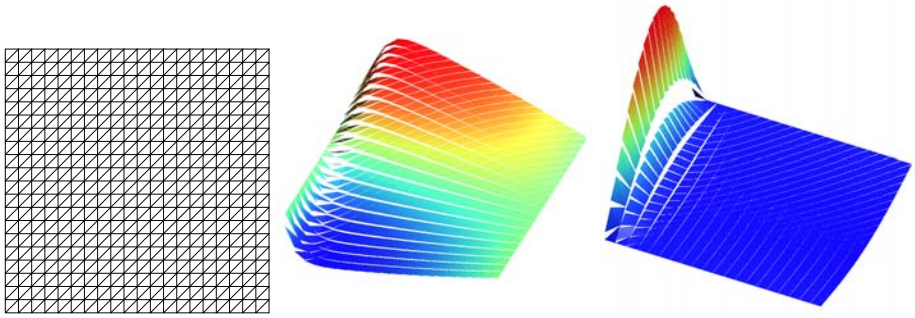

Figure 2.13: Zonal (center) and meridional (right) velocity field of the linear Stommel problem solved with the P_1^{DG}-P_1^{DG} pair on a structured mesh (left).

where we use an incomplete interior penalty method (IIPG method in the book Riviere (2008)). Still with DG, the same behavior is observed in Cockburn et al. (2002), using local-DG formulation, and proof that first and second order accuracy are expected for pressures and velocities, respectively, is given. All the finite element pairs do converge, but it cannot be excluded that some of them exhibit pressure modes on specific grids.

When Coriolis comes into play, the P_1^{DG}-P_1^{DG} pair lacks almost half an order of convergence for velocities. The velocity field in geostrophic equilibrium with a piecewise linear elevation field is piecewise constant. Then, interface terms are needed in the formulation to smooth the velocity field. Indeed, some flux terms exist for the normal velocity, but not for the tangent velocity. Therefore, some jumps on tangent velocities are allowed by the formulation, as shown in Figure 2.13 for the inviscid Stommel problem on a structured grid. The same half order of convergence is lost with second order shape functions ($P_2^{DG} - P_2^{DG}$) on the same meshes.

The nonlinear advection terms do not significantly change the behavior of the different schemes. For the P_1^{DG}-P_1^{DG}, in the inviscid case, the lack of convergence on the velocity field is propagated in the elevation field. The P_1^{NC}-P_1 and P_1^{DG}-P_1 velocity solutions are slightly smoothened by the numerical dissipation associated with the handling of the advective term, but the optimal convergence rates are not recovered. High Froude number are needed for the interface dissipation to be large enough to smooth the solution and recover the optimal behavior. Indeed, the Gulf of Mexico testcase from Hanert et al. (2005) corresponds to a maximum Froude number of more than 1/4, and the Williamson's testcases on the sphere, that were solved with optimal convergence rate in Comblen et al. (2009), are also advection dominated, with Froude numbers as high as 1/10.

The P_1^{NC}-P_1^{NC} pair has an overall quite encouraging behavior. The pair shows optimal convergence rate in all the testcases, except the Stokes flow. Those rates are never lower than the rates observed with the P_1^{DG}-P_2 pair. The error values are slightly higher than those for P_1^{DG}-P_2 or P_1^{DG}-P_1^{DG} (when optimal rates are observed), but it must be noticed that it only requires half the number of degrees of freedom of the discontinuous Galerkin method. Moreover, the P_1^{NC} element naturally treats diffusion terms, while P_1^{DG} requires interior penalty method.

2.6 Conclusions

We provide an unified framework to define finite element formulations of the shallow water equations with continuous, discontinuous or partially discontinuous discretizations. We then perform a systematic numerical comparison of five relevant finite element pairs used in oceanic and coastal flows.

We have considered convergence analyses on benchmark problems as the first meaningful numerical tests. Convergence analyses show whether the numerical solution is optimal or not, i.e. whether the approximation error is similar to the interpolation error or not. If it is not the case, we learn that there are issues with the discrete formulation. For finite element formulation that converge optimally, it would be interesting to consider further discrete properties, such as energy/enstrophy conservation and dispersion and dissipation properties.

In short, the following facts are observed:

- Large physical viscosity is required to obtain optimal order of convergence for P_1^{NC}-P_1 and P_1^{DG}-P_1 pairs.
- The accuracy of Discontinuous Galerkin discretization of Coriolis dominated flows is deteriorated by the lack of control on the jumps of tangent velocity.
- P_1^{DG}-P_2 gives accurate results in all ranges of flow, at the expense of second order shape function for elevation, hence higher order quadrature rules.
- P_1^{NC}-P_1^{NC} appears to behave optimally in all ranges of flow, with a reasonable number of degrees of freedom. The diffusion terms are naturally handled by the discrete space.

In terms of CPU efficiency, sharp conclusions are difficult to draw, as these are strongly implementation dependent. For explicit computations, using the same number of elements, P_1^{NC}-P_1^{NC} and P_1^{DG}-P_1^{DG} have truly similar cost per time-step, as most of the CPU time is spent computing the finite element integrals, that require the same accuracy for both finite element pairs. The computation of spatial operators for P_1^{DG}-P_2 is more expensive as the higher order of the shape function for elevation requires more accurate quadrature rules. The DG pair has all the degree of freedom associated with the triangles, giving a block structure that speeds up the assembling procedure. For implicit computations, CPU time spent in the linear solver is important. The size of the system depends on the number of degree of freedom per element. The requirements of $P_1^{DG} - P_1^{DG}$ and $P_1^{DG} - P_2$ pairs are similar, with respectively 9 and 8 dof per element. $P_1^{NC} - P_1^{NC}$ behaves optimally in all our testcases, and uses only 4.5 degree of freedom per element. Therefore, it is an interesting alternative that should be further studied to confirm its promising behavior.

CHAPTER 3

SOLVING THE SHALLOW WATER EQUATIONS ON THE SPHERE

This Chapter reproduces an updated version of the following paper, first submitted on 14 January 2008:

R. Comblen, S. Legrand, E. Deleersnijder, and V. Legat. A finite element method for solving the shallow water equations on the sphere. *Ocean Modelling*, 28:12–23, 2009. doi: 10.1016/j.ocemod.2008.05.004.

In the previous chapter, we have considered discretizations of the shallow water equations, that rule the vertically averaged marine flows. As the main objective of the thesis is to obtain a baroclinic model that can be used as hydrodynamic kernel for an ocean general circulation model (OGCM), it is mandatory for our model to operate on the sphere.

In the following chapter, we present an novel algorithm for solving vector set of equations on curved manifolds with second order finite elements, and we validate this methodology with standard benchmarks for the shallow water equations on the sphere.

The discrete formulation used in this paper is exactly the one described in the previous chapter. However, this work was realized during the first year of this PhD, and the comparison of Chapter 2 had not been performed yet. Its conclusions were therefore not known at the time of the writing. This explains why the $P_1^{NC} - P_1$ finite element pair was used, even if it is now known to have issues with such inviscid computations. Yet, the methodology described in this paper can be applied to any second order finite element discretization.

Further research has been carried out by Paul-Emile Bernard concerning Discontinuous Galerkin discretizations of vector PDEs on curved manifolds. A similar approach, relying on local frame of reference, has been investigated (Bernard et al., 2009). Indeed, if high order shape functions are resorted to, the geometry of the domain must itself be described with an equally high order representation, i.e. isoparametric finite elements. This is why Bernard et al. (2009) use a local tangent non-orthogonal frame of reference.

Abstract

Within the framework of ocean general circulation modeling, the present paper describes an efficient way to discretize partial differential equations on curved surfaces by means of the finite element method on triangular meshes. Our approach benefits from the inherent flexibility of the finite element method. The key idea consists in a dialog between a local coordinate system defined for each element in which integration takes place, and a nodal coordinate system in which all local contributions related to a vectorial degree of freedom are assembled. Since each element of the mesh and each degree of freedom are treated in the same way, the so-called pole singularity issue is fully circumvented.

Applied to the shallow water equations expressed in primitive variables, this new approach has been validated against the standard test set defined by Williamson et al. (1992). Optimal rates of convergence for the $P_1^{NC} - P_1$ finite element pair are obtained, for both global and local quantities of interest.

Finally, the approach can be extended to three-dimensional thin-layer flows in a straightforward manner.

3.1 Introduction

As the shape of Earth is almost spherical, it is critical for atmosphere and ocean modeling to develop efficient methods to solve partial differential equations on the sphere. On the latter, the most intuitive way to discretize a system of equations is to use spherical coordinates. Unfortunately, this coordinate system introduces two singular points, i.e. the poles. At these poles, the North and East directions are undefined and the metric is singular. Those issues need to be addressed, for the purposes of geophysical flow modeling.

We focus on the shallow water equations. Indeed, this two-dimensional model is a key building block for the dynamical core of ocean models. The horizontal momentum equation for a hydrostatic three-dimensional model is rather similar to the momentum part of the shallow water equations. Further, a classical approach in large scale ocean modeling is to resort to mode splitting. The idea of mode splitting is to use a different time stepping for the two-dimensional barotropic mode, whose fastest processes are external gravity waves, and the much slower three-dimensional baroclinic mode, whose fastest processes are internal waves and advection (Gadd, 1978; Madala, 1981; Blumberg and Mellor, 1987; Killworth et al., 1991; Deleersnijder and Campin, 1995; Hallberg, 1997; Higdon and de Szoeke, 1997; Higdon, 2002). In this case, the barotropic mode equations are the shallow water equations, with some additional coupling terms. This is why the shallow water equations are a relevant benchmark.

The pole problem is an issue that has been addressed in many ways:

- In classical longitude-latitude models, the solution can be filtered, the noise near the pole being removed, and the constraint on the time step being weakened (Murray and Reason, 2002).

- The spectral transform method applied to the equations rewritten with vorticity and divergence as prognostic variables rather than the two velocity components is a popular solution to the "pole problem" in atmospheric sciences. Swarztrauber (1996) reviews these methods. The absence of vector field, combined with the calculation of derivatives in spectral space, allows them to be exempt of pole prob-

lems. This approach cannot be applied in complex geometry. Hence, it is unlikely to become popular in ocean modeling.

- The use of a scalar expression of the momentum equation such as vorticity-divergence or stream function-velocity potential formulations, combined with an expression of the spatial operators in terms of a stencil circumvents the pole problem. Such a formulation using the icosahedral-hexahedral grid can be found in Sadourny et al. (1968); Heikes and Randall (1995); Thuburn (1997). For a model in primitive variables, Majewski et al. (2002) use a local spherical coordinate system at each grid point. The latter approach can be seen as a finite-difference counterpart of the present work.

- A lot of implementations use a single global Cartesian coordinate system. Therefore, velocity vectors are expressed with three components rather than two. These additional degrees of freedom are either deduced from the other d.o.f. (Priestley, 1992) or constrained by a Lagrange multiplier (Côté, 1988), ensuring that velocity vectors remain tangent to the surface of the sphere (Swarztrauber et al., 1997; Stuhne and Peltier, 1999; Giraldo, 2000; Tomita et al., 2001; Giraldo et al., 2002, 2003; Giraldo and Warburton, 2005; Giraldo, 2006). Further, Stuhne and Peltier (2006) applied this approach to three-dimensional oceanic flows in the framework of finite volume schemes.

- Splitting the sphere into several domains, each having its own curvilinear coordinate system appears as an attractive approach. The "cubed sphere" with six local curvilinear coordinate systems is introduced in several papers (Ronchi et al., 1996; Taylor et al., 1997; Adcroft et al., 2004; Nair et al., 2005; Rossmanith, 2006; St-Cyr et al., 2008). A spherical coordinate system, with two stereographic caps at the poles is also used in atmosphere modeling (Lanser et al., 2000). Ocean modelers use several spherical coordinate systems, for instance one rotated for the North-Atlantic and the Arctic Oceans, in addition to the classical one (Deleersnijder et al., 1993; Eby and Holloway, 1994; Coward et al., 1994; Webb et al., 1998).

- Finally, stretched or multipolar grids are often used in oceanography, with the poles located on dry land (Murray, 1996; Madec and Imbard, 1996; Roberts et al., 2006). This methodology is efficient for the world ocean, but cannot be used for simulating atmospheres or truly global oceans (aquaplanets) such as that of Europa, the moon of Jupiter.

In this paper, an efficient approach to handle partial differential equations on the sphere is developed for global ocean modeling. Our technique provides a good compromise between simplicity, efficiency and accuracy. It has been successfully applied in the development of SLIM (**S**econd-generation **L**ouvain-la-Neuve **I**ce-Ocean **M**odel - `http://www.climate.be/SLIM`). As all general circulation models, it uses primitive variables as prognostic quantities. We take advantage of the inherent geometrical flexibility of the finite element method to generalize the geometrical algorithm to any smooth manifold. The extension of this method to three-dimensional thin-layer flows is straightforward. In addition, the method only implies a few modifications in the finite element algorithm, and allows us to use the same model for both planar and curvilinear problems. Finally, the computational overhead to handle the spherical geometry is almost negligible.

The paper is organized as follows. Section 3.2 describes the methodology for dealing with curved geometry. Section 3.3 is devoted to the validation of the method on the test cases of Williamson et al. (1992). Finally, section 3.4 shows how our finite element scheme behaves for the difficult test case of Smith and Dritschel (2006).

3.2 An efficient methodology to handle PDEs in spherical geometry

The inviscid shallow water equations can be obtained by averaging the incompressible Navier-Stokes equations along the vertical direction. The usual non-conservative form reads:

$$\frac{\partial \mathbf{u}}{\partial t} + \mathbf{u}\cdot\nabla\mathbf{u} + f\mathbf{k}\times\mathbf{u} + g\nabla\eta = 0, \tag{3.1}$$

$$\frac{\partial \eta}{\partial t} + \nabla\cdot\big[(h+\eta)\mathbf{u}\big] = 0, \tag{3.2}$$

where $\mathbf{u}$ is the two-dimensional mean velocity, η is the elevation of the free-surface, f is the Coriolis parameter, $\mathbf{k}$ is a unit upward normal vector, g is the gravitational acceleration and h is the reference depth at rest.

Unlike finite differences, the finite element method does not need a global coordinate system to derive the discrete matrix operators. If the most obvious discrete finite difference differential operators on the sphere are directly built along meridians and parallels, the finite element local matrices, that define the local discrete differential operators, are usually built in the framework of a local coordinate system defined for each element. In other words, the finite elements intrinsically do not exhibit the classical coordinates singularity issue. The basic principle adopted herein is to write local problems in a local orthonormal curvilinear system $(\mathbf{e}_\xi, \mathbf{e}_\eta, \mathbf{e}_\zeta)$ defined for each element. Both $\mathbf{e}_\xi$ and $\mathbf{e}_\eta$ are tangent to the surface of the sphere, while the normal to the surface is given by $\mathbf{e}_\zeta$. The next step consists in assembling all the local problems in the global discrete algebraic system. As the local vectorial equations are written in distinct coordinate systems, it is required to perform suitable change of variables to rewrite the local contributions in the same coordinate system. As we cannot use a single coordinate system valid for each point on the sphere, we define a nodal orthonormal coordinate system $(\mathbf{e}_x, \mathbf{e}_y, \mathbf{e}_z)$ associated with each vectorial degree of freedom, $\mathbf{e}_x$ and $\mathbf{e}_y$ being tangent to the surface. A key advantage of the finite elements is that the support of a shape function is limited to only a few elements. Then, this nodal coordinate system needs to be valid only on the elements where the associated shape function does not vanish. Finally, a global reference system is needed only to define the position of the vertices and the components of both local and nodal basis vectors.

Basically, the pole problem arises when a vectorial equation of a vectorial quantity has to be solved. For notational convenience, we highlight the most important aspects on a simplified case, without any loss of generality. For instance, let us only consider the resolution of the momentum equation (3.1) of the shallow water model on the sphere. Equation (3.1) can be written in the following compact notation:

$$\mathbf{f}(\mathbf{u}) = 0, \tag{3.3}$$

where the vector **u** tangent to the surface is expressed in terms of local or nodal components:

$$\mathbf{u} = u^{\xi}\mathbf{e}_{\xi} + u^{\eta}\mathbf{e}_{\eta} = u^{x}\mathbf{e}_{x} + u^{y}\mathbf{e}_{y}. \tag{3.4}$$

In order to switch from the local to the nodal basis, a local linear operator is defined such as:

$$\underbrace{\begin{pmatrix} u^{x} \\ u^{y} \end{pmatrix}}_{{}_{x}\mathbf{U}} = \underbrace{\begin{pmatrix} \mathbf{e}_{x}\cdot\mathbf{e}_{\xi} & \mathbf{e}_{x}\cdot\mathbf{e}_{\eta} \\ \mathbf{e}_{y}\cdot\mathbf{e}_{\xi} & \mathbf{e}_{y}\cdot\mathbf{e}_{\eta} \end{pmatrix}}_{{}_{x}\mathbf{P}_{\xi}} \underbrace{\begin{pmatrix} u^{\xi} \\ u^{\eta} \end{pmatrix}}_{{}_{\xi}\mathbf{U}}. \tag{3.5}$$

Conversely, the transformation from the nodal to the local basis is defined by:

$$\underbrace{\begin{pmatrix} u^{\xi} \\ u^{\eta} \end{pmatrix}}_{{}_{\xi}\mathbf{U}} = \underbrace{\begin{pmatrix} \mathbf{e}_{\xi}\cdot\mathbf{e}_{x} & \mathbf{e}_{\xi}\cdot\mathbf{e}_{y} \\ \mathbf{e}_{\eta}\cdot\mathbf{e}_{x} & \mathbf{e}_{\eta}\cdot\mathbf{e}_{y} \end{pmatrix}}_{{}_{\xi}\mathbf{P}_{x}} \underbrace{\begin{pmatrix} u^{x} \\ u^{y} \end{pmatrix}}_{{}_{x}\mathbf{U}}. \tag{3.6}$$

If both systems are orthonormal curvilinear representations of the same $\mathscr{C}_1$ surface, the matrix ${}_{x}\mathbf{P}_{\xi}$ is the inverse of ${}_{\xi}\mathbf{P}_{x}$.

In order to solve the nonlinear equation (3.1), it is common to have recourse to standard linearization techniques, such as the Newton-Raphson method:

$$\mathbf{A}\mathbf{u} = \mathbf{b}, \tag{3.7}$$

where **A** is the gradient of **f** (or a suitable approximation of this gradient). Equation (3.7) may be viewed in terms of local components inside each element:

$$\underbrace{\begin{pmatrix} a_{\xi\xi} & a_{\xi\eta} \\ a_{\eta\xi} & a_{\xi\xi} \end{pmatrix}}_{{}_{\xi}\mathbf{A}_{\xi}} \underbrace{\begin{pmatrix} u^{\xi} \\ u^{\eta} \end{pmatrix}}_{{}_{\xi}\mathbf{U}} = \underbrace{\begin{pmatrix} b_{\xi} \\ b_{\eta} \end{pmatrix}}_{{}_{\xi}\mathbf{B}}. \tag{3.8}$$

The same equation can also be expressed in terms of nodal components:

$$\underbrace{\begin{pmatrix} a_{xx} & a_{xy} \\ a_{yx} & a_{yy} \end{pmatrix}}_{{}_{x}\mathbf{A}_{x}} \underbrace{\begin{pmatrix} u^{x} \\ u^{y} \end{pmatrix}}_{{}_{x}\mathbf{U}} = \underbrace{\begin{pmatrix} b_{x} \\ b_{y} \end{pmatrix}}_{{}_{x}\mathbf{B}}. \tag{3.9}$$

To assemble local contributions (3.8) into a common nodal version, it is required to transform equation (3.8) into equation (3.9). Such a transformation can be obtained easily by matrix operations, taking advantage of the relations (3.5-3.6):

$$\begin{aligned}
{}_{\xi}\mathbf{A}_{\xi}\ \ {}_{\xi}\mathbf{U} &= {}_{\xi}\mathbf{B} \\
\downarrow & \\
{}_{\xi}\mathbf{A}_{\xi}\ \overbrace{{}_{\xi}\mathbf{P}_{x}\ {}_{x}\mathbf{U}} &= {}_{\xi}\mathbf{B} \\
\underbrace{{}_{x}\mathbf{P}_{\xi}\ {}_{\xi}\mathbf{A}_{\xi}\ {}_{\xi}\mathbf{P}_{x}}\ {}_{x}\mathbf{U} &= \underbrace{{}_{x}\mathbf{P}_{\xi}\ {}_{\xi}\mathbf{B}} \\
\downarrow & \qquad\qquad \downarrow \\
{}_{x}\mathbf{A}_{x}\ \ {}_{x}\mathbf{U} &= {}_{x}\mathbf{B}.
\end{aligned}$$

Finite element formulation

To obtain a discrete algebraic system, it is required to define a piecewise polynomial approximation of the unknown field. In the local basis, such an approximation can be written as the linear combination of n local shape functions:

$$ {}_{\xi}\mathbf{U} \backsimeq \sum_{i=1}^{n} \phi_i(\xi,\eta) \underbrace{\begin{pmatrix} {}_{\xi}U_i \\ {}_{\eta}U_i \end{pmatrix}}_{{}_{\xi}\mathbf{U}_i^h}. \tag{3.10} $$

On each element, a weak formulation of (3.8) can be derived through the Galerkin procedure (Hughes, 2000):

$$ {}_{\xi}\mathbf{A}_{\xi}^h \, {}_{\xi}\mathbf{U}^h = {}_{\xi}\mathbf{B}^h, \tag{3.11} $$

where ${}_{\xi}\mathbf{U}^h = [{}_{\xi}U_1 \ {}_{\eta}U_1 \ {}_{\xi}U_2 \ {}_{\eta}U_2 \ \dots \ {}_{\xi}U_n \ {}_{\eta}U_n]^T$. For simplicity, let us restrict ourself to Turner triangles (linear conforming P_1 elements). In this case, only three nodes exist. The length of ${}_{\xi}\mathbf{U}^h$ and ${}_{\xi}\mathbf{B}^h$ is 6, and the size of the matrix ${}_{\xi}\mathbf{A}_{\xi}^h$ is 6×6. To obtain the global algebraic system, equation (3.11) must be expressed in terms of the nodal components:

$$ \begin{array}{rcl} {}_{\xi}\mathbf{A}_{\xi}^h \quad {}_{\xi}\mathbf{U}^h & = & {}_{\xi}\mathbf{B}^h \\ \downarrow & & \\ {}_{\xi}\mathbf{A}_{\xi}^h \overbrace{{}_{\xi}\mathbf{P}_x^h \, {}_x\mathbf{U}^h} & = & {}_{\xi}\mathbf{B}^h \\ \underbrace{{}_x\mathbf{P}_{\xi}^h \, {}_{\xi}\mathbf{A}_{\xi}^h \, {}_{\xi}\mathbf{P}_x^h} \, {}_x\mathbf{U}^h & = & \underbrace{{}_x\mathbf{P}_{\xi}^h \, {}_{\xi}\mathbf{B}^h} \\ \downarrow & & \downarrow \\ {}_x\mathbf{A}_x^h \quad {}_x\mathbf{U}^h & = & {}_x\mathbf{B}^h, \end{array} \tag{3.12} $$

where the transformation operator is now given by:

$$ {}_{\xi}\mathbf{P}_x^h = \left(\begin{array}{c|c|c} {}_{\xi}\mathbf{P}_{x_1} & & \\ \hline & {}_{\xi}\mathbf{P}_{x_2} & \\ \hline & & {}_{\xi}\mathbf{P}_{x_3} \end{array} \right). \tag{3.13} $$

The symbol ${}_{\xi}\mathbf{P}_{x_i}$ denotes the transformation operator from the local basis of the element onto the nodal basis associated to the i^{th} node of this element. Then the usual assembling procedure of the finite element method can be applied.

To consider the general coupled shallow water equations, we just need to define ${}_{\xi}\mathbf{U}^h$ and ${}_{\xi}\mathbf{P}_x^h$ as follows:

$$ {}_{\xi}\mathbf{U}^h = \left(\begin{array}{c} {}_{\xi}\mathbf{U}_1^h \\ E_1 \\ \hline {}_{\xi}\mathbf{U}_2^h \\ E_2 \\ \hline {}_{\xi}\mathbf{U}_3^h \\ E_3 \end{array} \right), \quad {}_{\xi}\mathbf{P}_x^h = \left(\begin{array}{cc|cc|cc} {}_{\xi}\mathbf{P}_{x_1} & & & & & \\ & 1 & & & & \\ \hline & & {}_{\xi}\mathbf{P}_{x_2} & & & \\ & & & 1 & & \\ \hline & & & & {}_{\xi}\mathbf{P}_{x_3} & \\ & & & & & 1 \end{array} \right), \tag{3.14} $$

where E_i denote the nodal values of elevation. The diagonal terms equal to unity corresponds to the elevation degrees of freedom.

Selection of the mapping

To obtain the discrete algorithm, we have to choose a local curvilinear coordinate system. The available choices range from the exact discretization of the surface (spherical triangles) to linear mapping (flat triangles). On the one hand, the spatial differential operators for spherical triangles must take into account the variations of the local basis vectors, as the mapping is nonlinear. These complex expressions can be derived with the help of differential geometry theory. An accurate quadrature rule has to be introduced to integrate the nonlinearities due to the mapping. On the other hand, flat triangles allows us to use the classical Cartesian expressions of differential operators, and low order quadrature rules are sufficient.

The geometrical error with flat triangles converge at the same rate as the discretization error when linear interpolations are used. Typically, the derivatives of the velocity field with respect to the local variables are:

$$\frac{\partial \mathbf{u}}{\partial \xi} = \left(\frac{\partial u^{\xi}}{\partial \xi} + \Gamma^{\xi}_{\xi\xi} u^{\xi} + \Gamma^{\xi}_{\xi\eta} u^{\eta} \right) \mathbf{e}_{\xi} + \left(\frac{\partial u^{\eta}}{\partial \xi} + \Gamma^{\eta}_{\xi\xi} u^{\xi} + \Gamma^{\eta}_{\xi\eta} u^{\eta} \right) \mathbf{e}_{\eta}, \tag{3.15}$$

$$\frac{\partial \mathbf{u}}{\partial \eta} = \left(\frac{\partial u^{\xi}}{\partial \eta} + \Gamma^{\xi}_{\eta\xi} u^{\xi} + \Gamma^{\xi}_{\eta\eta} u^{\eta} \right) \mathbf{e}_{\xi} + \left(\frac{\partial u^{\eta}}{\partial \eta} + \Gamma^{\eta}_{\eta\xi} u^{\xi} + \Gamma^{\eta}_{\eta\eta} u^{\eta} \right) \mathbf{e}_{\eta}, \tag{3.16}$$

where $\Gamma^{\alpha}_{\beta\gamma}$ are the second kind Christoffel symbols. In Appendix A.1, we show that those symbols scale as:

$$\Gamma^{\alpha}_{\beta\gamma} \approx \frac{h}{r^2}, \tag{3.17}$$

with r the radius of the sphere (or the local radius of curvature for a more complex manifold), and h the length of the largest edge.

Inspecting the order of magnitude in the discrete version of 3.15 yields:

$$\begin{aligned} \frac{\partial \mathbf{u}}{\partial \xi} &= \left(\frac{\partial u^{\xi}}{\partial \xi} + \Gamma^{\xi}_{\xi\xi} u^{\xi} + \Gamma^{\xi}_{\xi\eta} u^{\eta} \right) \mathbf{e}_{\xi} + (\dots)\, \mathbf{e}_{\eta} u^{\eta}_{i,j} \\ &= \left(\left[\frac{\partial u^{h,\xi}}{\partial \xi} + \mathcal{O}(h) \right] + \mathcal{O}\left(\frac{h}{r^2} \right) u^{\xi}_{i,j} + \mathcal{O}\left(\frac{h}{r^2} \right) \right) \mathbf{e}_{\xi} + (\dots)\, \mathbf{e}_{\eta} u^{\eta}_{i,j} \end{aligned}$$

where $\frac{\partial u^{h,\xi}}{\partial \xi}$ represents a component of the gradient of the discrete field, that is piecewise constant if linear shape functions are used. Therefore, we see that the errors made neglecting the curvature terms are $\mathcal{O}(h)$, as the error on the gradient of the field. Therefore, the errors due to the discrete representation of the geometry converge at the same rate as the error of a scheme using linear shape functions, i.e. we obtain a second order accurate scheme. Moreover, as long as $r \gg h$, this geometrical error will be much smaller than the discretization one. In ocean modeling, the sizes of all elements are always tiny in comparison to Earth radius. Therefore, when linear finite element are used, flat triangles are sufficient.

For vectorial degrees of freedom defined at nodes, it is now impossible to define a nodal coordinate system that is coplanar to all local coordinate systems of neighboring triangles. The most natural definition of the nodal basis located at a vertex consists in taking $\mathbf{e}_z$ as a weighted average of the normals of the surrounding elements, while the two other axes are chosen arbitrarily. This is the classical definition of the normal to a

mesh at a node (Gresho and Sani, 2000, p. 542). The transfer operator ${}_x\mathbf{P}_\xi$ can be defined by equation (3.5). The converse transfer operator ${}_\xi\mathbf{P}_x$ defined by equation (3.6) is not $\left({}_x\mathbf{P}_\xi\right)^{-1}$ anymore. To ensure consistency, ${}_x\mathbf{P}_\xi\,{}_\xi\mathbf{P}_x$ should be the identity operator, so we define ${}_\xi\mathbf{P}_x = ({}_x\mathbf{P}_\xi)^{-1}$.

For vectorial degrees of freedom defined along the edges, it exists a natural definition of ${}_x\mathbf{P}_\xi$. The two triangles sharing a common edge can be unfolded onto a plane. The nodal basis on the edge is defined so that $\mathbf{e}_x$ axis is aligned with the edge, and $\mathbf{e}_y$ axis is embedded in the plane. Then the transfer matrices between any of these bases are simply two-dimensional rotation matrices. Then the following property holds: ${}_x\mathbf{P}_\xi^{-1} = {}_x\mathbf{P}_\xi^T = {}_\xi\mathbf{P}_x$.

To sum up, a simple general methodology to handle curved geometry has been developed. It can be implemented into standard flat geometry softwares with only marginal modifications. The whole geometry is fully defined by the discrete vertices of the mesh. Therefore, such a methodology is valid for any manifold discretized by the vertices. It must be emphasized that all triangles will be handled in the same way. As a consequence, the pole problem is completely circumvented. The computational overhead is very small, since only local matrix/matrix and matrix/vector multiplications are added, as explained in equation (3.12). All the conservation properties of the discretization are preserved.

3.3 Validation with the shallow water equations

The methodology developed above is validated using the $P_1^{NC}-P_1$ discretization, applied to the shallow water equations. The non-conforming linear shape functions P_1^{NC} for velocities, and conforming linear ones P_1 for elevation are illustrated in figure 3.1. The velocity nodes are located at the mid-edge points, and the elevation ones on the vertices. This pair of elements is well suited for shallow water flows (Hanert et al., 2005). It enjoys attractive mathematical properties in terms of spurious elevation modes, that could appear in a mixed discretization of the steady state shallow water equations (Le Roux et al., 2005; Hanert and Legat, 2006). In addition, the shape functions for velocities are orthogonal, so the blocks of the mass matrix corresponding to the velocities are diagonal. It is particularly advantageous for an explicit time integration, without any mass lumping. The linear system is nondiagonal only for elevation nodes, which account only a seventh of the whole set of degrees of freedom. As the nonconforming linear shape functions are discontinuous on the edges, this approximation can be viewed as a hybrid choice between continuous and discontinuous approximations. In short, this element appears to combine most advantages of both continuous and discontinuous approaches. On the one hand, the discontinuous character allows us to stabilize the momentum equation with an approximate Riemann solver. On the other hand, sharing the same mid-edge value allow us to implement diffusive second order terms in a straightforward manner (Hanert et al., 2004, 2005).

Within the framework of the SLIM project, the time integration is performed by a family of so-called IMEX Runge-Kutta methods, where the linear terms can be treated implicitly (Ascher et al., 1997). In this case, the time step is only constrained by the usual Courant-Friedrichs-Lewy condition associated with advective terms. In most oceanic flows, such a condition is much less stringent than the stability condition related to the external gravity waves if we use a fully explicitly time integrator. The ratio between ex-

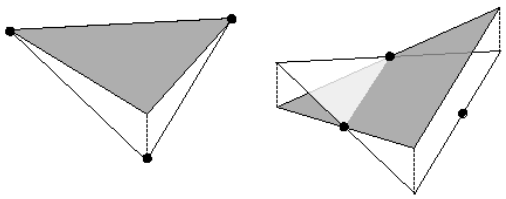

Figure 3.1: Conforming (left), and non-conforming (right) linear triangular shape functions. The former is used for the elevation, while the latter is resorted to the velocity components.

plicit and semi-implicit time steps is of the order of the Froude number. However, as all the test cases evaluated here are highly advective, the advantage of semi-implicit time-stepping is much smaller. As we want to evaluate the spatial discretization, explicit Runge-Kutta time-stepping schemes have been used, so that the stable time step ensure that the errors due to the time discretization are small.

Five of the seven standard test cases defined by Williamson et al. (1992, hereafter W92) are considered. The two remaining test cases are dropped because implementation of complicated source terms will be needed, or it will involve an initial condition problem for the atmosphere that is of no major interest for ocean modeling. All papers related to the shallow water equations on the sphere include validation results based on these test cases which can be now viewed as a de facto benchmark. Numerical solutions can be easily compared to analytical ones or to numerical reference results. To perform mesh refinement analysis, we consider four meshes deduced from the icosahedron, where the faces are recursively divided into four triangles and then projected onto the sphere. The meshes shown in figure 3.2 are made of almost equilateral triangles, with nearly uniform edge length.

W92 test case 1: advection of a cosine bell of tracer

Solving accurately the advection of a cosine bell on the sphere is a quite good test of the ability of a numerical scheme to represent efficiently any velocity field, anywhere on the sphere. The advection equation is the equation for elevation (3.2) with a uniform depth and a nondivergent velocity field constant in time. Using a single spherical coordinate system, the velocity field of this problem exhibits discontinuities for both North and East component at the poles. The finite element method naturally circumvents this issue. Calculations are performed with an initial tracer field defined as a cosine bell, with values between 0 and 1000. This bell is advected with a constant velocity field corresponding to a solid body rotation. The orientation of the velocity field is tilted of 0.05 radian to avoid any effect of symmetry. P_1^{NC} elements are used. Advection is stabilized using upwind fluxes, as described in Hanert et al. (2004). The initial condition and the solution obtained after one revolution cannot be distinguished in figure 3.3. It can also be observed that the L_2 error norm converges at the optimal quadratic rate.

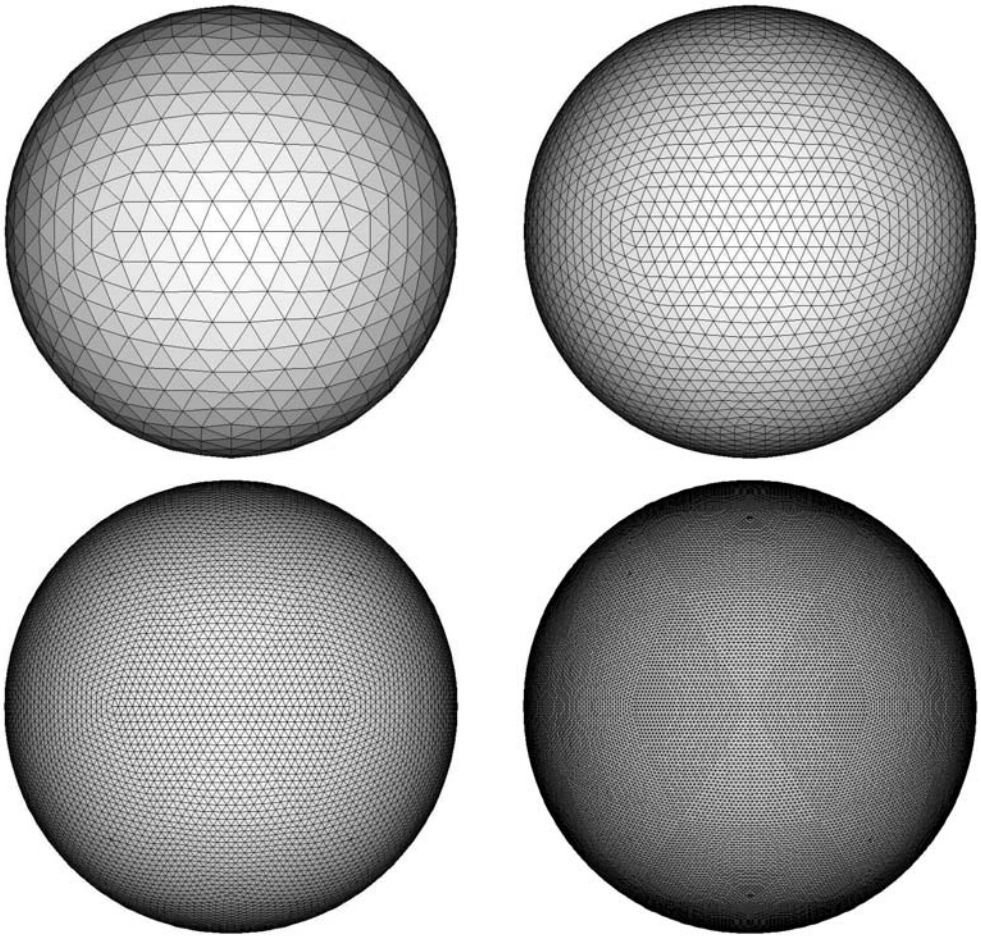

Figure 3.2: Meshes based upon the icosahedron, with each face recursively refined 3, 4, 5 and 6 times. The number of triangles are respectively 1280, 5120, 20480 and 81920.

W92 test cases 2 and 3: zonal geostrophic flows

Williamson's two next benchmarks are steady-state solutions to the nonlinear inviscid shallow water equations. In the first case, the velocity field corresponds to a solid body rotation along the axis of rotation of the Earth, whereas in the second case, it is nonzero only for latitude ranging between 30°South and 90°North. The elevation is defined so that it balances the Coriolis and advection terms of the momentum equation. W92 recommends to compute the error after five physical days. The results of a convergence analysis on both flows are detailed in figure 3.4. The optimal rate of convergence for this linear finite element pair in L_2 norm is observed for both elevation and velocity fields.

W92 test case 5: zonal flow over an isolated mountain

This is the first unsteady test case evaluated. The initial condition is similar to the one of test case 2: a solid body rotation velocity field, with the elevation in geostrophic balance. The only difference is the bathymetry: a seamount conical in the longitude-latitude representation is added, centered on a point with latitude 30°North. The radius of the sea-

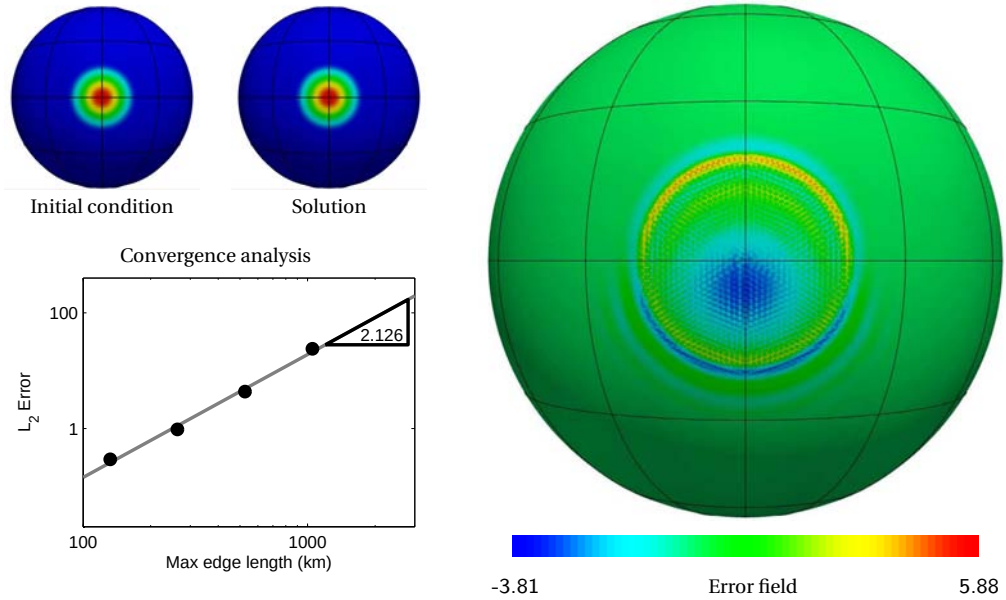

Figure 3.3: Advection of a cosine bell. Graphical comparison between the initial condition and the numerical solution after one revolution, on a mesh of 81920 triangles (top left). Error distribution on this mesh exhibits small amplitude wiggles (right), and the convergence plot of the L_2 error illustrates the observed quadratic rate of convergence (bottom left). L_2 error is defined as $\sqrt{\int_\Omega (c^h - c)^2 d\Omega / \int_\Omega 1 d\Omega}$.

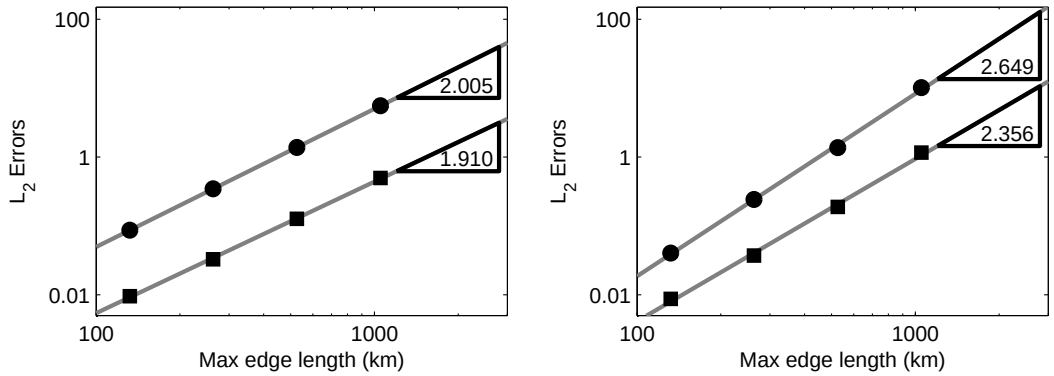

Figure 3.4: Convergence analysis for test case 2 (left) and test case 3 (right). L_2 error norms on the elevation η (dots) and velocities $\mathbf{u}$ (squares) after five days of simulation on the different meshes built upon the icosahedron (figure 3.2). L_2 errors are defined as $\sqrt{\int_\Omega (c^h - c)^2 d\Omega / \int_\Omega 1 d\Omega}$.

mount at its base is 20°, and its height is roughly a third of the fluid mean depth. The flow is going eastward.

In figure 3.5, our solution is compared to a very high resolution one from the German Weather Service. They simulate this benchmark with a spectral transform shallow water model, based on the NCAR's model (Jakob-Chien et al., 1995) (model truncation: T-426,

1280x640 grid points, time-step of 90 s)[1]. We use our finest mesh with 81920 triangles. The time step is 90 s. The spectral model has a hyperviscous dissipation term ∇^4 (with coefficient 4.97×10^{11} m^4/s), whereas our model does not have any explicit dissipation term, the subgrid-scale features being filtered out by the upwinding of the numerical scheme. The finite element model has 286720 degrees of freedom, while the spectral model has in its grid component more than two million of unknowns. Thus, the spectral solution should be much more resolved than the finite element one.

Spectral methods are subject to the Gibbs phenomenon. Angles cannot be represented accurately with a spectral method, and oscillations are induced in the discrete representation, that do not converge when the grid is refined. For this testcase, the mountain has sharp angles, and therefore the representation of the bathymetry is subject to such Gibbs phenomenon in the reference model. In a spectral method, the errors would be localized at the vicinity of the angle or discontinuity. However, the reference method is a pseudo-spectral method, i.e. some operators are computed with a spectral algorithms while some others are computed with finite differences on a structured longitude-latitude grid. Therefore, these oscillations can be propagated by the finite difference advection. It is believed that the difference plots of Figure 3.5 are mainly due to this Gibbs phenomenon. The amplitude of the difference field is less than one percent of the initial range of elevation. It is believed that the pattern of the difference field is mainly the wiggles due to the spectral method, since this pattern does not change between our two finest meshes, whereas scalar diagnostics do converge. Indeed, figure 3.6 shows that the maximum and minimum values of elevation converge both at the optimal quadratic rate. Further, the error on the total energy of the system after five days, illustrated in figure 3.7, converges at an higher rate than expected. Finally, similar behavior is observed in Rípodas et al. (2009) for the vorticity field, while validating their model.

W92 test case 6: Rossby-Haurwitz waves

This test case has been widely used for model intercomparison. It consists of slow waves, which are steadily evolving solutions of the nondivergent barotropic vorticity equations (Haurwitz, 1940). The initial patterns of elevation and velocities are shown in figure 3.8. When this flow was chosen as a test case by W92, it was thought to be stable for the inviscid nonlinear shallow water equations. In fact, Thuburn and Li (2000) showed that it is dynamically unstable, the wave pattern breaking down if initially perturbed.

Figure 3.9 compares our solution to a reference one. The latter was obtained by the German Weather Service by means of the model that was also used in test case 5, with T-511 resolution (1536x768 grid points), and a 90 s time step. Our model was used with a 60 s time step, on the icosahedral grid refined six times.

As seen in the plots of the right panel, the 4-periodic shape of the difference field evolves toward a 2-periodic shape. This can be understood easily. As explained by Thuburn and Li (2000), the flow is unstable to small perturbations. The spectral method does not trigger this instability because of its high degree of symmetry: truncation errors will always be 4-periodic, since both the grid and the initial condition are 4-periodic. This is why the spectral model keeps the 4-periodic wave pattern so long: only rounding errors excite the instability. The icosahedral mesh is only 2-periodic. Therefore, the truncation errors are 2-periodic. Hence, they excite the 2-periodic component of the unstable

[1] Data are available at `http://icon.enes.org/swm/stswm/node5.html`

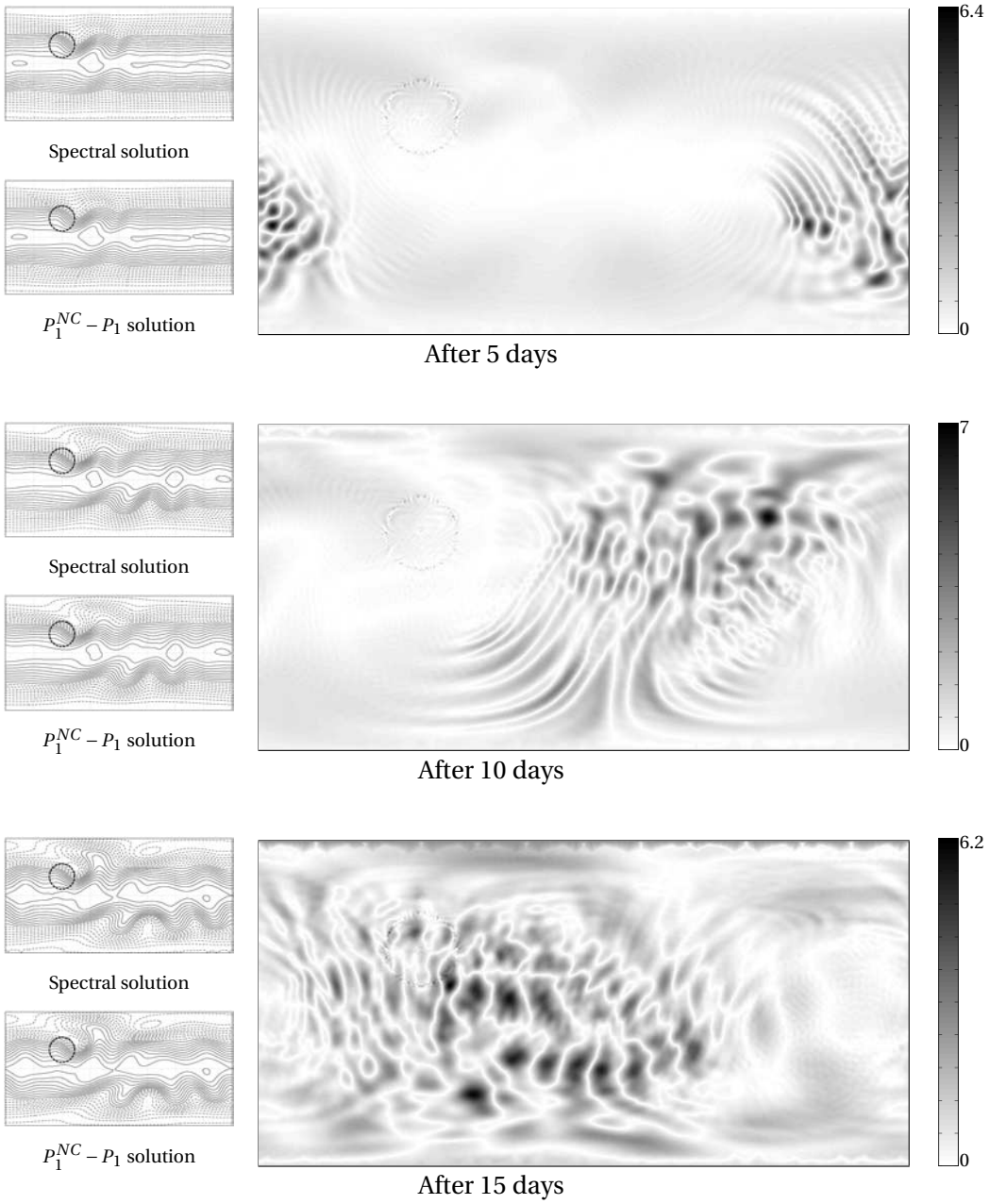

Figure 3.5: Comparison of the elevation field with reference solution from the German Weather Service for test case 5. The fields are presented in longitude-latitude projection. Left panel: spectral solution on top, and finite element solution on bottom. The interval between contourlines is 50m, the dashed lines are contourlines under the mean level, and the solid lines are contourlines above the mean level. Right panel: visualization of the absolute value of the difference between the reference solution and the finite element solution. The colormaps for the difference range in $[0;6.4]$, $[0;7]$ and $[0;6.2]$ (white is 0, black is maximum).

mode, which is seen on figure 3.9. The difference field is an image of the asymmetry of the mesh.

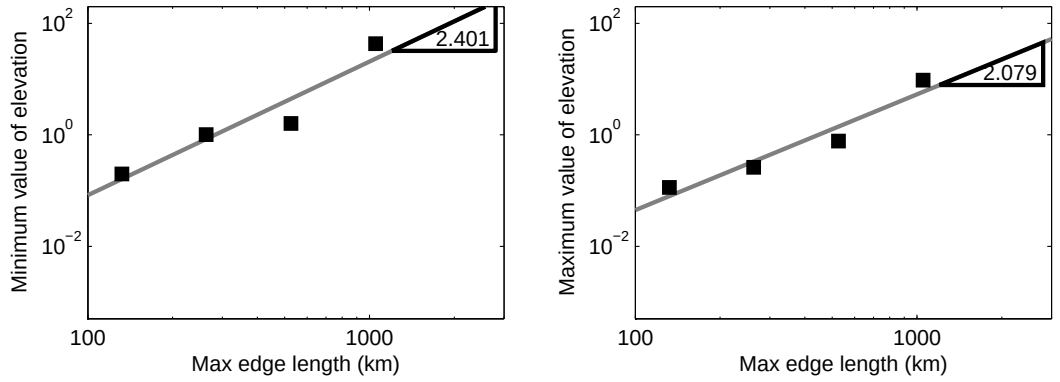

Figure 3.6: Convergence of the difference between reference solution and finite element solution for minimum (left) and maximum (right) values of elevation for test case 5 of W92.

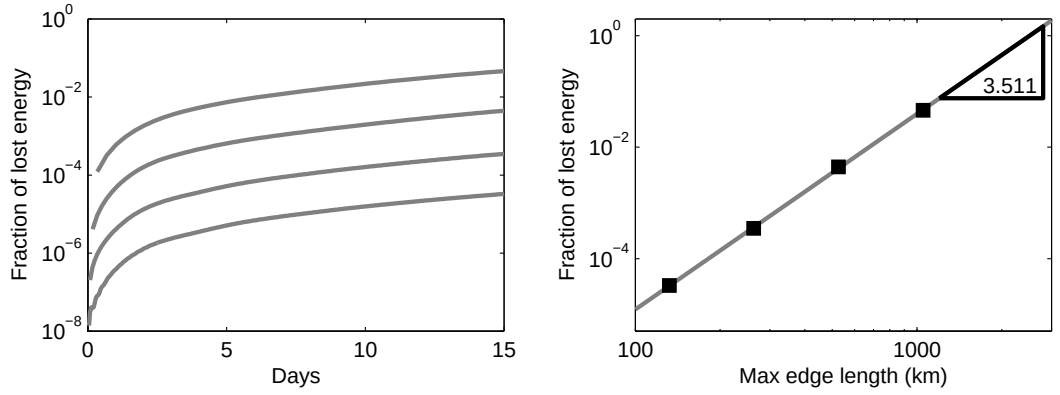

Figure 3.7: Fraction of total energy lost by the scheme for test case 5 of W92. Left: time series for the four meshes, right: convergence after 15 physical days.

3.4 Perturbed Rossby-Haurwitz waves

As the Rossby-Haurwitz flow of W92 is unstable to small perturbations (Thuburn and Li, 2000), Smith and Dritschel (2006) proposed a small variation of it, so that the instability is initially excited, and the numerical methods behave in a deterministic way. A small perturbation is added to the initial elevation field. This perturbation is defined as :

$$H\frac{(xx_0+yy_0+zz_0)}{40r^2}, \tag{3.18}$$

with H the mean fluid height (i.e. 9523 m), (x,y,z) the coordinates of the point in the global Cartesian frame of reference with origin at the center of the sphere, (x_0,y_0,z_0) a specific point located at latitude 40°North and longitude 50°East, and r is the radius of the Earth.

The advantage of this test case over its W92 counterpart is that it is reproducible: Thuburn and Li (2000) showed that for the classical Rossby-Haurwitz test case, the flow is unstable, and thus the behavior of the simulation is completely dependent on the way the numerical scheme excites the unstable mode(s).

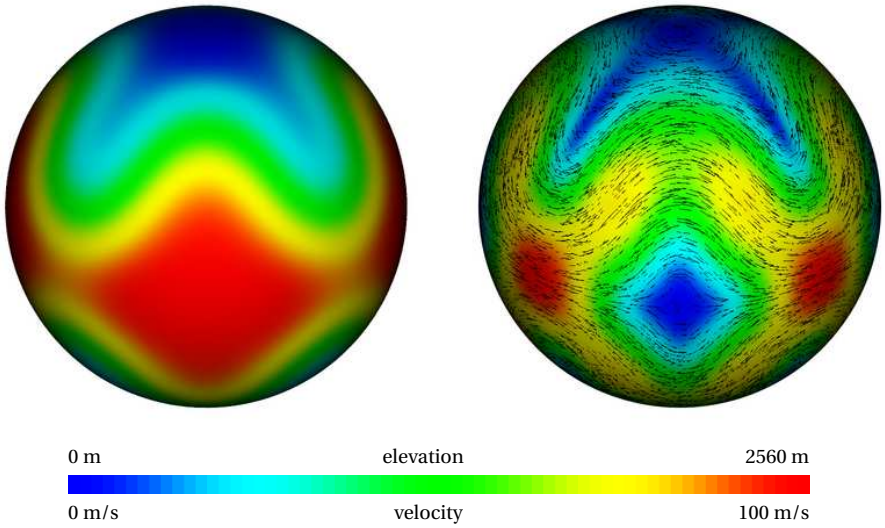

Figure 3.8: Initial elevation (left) and velocity (right) fields for test case 6 of W92.

Figure 3.10 compares our solution to that of Smith and Dritschel (2006), who used a contour-advective semi-Lagrangian method on a 256x256 grid, with a 108 s time-step. By contrast, our simulation was carried out with the same configuration as for initial Rossby-Haurwitz waves test case, i.e. with the icosahedral grid refined six times and a 60 s time-step. The flow pattern is relatively well represented, but the difference with respect to the reference solution is not negligible (the maximum differences after 5, 10 and 15 days are respectively 42, 147 and 221 m). This is probably due to a bias either in the reference solution or in our initial condition. To ensure that our method converges to a unique solution, we have considered as exact solution the result of a simulation carried out on the icosahedral mesh refined seven times (counting 327680 triangles), and observed how scalar diagnostics converge. This is illustrated in figure 3.11. We see that the maximum and minimum values of elevation converge both at an acceptable rate. Further, the error on the total energy of the system after fifteen days, illustrated in figure 3.12, converges at a higher rate than expected.

3.5 Conclusions

In this article, we propose an original solution for solving PDEs on the sphere — or on any other curved manifold. Taking advantage of the geometrical flexibility inherent to the finite element method, the presented methodology consists in a clever dialogue between a local and a nodal coordinate systems. As all elements are handled in the same way, the pole singularity issues are completely circumvented.

In order to assess the methodology, we show how to easily convert a finite element code operational in planar geometry into an efficient PDEs solver in spherical geometry, with a very small computational overhead. We prove that this new solver is able to reproduce accurately the solutions of the traditional test case flows for the shallow water equations. We observe optimal rates of convergence on both elevation and velocity fields

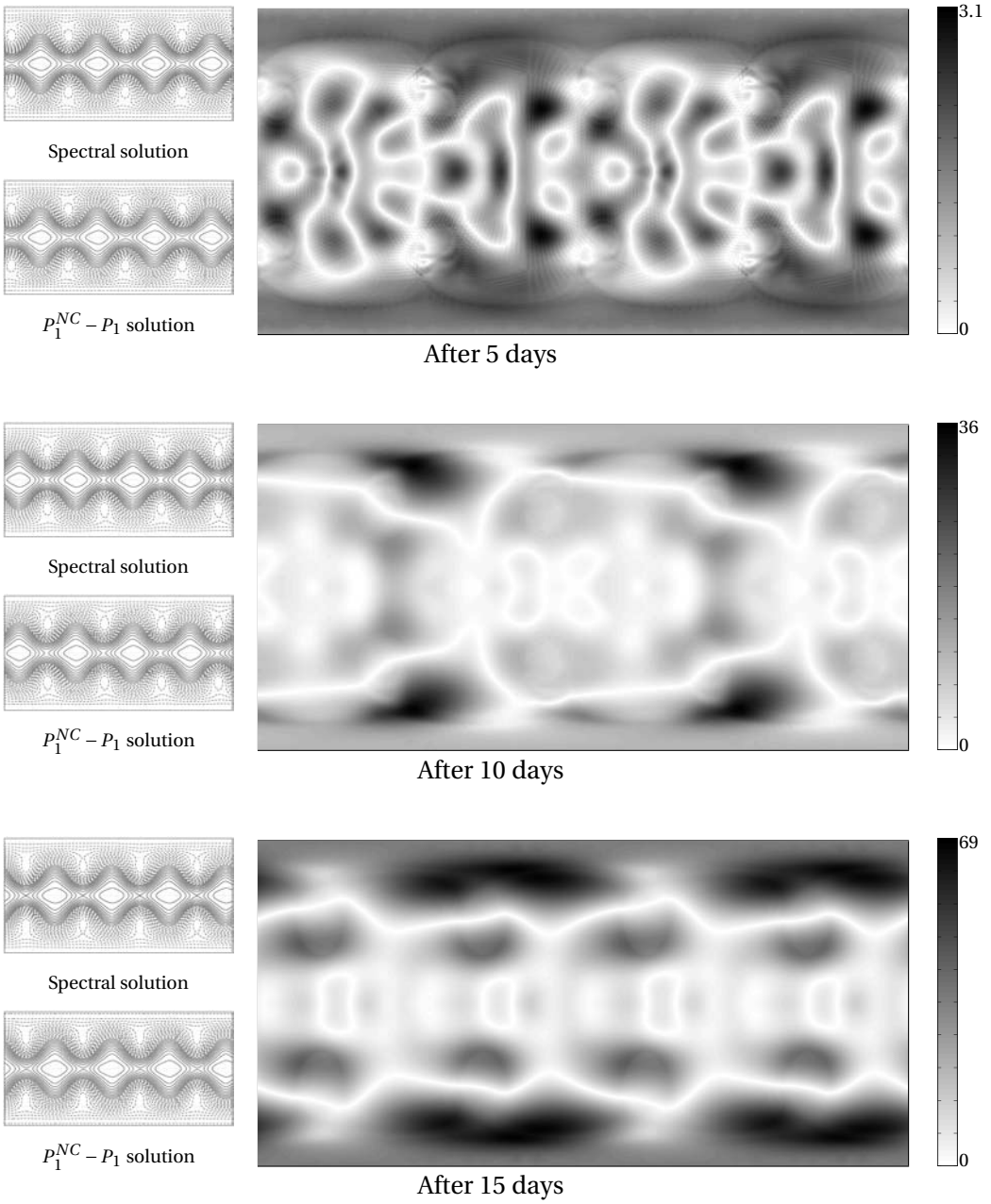

Figure 3.9: Comparison of the elevation field with reference solution from the German Weather Service for test case 6. The fields are presented in longitude-latitude projection. Left panel: spectral solution on top, and finite element solution on bottom. The interval between contourlines is 50m, the dashed lines are contourlines under the mean level, and the solid lines are contourlines above the mean level. Right panel: visualization of the absolute value of the difference between the reference solution and the finite element solution. The colormaps for the difference ranges in [0;3.1], [0;36] and [0;69] (white is 0, black is maximum).

on steady state flows, as well as on different diagnostics for unsteady flows. Our solution of complex flows compares well with published results.

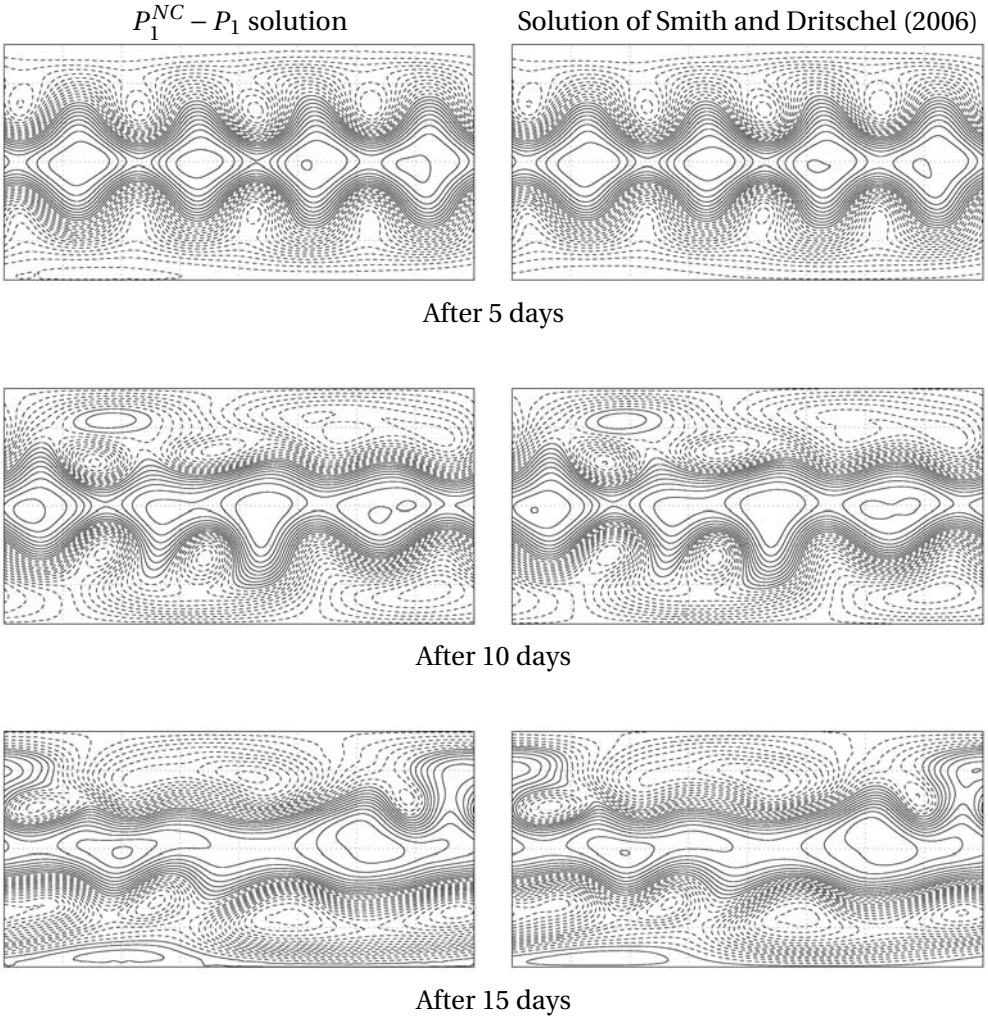

Figure 3.10: Comparison of the results for the modified Rossby-Haurwitz waves test case. The fields are presented in longitude-latitude projection. Reference solution of Smith and Dritschel (2006) (left) and our finite element solution (right). The interval between contourlines is 100m, the dashed lines are contourlines under the mean level, and the solid lines are contourlines above the mean level.

If the article mainly focuses on two-dimensional horizontal flows, the extension the three-dimensional case is rather straightforward. As explained by White et al. (2008b,a), our three-dimensional finite element model uses prisms as three-dimensional elementary unit. They are obtained by vertically extruding a two-dimensional triangular mesh. Section 3.2 showed that all the integrals are computed in the local coordinate system $\mathbf{e}_\xi$, $\mathbf{e}_\eta$, $\mathbf{e}_\zeta$. If the extrusion of the mesh is realized in the local coordinate system, aligned with the local vertical direction $\mathbf{e}_\zeta$, all the previous considerations are valid, if we consider the three-dimensional vector quantity as the combination of a two-dimensional vector tangent to the surface with a scalar value, which is its normal component. Note that we have implicitly assumed that we deal with a thin layer of fluid, since the extrusion is achieved along a constant direction within the triangle (parallel extrusion), rather than extrusion toward the center of the sphere.

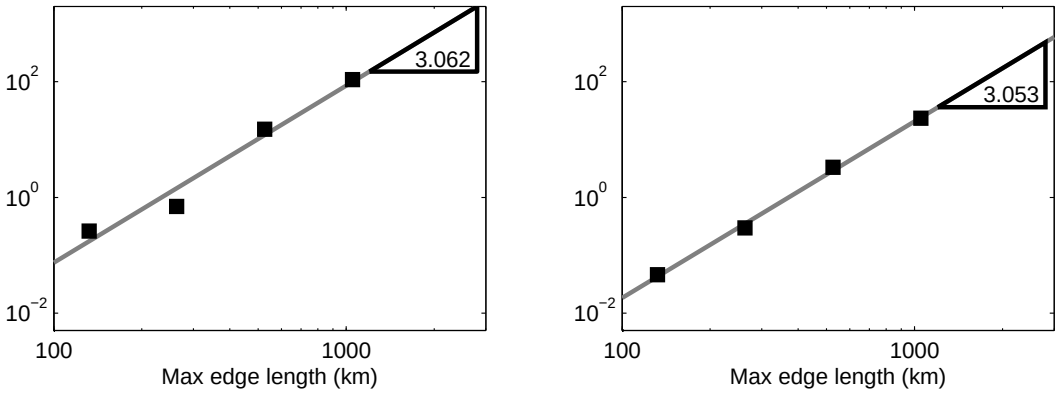

Figure 3.11: Convergence of the difference between reference solution and finite element solution for minimum (left) and maximum (right) values of elevation for perturbed Rossby-Haurwitz waves test case after five days.

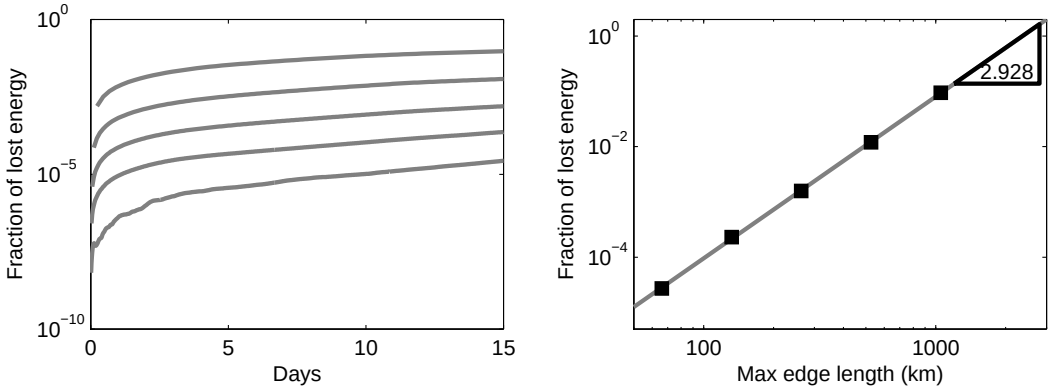

Figure 3.12: Fraction of total energy lost by the scheme for perturbed Rossby-Haurwitz waves test case. Left: time series for the four meshes, right: convergence after 15 physical days.

CHAPTER 4

A THREE-DIMENSIONAL BAROCLINIC MODEL: SPATIAL DISCRETIZATION

This Chapter reproduces the following paper, first submitted on 7 July 2010:

S. Blaise, **R. Comblen**, V. Legat, J.-F. Remacle, E. Deleersnijder, and J. Lambrechts. A discontinuous finite element baroclinic marine model on unstructured prismatic meshes. Part I: space discretization. *Ocean Dynamics (submitted)*, 2010.

Abstract

We describe the space discretization of a three-dimensional baroclinic finite element model, based upon a Discontinuous Galerkin method, while the companion paper Comblen et al. (2010a) (reproduced in Chapter 5) describes the discretization in time. We solve the hydrostatic Boussinesq equations governing marine flows on a mesh made up of triangles extruded from the surface toward the seabed to obtain prismatic three-dimensional elements. Diffusion is implemented using the symmetric interior penalty method, with modified penalty coefficients to handle anisotropy. The tracer equation is consistent with the continuity equation. A Lax-Friedrichs flux is used to take into account internal wave propagation. By way of illustration, a flow exhibiting internal waves in the lee of an isolated seamount on the sphere is simulated. This enables us to show the advantages of using an unstructured mesh, where the resolution is higher in areas where the flow varies rapidly in space, the mesh being coarser far from the region of interest. The solution exhibits the expected wave structure. Linear and quadratic shape functions are used and the extension to higher order discretization is straightforward.

4.1 Introduction

Ocean models have reached a high level of complexity and eddy resolving simulations are now much more affordable than in the past. However, mainstream models still fit into the same framework as the pionneering model published by Bryan (1969). This approach, which uses conservative finite differences on structured grids, approximates the coastlines as staircases and prevents flexible implementation of variable resolution. Yet, during the last forty years, numerical methods have dramatically evolved. It is now time for ocean modeling to benefit from all those advances by developing ocean models using state of the art numerical methods on unstructured grids (Griffies et al., 2009).

Unstructured grid methods are mainly of two kinds: finite volumes and finite elements. In short, finite volumes were first developed for problems predominantly hyperbolic (i.e. dominated by waves or advective transport), while finite element methods were first developed for problems dominated by elliptic terms. The two research communities have evolved towards solutions that manage to treat efficiently both hyperbolic and elliptic problems. Unstructured grid marine modeling is an active area of research for coastal applications (Deleersnijder and Lermusiaux, 2008). Indeed, the coastlines must be accurately represented, as they have a much stronger influence at the regional scale than at the global-scale. Finite volume methods are now widely used, and models like FVCOM (Finite Volume Community Ocean Model, Chen et al. (2003)) have a large community of users. Many other groups are developing finite volume codes for ocean, coastal and estuarine areas, such as Fringer et al. (2006), Ham et al. (2005), Stuhne and Peltier (2006) and Casulli and Walters (2000). Nonhydrostatic finite element methods are found in Labeur and Wells (2009) for small scale problems. For large scale ocean modeling, continuous finite element methods are used in FEOM (Finite Element Ocean Model, Wang et al. (2008a,b); Timmermann et al. (2009)), and ICOM (Imperial College Ocean Model, Ford et al. (2004b)) relies on mesh adaptivity to capture the multiscale aspects of the flow (Piggott et al., 2008).

In the realm of finite difference methods, Arakawa's C grid allows for a stable and relatively noise-free discretization of the shallow water equations, and is now very popular for ocean modeling (Arakawa and Lamb, 1977; Griffies et al., 2000). However, the search for an equivalent optimal finite element pair for the shallow water equations is still an open issue. Le Roux et al. (1998) gave the first review of available choices. More recent mathematical and numerical analysis of finite-element pairs for gravity and Rossby waves are provided in Le Roux et al. (2007, 2008); Rostand and Le Roux (2008); Rostand et al. (2008). Hanert et al. (2005) proposed to use the $P_1^{NC} - P_1$ pair, following Hua and Thomasset (1984). It appears that the $P_1^{NC} - P_1$ pair is a stable discretization, but its rate of convergence is suboptimal on unstructured grids (Bernard et al., 2008b). Following the same philosophy, the $P_1^{DG} - P_2$, pair was proposed by Cotter et al. (2009a). Such an element exhibits both stability and optimal rates of convergence for the Stokes problem and the wave equation (Cotter et al., 2009b) . FEOM (Wang et al. (2008b)) uses stabilized continuous finite elements, as well as ICOM (Ford et al. (2004b)). A detailed comparison of pairs stabilized by interface terms (including Discontinuous Galerkin methods) was provided by Comblen et al. (2010b).

This paper focuses on the development of a marine model, called SLIM (Second-generation Louvain-la-Neuve Ice-ocean Model[1]), that should be able to deal with prob-

[1] `http://www.climate.be/slim`

lems ranging from local and regional scales to global scales. In this model, we choose equal-order discontinuous interpolations for the elevation and velocity fields because of the inherent advantages of the usual Discontinuous Galerkin methods for advection dominated processes. It also allows us to decouple horizontal and vertical dynamics, thanks to the block-diagonal nature of the corresponding mass matrix. Discontinuous Galerkin methods (DG) can be viewed as a kind of hybrid between finite elements and finite volumes. They enjoy most the strengths of both schemes while avoiding most of their weaknesses: advection schemes take into account the characteristic structure of the equations, as for finite volume methods, and the polynomial interpolation used inside each element allows for a high order representation of the solution. Moreover, no degree of freedom is shared between two geometric entities, and this high level of locality considerably simplifies the implementation of the method. Finally, the mass matrix is block diagonal, and for explicit computations, no linear solver is needed. We also observe a growing interest for the Discontinuous Galerkin methods in coastal and estuarine modeling (Aizinger and Dawson, 2002; Dawson and Aizinger, 2005; Kubatko et al., 2006; Aizinger and Dawson, 2007; Bernard et al., 2008a; Blaise et al., 2010c). For atmosphere modeling, the high order capabilities of this scheme are really attractive (Nair et al., 2005; Giraldo, 2006), and the increasing use of DG follows the trend to replace spectral transform methods with local ones.

Herein, we provide the detailed description of the spatial discretization used in our Discontinuous Galerkin finite element marine model SLIM, as well as an illustrative example of the ability of the model to represent complex baroclinic flows. Section 4.2 describes the partial differential equations considered. Sections 4.3 and 4.4 provide the numerical tools needed to derive an efficient stable and accurate discrete formulation. Section 4.5 details the discrete discontinuous formulation. Finally, in Section 4.6, we study the internal waves generated in the lee of an isolated seamount as computed with our model.

In a companion paper (reproduced in Chapter 5), the time integration procedure will be discussed.

4.2 Governing equations

Large scale ocean models usually solve the hydrostatic Boussinesq equations. As a result of the hydrostatic approximation, the vertical momentum equation is reduced to a balance between the pressure gradient force and the weight of the fluid. The conservation of mass degenerates into volume conservation, and the density variations are taken into account in the buoyancy term only. This set of equations is defined on a moving domain, as the sea-surface evolves according to the flow.

Using the notations given in Table 4.1, the governing equations read:

- Horizontal momentum equation:

$$\frac{\partial \boldsymbol{u}}{\partial t} + \nabla_h \cdot (\boldsymbol{u}\boldsymbol{u}) + \frac{\partial (w\boldsymbol{u})}{\partial z} + f\mathbf{e}_z \wedge \boldsymbol{u} + \frac{1}{\rho_0}\nabla_h p + g\nabla_h \eta = \nabla_h \cdot (\nu_h \nabla_h \boldsymbol{u}) + \frac{\partial}{\partial z}\left(\nu_v \frac{\partial \boldsymbol{u}}{\partial z}\right), \quad (4.1)$$

- Vertical momentum equation:

$$\frac{\partial p}{\partial z} = -g\rho(T,S) \qquad \text{with} \qquad \rho = \rho_0 + \rho'(T,S). \tag{4.2}$$

- Continuity equation:

$$\nabla_h \cdot \boldsymbol{u} + \frac{\partial w}{\partial z} = 0, \tag{4.3}$$

- Free-surface equation:

$$\frac{\partial \eta}{\partial t} + \boldsymbol{u}^{\eta} \cdot \nabla_h \eta - w^{\eta} = 0. \tag{4.4}$$

- Tracer equation:

$$\frac{\partial c}{\partial t} + \nabla_h \cdot (\boldsymbol{u}c) + \frac{\partial (wc)}{\partial z} = \nabla_h \cdot (\kappa_h \nabla_h c) + \frac{\partial}{\partial z}\left(\kappa_v \frac{\partial c}{\partial z}\right), \tag{4.5}$$

This set of equations defines the mathematical three-dimensional baroclinic marine model and must be solved simultaneously with the suitable initial and boundary conditions. In particular in the inviscid limit, impermeability cannot be imposed on lateral boundaries for the three-dimensional momentum equation, as *"In the absence of viscosity, it is known that the primitive equations are not well-posed for any set of boundary conditions of local type"* (Rousseau et al., 2004). Particular attention must therefore be paid to the lateral boundary conditions..

In order to build a numerical discrete spatial scheme, it is usual to associate the unknown field with a given equation. The horizontal velocity $\boldsymbol{u}(x,y,z,t)$ is obtained from the horizontal momentum equation (4.1), while the vertical velocity $w(x,y,z,t)$ is deduced from the continuity equation (4.3). The three-dimensional tracers $c(x,y,z,t)$, which can be T or S, are associated with the tracer equation (4.5). The density deviation $\rho'(x,y,z,t)$ is then deduced from temperature and salinity using an appropriate equation of state $\rho'(T,S)$. As we only need the pressure gradient and not the pressure itself, we follow Wang et al. (2008b) and we only calculate the pressure gradient $\boldsymbol{p}(x,y,z,t) = \nabla_h p(x,y,z,t)$ from

$$\frac{\partial \boldsymbol{p}}{\partial z} = -g\nabla_h \rho'(T,S), \tag{4.6}$$

which is the horizontal gradient of equation (4.2), as ρ_0 is constant. Such an approach allows us to partly circumvent the numerical inaccuracies observed in the calculation of the baroclinic pressure gradient term in the momentum equation with a transformed vertical coordinate (e.g. sigma coordinates) (Deleersnijder and Beckers, 1992; Haney, 1991). Finally, the sea elevation $\eta(x,y,t)$ can be deduced from an modified form of the free-surface equation (4.4) which specifies the associated impermeability condition at the sea surface. Integrating the continuity equation (4.3) along the vertical direction yields

$$w^{\eta} - w^{-h} + \int_{-h}^{\eta} \nabla_h \cdot \boldsymbol{u} dz \quad = \quad 0,$$

which may be transformed to:

$$\underbrace{\frac{\partial \eta}{\partial t} + \boldsymbol{u}^{\eta} \cdot \nabla_h \eta}_{w^{\eta}} - \underbrace{\boldsymbol{u}^{-h} \cdot \nabla_h (-h)}_{w^{-h}} + \int_{-h}^{\eta} \nabla_h \cdot \boldsymbol{u} dz \quad = \quad 0,$$

Coordinates and spatial operators	
x, y	Horizontal coordinates
z	Vertical coordinate, pointing upwards with its origin at the sea surface at rest
∇_h	Horizontal gradient operator
$\boldsymbol{e}_z$	Upward unit normal
$\wedge$	Cross product symbol
Material parameters or functions	
g	Gravitational acceleration
ρ_0	Reference density
f	Coriolis parameter
h	Depth at rest
ν_h	Horizontal turbulent viscosity parameter
ν_t	Vertical turbulent viscosity parameter
κ_h	Horizontal turbulent diffusivity parameter
κ_t	Vertical turbulent diffusivity parameter
Variables	
$\boldsymbol{u}$	Horizontal three-dimensional velocity vector
w	Vertical three-dimensional velocity vector
$\boldsymbol{u}^\eta$	Surface horizontal three-dimensional velocity vector
w^η	Surface vertical three-dimensional velocity vector
$\boldsymbol{u}^{-h}$	Bottom horizontal three-dimensional velocity vector
w^{-h}	Bottom vertical three-dimensional velocity vector
η	Sea surface elevation
p	Baroclinic pressure
$\boldsymbol{p}$	Baroclinic pressure gradient
c	Three-dimensional tracer, can be S or T
S	Salinity
T	Temperature

Table 4.1: Notations for the governing equations of the three-dimensional baroclinic marine model

where we substitute the vertical velocities by using both associated impermeability conditions at the sea surface and the sea bottom. Applying the Leibniz integral rule leads to

$$\frac{\partial \eta}{\partial t} + \nabla_h \cdot \int_{-h}^{\eta} \boldsymbol{u} dz = 0. \tag{4.7}$$

The integral free-surface equation (4.7) corresponds exactly to the mass conservation of the shallow water equations. This prompts us to use this form rather than the local form. Mode-splitting procedures, where baroclinic (i.e. three-dimensional) and barotropic (i.e. two-dimensional) modes are time-stepped separately, are often resorted to. Therefore, it is very useful to have the same free-surface equation for the three-dimensional and two-dimensional formulations. The three-dimensional equations are designed so that the discretely depth-integrated equations are as close as possible to an accurate discretization of the shallow water equations (Comblen et al., 2010b). To achieve this, we rely on the integral form of the free-surface equation for the baroclinic three-dimensional model.

The diffusion terms are split into an horizontal part and a vertical part, preventing the implementation of rotated diffusion tensors as described for instance in Redi (1982). This reflects the fact that such rotated diffusion is not available yet in our discretization. Viscosity and diffusivity coefficients are chosen to represent the different effects of each of the many unresolved physical processes. The viscosity and diffusivity are strongly anisotropic (Griffies, 2004). If we consider a fluid stratified only in the vertical direction, stratification tends to annihilate vertical turbulent transport. As a consequence, many transport processes tend to spread properties more efficiently along isopycnal surfaces (horizontal direction) rather than across them (vertical direction). Measurements of the tracer diffusivity in the ocean by Ledwell et al. (1993) showed that, at the larger scales (order of hundreds of kilometers), the ratio between horizontal and vertical mixing coefficients is as large as 10^8. Particular attention must be paid to ensure the stability and accuracy of the anisotropic diffusion scheme. The subgrid scale phenomena are completely different depending whether they are related to the horizontal or the vertical direction. Processes modeled by vertical eddy viscosity consist of small scale (from millimeters to meters) turbulence, mainly generated by shear instabilities and gravitational instabilities. Due to their very small scales, these processes are never resolved in ocean models. Horizontal dominant subgrid scale processes correspond to larger scales of motions such as the mesoscale eddies (tens of kilometers). In that case, larger phenomena can be resolved by the model, depending of the resolution, and the eddy diffusivity must increase with the mesh size.

4.3 Geometrical numerical tools

Before deriving the discrete formulation, we first present the geometrical tools that are valid for all finite element (continuous or discontinuous) discretizations.

- The computational domain evolves with time and it is required to take into account the evolution of the domain in the discrete model. In Section 4.3.1, the standard ALE technique (Arbitrary Lagrangian Eulerian) implemented in the model is described.

- Moreover, the computational domain lies on a sphere. In Section 4.3.2, we recall the algorithm that renders the model able to operate on any manifold including an arbitrary shaped surface including a sphere or a planar surface.

4.3.1 Arbitrary Lagrangian Eulerian Methods

As the variation of the sea surface elevation modifies the domain of integration, the position of the nodes at the sea surface will move in the vertical direction as prescribed by the elevation field η. Moving the free surface nodes without changing the position of interior nodes will lead to unacceptable element distortions along the sea surface. Then, we must propagate the motion of the boundary nodes into the domain by means of a *moving mesh algorithm*. Its purpose is to avoid mesh distortion due to the sea surface motion and to maintain the original element density in the deformed mesh. In the model, the computational domain is stretched uniformly in the vertical direction. If we denote z^*

the original vertical coordinate of the nodes in the initial reference fixed domain Ω^* (the computational domain with the sea surface at rest), the vertical position $z(x,y,z^*,t)$ and the vertical velocity $w_z(x,y,z^*,t)$ of the nodes in the moving domain $\Omega(t)$ are prescribed by

$$z(x,y,z^*,t) = z^* + \eta(x,y,t)\,\frac{h(x,y)+z^*}{h(x,y)}, \tag{4.8}$$

$$\underbrace{\frac{\partial z}{\partial t}(x,y,z^*,t)}_{w_z} = \frac{\partial \eta}{\partial t}(x,y,t)\,\frac{h(x,y)+z^*}{h(x,y)}. \tag{4.9}$$

The mesh velocity w_z is relative to the arbitrary motion of the mesh that is stretched uniformly only to maintain the original aspect ratio in the deformed mesh. Such a velocity is fully arbitrary and is fully independent of the real velocity of the fluid particle. This is why such an approach is usually called an Arbitrary Lagrangian Eulerian method. Dealing with a moving domain requires the modification of the material derivative of a field c

$$\frac{Dc}{Dt} = \frac{\partial c}{\partial t} + \boldsymbol{u}\cdot\nabla_h c + (w - w_z)\frac{\partial c}{\partial z}. \tag{4.10}$$

Therefore, the tracer equation (4.5) has to be modified to take into account the moving mesh algorithm

$$\frac{\partial c}{\partial t} + \nabla_h\cdot(\boldsymbol{u}c) + \frac{\partial (wc - w_z c)}{\partial z} + c\frac{\partial w_z}{\partial z} = \nabla_h\cdot(\kappa_h\nabla_h c) + \frac{\partial}{\partial z}\left(\kappa_v\frac{\partial c}{\partial z}\right), \tag{4.11}$$

where the mesh velocity is subtracted from the vertical fluid velocity in the vertical advection term. The second additional term can be viewed as a correction to the volume modification introduced by the displacement of the moving mesh. The vertical derivative of the mesh velocity can be directly deduced from (4.9)

$$\frac{\partial w_z}{\partial z} = \frac{\partial \eta}{\partial t}\,\frac{1}{h}. \tag{4.12}$$

A similar adaptation must be applied for the horizontal momentum equation (4.1).

In a full standard ALE approach, all integrals and spatial operators appearing in finite element discrete formulation have to be considered in the deformed mesh. This is mandatory to obtain both global conservation and consistency (White et al., 2008b). However, incorporating the deformation of the mesh into all integrals and spatial differential operators of the discrete formulation will require at each time step the geometrical mapping between the parent element and the deformed physical element. For single stage time integrators, typically a θ scheme for implicit terms, and forward Euler for explicit terms as used by White et al. (2008b), such a general accurate approach can be applied. The generalization of such an approach for a multi-stage time-stepping scheme is a quite tedious and complex task. Therefore, it is not the main objective of this paper. Taking into account the deformation of the mesh in the integrals and the spatial operators is expensive in terms of CPU.. Moreover as for large scale oceanography problems, approximating the exact spatial differential operators by the same operators on the fixed reference grids can be considered as an acceptable approximation if the fluctuations of the free surface are significantly small compared to the depth of the ocean. In the same way, integrating the discrete formulation on the fixed domain (and not on the deformed

domain) only slightly modifies the discrete formulation where the relative weights of the elements are given with the surface of those elements in the reference fixed mesh and not in the deformed domain. Again, if the free surface fluctuations are small, both discrete formulations are perfectly acceptable from a numerical point of view. For coastal problems where the free surface motion is not tiny compared to the current depth, those approximations must be avoided and the generalization of the moving procedure with multi-stage time integrators is mandatory. Using the *linear free surface approximation*, several errors have to be monitored. Both vertical and horizontal spatial operators will be slightly biased, as the geometrical mapping of each finite element will be performed on the fixed domain and not on the moving computational domain. Conservation properties are also altered by the linear surface approximation. The scheme still exhibits consistency (i.e. the ability to exactly transport a constant tracer concentration). In summary, the *linear free surface approximation* takes into account the motion of the moving domain, but the local mapping of each element to the deformed mesh is approximated by the mapping to a reference fixed domain. From this point of view, the calculations with such an approximation can be really considered as an arbitrary Lagrangian Eulerian formulation on a moving domain, even if the integrations are performed on a fixed mesh.

4.3.2 Dealing with flows on the sphere

The model operates on arbitrary shaped surfaces, including the sphere or plane surfaces, following Comblen et al. (2009). The basic idea of the procedure is that each local geometrical entity supporting vectorial degrees of freedom has its own Cartesian coordinate system. There are also coordinate systems associated with each vector test and shape functions for the horizontal velocity field. To supply a vectorial degree of freedom from a frame of reference to another, we only need to build local rotation operators.

The global linear system of discrete equations is then formulated in terms of the vector degrees of freedom expressed in their own frame of reference. To build and assemble the local matrix corresponding to an element, we first fetch all the needed vectorial degrees of freedom into the coordinate system of this element, then we compute the local matrix or vector. We then apply rotation matrices to this matrix so that its lines and columns are expressed in the frame of reference of the corresponding test and shape functions, respectively. The transformation of the local linear system can be expressed in terms of ${}_x\mathbf{P}_\xi$ and ${}_\xi\mathbf{P}_x$, the rotation matrices from and to the frame of reference in which the integration is performed, respectively (Comblen et al., 2009):

$$
\begin{array}{rcl}
{}_\xi\mathbf{A}_\xi \quad {}_\xi\mathbf{U} & = & {}_\xi\mathbf{B} \\
\quad \downarrow & & \\
{}_\xi\mathbf{A}_\xi \overbrace{{}_\xi\mathbf{P}_x \, {}_x\mathbf{U}} & = & {}_\xi\mathbf{B} \\
\underbrace{{}_x\mathbf{P}_\xi \, {}_\xi\mathbf{A}_\xi \, {}_\xi\mathbf{P}_x} \, {}_x\mathbf{U} & = & \underbrace{{}_x\mathbf{P}_\xi \, {}_\xi\mathbf{B}} \\
\downarrow & & \downarrow \\
{}_x\mathbf{A}_x \quad {}_x\mathbf{U} & = & {}_x\mathbf{B}.
\end{array}
$$

Similarly, to assemble local matrices and vectors corresponding to the integral over an interface between two elements with different coordinate systems, we first fetch all the information in the frame of reference of the interface, then compute the integral,

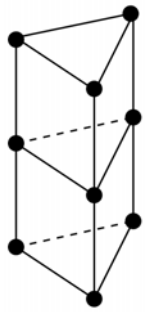

Figure 4.1: Sketch of prismatic elements. The vertical length scale is typically much smaller than the horizontal length scale, i.e. the prisms are thin.

and fetch back the lines and columns of the matrices in the frame of reference of the corresponding test and shape functions. All the curvature treatment is embedded in the rotation matrices, and the discrete equations are expressed exactly as if the domain was planar.

With such a procedure, it is possible to solve the equations on the sphere, circumventing completely any possible singularity problem. For notational convenience, the full discrete formulation will be presented within a Cartesian framework, but it is important to note that the model is fully implemented to operate on the sphere.

4.4 Discontinuous Galerkin Methods

Now, let us introduce the finite element mesh and the discrete discontinuous approximations of the field variables of the model (η, $\boldsymbol{u}$, w, c, ρ', $\boldsymbol{p}$). The three-dimensional mesh is made up of prismatic elements, as illustrated in Figure 4.1 and is obtained from the extrusion of triangular two-dimensional elements. The vertical length scale is typically much smaller than the horizontal length scale. In other words, the prisms are thin. We choose prismatic elements to obtain a mesh unstructured in the horizontal direction, and structured in the vertical direction. On the sphere, these columns of prisms are obtained by extruding the surface triangles in the direction normal to these triangles. As the extrusion is parallel, the prisms have the same width at the sea surface and at the sea bottom. This alignment of the elements along the vertical axis allows natural treatment of the continuity equation (4.3) and the pressure gradient equation (4.6), that can be integrated along the vertical direction.

The three-dimensional fields ($\boldsymbol{u}$, w, c, ρ', $\boldsymbol{p}$) are discretized on the mesh of prisms. The two-dimensional elevation field η is discretized onto the two-dimensional mesh of triangles. The shape functions for $\boldsymbol{u}$, w, c are obtained as the tensorial product of the linear discontinuous triangle P_1^{DG} and the linear discontinuous one-dimensional element L_1^{DG}. The shape functions of the density deviation and the baroclinic pressure gradient are $P_1^{DG} \times L_1$. The use of different discrete vertical spaces for ρ' and the tracer c can be viewed as an appropriate way to average the vertical variation of the tracers in the calculation of the baroclinic pressure gradient. The summary of the finite element spaces are given in Table 4.2. For the procedure to simulate flow on the sphere, each column of prisms defines the basic geometrical entity to assemble. It has its own coordinate sys-

Field		Finite element space
Free surface elevation	η	P_1^{DG}
Horizontal three-dimensional velocity vector	$\boldsymbol{u}$	$P_1^{DG} \times L_1^{DG}$
Vertical three-dimensional velocity	w	$P_1^{DG} \times L_1^{DG}$
Three-dimensional tracer	c	$P_1^{DG} \times L_1^{DG}$
Density deviation	ρ'	$P_1^{DG} \times L_1$
Baroclinic pressure gradient	$\boldsymbol{p}$	$P_1^{DG} \times L_1$

Table 4.2: Summary of the finite element spaces used for each field. Triangular linear elements are noted P_1 while vertical linear elements are noted L_1. The superscript DG stands for Discontinuous Galerkin.

tem, as the degrees of freedom for a discontinuous approximations are all associated with elements, and not with interfaces or vertices.

- The way to compute the discrete values at the inter-element interfaces is the critical ingredient to obtain a stable and accurate discrete formulation in the framework of the DG methods. The discrete fields are dual-valued at the inter-element interfaces. For the advective fluxes at these interfaces, the values of the variables are obtained on Riemann solvers applied to the hyperbolic terms of the model. Details about the Riemann solvers are given in Section 4.4.1.

- Incorporating the diffusion operators inside a DG formulation also requires special care. We use the SIPG technique (Symmetric Interior Penalty Galerkin) to accommodate diffusion operators. Moreover, the mathematical formulation exhibits anisotropic diffusion and the algorithm is adapted by computing the interior penalty coefficients on a virtual stretched geometry. The methodology used is summarized in Section 4.4.2.

4.4.1 Riemann solvers

A two-dimensional set of barotropic discrete equations can be obtained by the vertical depth-integration (or the algebraic stacking of the resulting lines and columns of the global system) of the three-dimensional set of discrete equations. The basic idea is to define the lateral interface in the discrete three-dimensional baroclinic equations in such a way that the corresponding two-dimensional discretization by depth-integration is a robust stable formulation. In particular, the use of the integral free-surface equation (4.7) and the selection of the discrete spaces lead to a stable and accurate corresponding two-dimensional discrete problem. Here, the resulting corresponding discrete problem is close to the discretization of the shallow water equations with P_1^{DG} shape functions for the two-dimensional velocities and elevation. A stable and accurate formulation can be derived for this problem, following Comblen et al. (2010b).

The key ingredient of a stable and accurate DG formulation is the choice of the definition for a common value for the variables along the interfaces. Due to the discontinuous representation of the variables, they are double-valued at the interface between elements. It is necessary to define adequately these common values provided by the

Riemann solvers. A Riemann solver simply consists of upwinding the characteristic variables. For nonlinear problems, it can be quite complicated to compute the exact Riemann solver and approximate Riemann solvers are usually resorted to. For the shallow water equations, approximate Riemann solvers are deduced from the conservative form of the equations (LeVeque, 2002; Toro, 1997; Comblen et al., 2010b).

For the linear shallow water equations, the exact solver yields the following interfacial values:

$$\boldsymbol{u}^{\text{riemann}} \cdot \mathbf{n} = \{\boldsymbol{u}\} \cdot \mathbf{n} + \sqrt{\frac{g}{h}}[\eta], \tag{4.13}$$

$$\eta^{\text{riemann}} = \{\eta\} + \sqrt{\frac{h}{g}}[\boldsymbol{u}] \cdot \mathbf{n}, \tag{4.14}$$

where $\{\}$ and $[\,]$ denote the mean or the jump operators, respectively [2]. The vector $\mathbf{n}$ is the rightward normal corresponding to the jump operator. Here, we have a simple wave equation and these values are used in the terms accounting for surface gravity waves. Indeed, the two-dimensional problem is not linear but, as oceanic flows usually have really small Froude numbers, the linear Riemann solver is a pretty good approximation of the nonlinear solver.

The three-dimensional equations allow several hyperbolic phenomena to take place. Surface gravity waves are the fastest phenomenon, with phase speed $\sqrt{gh}$. The second fastest phenomena are the internal gravity waves. Their propagation speed depends on the stratification. It can be as large as a few meters per second. As the set of the three-dimensional baroclinic marine flow equations cannot be cast into a conservative form, it is not possible deduce an approximate Riemann solver such as the Roe solver by simply linearizing the problem. Therefore, we selected a Lax-Friedrichs flux. This flux is commonly used due to its simplicity. The flux is simply defined as the sum of the mean flux and the jump of the variables multiplied by an upper bound γ on the phase speed of the fastest wave (the maximum eigenvalue of the Jacobian matrix):

$$\text{flux}^{\text{lax-friedrichs}} = \{\text{flux}\} + \gamma\,[\text{variable}] \tag{4.15}$$

In this work, we use the Riemann solver of the linear shallow-water equations (4.13, 4.14) for the terms corresponding to surface gravity waves (i.e. elevation gradient in the two-dimensional, depth-averaged momentum equation and velocity divergence in the continuity equation). In the three-dimensional problem, i.e. in the momentum equation and in the active tracers equations (typically temperature and salinity), we add to the mean flux the jump of the variables multiplied by an upper bound on the second fastest wave, which is the sum of the fastest internal wave phase speed and the advection velocity. Determining the phase speed of the fastest internal wave is not easy for a complicated stratification profile. In our examples, we simply use values deduced from our numerical experience, by a trial and error procedure.

4.4.2 Symmetric Interior Penalty Galerkin methods

In the realm of Discontinuous Galerkin methods, various discretizations of the Laplacian operator are reviewed in e.g. Arnold et al. (2002). Two of them are especially popular: the

[2] In particular, the jump is defined by $[a] = (a_L - a_R)/2$ and the mean by $\{a\} = (a_L + a_R)/2$ where a_L and a_R are the right and left values of the field a.

interior penalty methods (Riviere, 2008) and the local-DG approach (Cockburn and Shu, 1998a). The latter approach introduces a mixed formulation for the field and its gradient and can be difficult to handle with an implicit time-stepping.

To accurately handle the diffusion terms, we use the SIPG technique (Symmetric Interior Penalty Galerkin). Basically, the weak form of the Laplace equation $\nabla^2 c = 0$ can be obtained by integrating the product of this equation by a test a function on the whole domain. Integrating by parts and choosing the mean values at the interfaces yields:

$$\sum_{e=1}^{N_e} \left[\ll \hat{c}\{\nabla c\} \cdot \boldsymbol{n} \gg_e - < \nabla \hat{c} \cdot \nabla c >_e \right] = 0, \tag{4.16}$$

where $<>_e$ and $\ll\gg_e$ denote respectively the integral over the element Ω_e and its boundary. The number of elements is N_e. Choosing the mean values at the interface seems natural for an elliptic operator where the information propagates along all directions. However, such a simple and intuitive treatment of the Laplacian operator is incomplete. Indeed, the discrete solution is not unique, as at the boundary of each element, only Neumann boundary conditions are prescribed. In order to partly complete the discrete formulation, the Incomplete Interior Penalty Method (IIPG) consists in adding a penalty term on the discontinuities of the field at the inter-element interfaces

$$\sum_{e=1}^{N_e} \left[\ll \hat{c}\{\nabla c\} \cdot \boldsymbol{n} \gg_e + \sigma \ll \hat{c}\,[c] \gg_e - < \nabla \hat{c} \cdot \nabla c >_e \right] = 0, \tag{4.17}$$

where σ is a penalty parameter scaled in such a way that $\sigma\,[c]$ is a term similar to a gradient, at the interface level. In other words, $1/\sigma$ has to be an suitable lengthscale. It is shown in Riviere (2008) that this formulation provides optimal results when shape functions of odd polynomial order are used (i.e. P_1, P_3, ...), but lacks convergence for even polynomial orders. Further, the resulting discrete matrix is not symmetric, while the continuous operator is symmetric. The Symmetric Interior Penalty Method (SIPG) solves both of these issues, by adding a symmetrizing term to the IIPG formulation (4.17).

$$\sum_{e=1}^{N_e} \left[\ll \hat{c}\{\nabla c\} \cdot \boldsymbol{n} \gg_e + \ll \nabla \hat{c} \cdot \boldsymbol{n}\,[c] \gg_e + \sigma \ll \hat{c}\,[c] \gg_e - < \nabla \hat{c} \cdot \nabla c >_e \right] = 0. \tag{4.18}$$

There is a lower bound on σ that ensures optimal convergence. This bound must be as tight as possible, as the larger the value of σ, the worse the conditioning of the operator. Shahbazi (2005) suggests to use the following formula:

$$\sigma = \left[\frac{2(k+1)(k+d)}{3} \frac{A(\Gamma_k)}{V(\Omega_e, \Omega_f)} \right], \tag{4.19}$$

where k the order of the interpolation, $A(\Gamma_k)$ is the area of the interface Γ_k between the two considered elements, and $V(\Omega_e, \Omega_f)$ is the mean volume of the two neighboring elements Ω_e and Ω_f.

Finally, the diffusion operators that appear in three-dimensional baroclinic marine models are strongly anisotropic. In fact, both the diffusion operator and the mesh are anisotropic. A very simple idea consists then in virtually stretching the mesh in the vertical direction so that we recover an isotropic diffusion in the deformed geometry. The mesh is not really modified, but the local interior penalty coefficients are chosen is such a way that they correspond to an isotropic diffusion on the modified mesh. As an illustrative example, let us consider a general large scale tracer problem, on a mesh whose

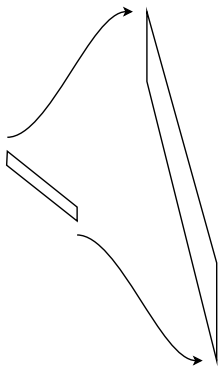

Figure 4.2: Dimensionless equivalent problem on stretched mesh involves to isotropic diffusion. The mesh is highly distorted as it does not respect the hydrostatic consistency principle.

typical horizontal and vertical elements sizes are 100 km and 10 m. Considering unresolved phenomena for this mesh scale, typical values of turbulent diffusivity in the ocean interior are of the order $\kappa_h = 10^4\ m^2 s^{-1}$ and $\kappa_v = 10^{-4}\ m^2 s^{-1}$ (Griffies, 2004; Ledwell et al., 1993; Mellor and Blumberg, 1985). The modified problem with a vertical diffusivity $\kappa_v = 10^4\ m^2 s^{-1}$ corresponds to a mesh stretched by a factor 10^4 in the vertical direction. The typical vertical mesh size would be 100 km and we would recover isotropic diffusion on an isotropic mesh. If we were to consider the surface layer of the ocean, or simply flows in the continental seas, the vertical eddy viscosity would be much larger, and the equivalent problem with an isotropic diffusion would involve elements with a relatively high aspect ratio. If the elements are too shallow, the stretched grid is highly distorted, as illustrated in Figure 4.2.

4.5 Discrete DG finite element formulations

For the sake of completeness, we provide here the full weak DG finite element formulations for each equation of the three-dimensional baroclinic marine model (4.1, 4.3, 4.5, 4.6, 4.7) using the numerical tools described in both previous sections. The discrete formulations can be then derived by replacing the test functions and the solution by the corresponding DG polynomial approximation.

4.5.1 Horizontal momentum equation

The discrete formulation of the horizontal momentum equation is obtained by multiplying equation (4.1) by a test function $\widehat{\boldsymbol{u}}$ and integrating over the whole domain Ω:

$$< \widehat{\boldsymbol{u}} \cdot \frac{\partial \boldsymbol{u}}{\partial t} > + < \widehat{\boldsymbol{u}} \cdot (\nabla_h \cdot (\boldsymbol{u}\boldsymbol{u})) > + < \widehat{\boldsymbol{u}} \cdot \frac{\partial (w - w_z)\boldsymbol{u}}{\partial z} > + < \widehat{\boldsymbol{u}} \cdot f \mathbf{e}_z \wedge \boldsymbol{u} > + < \widehat{\boldsymbol{u}} \cdot \frac{\boldsymbol{p}}{\rho_0} > + < \widehat{\boldsymbol{u}} \cdot g \nabla_h \eta > - < \widehat{\boldsymbol{u}} \cdot (\nabla_h \cdot (\nu_h \nabla_h \boldsymbol{u})) > - < \widehat{\boldsymbol{u}} \cdot \frac{\partial}{\partial z} \left(\nu_v \frac{\partial \boldsymbol{u}}{\partial z} \right) >= 0, \quad (4.20)$$

where $< >$ denotes the volume integral over the domain Ω. In order to be able to introduce discontinuous approximations, this integral is split into N_e integrals on each element Ω_e.

$$\sum_{e=1}^{N_e}\Bigg[< \widehat{\boldsymbol{u}}\cdot\frac{\partial \boldsymbol{u}}{\partial t} >_e + \underbrace{< \widehat{\boldsymbol{u}}\cdot(\nabla_h\cdot(\boldsymbol{u}\boldsymbol{u})) >_e}_{\text{horizontal advection}} + \underbrace{\widehat{\boldsymbol{u}}\cdot\frac{\partial (w-w_z)\boldsymbol{u}}{\partial z}}_{\text{vertical advection}}$$
$$+ \underbrace{< \widehat{\boldsymbol{u}}\cdot f\mathbf{e}_z\wedge\boldsymbol{u} >_e}_{\text{Coriolis}} + \underbrace{< \widehat{\boldsymbol{u}}\cdot\frac{\boldsymbol{p}}{\rho_0} >_e}_{\text{baroclinic pressure gradient}} + \underbrace{< \widehat{\boldsymbol{u}}\cdot g\nabla_h\eta >_e}_{\text{elevation gradient}}$$
$$- \underbrace{< \widehat{\boldsymbol{u}}\cdot(\nabla_h\cdot(\nu_h\nabla_h\boldsymbol{u})) >_e}_{\text{horizontal diffusion}} - \underbrace{< \widehat{\boldsymbol{u}}\cdot\frac{\partial}{\partial z}\left(\nu_v\frac{\partial \boldsymbol{u}}{\partial z}\right) >_e}_{\text{vertical diffusion}}\Bigg] = 0. \quad (4.21)$$

Apart from the baroclinic pressure terms, all terms containing spatial derivatives are integrated by parts on each element. Therefore, Neumann boundary fluxes appear along the interfaces between the elements. If we use discontinuous approximations, the key ingredient of the weak formulation is the way to define those fluxes as the variables are not uniquely defined on those interfaces. Each term of (4.21) is then derived as follows:

- Horizontal advection:

$$\sum_{e=1}^{N_e}\Big[- < \nabla_h\widehat{\boldsymbol{u}} : \boldsymbol{u}\boldsymbol{u} >_e + \ll (\{\boldsymbol{u}\}\{\boldsymbol{u}\}\cdot\widehat{\boldsymbol{u}})\cdot\boldsymbol{n}_h \gg_e + \ll \gamma[\boldsymbol{u}]\cdot\boldsymbol{n}_h \gg_e \Big]$$

- Vertical advection:

$$\sum_{e=1}^{N_e}\Big[- < \frac{\partial\widehat{\boldsymbol{u}}}{\partial z}\cdot(w-w_z)\boldsymbol{u} >_e + \ll \left(\widehat{\boldsymbol{u}}\cdot(w-w_z)^{\text{down}}\boldsymbol{u}^{\text{upwind}}\right)n_z \gg_e \Big]$$

- Elevation gradient:

$$\sum_{e=1}^{N_e}\Big[- < \nabla_h\cdot\widehat{\boldsymbol{u}}\, g\eta >_e + \ll g\eta^{\text{riemann}}\,\widehat{\boldsymbol{u}}\cdot\boldsymbol{n}_h \gg_e \Big]$$

- Horizontal diffusion:

$$\sum_{e=1}^{N_e}\Big[- < \nu_h(\nabla_h\widehat{\boldsymbol{u}}) : (\nabla_h\boldsymbol{u})^T >_e + \ll \nu_h\widehat{\boldsymbol{u}}\cdot\{\nabla_h\boldsymbol{u}\}\cdot\boldsymbol{n} \gg_e$$
$$+ \tfrac{1}{2} \ll \nu_h\nabla_h\widehat{\boldsymbol{u}}\cdot\boldsymbol{n}\cdot[\boldsymbol{u}] \gg_e + \sigma \ll \nu_h\widehat{\boldsymbol{u}}\cdot[\boldsymbol{u}] \gg_e \Big]$$

- Vertical diffusion:

$$\sum_{e=1}^{N_e}\Big[- < \nu_v\frac{\partial\widehat{\boldsymbol{u}}}{\partial z}\cdot\frac{\partial \boldsymbol{u}}{\partial z} >_e + \ll \nu_v\widehat{\boldsymbol{u}}\cdot\left\{\frac{\partial \boldsymbol{u}}{\partial z}\right\}n_z \gg_e$$
$$+ \tfrac{1}{2} \ll \nu_v\frac{\partial\widehat{\boldsymbol{u}}}{\partial z}n_z\cdot[\boldsymbol{u}] \gg_e + \sigma \ll \nu_v\widehat{\boldsymbol{u}}\cdot[\boldsymbol{u}] \gg_e \Big]$$

Baroclinic pressure gradient:

$$\sum_{e=1}^{N_e} \left[< \widehat{\boldsymbol{u}} \cdot \frac{\boldsymbol{p}}{\rho_0} >_e \right]$$

where $\boldsymbol{n}_h = (n_x, n_y)$ and n_z are respectively the horizontal and the vertical components of the outgoing normal of the boundary of the element. In the interface term for vertical advection, we perform upwinding of the advected variable $\boldsymbol{u}$, and we use the vertical velocity of the prism below the interface, so that the discrete vertical advection term is as close as possible to the corresponding term in the continuity equation. As we use the Riemann solver associated to the non-conservative $P_1^{DG} - P_1^{DG}$ discrete formulation of the two-dimensional shallow water equations for the gravity waves, it is critical that the resulting two-dimensional discrete equations obtained by integrating the momentum equation along the vertical axis approximately degenerate to this discrete formulation of the two-dimensional shallow water equations. To achieve this, the usual test function is divided by the depth at rest to obtain $\widehat{\boldsymbol{u}}$. Finally, the Lax-Friedrichs flux for the internal waves requires the additional boundary term $\ll \gamma [\boldsymbol{u}] \cdot \boldsymbol{n}_h \gg_e$ where γ is an upper bound of the fastest propagation speed of a three-dimensional phenomena, namely the sum of the phase speed of the fastest internal wave and the advection velocity. The interface terms for horizontal and vertical diffusion are directly derived from the SIPG procedure described by equation (4.18).

4.5.2 Vertical momentum equation

As the discrete variable associated with the vertical momentum equation is the vector field $\boldsymbol{p}$ that stands for the numerically computed baroclinic pressure horizontal gradient, we discretize the gradient of the balance of the vertical momentum (4.6) as follows:

$$\sum_{e=1}^{N_e} \left[< \widehat{\boldsymbol{p}}^{\text{up}} \cdot \frac{\partial \boldsymbol{p}}{\partial z} >_e \right] = \sum_{e=1}^{N_e} \left[- < \widehat{\boldsymbol{p}}^{\text{up}} \cdot (g \nabla_h \rho'(T,S)) >_e \right]. \tag{4.22}$$

To take into account that the integration is performed from top to bottom with a constant pressure at the sea surface (and therefore a vanishing pressure gradient), we use some fully upwinded test functions derived as the tensorial product between the usual P_1^{DG} triangle and the upwinded linear unidimensional element, whose value are 1 for the degree of freedom above the element and 0 for the degree of freedom below the element.

4.5.3 Continuity equation

The continuity equation can be viewed as a steady vertical transport equation along the vertical direction where the divergence of the horizontal velocity acts as a source term. The continuity equation is used to deduce the vertical velocity by integrating the horizontal velocity divergence from bottom to top. The discrete formulation of the continuity equation is obtained by multiplying equation (4.3) by a test function $\hat{w}$ and integrating over the whole domain Ω:

$$\sum_{e=1}^{N_e} \left[< \hat{w} \frac{\partial w}{\partial z} >_e + < \hat{w} \nabla_h \cdot \boldsymbol{u} >_e \right] = 0. \tag{4.23}$$

where the integral on the domain Ω is split into N_e integrals on Ω_e. Integrating by parts all terms containing spatial derivatives yields:

$$\sum_{e=1}^{N_e} \Big[\ll \hat{w} w^{\text{down}} n_z \gg_e - < \frac{\partial \hat{w}}{\partial z} w >_e + \ll \hat{w} \boldsymbol{u}^{\text{riemann}} \cdot \boldsymbol{n}_h \gg_e - < \nabla_h \hat{w} \cdot \boldsymbol{u} >_e \Big] = 0. \tag{4.24}$$

where we use w^{down} the value from the bottom element at the interfaces between layers of prisms, as the information goes from bottom to top in this pure transport equation. Moreover, a impermeability condition has to be prescribed at the sea bed, namely:

$$w^{-h} + \boldsymbol{u}^{-h} \cdot \nabla_h h = 0, \tag{4.25}$$

This boundary condition is weakly imposed by using $-\boldsymbol{u}^{-h} \cdot \nabla_h h$ for w^{down} in the first term of (4.24) at the sea bed. This only occurs on the first layer of prisms.

In the lateral interface, we use $\boldsymbol{u}^{\text{riemann}}$ because the discrete two-dimensional integral free surface equations will be obtained by aggregating the three-dimensional discrete continuity equations. In fact, the discrete procedure mimics the algebra performed to obtain the integral free-surface equation (4.7) by integrating the equation of continuity (4.3) and substituting the impermeability conditions at both the sea bed and the sea surface. The sea bed impermeability is already included in the discrete formulation of the continuity equation and the sea-surface condition will be incorporated by the motion of the free-surface. Finally, let us recall that we deduce $\boldsymbol{u}^{\text{riemann}}$ and η^{riemann} with the exact Riemann solver of the linear shallow water equations, we use the fact that the depth-integration of the momentum equation coupled with the free surface equation has to degenerate into a stable and an accurate $P_1^{DG} - P_1^{DG}$ discretization of the two-dimensional shallow water equations. Therefore, as the discrete free-surface equation will be obtained by aggregating the discrete continuity equation, it is mandatory to use $\boldsymbol{u}^{\text{riemann}}$ here, to have it in the resulting free-surface equation. As a last remark, it is also important to emphasize that the vertical velocity is not a prognostic field. It is a by-product used to deduce the vertical advection terms in the momentum and tracer equations. Elevation, velocities and tracer are prognostic fields. An accurate DG discretization of our set of equation should be such that these fields are computed with an optimal accuracy, i.e. $p+1$ convergence rate if order p shape functions are used. It is *not* the case for vertical velocity. Vertical velocity is not smooth, because it results from the integration of the divergence of the horizontal velocity. It behaves similarly to the volume term from an advection term integrated by parts: it is not smooth, but it does not impair the optimal convergence of the other fields. Indeed, at the discrete level, it is easily seen that, if the prisms are straight, the vertical velocity lives in a discrete space that is piecewise constant in the horizontal direction, rather than linear. The smoothness of tracer and horizontal velocity field is recovered as usual in DG, using the interface term, acting as a penalty term.

4.5.4 Free-surface equation

The free-surface equation (4.7) can be viewed as the two-dimensional counterpart of the continuity equation, as the vertical integration of the continuity equation will lead to:

$$w^{\eta} - w^{-h} + \int_{-h}^{\eta} \nabla_h \cdot \boldsymbol{u} dz = 0,$$

if we incorporate impermeability conditions at the sea bed and sea surface, we exactly obtain the mass conservation equation of the shallow water problem that can be written as:

$$\frac{\partial \eta}{\partial t} + \boldsymbol{u}^{\eta} \cdot \nabla_h \eta + \boldsymbol{u}^{-h} \cdot \nabla_h h + \int_{-h}^{\eta} \nabla_h \cdot \boldsymbol{u} dz = 0 \tag{4.26}$$

Formally, the discrete formulation of the free-surface equation is obtained by multiplying equation (4.26) by a test function $\hat{\eta}$ and integrating over the two-dimensional basement of the three-dimensional computational domain Ω. This basement is paved of N_f triangles Δ_f that are the elements of the initial two-dimensional mesh that was extruded to produce the three-dimensional mesh of prisms. This discrete formulation reads:

$$\sum_{f=1}^{N_f} \Big[\ll \hat{\eta} \frac{\partial \eta}{\partial t} \gg_{\Delta f} + \ll \hat{\eta}\ \boldsymbol{u}^{\eta} \cdot \nabla_h \eta \gg_{\Delta f} \underbrace{+ \ll \hat{\eta}\ \boldsymbol{u}^{-h} \cdot \nabla_h h \gg_{\Delta f} + \ll \hat{\eta} \int_{-h}^{\eta} \nabla_h \cdot \boldsymbol{u} dz \gg_{\Delta f}}_{\text{aggregated discrete continuity equations}} \Big] = 0. \tag{4.27}$$

where $\ll \gg_{\Delta f}$ denotes the integral over the triangle Δ_f of the two-dimensional mesh of N_f triangles.

The last two terms can be obtained by the aggregation of the discrete continuity equation (4.24). One term is exactly the depth-integration of the velocity divergence term corresponding to the continuity equation (4.3). Rather than computing this term twice at the risk of introducing inconsistencies which would break mass conservation, the velocity divergence operator is computed only once for the continuity equation. The second step consists in performing an exact vertical integral by aggregating the lines and columns of the three-dimensional discrete matrix whose corresponding nodes are aligned on the same vertical line. It can be shown that this aggregation exactly corresponds to the discrete form of the depth-integration of the continuous equation. An interface term in the first layer of prisms in the discrete formulation (4.24) imposes the impermeability at the sea bed. It can also be shown that this term exactly corresponds to the term:

$$\sum_{f=1}^{N_f} \Big[\ll \hat{\eta}\ \boldsymbol{u}^{-h} \cdot \nabla_h h \gg_{\Delta f} \Big].$$

The opposite sign and the difference between the areas of integration are counterbalanced by the vertical component of the outgoing normal n_z.

Now, using the *linear surface approximation* simply consists of substituting equation (4.27) by:

$$\sum_{f=1}^{N_f} \Big[\ll \hat{\eta} \frac{\partial \eta}{\partial t} \gg_{\Delta f} \underbrace{+ \ll \hat{\eta}\ \boldsymbol{u}^{-h} \cdot \nabla_h h \gg_{\Delta f} + \ll \hat{\eta} \int_{-h}^{0} \nabla_h \cdot \boldsymbol{u} dz \gg_{\Delta f}}_{\text{aggregated discrete continuity equation}} \Big] = 0. \tag{4.28}$$

Again, such an approximation may be convenient in some large scale application, but must be avoided in coastal problems. Equation (4.28) can also be viewed as the discretization of

$$\frac{\partial \eta}{\partial t} + \nabla_h \cdot \int_{-h}^{0} \boldsymbol{u} dz = 0., \tag{4.29}$$

which is the mass conservation equation of the linear shallow water problem.

4.5.5 Tracer equation

As for the momentum equation, the weak formulation for the tracer equation can be written on each element as follows:

$$\sum_{e=1}^{N_e}\Bigg[< \hat{c}\frac{\partial c}{\partial t} >_e + \underbrace{< \hat{c}\ (\nabla_h \cdot (\boldsymbol{u}c)) >_e}_{\text{horizontal advection}} + \underbrace{< \hat{c}\frac{\partial (w-w_z)c}{\partial z} >_e}_{\text{vertical advection}} - \underbrace{< \hat{c}\ (\nabla_h \cdot (\kappa_h \nabla_h c)) >_e}_{\text{horizontal diffusion}} - \underbrace{< \hat{c}\ \frac{\partial}{\partial z}\left(\kappa_v \frac{\partial c}{\partial z}\right) >_e}_{\text{vertical diffusion}}\Bigg] = 0. \quad (4.30)$$

We integrate by parts the transport and diffusion terms and choose the suitable values for the interface terms. As for the momentum equation, we add the interface term $\ll \gamma\,[c] \gg_e$ that is deduced from the Lax-Friedrichs solver for internal waves. It is a very important term for the numerical properties of the model as internal waves are a phenomenon that couples momentum and tracers. Each term of (4.30) is then derived as follows:

- Horizontal advection:

$$\sum_{e=1}^{N_e}\Big[- < \nabla_h \hat{c} \cdot \boldsymbol{u}c >_e + \ll \hat{c}\,\{c\}\,\boldsymbol{u}^{\text{riemann}} \cdot \boldsymbol{n}_h \gg_e + \ll \gamma\,[c] \gg_e \Big]$$

- Vertical advection:

$$\sum_{e=1}^{N_e}\Big[- < \frac{\partial \hat{c}}{\partial z}\,(w-w_z)c >_e + \ll \left(\hat{c}\,(w-w_z)^{\text{down}} c^{\text{upwind}}\right) n_z \gg_e \Big]$$

- Horizontal diffusion:

$$\sum_{e=1}^{N_e}\Big[- < \kappa_h\,(\nabla_h \hat{c}) \cdot (\nabla_h c) >_e + \ll \kappa_h \hat{c}\,\{\nabla_h c\} \cdot \boldsymbol{n} \gg_e + \tfrac{1}{2} \ll \kappa_h \nabla_h \hat{c} \cdot \boldsymbol{n} \cdot [c] \gg_e + \sigma \ll \kappa_h \hat{c}\,[c] \gg_e \Big]$$

- Vertical diffusion:

$$\sum_{e=1}^{N_e}\Big[- < \kappa_v \frac{\partial \hat{c}}{\partial z}\frac{\partial c}{\partial z} >_e + \ll \kappa_v \hat{c}\left\{\frac{\partial c}{\partial z}\right\} n_z \gg_e + \tfrac{1}{2} \ll \kappa_v \frac{\partial \hat{c}}{\partial z} n_z\,[c] \gg_e + \sigma \ll \kappa_v \hat{c}\,[c] \gg_e \Big]$$

To ensure consistency, it is mandatory that the discrete advection term degenerates to the continuity equation when a unit tracer concentration is considered (White et al., 2008b). Therefore, one must use the same interpolation for both c and w. Indeed, $\boldsymbol{u}$ and w must follow the same definition as in the continuity equation, i.e. we use $\boldsymbol{u}^{\text{riemann}}$ in the interface term for the horizontal advection, and we use w^{down} in the interface

term for the vertical advection. However, the choice of the interface value for the tracer concentration c at the interface is not constrained by consistency considerations. We can use upwind or centered values. The additional term from the Lax-Friedrichs solver does not impair consistency as it is exactly nil for a constant tracer. The bottom boundary conditions must also be compatible, this being ensured by suppressing the boundary terms for advection at the sea bottom.

4.6 Numerical results

To demonstrate the accuracy of the model, we simulate the internal waves in the lee of a moderately tall seamount. The simulation of such a complex flow can be considered as a relevant test case to validate the accuracy and the robustness of a three-dimensional marine model. Complicated phenomena can be observed in the wake of mountains, such as internal wave structures (see Figure 4.3) and vortex streets (see Figure 4.4). (Chapman and Haidvogel, 1992, 1993; Ford et al., 2004a). Such a problem was simulated with three-dimensional baroclinic finite difference (Huppert and Bryan, 1976; Chapman and Haidvogel, 1992, 1993), finite volume (Adcroft et al., 1997), finite element models (Ford et al., 2004a; Wang et al., 2008a,b). It exhibits similar dynamics as atmospheric flows, but with lower Rossby and Froude numbers. If the seamount is small enough, a complicated structure of standing internal waves can develop in the wake of the seamount. Chapman and Haidvogel (1993) provide a detailed numerical study of internal lee waves trapped over isolated Gaussian shaped seamounts. Such a testcase is also used by Ford et al. (2004a) to assess the qualities and drawbacks of their model. With our three-dimensional baroclinic marine model, we simulate the internal lee waves for a seamount whose the height is 30% of the total depth. The complicated internal wave structure developed in the wake of the seamount can be considered as a relevant test case for assessing the accuracy of the spatial discretization. In this paper, we thus focus on the accurate representation of the spatial structure of these waves in the area where the flow structure is established in time.

The set up of the problem can be summarized as follows. A Gaussian seamount is located at 45 degrees North with a bathymetry given by:

$$1 - \frac{h(x,y)}{H} = \delta \exp\left(\frac{\left(x - \frac{R}{2}\right)^2 + \left(y - \frac{R}{2}\right)^2 + \left(z - \frac{R}{\sqrt{2}}\right)^2}{-L^2} \right), \tag{4.31}$$

where $H = 4.5\ km$ is the maximum depth, $\delta = 0.3$ is the relative height of the seamount, $R = 6\,372\ km$ is Earth radius and $L = 25\ km$ is the length scale of the seamount. The coordinates x, y and z are relative to the global Cartesian frame of reference. The flow simulation is initiated with a global zonal geostrophic equilibrium ignoring the seamount. In other words, the initial guess of the calculation is selected as in the Testcase 5 of Williamson where the velocity field only exhibits a non vanishing East component u_e. In this testcase (Williamson et al., 1992), the elevation and velocity fields are shown in Figure 4.5 and are respectively given by

$$\frac{\eta}{U^2/g} = -\frac{z^2}{R^2}\left(1 + \sqrt{2}\,\frac{R\Omega}{U}\right), \tag{4.32}$$

$$\frac{u_e}{U} = \sqrt{\frac{x^2 + y^2}{R^2}}, \tag{4.33}$$

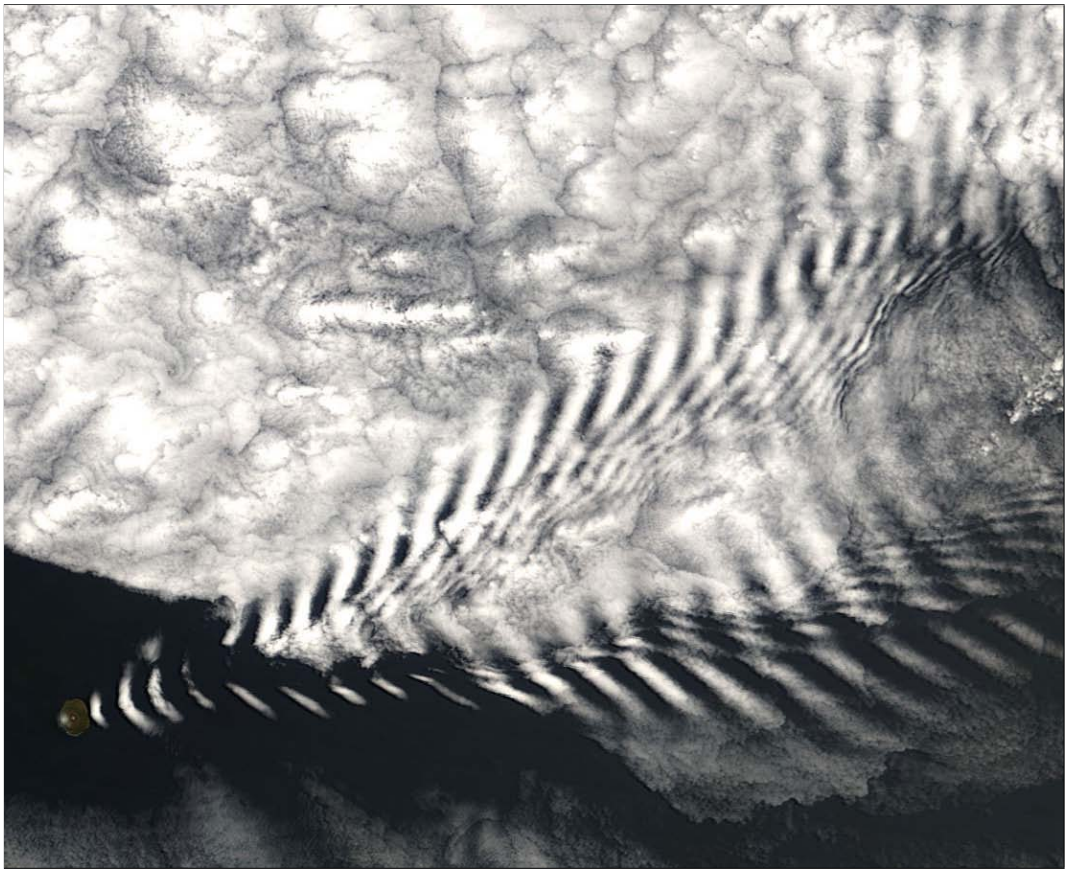

Figure 4.3: Cloud waves in the lee of Amsterdam Island, located in the Indian ocean. NASA image courtesy Jeff Schmaltz, MODIS Land Rapid Response Team at NASA GSFC (`http://earthobservatory.nasa.gov/IOTD/view.php?id=6151`).

Figure 4.4: Vortex street in the lee of Jan Mayen island, located about 650 km northeast of Iceland. Image courtesy NASA/GSFC/LaRC/JPL, MISR Team (`http://earthobservatory.nasa.gov/IOTD/view.php?id=2270`).

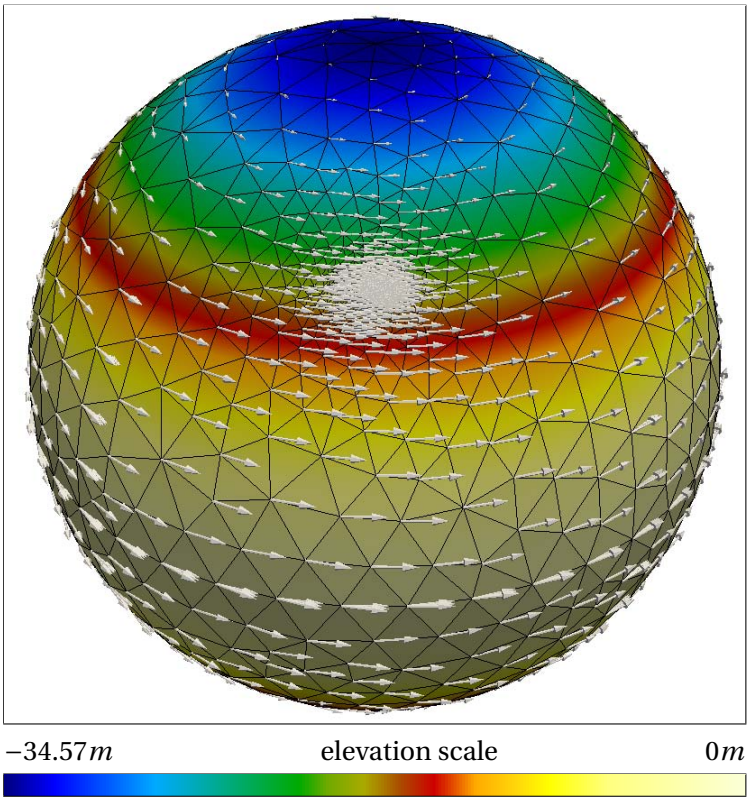

Figure 4.5: Initial condition for sea-surface elevation and velocities. The mesh is refined in the lee of the seamount.

where $U = 0.516\ m\ s^{-1}$ is the velocity scale at 45 degree North, $\Omega = 7.292 \times 10^{-}5\ s^{-1}$ is Earth rotation rate, and $g = 9.81\ ms^{-2}$ is the gravitational acceleration. We consider the density deviation ρ' as the unique tracer of the model and the initial value of the density deviation is a linear function of the vertical coordinate, with vanishing mean. The derivative of the density with respect to the vertical coordinate is given by $\partial\rho/\partial z = -3.43 \times 10^{-5}\ kg\ m^{-4}$ and the reference density is selected as $\rho_0 = 1025\ kg\ m^{-3}$. The turbulent viscosities and diffusivities are given by: $\nu_h = \kappa_h = 12.9\ m^2\ s^{-1}$, $\nu_v = 0.0001\ m^2\ s^{-1}$ and $\kappa_v = 0$. With those parameters, the flow is characterized by the same four dimensionless numbers as that of the Section 3d of Ford et al. (2004a). These dimensionless number are defined as follows:

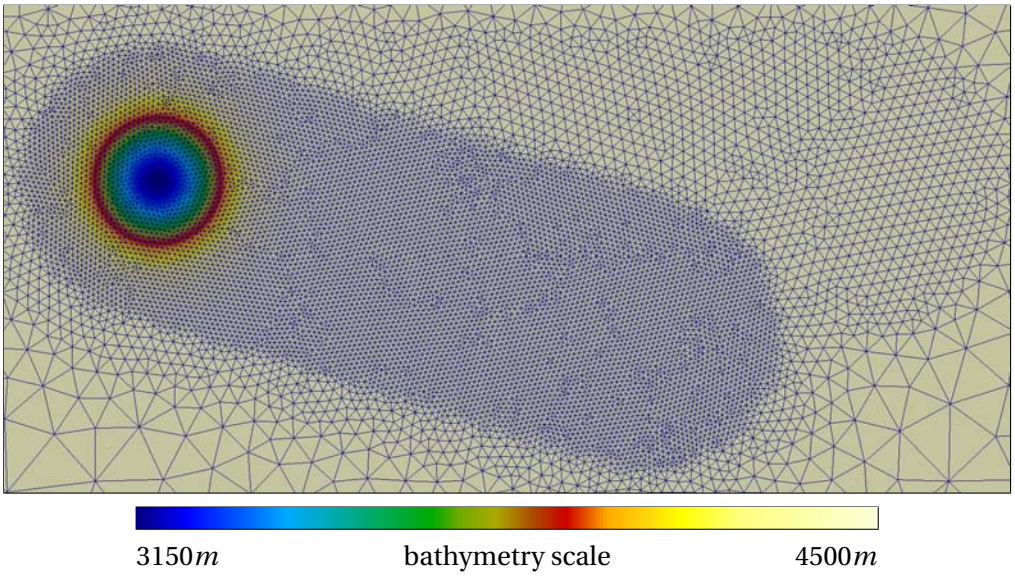

Figure 4.6: Close-up view on the mesh and the bathymetry around the seamount. The mesh is refined in the lee of the seamount.

- Seamount ratio $\delta = 0.3$

- Rossby number $Ro = \dfrac{U}{fL} = 0.2$

- Reynolds number $Re = \dfrac{UL}{\nu_h} = 1000$

- Burger number $Bu = \dfrac{NH}{fL} = \sqrt{\dfrac{-g}{\rho_0}\dfrac{\partial\rho}{\partial z}}\dfrac{H}{fL} = 1$

where N is the Brunt-Väisälä frequency.

The computational domain is the whole sphere, as we can take advantage of a highly variable mesh density. It allows us to avoid open boundary conditions, while previous publications use rectangular domains, with imposed inflow, sponge layer as outflow condition, and lateral walls (Chapman and Haidvogel, 1992). Figure 4.6 shows a close-up view of the mesh and the bathymetry near the seamount. The mesh resolution is refined in the lee of the seamount to capture accurately the flow structure. Indeed, we know *a priori* that the structures generated in the lee of the seamount are deviated to the right, due to the mean transverse flow generated between the two vortices that are generated. In this zone, we refined the mesh so that the element size is sufficiently small compared to the wave length of the generated internal waves. The edge-length in this refined zone is 2 km. This mesh is made up of 23562 triangles extruded into 25 σ layers. Basically, it can also be viewed as a trial and error procedure where a preliminary calculation allows us to a fine tuning of the mesh refinement. Obviously, the automatic adaptive refinement procedure will be a more general approach.

The only numerical parameter that has to be selected in the three-dimensional baroclinic model is the jump penalty parameter γ in the Lax-Friedrichs solver. For this problem, we select $\gamma = 4\ m\ s^{-1}$. This parameter must be an upper bound of the phase speed of the fastest wave. From the linear theory, we know that with the prescribed stratification, the maximum phase speed of an internal wave is about $c = 1\ m\ s^{-1}$, so that the fastest three-dimensional phenomenon propagates at $c+U \approx 1.5\ m\ s^{-1}$. For discontinuous linear elements combined with the second order explicit Runge-Kutta time-stepper (Chevaugeon et al., 2007) used in this simulation, the relevant CFL conditions leads us to select a time step of 30 s with a second order explicit Runge-Kutta time-stepper.

The two-dimensional mesh on the sea bottom and the time evolution for the isosurfaces of the density perturbations are show in Figure 4.7. The density perturbation is defined as the density deviation field ρ' from which the initial density deviation has been removed. The density perturbation can be considered as a good diagnostics: as the flow is dominated by geostrophy, it is directly an image of the vorticity induced by the fact that the flow is impulsively started. The free surface is raised upstream of the seamount, and lowered downstream, leading thanks to geostrophic adjustment to an upstream clockwise vortex, and a downstream counter-clockwise vortex, which are both clearly visible in Figure 4.7. The flow is strong enough to directly shed the counter-clockwise eddy away from the seamount. The mean flow is deviated rightward downstream of the seamount. The clockwise eddy is trapped over the seamount. In the zone between the two eddies, internal waves are generated. Rather than being radiated away from the seamount, they are trapped in the lee of the seamount.

In Figure 4.8, we also see that these waves have a particular structure. In the plots of the time evolution of the density perturbation at a 400 m depth, we observe that the waves are generated by the shedded eddy, propagate westward and stack in the lee of the seamount. Again, the upstream clockwise vortex, and the downstream counter-clockwise vortex, are both clearly visible in Figure 4.8.

At the seventh day, two well separated modes in the density perturbation field are clearly visible as shown in Figure 4.9. In the left side of the lee, looking downstream, an internal mode with two extrema appear. In the right side of the lee, an internal wave mode with three extrema appear. These numerical results can be compared with the theoretical analysis of the internal waves given in Lecture 17 of the book of Pedlosky (2003). The theory of the internal waves in a flat bottom ocean with uniform stratification implies the occurrence of eigenmodes. The vertical wave number is:

$$m = \frac{i\pi}{H}, \tag{4.34}$$

with the integer i being the number of extrema of the vertical wave profile. In a linear analysis, these modes are independent and each of these modes behaves as a shallow water layer, with an equivalent depth defined as:

$$h_i = \frac{N^2 H^2}{i^2 \pi^2 g}. \tag{4.35}$$

As for the usual shallow water equations, Kelvin waves along coastlines, Poincaré waves and Rossby waves can be observed. However, as we are interested in a flow over a relatively short period of time on a aquaplanet without coastlines , only the Poincaré

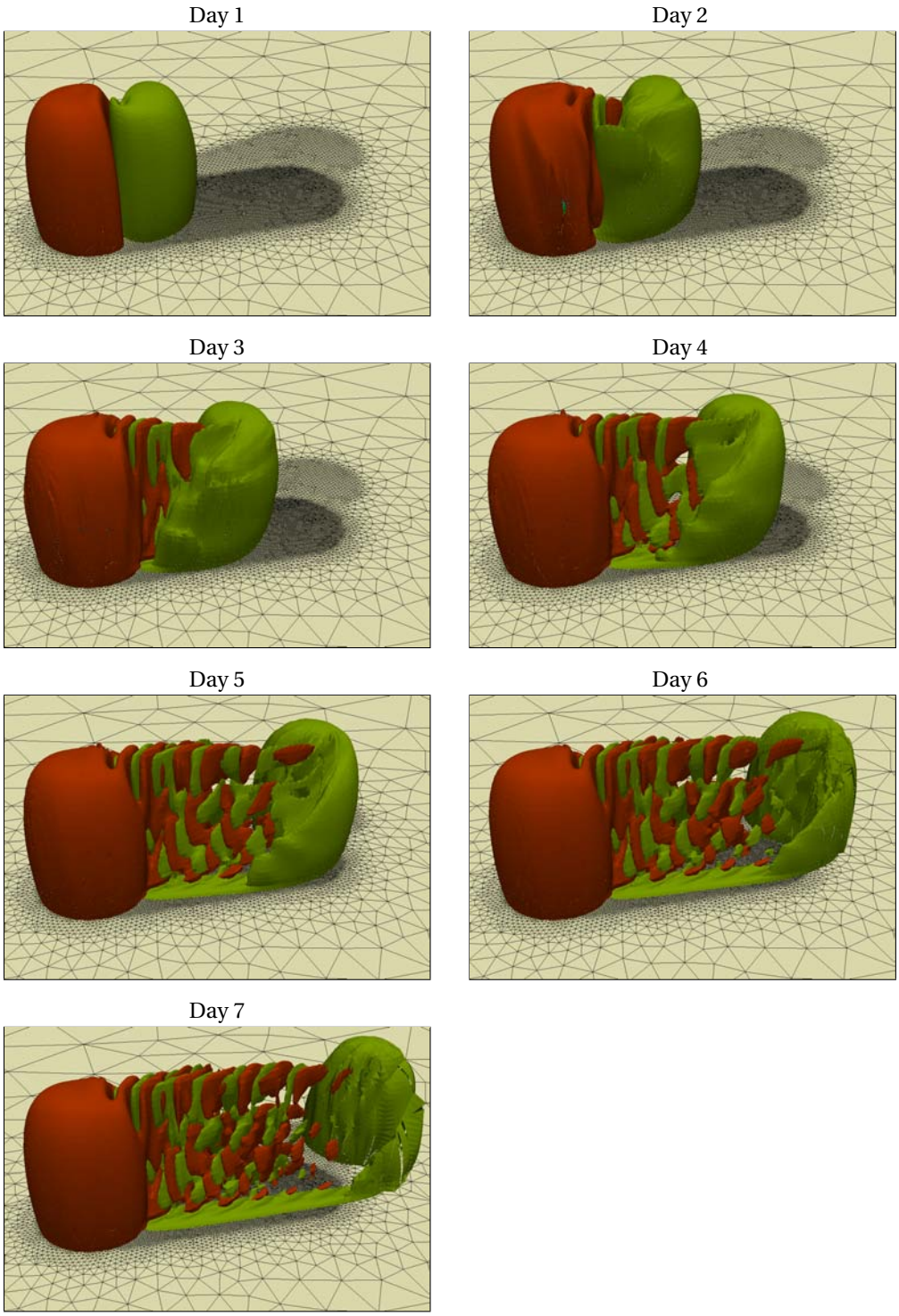

Figure 4.7: Time evolution of the isosurfaces of the density perturbation. Isovalues for the density perturbation of $-0.001\ kg\ m^{-3}$ are in green. Isovalues for the density perturbation of $0.001\ kg\ m^{-3}$ are in orange. The two-dimensional mesh is given on the sea bottom.

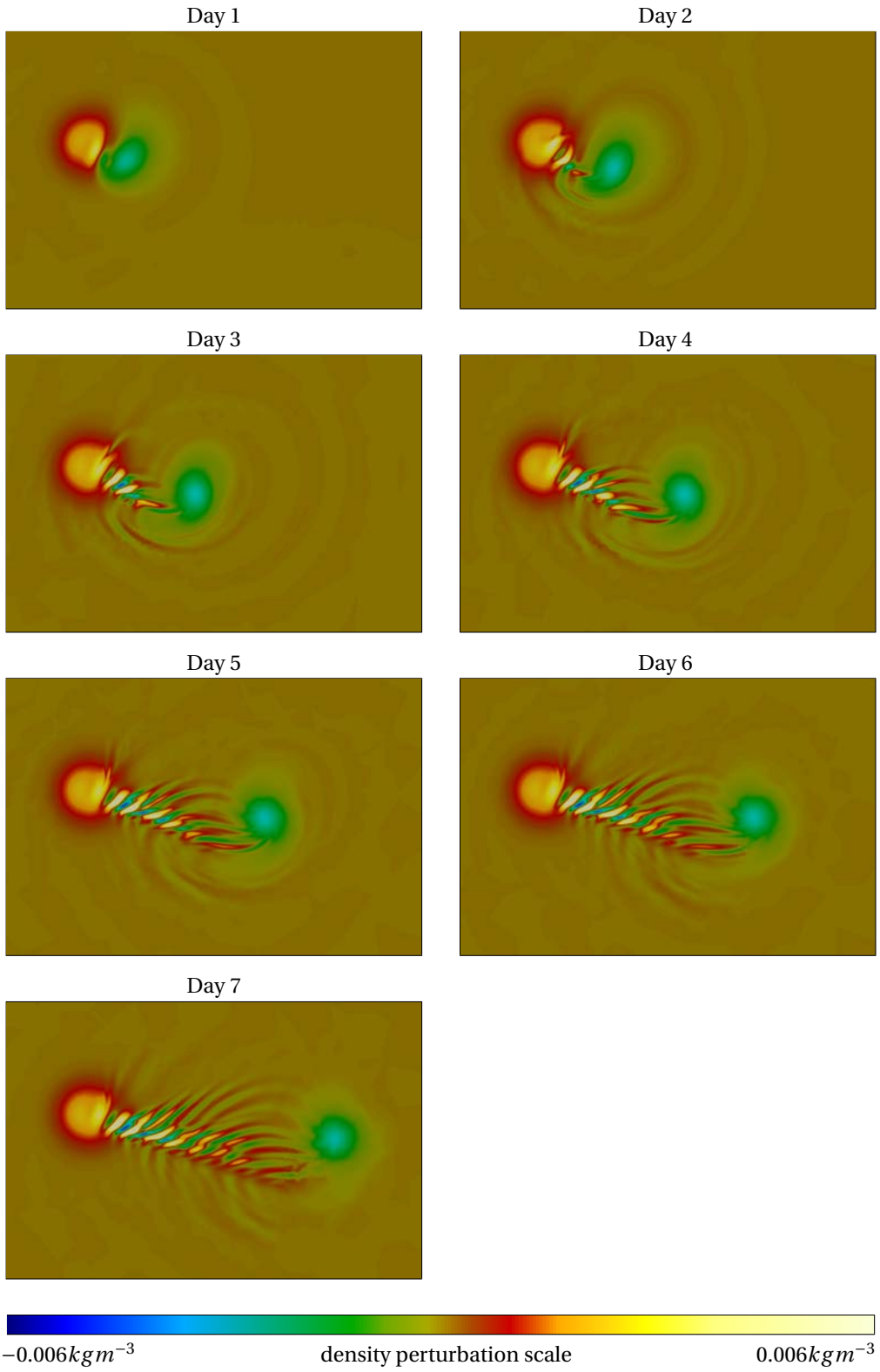

Figure 4.8: Time evolution of the density perturbation field at a 400 m depth. The internal waves lying between the two vortices are clearly visible.

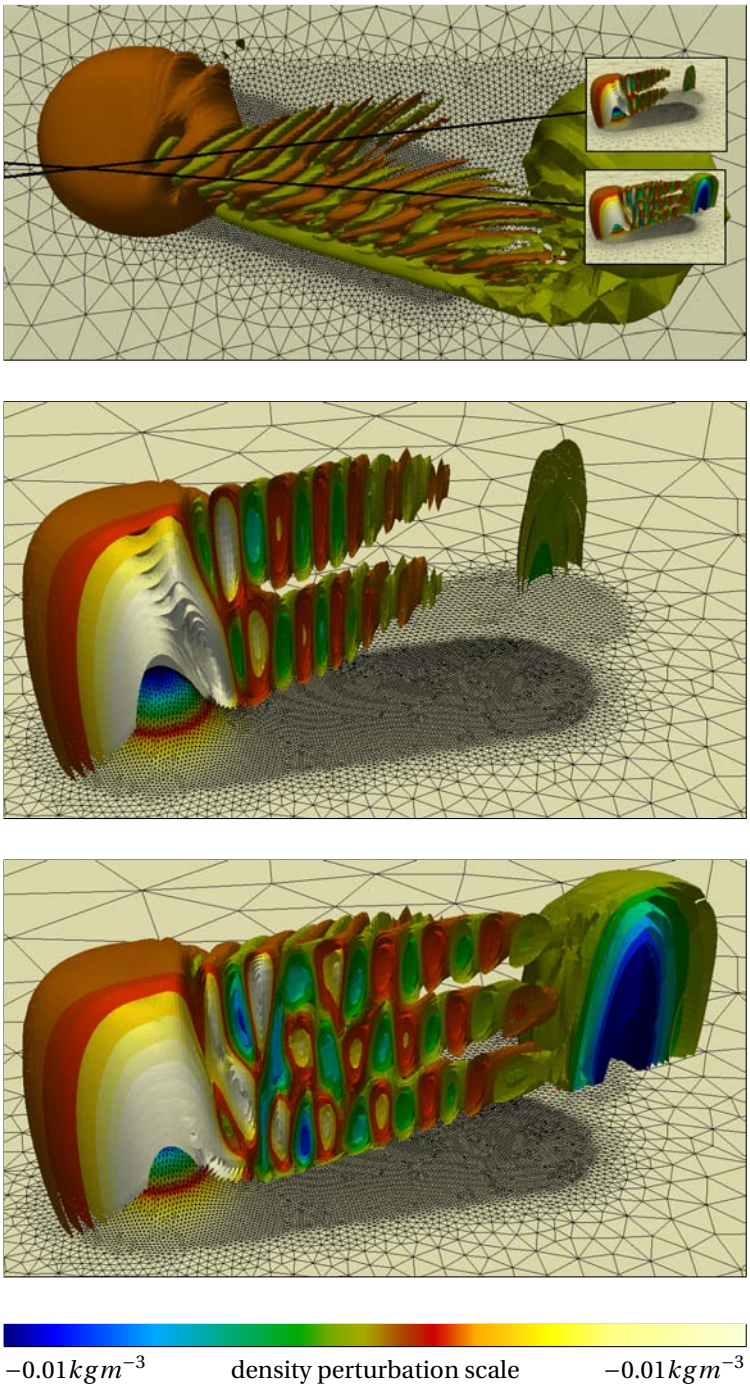

Figure 4.9: Illustration of the two well separated modes at day 7. The top panel shows a view of the isocontours of the density perturbation. Two cuts are defined and are given on the two lower panels. Isocontours values range from -0.02 to 0.02 $kg\ m^{-3}$ with an interval of 0.002. Isovalues of -0.005 and 0.005 are added, while the zero isovalue is removed.

waves are relevant here. The phase speed of the Poincaré waves is given by:

$$c_i = \sqrt{g h_i + \frac{f^2}{k^2}} = \sqrt{\frac{N^2 H^2}{i^2 \pi^2} + \frac{f^2}{k^2}}, \tag{4.36}$$

where k is the horizontal wavenumber. For the flow to support standing waves, the propagation speed of internal waves in the opposite direction of the mean flow must be equal to the mean flow speed:

$$c_i = U \cos(\alpha), \tag{4.37}$$

where α is the angle between the mean flow speed and the direction of the waves propagation. The direction of waves propagation is normal to the waves crests.

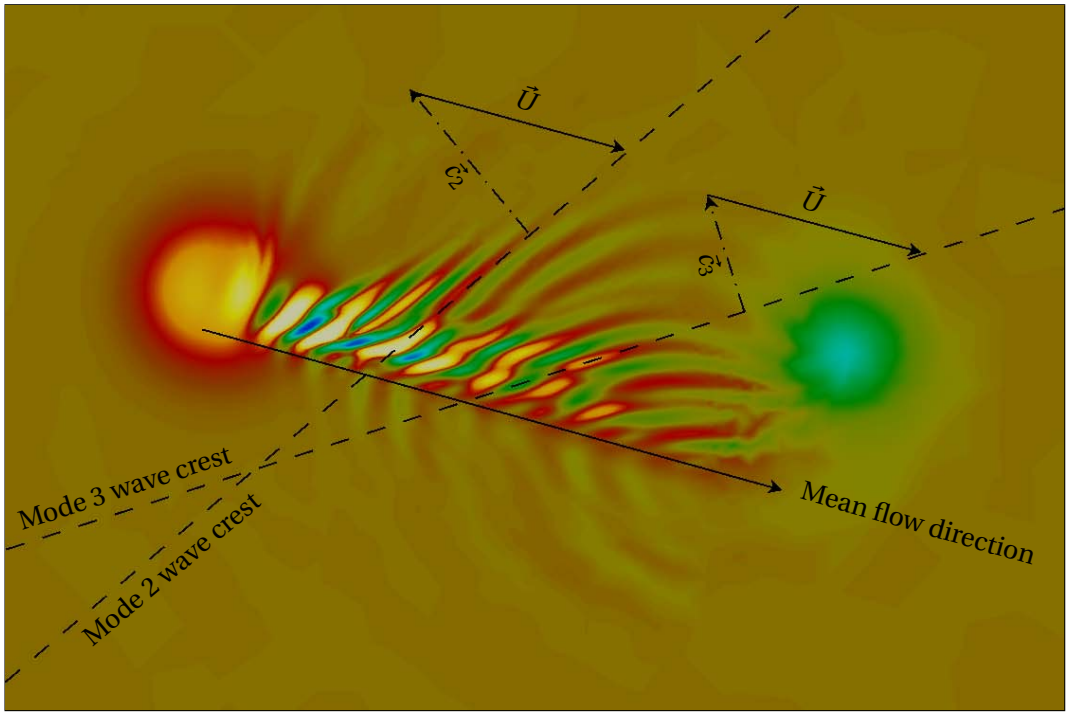

Figure 4.10: Sketch of the wave modes and propagation speeds. $\vec{U}$ denotes the mean velocity vector. It is not horizontal because the mean flow is deviated to the right by the seamount. $\vec{c}_2$ and $\vec{c}_3$ denotes the phase speed vector for mode 2 and mode 3 internal waves, respectively. The amplitude of the phase speed vectors is taken for the waves to be stationary.

In Figure 4.10, we represent the wave modes and propagation speeds. The mean velocity vector is not aligned because the mean flow is deviated to the right by the seamount. The phase speed vector for mode 2 and mode 3 internal waves are also given, with the amplitude of the phase speed vectors selected for stationary waves. From such a picture, the angle α between the mean flow speed and the propagation of the waves propagation can be deduced. For mode 2 waves, the observed angle between mean flow velocity and horizontal wave vector is about $\alpha \approx 35\,^\circ$ in Figure 4.10. Taking advantage of the theoretical linear analysis, we use equation (4.36) and equation (4.37), to estimate the horizontal wavenumber of the waves from the observed angle α and the vertical

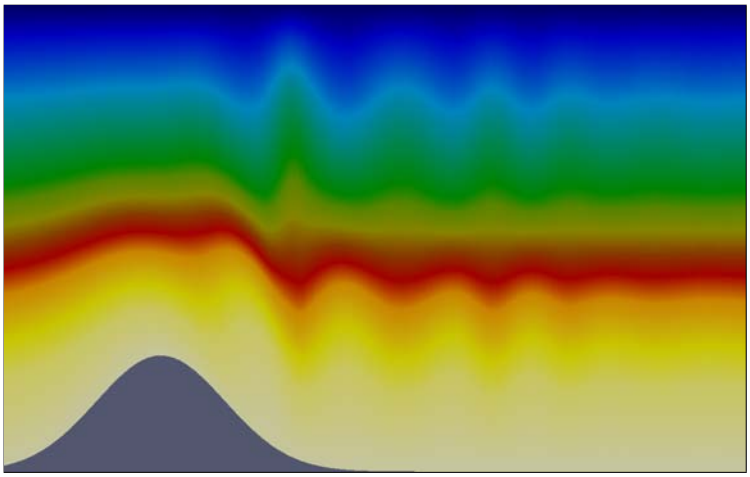

Figure 4.11: Cut in the density field at day 7, along the cut plane for mode 2 defined in Figure 4.9. We observe large amplitude internal waves.

wavenumber (i.e. the number. of modes)

$$\begin{aligned} c &= 0.42\ ms^{-1}, \\ k &= 1.03 \times 10^{-3}. \end{aligned}$$

This speed is close to the threshold value 0.410 ms^{-1}, under which the flow is subcritical for mode 2, and stationary lee waves cannot exists. From the calculated horizontal wavenumber, the wave length is estimated to be $2\pi/k = 6.1\ km$ and should corresponds to the crest to crest distance. However, in Figure 4.10, we observe a crest to crest distance of 18.75 km for mode 2. Such a discrepancy between those two results can be explained by the fact that the phase speed is very close to the threshold value for which no wave can exist. Therefore, the phase speed does not depend so strongly on the wavenumber. Moreover, if we perform a vertical slice in the density deviation field ρ', we observe that the amplitude of the waves is significant compared to the total depth in Figure 4.11. Therefore, considering the linear regime for the theoretical computation of the dispersion relation is probably a bad assumption and can induce significant errors.

4.7 Conclusions

The spatial discretization of a three-dimensional baroclinic free-surface marine model is introduced. This model relies on a Discontinuous Galerkin method with a mesh of prisms extruded in several layers from an unstructured two-dimensional mesh of triangles. As the prisms are vertically aligned, the calculation of the vertical velocity and the baroclinic pressure gradient can be implemented in an efficient and accurate way. All discrete fields are defined in discontinuous finite element spaces, to take advantage of the good numerical properties of the Discontinuous Galerkin methods for advection dominated problems and for wave problems. To be able to use the Riemann solver of the shallow water equations, the discretization of the three-dimensional horizontal momentum and the continuity equations are defined in such a way that their discrete integration along the vertical axis provide a stable $P_1^{DG} - P_1^{DG}$ formulation of the shallow water

equations. Therefore, we can stabilize the discrete equations by using the exact Riemann solver of the linear shallow water for the gravity waves. For internal waves, an additional stabilizing term is derived from a Lax-Friedrich solver. In the baroclinic dynamics, the vertical velocity acts as a source term, while the role of the approximate Riemann solver is to penalize inter-element jumps to recover optimal accuracy. Consistency is ensured. The model is able to advect exactly a tracer with a constant concentration, meaning that the discrete transport term is compatible with the continuity equation.

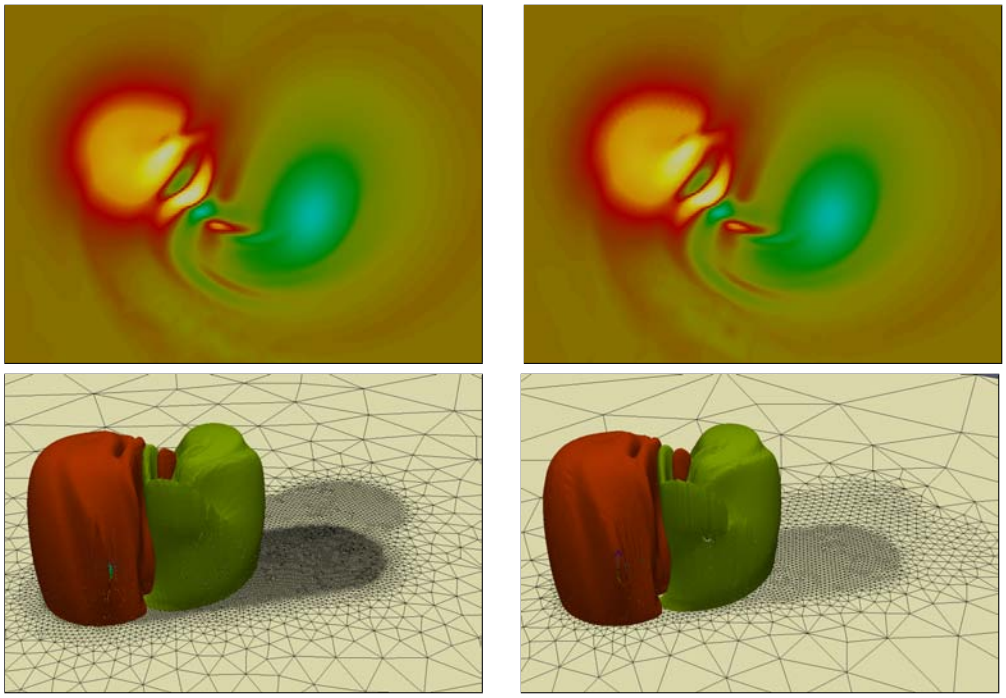

Figure 4.12: Comparison of linear (top) and quadratic (bottom) spatial discretization for the 30% height case. Density perturbation isocontours after two days.

A key advantage of Discontinuous Galerkin finite elements is their ability to naturally handle higher order discretizations. The discrete formulation with the same approximate Riemann solvers can be used for high order shape functions. As an illustrative example, we simulate the same problem as in Section 4.6 with second order shape functions and a mesh two times coarser involving 12 layers. The triangles are twice larger than in the previous calculation. A comparison of the density perturbation field after two days is shown in Figure 4.12. We observe the same behavior, as both simulations are performed on a sufficiently fine mesh. However, some small oscillations are induced by the subparametric representation of the bottom topography. They appear above the seamount for the quadratic shape functions computation. Indeed, the bathymetry is still represented using piecewise linear polynomials, while the fields are represented using piecewise quadratic polynomials. But, we think that such a discretization of a three-dimensional baroclinic finite element marine model is an effective way for higher order elements, paving the way for high order ocean models based on Discontinuous Galerkin methods.

In conclusion, we use a three-dimensional finite element baroclinic free-surface model to represent accurately the complex structure of the internal waves in the lee of an isolated seamount, using either linear or quadratic shape functions. The model does not yet handle internally supercritical flows, that occur for instance when internal waves break or in steed gravity currents. Including a limiting strategy to handle shockwaves would be the next required step. Finally, the second key ingredient for an efficient three-dimensional marine model is the definition of a good time integration procedure. This will be the topic of the second part of this contribution.

CHAPTER 5

A THREE-DIMENSIONAL BAROCLINIC MODEL: TEMPORAL DISCRETIZATION

This Chapter reproduces the following paper, first submitted on 7 July 2010:

R. Comblen, S. Blaise, V. Legat, J.-F. Remacle, E. Deleersnijder, and J. Lambrechts. A discontinuous finite element baroclinic marine model on unstructured prismatic meshes. Part II: implicit/explicit time discretization. *Ocean Dynamics (submitted)*, 2010.

Abstract

We describe the time discretization of a three-dimensional baroclinic finite element model for the hydrostatic Boussinesq equations based upon a Discontinuous Galerkin finite element method. On one hand, the time stepper is based on an efficient mode splitting. To ensure compatibility between the barotropic and baroclinic modes in the splitting algorithm, we introduce Lagrange multipliers in the discrete formulation. On the other hand, the use of implicit-explicit Runge-Kutta methods enables us to treat stiff linear operators implicitly, while the rest of the nonlinear dynamics is treated explicitly. By way of illustration, the time evolution of the flow over a tall isolated seamount on the sphere is simulated. The seamount height is 90% of the mean sea depth. Vortex shedding and Taylor caps are observed. The simulation compares well with results published by other authors.

5.1 Introduction

The spatially discretized ocean system is a dynamical system with a very large number of unknowns. It is the case for many computational fluid dynamics problems. However, oceanic problems typically consider very large timescales compared to those of the rapidly varying dynamics of local flows. Indeed, for climate modeling, centuries are considered, while it only takes a few hours for a surface gravity wave to propagate around the world. Therefore, if a completely explicit scheme is considered, hundreds of millions of time steps are required to model the ocean system for a few centuries (considering a 2×2 degree model, that requires a 90 second time step). This must be compared to engineering problems where typically fewer time steps are needed. For instance, consider the unsteady flow around a commercial aircraft, with elements of a centimeter (that means many elements ...), at cruise speed. This would require about one million time steps to compute the flow during 10 seconds. We see that the number of time steps required to perform the simulation are two orders of magnitude larger for climate problems than for engineering problems.

Early models used the rigid-lid approximation, where the sea surface is assumed to be a rigid horizontal, impermeable boundary. This approximation filters out the fast surface gravity waves. The two-dimensional mean problem is solved either using a streamfunction formulation (Bryan, 1969) or a surface pressure formulation (Dukowicz et al., 1993). The computation of the surface pressure or streamfunction leads to elliptic two-dimensional problems, the rest of the dynamics being computed with explicit methods such as leap-frog with filtering (Griffies et al., 2000). Explicit methods for hyperbolic problems are subject to the Courant-Friedrichs-Lewy stability condition: the time step must be sufficiently small that the information in a cell only influences its direct neighbors, i.e. the time step scales as the ratio of the grid size to the fastest wave speed. For rigid-lid models, the fastest phenomena are internal gravity waves. When free-surface is taken into account, much faster phenomena occur: surface gravity waves propagates roughly two orders of magnitude faster than internal gravity waves. Reducing the baroclinic time step by a factor of a hundred was not an option for the first free-surface models (Blumberg and Mellor, 1987; Killworth et al., 1991), and specific algorithms were designed to overcome this problem.

The purely explicit mode-splitting procedure, used in a large number of models, consists in integrating the two-dimensional barotropic equations with many explicit time steps while the three-dimensional baroclinic equations are solved with a single, much larger time step. For long term computations, the numerical model must be consistent by being able to advect a constant concentration of a given tracer exactly, up to machine accuracy. To achieve this so-called consistency requirement, the advection term of the tracer equation must degenerate to the continuity equation when a constant tracer concentration is considered (White et al., 2008b). Compatibility between the two-dimensional and the three-dimensional approximations of the velocity field is a mandatory requirement to ensure consistency (Deleersnijder, 1993). Therefore, the three-dimensional velocities are a posteriori corrected so that their average matches the velocities of the barotropic mode (Blumberg and Mellor, 1987), i.e. to obtain compatibility. Averaging in time the two-dimensional quantities in the three-dimensional dynamics is usually needed to ensure stability (Griffies et al., 2000; Higdon and de Szoeke, 1997; Hallberg, 1997).

To get rid of this a posteriori correction step of the three-dimensional velocities, the barotropic mode can be time stepped implicitly, using the same time step as the baroclinic mode (Dukowicz and Smith, 1994). Therefore, no correction step is needed, when all three-dimensional terms are advanced explicitly in time. The model can therefore be both compatible and consistent. Let us emphasize that solving explicitly the whole three-dimensional is not an acceptable option as the stability conditions would require to use $1s$ as typical time step! However, if some terms in the three-dimensional momentum equation are advanced implicitly in time, such an approach assumes that those implicit terms have no influence on the barotropic mode (Wang, 2007, p29, last paragraph), and the solution is not naturally compatible anymore. An efficient strategy to discretize implicitly the free-surface equation is to solve a smaller system corresponding to the Schur complement of the system. If the linear discrete system corresponding to the horizontal three-dimensional momentum and free-surface equations reads:

$$\begin{bmatrix} M_{\boldsymbol{u}} & G \\ D & M_\eta \end{bmatrix} \begin{bmatrix} X_{\boldsymbol{u}} \\ X_\eta \end{bmatrix} = \begin{bmatrix} F_{\boldsymbol{u}} \\ F_\eta \end{bmatrix},$$

where $M_{\boldsymbol{u}}$, M_η and $X_{\boldsymbol{u}}$, X_η are the mass matrices and vectors of degrees of freedom for velocities and elevation, respectively, G and D correspond to the elevation gradient term of the horizontal momentum equation and the velocity divergence term of the free-surface elevation equation, while $F_{\boldsymbol{u}}$ and F_η are their right-hand sides. An equivalent smaller system for the elevation is obtained substituting $X_{\boldsymbol{u}}$ in the last line of the system:

$$\left[M_\eta - D M_{\boldsymbol{u}}^{-1} G\right] X_\eta = F_\eta - D M_{\boldsymbol{u}}^{-1} F_{\boldsymbol{u}}.$$

Such a methodology was used by Dukowicz and Smith (1994) as well as by Marshall et al. (1997) for global-scale models, but also by Giraldo et al. (2003) for shallow water problems on the sphere. For this approach to be efficient, the mass matrix for velocities $M_{\boldsymbol{u}}$ must be easily invertible, i.e. diagonal or block-diagonal. For continuous finite elements, mass lumping must be performed for such a methodology to apply. Discontinuous finite elements are ideally suited for such a procedure, as the mass matrix is block diagonal. Such an implicit free-surface procedure is naturally compatible and consistent only if the three-dimensional mode is time-stepped explicitly. Moreover, the inversion of $M_{\boldsymbol{u}}$ may become impracticable if some differential implicit operators have to be incorporated in this matrix. Unfortunately, vertical diffusion deduced from a turbulence scheme or used as a convective adjustment algorithm is often large enough for the corresponding constraint on the time step to be much more severe than the one deduced from internal gravity waves. Therefore, the vertical diffusion and advection terms must be treated implicitly.

The Finite Element Ocean Model (FEOM) uses a similar approach with an implicit vertical diffusion (Wang, 2007; Wang et al., 2008b). The momentum equation is split in two steps and an intermediate velocity is introduced to perform the implicit calculation of the elevation. Implicit vertical viscosity is neglected in the correction step, meaning that this term is computed using this intermediate velocity rather than the final corrected value. This is needed to derive the equation associated with the elevation. Details are provided in the Appendix B.1. Such a method of substitution is similar to the Schur complement approach used by Dukowicz and Smith (1994), but the substitution is performed in the continuous space rather than at the discrete level. Working within a continuous framework, the inverse of the mass matrix $M_{\boldsymbol{u}}^{-1}$ disappears in what corresponds to the

Schur complement. Therefore, the discrete operator is not the same and the two-dimensional discrete system for the elevation reads:

$$\left[M_\eta - \Delta_t L\right] X_\eta = f_\eta - \Delta t D F_{\boldsymbol{u}},$$

where L is the discrete Laplacian matrix and Δ_t is the time step. The operator $\Delta t L$ is used rather than $DM_{\boldsymbol{u}}^{-1}G$ and can be viewed as an approximation or an alternative choice. The same remark applies for $\Delta t D F_{\boldsymbol{u}}$ that acts as a substitute of $DM_{\boldsymbol{u}}^{-1}F_{\boldsymbol{u}}$. Here, the compatibility between the vertical velocity and the sea surface elevation cannot be guaranteed easily.

In this paper, we present an implicit time splitting procedure used for a marine model, called SLIM (Second-generation Louvain-la-Neuve Ice-ocean Model[1]) that should be able to deal with problems ranging from local and regional scales to global scales. In a first step of the time stepper, the new elevation field is implicitly computed, and afterwards we use this value and the corresponding two-dimensional velocities in the baroclinic mode. The main contribution of the time marching procedure of this three-dimensional free-surface baroclinic model is that a correction term is embedded in the three-dimensional momentum equation to ensure compatibility between two- and three-dimensional velocities. Identity between depth-averaged three-dimensional velocity and two-dimensional velocity is enforced using Lagrange multipliers in the three-dimensional system It provides an implicit accurate coupling between two- and three-dimensional modes.

To illustrate the accuracy of this time discretization, we consider the simulation of Taylor caps of a tall seamount . We define the parameters of the simulation to compare the transient dynamics with results published by Chapman and Haidvogel (1992) and Ford et al. (2004a). The main reason to analyze this problem is the fact that subgrid-scale parametrization is not required to generate complex baroclinic phenomena (Chapman and Haidvogel, 1992). In other popular benchmark problems as the Dynamics of Overflow Mixing and Entrainment testcase (DOME), flow features rely heavily on parametrization: supercritical front, open boundary conditions, vertical mixing, nonhydrostatic effects (Özgökmen and Chassignet, 2002; Ezer and Mellor, 2004; Ezer, 2005, 2006; Tseng and Dietrich, 2006; Legg et al., 2006; Wang et al., 2008a). Therefore, using two different models and comparing the two numerical simulations of a gravity current in an idealized basin is only relevant if both models strictly rely on the same set of parameterizations. For unstructured grid models, it is very difficult, as these parameterizations depend on the grid size, and as we use a variable resolution where common models have fixed grid-size. Even if these problems are physically fascinating, they involve a too large spectrum of phenomena to be useful as hydrodynamic kernel benchmarks to ensure the validation of a three-dimensional baroclinic marine model.

In a companion paper (Blaise et al., 2010a) (reproduced in Chapter 4), we introduced the detailed description of the space discretization. Equal-order discontinuous interpolations for the elevation and velocity fields are used to take advantage of the inherent advantages of the usual Discontinuous Galerkin methods for advection dominated processes. The model operates on prismatic meshes, obtained by extruding vertically a triangular surface grid. It relies on approximate Riemann solvers based on the wave dynamics of the system. The consistency, the accuracy and the stability of the spatial discretization were analyzed. Herein, the time integration procedure will be provided.

[1] `http://www.climate.be/slim`

Section 5.2 describes the partial differential equations considered. Section 5.3 defines a new time-splitting procedure with compatible discrete barotropic 2D and the baroclinic 3D problems. Implicit-Explicit (IMEX) Runge-Kutta time integrators used in the three-dimensional baroclinic marine model are explained in Section 5.4. Finally, in Section 5.5, a first validation of the dynamics of the model is given. Revisiting a modified version of the flow over a tall seamount described in Blaise et al. (2010a), we analyze the dynamics behavior and we compare our results with previous publications. Concluding remarks are given in Section 5.6.

5.2 Governing equations

Using material parameters and notations defined in Table 5.1, the set of partial differential equations of the three-dimensional baroclinic free-surface model described in Blaise et al. (2010a) reads:

$$\begin{aligned}
&\frac{\partial \boldsymbol{u}}{\partial t} + \nabla_h \cdot (\boldsymbol{u}\boldsymbol{u}) + \frac{\partial w \boldsymbol{u}}{\partial z} \\
&\qquad + f\mathbf{e}_z \wedge \boldsymbol{u} + \frac{\boldsymbol{p}}{\rho_0} + g\nabla_h \eta &=& \nabla_h \cdot (\nu_h \nabla_h \boldsymbol{u}) + \frac{\partial}{\partial z}\left(\nu_v \frac{\partial \boldsymbol{u}}{\partial z}\right), && (5.1)\\
&\qquad \frac{\partial \boldsymbol{p}}{\partial z} &=& -g\nabla_h \rho'(T,S), && (5.2)\\
&\qquad \nabla_h \cdot \boldsymbol{u} + \frac{\partial w}{\partial z} &=& 0, && (5.3)\\
&\qquad \frac{\partial \eta}{\partial t} + \nabla_h \cdot \int_{-h}^{\eta} \boldsymbol{u} dz &=& 0, && (5.4)\\
&\qquad \frac{\partial c}{\partial t} + \nabla_h \cdot (\boldsymbol{u}c) + \frac{\partial w c}{\partial z} &=& \nabla_h \cdot (\kappa_h \nabla_h c) + \frac{\partial}{\partial z}\left(\kappa_v \frac{\partial c}{\partial z}\right). && (5.5)
\end{aligned}$$

where the unknown fields are the horizontal velocity $\boldsymbol{u}(x,y,z,t)$, the baroclinic pressure gradient $\boldsymbol{p}(x,y,z,t) = \nabla_h p(x,y,z,t)$, the vertical velocity $w(x,y,z,t)$, the sea surface elevation $\eta(x,y,t)$ and the tracer concentrations $c(x,y,z,t)$ that can be the temperature and/or the salinity.

Now, let us define the two-dimensional depth-averaged horizontal mean velocity:

$$\boldsymbol{U}(x,y,t) = \frac{1}{h(x,y)+\eta(x,y,t)} \int_{-h(x,y)}^{\eta(x,y,t)} \boldsymbol{u}(x,y,z,t)\, dz. \tag{5.6}$$

and the corresponding two-dimensional depth-averaged barotropic equations:

$$\begin{aligned}
&\frac{\partial \boldsymbol{U}}{\partial t} + f\mathbf{e}_z \wedge \boldsymbol{U} + g\nabla\eta &=& \mathbf{f}_{\mathbf{U}}, && (5.7)\\
&\frac{\partial \eta}{\partial t} + \nabla \cdot \big[(h+\eta)\boldsymbol{U}\big] &=& 0, && (5.8)
\end{aligned}$$

where $\mathbf{f}_{\mathbf{U}}$ includes all the remaining terms resulting from the integration of (5.1). Namely, it contains the depth-averaged integration of the advection terms, the diffusion terms

Coordinates and spatial operators	
x, y	Horizontal coordinates
z	Vertical coordinate, pointing upwards with its origin at the sea surface at rest
∇_h	Horizontal gradient operator
$\boldsymbol{e}_z$	Upward unit normal
$\wedge$	Cross product symbol
Material parameters and functions	
g	Gravitational acceleration
ρ_0	Reference density
f	Coriolis parameter
h	Depth at rest
ν_h	Horizontal turbulent viscosity parameter
ν_t	Vertical turbulent viscosity parameter
κ_h	Horizontal turbulent diffusivity parameter
κ_t	Vertical turbulent diffusivity parameter
$\boldsymbol{U}$	Two-dimensional horizontal mean velocity vector
Variables	
$\boldsymbol{u}$	Horizontal three-dimensional velocity vector
w	Vertical three-dimensional velocity vector
$\boldsymbol{u}^\eta$	Surface horizontal three-dimensional velocity vector
w^η	Surface vertical three-dimensional velocity vector
$\boldsymbol{u}^{-h}$	Bottom horizontal three-dimensional velocity vector
w^{-h}	Bottom vertical three-dimensional velocity vector
η	Sea surface elevation
p	Baroclinic pressure
$\boldsymbol{p}$	Baroclinic pressure gradient
c	Three-dimensional tracer, can be S of T
S	Salinity
T	Temperature

Table 5.1: Notations for the three-dimensional baroclinic free-surface marine model

and the baroclinic pressure gradient. Theoretically, it should also contain some additional terms ensuing from the commutation of the depth-averaged integration operator and the time derivative operator in the first term. As the free-surface evolution only depends on the depth-integrated horizontal velocity $\boldsymbol{U}$, and not on the details of the three-dimensional velocity field $\boldsymbol{u}$, a *mode-splitting procedure* is often introduced, in which the two-dimensional depth-integrated barotropic equations and the three-dimensional baroclinic equations are advanced in time with different schemes and/or steps. The theoretical underpinning is that the surface gravity waves propagate roughly two orders of magnitude faster than internal gravity waves: therefore, the baroclinic time step could be quite a lot larger than the barotropic time step required by the CFL stability condition. It would also appear attractive to have an implicit time-splitting approach where the elevation is obtained by solving a two-dimensional barotropic problem independently of the three-dimensional baroclinic mode.

The mode-splitting procedure consists in integrating the two-dimensional barotropic equations with many time steps or an implicit scheme while the three-dimensional baro-

clinic equations are solved with a single step. When performing a mode-splitting, the three-dimensional velocities must be computed in such a way that their average matches the velocities of the barotropic mode to obtain compatibility. Indeed, two essentials conditions must be fulfilled:

- The two-dimensional $\boldsymbol{U}$ and three-dimensional $\boldsymbol{u}$ discrete representations of the velocities must be compatible. In other words, using the discrete version of equation (5.4) or (5.8) must produce exactly the same result. It means that $\boldsymbol{U}$ must be recovered by performing at a discrete level the depth-average of $\boldsymbol{u}$. The basic idea is that the equivalence properties that exist in the continuous realm must be preserved in the discrete realm. It is the so-called *compatibility condition*.

- The discrete numerical mode must be consistent by being able to advect a constant concentration of a given tracer exactly, up to machine accuracy. To achieve this, the advection term of the tracer equation must degenerate to the continuity equation when a constant tracer concentration is considered (White et al., 2008b). As the compatibility of $\boldsymbol{u}$ and $\boldsymbol{U}$ is needed to obtain the compatibility of w and η, ensuring impermeability at the sea surface, the compatibility can be viewed as a mandatory requirement to ensure this *consistency condition*.

5.3 Compatible discrete barotropic and baroclinic problems

In our model, we wish to use an implicit time splitting procedure. First, the new elevation field is implicitly computed, and afterwards we use this value and the corresponding two-dimensional velocities in the baroclinic mode. The first step is the barotropic mode and the second one is the baroclinic mode. The major novelty of the implemented approach of this three-dimensional free-surface baroclinic model is that a correction term is embedded in the three-dimensional momentum equation to ensure compatibility between two- and three-dimensional velocities. Identity between depth-averaged three-dimensional velocity and two-dimensional velocity is enforced using Lagrange multipliers in the three-dimensional system. The use of Lagrange multipliers enables an implicit coupling between two- and three-dimensional modes. Indeed, the implicit terms in the momentum equation are computed using a three-dimensional velocity in agreement with the two-dimensional mode. This ensures for instance that, if the Coriolis term is treated semi-implicitly, it behaves in the same way in both modes.

To describe the methodology, let us first define both compatible modes.

- The barotropic problem consists in finding $(\boldsymbol{U},\eta)$ such that:

$$\frac{\partial \boldsymbol{U}}{\partial t} + f\mathbf{e}_z \wedge \boldsymbol{U} + g\nabla\eta = \mathbf{f}_{\mathbf{U}}, \tag{5.9}$$

$$\frac{\partial \eta}{\partial t} + \nabla\cdot\left[(h+\eta)\boldsymbol{U}\right] = 0, \tag{5.10}$$

- The baroclinic problem consists in finding $(\boldsymbol{u},\boldsymbol{\lambda})$ such that:

$$\frac{\partial \boldsymbol{u}}{\partial t} + f\mathbf{e}_z \wedge \boldsymbol{u} + \frac{\partial w\boldsymbol{u}}{\partial z} - \frac{\partial}{\partial z}\left(\nu_v \frac{\partial \boldsymbol{u}}{\partial z}\right) + \boldsymbol{\lambda}, = \mathbf{f}_{\mathbf{u}}, \tag{5.11}$$

$$\int_{-h}^{\eta} \boldsymbol{u}\, dz = \boldsymbol{U}, \tag{5.12}$$

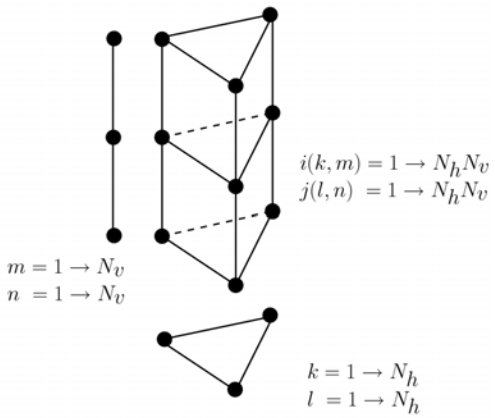

Field		Finite element space
Free surface elevation	η	P_1^{DG}
Lagrange multiplier	λ	P_1^{DG}
Horizontal two-dimensional velocity vector	$\boldsymbol{U}$	P_1^{DG}
Horizontal three-dimensional velocity vector	$\boldsymbol{u}$	$P_1^{DG} \times L_1^{DG}$

Figure 5.1: Summary of the finite element spaces used for each field. Triangular linear elements are noted P_1 while vertical linear elements are noted L_1. Indices indicated on the mesh correspond to the nodal discrete values. The global indices $i(k,m)$ and $j(k,m)$ are a function of the horizontal position and the vertical position.

where all terms explicitly time-integrated are included in the right-hand side $\mathbf{f_U}$ and $\mathbf{f_u}$ respectively. In the three-dimensional momentum equation, we add a volume force $\boldsymbol{\lambda}$. This force will act to ensure compatibility between both velocity representations. Equations (5.11)-(5.12) are the usual Euler-Lagrange equations of the saddle-point problem.

Now, we introduce the finite element mesh and the discrete discontinuous approximations of the field variables of the model (η, $\boldsymbol{u}$, $\boldsymbol{U}$, $\boldsymbol{\lambda}$) involved in the barotropic and the baroclinic modes. The three-dimensional mesh is made up of prismatic elements, as illustrated in Figure 5.1, and is obtained from the extrusion of triangular two-dimensional elements. The vertical length scale is typically much smaller than the horizontal length scale. In other words, the prisms are thin. We choose prismatic elements to obtain a mesh unstructured in the horizontal direction, and structured in the vertical direction. The two-dimensional fields η, $\boldsymbol{U}$ and $\boldsymbol{\lambda}$ are discretized with P_1^{DG} elements onto the two-dimensional mesh of triangles. The three-dimensional fields ($\boldsymbol{u}$) are discretized on the mesh of prisms and the corresponding shape functions are obtained as the tensorial product of the linear discontinuous triangle P_1^{DG} an the linear one-dimensional element L_1^{DG}.

In the space discretization of the three-dimensional baroclinic model (Blaise et al., 2010a), the discrete free-surface equation is obtained as the aggregation of the discrete horizontal divergence of the three-dimensional horizontal velocity with a bottom boundary term. A similar approach can be done for the barotropic and baroclinic momentum equations. The three-dimensional horizontal momentum equation (5.11) can be depth

integrated to obtain equation (5.9), which is close to the non-conservative form of the momentum equation of the shallow water equations. To achieve this, the test function of the three-dimensional momentum equation is divided by the depth so that the depth-integrated discrete equations are exactly similar to a non-conservative formulation of the shallow water equations. This depth-integration can be obtained by summing the lines and columns of the three-dimensional discrete system matrix and vector whose corresponding nodes share the same vertical. We derive the barotropic equations by discretely adding all three-dimensional contributions onto the corresponding two-dimensional degree of freedom. We neglect terms in the barotropic mode, that introduce a small horizontal coupling due to the nondiagonal mass matrix. Indeed, if the depth integration is performed at the continuous level, those terms naturally disappear, as they introduce momentum fluxes between layers that are subsequently aggregated. We therefore introduce a slight gap between the two- and three-dimensional discretization. This is also possible to treat these terms explicitly in the barotropic mode, and obtain an approximation similar to Wang (2007).

Then we add to the linear system corresponding to the horizontal three-dimensional momentum equation for the degrees of freedom of a column of prisms, six lines and columns corresponding to the two Lagrange multipliers for each of the three surface nodes (considering linear shape functions). The lines correspond to the compatibility constraint:

$$\sum_{e=1}^{N_e} < \widehat{\lambda} \cdot (\boldsymbol{u} - \boldsymbol{U}) >_e = 0, \tag{5.13}$$

while the columns correspond to the fictitious force:

$$\sum_{e=1}^{N_e} \left[< \widehat{\boldsymbol{u}} \cdot \frac{\partial \boldsymbol{u}}{\partial t} >_e + \cdots + < \widehat{\boldsymbol{u}} \cdot \boldsymbol{\lambda} >_e \right] = 0, \tag{5.14}$$

with λ the Lagrange multiplier field, and $\hat{\boldsymbol{\lambda}}$ the corresponding test functions. The baroclinic mode is compatible with the barotropic mode, and mass conservation is ensured. The inconsistency is only due to the commutation between spatial discretization and depth integration needed to make the vertical dynamics terms disappear in the two-dimensional momentum equation.

Both discrete barotropic and baroclinic problems can be then written with matrix notations.

- The two-dimensional discrete barotropic problem reads:

$$\begin{bmatrix} M_{\boldsymbol{U}} & G \\ D & M_\eta \end{bmatrix} \begin{bmatrix} X_{\boldsymbol{U}} \\ X_\eta \end{bmatrix} = \begin{bmatrix} F_{\boldsymbol{U}} \\ 0 \end{bmatrix}, \tag{5.15}$$

- The three-dimensional discrete baroclinic problem reads:

$$\begin{bmatrix} M_{\boldsymbol{u}} & E^T \\ E & 0 \end{bmatrix} \begin{bmatrix} X_{\boldsymbol{u}} \\ X_\lambda \end{bmatrix} = \begin{bmatrix} F_{\boldsymbol{u}} \\ F_\lambda \end{bmatrix}, \tag{5.16}$$

where E is the matrix associated with the discrete compatibility constraint. The effect of these Lagrange multipliers is to correct the discrepancy due to the different treatment of vertical terms in the baroclinic and barotropic modes.

The global time stepping algorithm can be described in details as follows. For the momentum and free-surface equations, the terms related to surface gravity waves, vertical advection, vertical diffusion, and Coriolis are treated (semi-)implicitly, while horizontal advection and diffusion are explicit. We build the global matrix for the two-dimensional barotropic mode, and solve the corresponding linear system with a preconditioned iterative solver, using for instance as preconditioner a block factorization combined with additive-Schwartz coupling, and a GMRES iterative solver. For the three-dimensional momentum equation, the linear system does not need to be assembled. Indeed, the mass matrix for Discontinuous Galerkin methods is block-diagonal per element, and the terms treated implicitly either are local, i.e. Coriolis, or only couple vertically aligned prisms. Therefore, the linear system is block-diagonal, each block corresponding to a column of prisms. Each block is then solved locally using a sparse direct solver. The memory usage is not larger than for an explicit method, and this solution strategy is intrinsically scalable. The continuity equation is an implicit problem, but as for the momentum equation, only stacked prisms are coupled together, and therefore, the system can be solved locally. Further, the information only goes from bottom to top, as we treat this equation as a steady advection equation, so that block per element Gauss-Seidel sweeping from bottom to top gives the exact result in a single iteration, i.e. the matrix for a column of prisms is block triangular. The equation for the pressure gradient force can also be solved for each column of prisms independently. Different equations are solved at each time step in an order defined as follows:

1. Evaluate the terms common for both 2D and 3D problems
2. Solve the 2D barotropic problem to obtain $\boldsymbol{U}$ and η
3. For each column of prisms, solve the 3D baroclinic problem
   a) Evaluate the implicit terms for the momentum equation
   b) Evaluate the terms for the compatibility constraint
   c) Solve the local linear system to obtain $\boldsymbol{u}$ and λ
4. Integrate the continuity equation to obtain w
5. For each column of prisms, solve the tracer equations
   a) Evaluate the implicit terms
   b) Solve the local linear system to obtain T and/or S
6. Calculate the density ρ
7. Integrate the baroclinic pressure gradient $\boldsymbol{p}$

Finally, we only need to select the time-integration scheme. In a large number of applications, the time step of an explicit method is constrained by some stiff linear term. It is also the case for the barotropic and baroclinc problems. In the barotropic mode, the surface gravity waves are essentially linear, and are much faster than advection. It seems therefore natural to treat implicitly the linear terms corresponding to gravity waves, while treating explicitly the nonlinear terms corresponding to advection. In the baroclinic mode, there is a similar separation: vertical diffusion and advection can be stiff, and must therefore be treated implicitly, while horizontal diffusion and advection is a much slower phenomena that can be treated explicitly. An efficient approach consists then to use implicit-explicit (IMEX) methods.

5.4 Implicit-explicit Runge-Kutta methods

In IMEX methods (Ascher et al., 1995, 1997), only the most critical terms are integrated implicitly. In our three-dimensional baroclinic free-surface model, we use Runge-Kutta IMEX methods. Those methods are self-starting. Moreover, the combination of Discontinuous Galerkin methods with Runge-Kutta methods is known to be efficient (Cockburn and Shu, 2001).

The spatial discretization of the three-dimensional baroclinic problem and the two-dimensional barotropic problem leads to systems of ordinary differential equations of the form:

$$\boldsymbol{y}'(t) = \boldsymbol{f}(\boldsymbol{y}(t), t), \tag{5.17}$$

where $\boldsymbol{y}(t)$ denotes the vector of all discrete degrees of freedom of a step (barotropic, baroclinic or tracer problems) of the time marching algorithm. To integrate such an ordinary differential equation, explicit Runge-Kutta methods are quite popular. As a typical example, the second order explicit method of Heun consists of calculating $\boldsymbol{y}_{n+1} \approx \boldsymbol{y}(t_{n+1})$ from $\boldsymbol{y}_n = \boldsymbol{y}(t_n)$ with the following sequence:

$$\left\{ \begin{array}{rcl} \boldsymbol{K}_1 & = & \boldsymbol{f}(\boldsymbol{y}_n, t_n), \\ \boldsymbol{K}_2 & = & \boldsymbol{f}(\boldsymbol{y}_n + \Delta_t \boldsymbol{K}_1, t_n + \Delta_t), \\ \boldsymbol{y}_{n+1} & = & \boldsymbol{y}_n + \Delta_t \left(\boldsymbol{K}_1 + \boldsymbol{K}_2\right)/2, \end{array} \right. \tag{5.18}$$

where Δ_t is the time interval. The accuracy of the discrete time integration performed with the Heun scheme is $\mathcal{O}(\Delta_t)^2$. Typically, the accuracy is often directly related to the number of stages (the number of $\boldsymbol{K}_i$ to be computed). In a more general way, a explicit or implicit Runge-Kutta method with k stages is defined by the following procedure:

$$\left\{ \begin{array}{rcll} \boldsymbol{K}_i & = & \boldsymbol{f}\left(\boldsymbol{y}_n + \sum_{j=1}^{k} a_{ij} \Delta_t \boldsymbol{K}_j, t_n + c_i \Delta_t\right), & i = 1 \ldots k, \\ \boldsymbol{y}_{n+1} & = & \boldsymbol{y}_n + \Delta_t \left(\sum_{j=1}^{k} b_j \boldsymbol{K}_j\right). & \end{array} \right. \tag{5.19}$$

A very convenient and compact way to define a Runge-Kutta method consists in having recourse to the three arrays a_{ij}, b_j, and c_i, usually represented as the so-called *Butcher tableau* defined by:

$$\left[\begin{array}{c|c} c_i & a_{ij} \\ \hline & b_j \end{array}\right] \tag{5.20}$$

In explicit Runge-Kutta schemes, the non-vanishing entries of the array a are only located in the left lower triangular part of the matrix with zeros on the diagonal and the right upper triangular part. As an example, the Butcher tableau of the Heun explicit method (5.18) is given by:

$$\left[\begin{array}{c|c} c_i & a_{ij} \\ \hline & b_j \end{array}\right] = \left[\begin{array}{c|cc} 0 & 0 & 0 \\ 1 & 1 & 0 \\ \hline & \frac{1}{2} & \frac{1}{2} \end{array}\right]$$

In implicit Runge-Kutta methods, the upper triangular of the array a contains non-zero entries. In these implicit schemes, it is possible to consider two classes: implicit Runge-Kutta methods (IRK) and diagonally implicit Runge-Kutta (DIRK). For IRK schemes, the array a is full and it is required to solve all the stages at the same time. Obviously, it can be extremely expensive and it is not very popular. In general, Diagonal Implicit Runge-Kutta (DIRK) schemes are usually resorted to, where the upper right triangular part of the array a is empty. In this case, each stage can be solved in an independent way. Moreover, Single Diagonally Implicit Runge-Kutta (SDIRK) are often used when the diagonal coefficients are equal. Accordingly for a linear problem, the matrix of the corresponding linear system will be the same for all stages.

Implicit-Explicit Runge Kutta (IMEX) schemes simply requires the splitting of the function $\boldsymbol{f}$ into a part to be integrated explicitly and a part that will be handled by an implicit scheme. We decompose the ordinary differential equation (5.17) in the following way:

$$\boldsymbol{y}'(t) = \overbrace{\boldsymbol{f}^{\text{expl}}(\boldsymbol{y}(t),t) + \boldsymbol{f}^{\text{impl}}(\boldsymbol{y}(t),t)}^{\boldsymbol{f}(\boldsymbol{y}(t),t)}, \tag{5.21}$$

where $\boldsymbol{f}^{\text{expl}}$ and $\boldsymbol{f}^{\text{impl}}$ represent the terms treated explicitly and implicitly, respectively. The explicit part of the three-dimensional baroclinic model are typically the nonlinear advection and the horizontal diffusion terms, while the terms corresponding to the gravity waves, the Coriolis force and the vertical diffusion are solved with the (semi-)implicit method.

The IMEX method of order k consists to use a SDIRK method with $k-1$ stages combined with a explicit RK scheme with k stages. This time stepper scheme is defined by:

$$\boldsymbol{K}_1^{\text{expl}} = \boldsymbol{f}^{\text{expl}}(\boldsymbol{y}_n, t_n)$$

For $i = 2 \dots k$

$$\begin{cases} \boldsymbol{K}_i^{\text{impl}} &= \boldsymbol{f}^{\text{impl}}(\underbrace{\boldsymbol{y}_n + \Delta_t \left(\sum_{j=1}^{i} a_{ij}^{\text{impl}} \boldsymbol{K}_j^{\text{impl}} + \sum_{j=1}^{i-1} a_{ij}^{\text{expl}} \boldsymbol{K}_j^{\text{expl}} \right)}_{\widehat{\boldsymbol{y}}_i}, t_n + c_i \Delta_t), \\ \boldsymbol{K}_i^{\text{expl}} &= \boldsymbol{f}^{\text{expl}}(\widehat{\boldsymbol{y}}_i, t_n + c_i \Delta_t), \end{cases} \tag{5.22}$$

$$\boldsymbol{y}_{n+1} = \boldsymbol{y}_n + \Delta_t \left(\sum_{j=1}^{k} b_j^{\text{impl}} \boldsymbol{K}_j^{\text{impl}} + b_j^{\text{expl}} \boldsymbol{K}_j^{\text{expl}} \right).$$

IMEX schemes can also be defined with two Butcher tableau corresponding to the implicit and the explicit part respectively. In order to synchronize the stages, a unique c array applies to both methods and an initial empty stage is added to the implicit scheme and the corresponding arrays are padded with zeros.

To obtain a suitable discretization for linear finite elements, it seems logical to have the same accuracy in time and space and to consider a second order scheme in time. Spatial and temporal discretization errors will then converge at the same rate when the mesh is refined, the time step being adapted in accordance with the CFL condition. The implicit explicit Runge-Kutta methods used in the three-dimensional baroclinic model were derived in Ascher et al. (1997) and his Butcher tableaux read:

$$\left[\begin{array}{c|c} c_i & a_{ij}^{\text{impl}} \\ \hline & b_j^{\text{impl}} \end{array} \right] = \left[\begin{array}{c|ccc} 0 & 0 & 0 & 0 \\ \gamma & 0 & \gamma & 0 \\ 1 & 0 & 1-\gamma & \gamma \\ \hline & 0 & 1-\gamma & \gamma \end{array} \right], \tag{5.23}$$

$$\left[\begin{array}{c|c} c_i & a_{ij}^{\text{expl}} \\ \hline & b_j^{\text{expl}} \end{array} \right] = \left[\begin{array}{c|ccc} 0 & 0 & 0 & 0 \\ \gamma & \gamma & 0 & 0 \\ 1 & \delta & 1-\delta & 0 \\ \hline & \delta & 1-\delta & 0 \end{array} \right], \tag{5.24}$$

with $\gamma = (2 - \sqrt{2})/2$ and $\delta = 1 - 1/(2\gamma)$. The IMEX method consists in using a SDIRK method with 2 stages combined with a explicit RK scheme with 3 stages. Some simplifications in the calculation can be deduced from those Butcher tableau. As the last line of the matrix a exactly corresponds to the line b, the final update can be obtained directly from the last estimate $\widehat{\boldsymbol{y}}_3$ obtained for the vector $\boldsymbol{y}$. Finally the last entry of b^{expl} is zero and the last explicit stage is not needed. In short, we only need to calculate two times the explicit part $\boldsymbol{f}^{\text{expl}}$ and to solve two times the implicit system associated with $\boldsymbol{f}^{\text{impl}}$. This systems has the same matrix but a different right-hand side. In a systematic way, the IMEX procedure for the three-dimensional baroclinic model can be cast in the following sequence:

1. Calculate $\boldsymbol{K}_1^{\text{expl}} = \boldsymbol{f}^{\text{expl}}(\boldsymbol{y}_n, t_n)$

2. Obtain $\boldsymbol{K}_2^{\text{impl}}$ and $\widehat{\boldsymbol{y}}_2$ by solving:

$$\boldsymbol{K}_2^{\text{impl}} = \boldsymbol{f}^{\text{impl}}(\underbrace{\boldsymbol{y}_n + \Delta_t(\gamma\ bf K_1^{\text{expl}} + \gamma \boldsymbol{K}_2^{\text{impl}})}_{\widehat{\boldsymbol{y}}_2}, t_n + \Delta_t\gamma)$$

3. Calculate $\boldsymbol{K}_2^{\text{expl}} = \boldsymbol{f}^{\text{expl}}(\widehat{\boldsymbol{y}}_2, t_n + \Delta_t\gamma)$

4. Obtain $\boldsymbol{K}_3^{\text{impl}}$ and $\widehat{\boldsymbol{y}}_3$ by solving:

$$\boldsymbol{K}_3^{\text{impl}} = \boldsymbol{f}^{\text{impl}}(\underbrace{\boldsymbol{y}_n + \Delta_t(\delta \boldsymbol{K}_1^{\text{expl}} + (1-\delta)\boldsymbol{K}_2^{\text{expl}} + (1-\gamma)\boldsymbol{K}_2^{\text{impl}} + \gamma \boldsymbol{K}_3^{\text{impl}})}_{\widehat{\boldsymbol{y}}_3}, t_n + \Delta_t)$$

5. Set $\boldsymbol{y}_{n+1} = \widehat{\boldsymbol{y}}_3$

5.5 Numerical results

Internal waves in the lee of a moderately tall seamount were simulated in Blaise et al. (2010a). In this paper, we consider a similar set-up to compare the transient dynamics with results published by Chapman and Haidvogel (1992) and in Section 3c of Ford et al. (2004a). This set-up is selected because there is no need for subgrid-scale parametrization to create complex baroclinic phenomena. The flow is stratified, but subcritical: there is no internal wave break-up. No boundary layer appears, as a slip condition at the seabed is prescribed. In the first part of this work (Blaise et al., 2010a), the height of the seamount was 30% of the total depth, and a complicated internal wave structure developed in the wake of the seamount. Now, we consider that the height of the seamount is 90% of the total depth in order to observe some recirculation patterns in the wake of the seamount.

The first computation of a three-dimensional linearly stratified flow over a Gaussian seamount was done Huppert and Bryan (1976) with the model of Bryan (1969). A detailed numerical study of flows past Gaussian seamounts can be found in Chapman and Haidvogel (1992, 1993). The strengths and weaknesses of a few other models have been assessed by simulating flow past seamounts: mitGCM (Adcroft et al., 1997), ICOM (Ford et al., 2004a) and FEOM (Wang et al., 2008b). Our numerical simulations will be performed in order to draw some comparisons with previous computations.

The computational domain is an aquaplanet, as it allows us to avoid open boundary conditions. Figure 5.2 shows a close-up view of the mesh and the bathymetry near the seamount. The mesh resolution is refined in the lee of the seamount, to allow for an accurate representation of the shedded vortex described in Chapman and Haidvogel (1992)

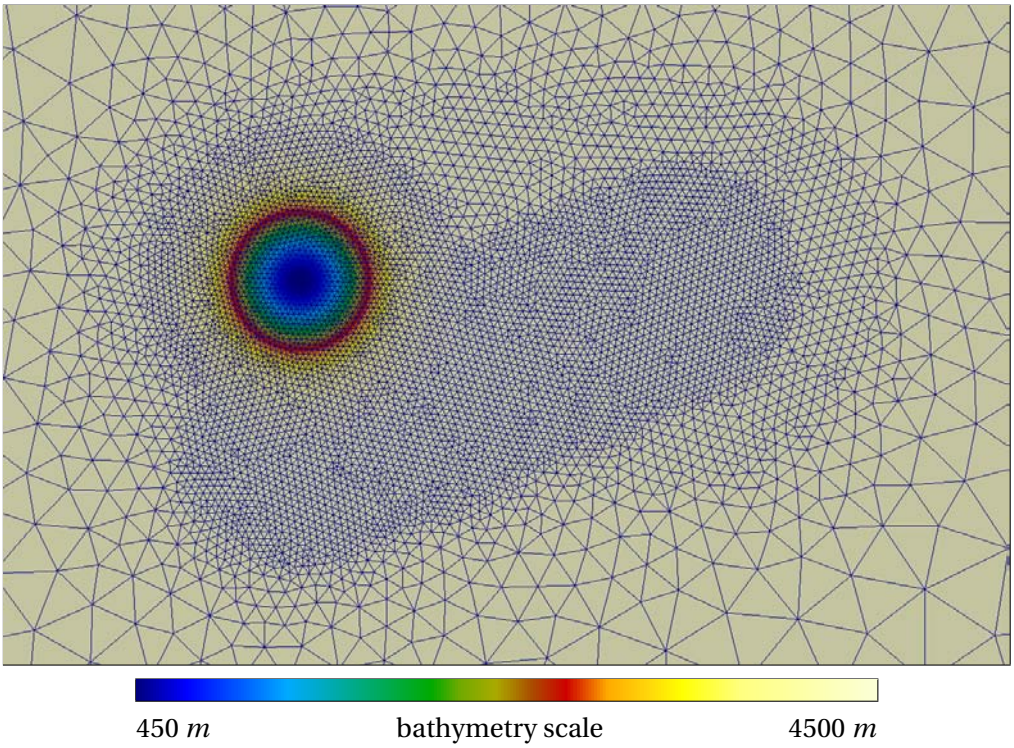

Figure 5.2: Close-up view on the mesh and the bathymetry around the seamount. The mesh is refined in the lee of the seamount.

and Ford et al. (2004a). The edge-length in the most refined zone is 2 km. This mesh is made up of 13836 triangles extruded into 20 σ layers.

The geometry of the problem is defined by a Gaussian seamount located at 45 degrees North. The bathymetry reads:

$$1 - \frac{h(x,y)}{H} = \delta \exp\left(\frac{\left(x - \frac{R}{2}\right)^2 + \left(y - \frac{R}{2}\right)^2 + \left(z - \frac{R}{\sqrt{2}}\right)^2}{-L^2} \right), \tag{5.25}$$

where $H = 4.5$ km is the total depth, $\delta = 0.9$ is the relative height of the seamount, $R = 6\,372$ km is Earth radius and $L = 25$ km is the length scale of the seamount. The coordinates x, y and z are relative to the global Cartesian reference coordinates axis located in the center of the sphere. The flow simulation is initiated with a global zonal geostrophic equilibrium ignoring the seamount. In other words, the initial guess of the calculation is the same as in the Testcase 5 of Williamson where the velocity field only exhibits a non vanishing East component u_e. In this testcase (Williamson et al., 1992), the elevation and velocity fields are respectively given by

$$\frac{\eta}{U^2/g} = -\frac{z^2}{R^2}\left(1 + \sqrt{2}\,\frac{R\Omega}{U}\right), \tag{5.26}$$

$$\frac{u_e}{U} = \sqrt{\frac{x^2 + y^2}{R^2}}, \tag{5.27}$$

where $U = 0.258\ m\ s^{-1}$ is the velocity scale at 45 degree North, $\Omega = 7.292 \times 10^{-5}\ s^{-1}$ is Earth rotation rate, and $g = 9.81\ ms^{-2}$ is the gravitational acceleration. We only consider the density deviation ρ' as the unique tracer of the model and the initial value of the density deviation is a linear function of the vertical coordinate, with vanishing mean. The derivative of the density with respect to the vertical coordinate is given by $\partial\rho/\partial z = -3.43 \times 10^{-5}\ kg\ m^{-4}$ and the reference density is selected as $\rho_0 = 1025\ kg\ m^{-3}$. The turbulent viscosities and diffusivities are given by: $\nu_h = \kappa_h = 6.45\ m^2\ s^{-1}$, $\nu_v = 0.0001\ m^2\ s^{-1}$ and $\kappa_v = 0$. With those parameters, we consider that the flow is characterized by the same four dimensionless numbers as that in Section 3.c of Ford et al. (2004a). These dimensionless number are defined as follows:

- Seamount ratio $\delta = 0.9$

- Rossby number $Ro = \dfrac{U}{fL} = 0.1$

- Reynolds number $Re = \dfrac{UL}{\nu_h} = 1000$

- Burger number $Bu = \dfrac{NH}{fL} = \sqrt{\dfrac{-g}{\rho_0}\dfrac{\partial\rho}{\partial z}}\dfrac{H}{fL} = 1$

where N is the Brunt-Väisälä frequency.

The critical numerical parameter in the three-dimensional baroclinic model is the jump penalty coefficient γ of the Lax-Friedrichs solver. For this problem, we select $\gamma = 6\ m\ s^{-1}$. Here, we select a slightly higher γ than for the simulations presented in Blaise et al. (2010a), because the height of the seamount is quite larger. Above the seamount, the density profile may be significantly altered and this parameter must be an upper bound of the phase speed of the fastest wave. For discontinuous linear elements combined with the second order explicit Runge-Kutta time stepper (Chevaugeon et al., 2007) used in this simulation, the relevant CFL conditions reads:

$$\Delta_t < \frac{\Delta_x}{3\gamma} \tag{5.28}$$

The smallest edge length is $2\ km$ and the relevant length is the inradius of this smallest triangle. Therefore, $\Delta_x = 0.29 \times 2\ km$ and the greatest time step to avoid instabilities is $32\ s$. In this simulation, we use a time step of $20\ s$.

The two-dimensional dynamics of flows past isolated obstacles is already complicated. Verron and Le Provost (1985) give a detailed analysis of the flows that occurs over an isolated seamount, using a two-dimensional model of the quasi-geostrophic equations. A clockwise vortex is always trapped over the seamount, but several transient regimes can occur. For strong flows, such as the configuration given in Blaise et al. (2010a), the counter-clockwise vortex generated in the initiation flow phase is directly advected downstream. For weak flows, such as the current configuration, a stronger interaction between the two eddies occurs and the counter-clockwise vortex is shifted to the right and trapped in the vicinity of the seamount, leading to a double vortex structure.

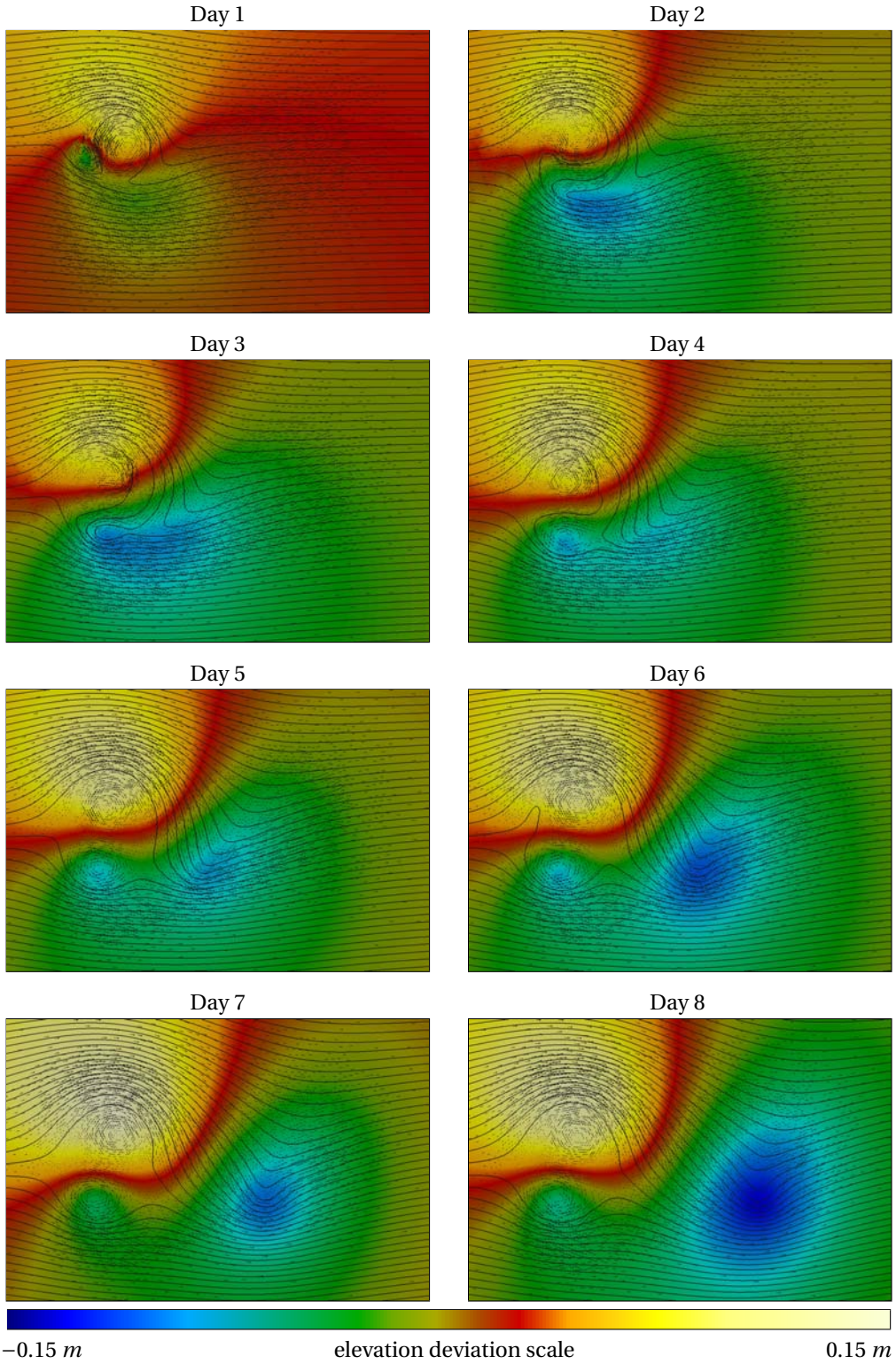

Figure 5.3: Two-dimensional flow ($\delta = 0.9$). Colors denotes sea surface deviation with respect to initial geostrophic equilibrium. Glyphs represents two-dimensional mean velocities. The black continuous lines are the instantaneous streamlines.

Two-dimensional daily depth-averaged velocities and the sea surface deviation are shown in Figure 5.3. The sea surface deviation is defined as the difference between the sea-surface elevation and initial elevation corresponding to the geostrophic elevation. As the flow is impulsively started, the free-surface is raised in front of the seamount, and lowered behind it. Geostrophic adjustment induces two counter-rotating eddies, the one in front of the seamount being clockwise. Under a rigid-lid approximation, this adjustment can be interpreted in terms of vortex compression and stretching (Verron and Le Provost, 1985). These two vortices progress clockwise around the seamount, with a timescale much smaller than the advective one. In Figure 5.3, we see that at day one, the two vortices have already rotated almost half a turn clockwise. The rotation of this vortex pair can be explained in terms of topographic Rossby waves. Depth variation induces effects similar to Coriolis parameter variation, i.e. the β effect. These waves propagate with the shallowest area on their right (Cushman-Roisin, 1994, Section 6.5). This leads to a clockwise progression of the vortex pair. The phase speed aligned with isobaths is proportional to the bottomslope. For a Gaussian shaped bathymetry, the maximum speed will therefore occur at a radius corresponding to the inflexion point of the Gaussian, which in this case is $L/\sqrt{2}$. The initially circularly shaped vortices tend to become spiral shaped, as explained in Johnson (1984). These phenomena are essentially two-dimensional, and have been modeled with two-dimensional approximations such as quasi-geostrophic equations (Johnson, 1984; Verron and Le Provost, 1985).

The vertical structure of the flow can be observed from the isosurfaces of the density perturbation given in Figure 5.4. The density perturbation is defined as the difference between density deviation field ρ' and the initial density deviation. As the flow is quasi-geostrophic, the density perturbation is an image of the vorticity, as the elevation deviation. In fact, a complex interaction takes place, where the counter-clockwise vortex undergoes a stretching and breaking sequence that generates internal waves upstream of the seamount. This can be observed in Figure 5.5 where a horizontal slice in the density perturbation at a depth of 400 m is displayed.

Using the quasi-geostrophic equations, Johnson (1984) shows that the starting flow over a smooth obstacle leads to topographic Rossby waves that rotate clockwise around the obstacle. For a parabolic obstacle, spiral waves are observed. These internal topographic Rossby waves are progressing as spirals between days 2 and 3. These waves can be clearly detected from the density perturbation isovalues at a depth of 4000 m in Figure 5.6. The counter-clockwise vortex then breaks into two well separated parts. The first one is trapped on the right side of the seamount (looking downstream), while the second one is ejected and transported at the mean speed of the flow. Indeed, two recirculation cells exist. One is trapped over the seamount, and the other one is located on the right side of the seamount.

Finally, it is instructive to perform some comparisons between our numerical simulations and some previous calculations. A quite similar flow in a rectangular domain with constant Coriolis parameter was simulated by several authors:

- Chapman and Haidvogel (1992) use a rigid lid model with finite-difference horizontal discretization and spectral vertical discretization, and along sigma levels hyperviscous dissipation.
- Adcroft et al. (1997) use a rigid lid non-hydrostatic finite-volume model, but only provide results after 10 days. Therefore, comparison cannot be performed with this model.

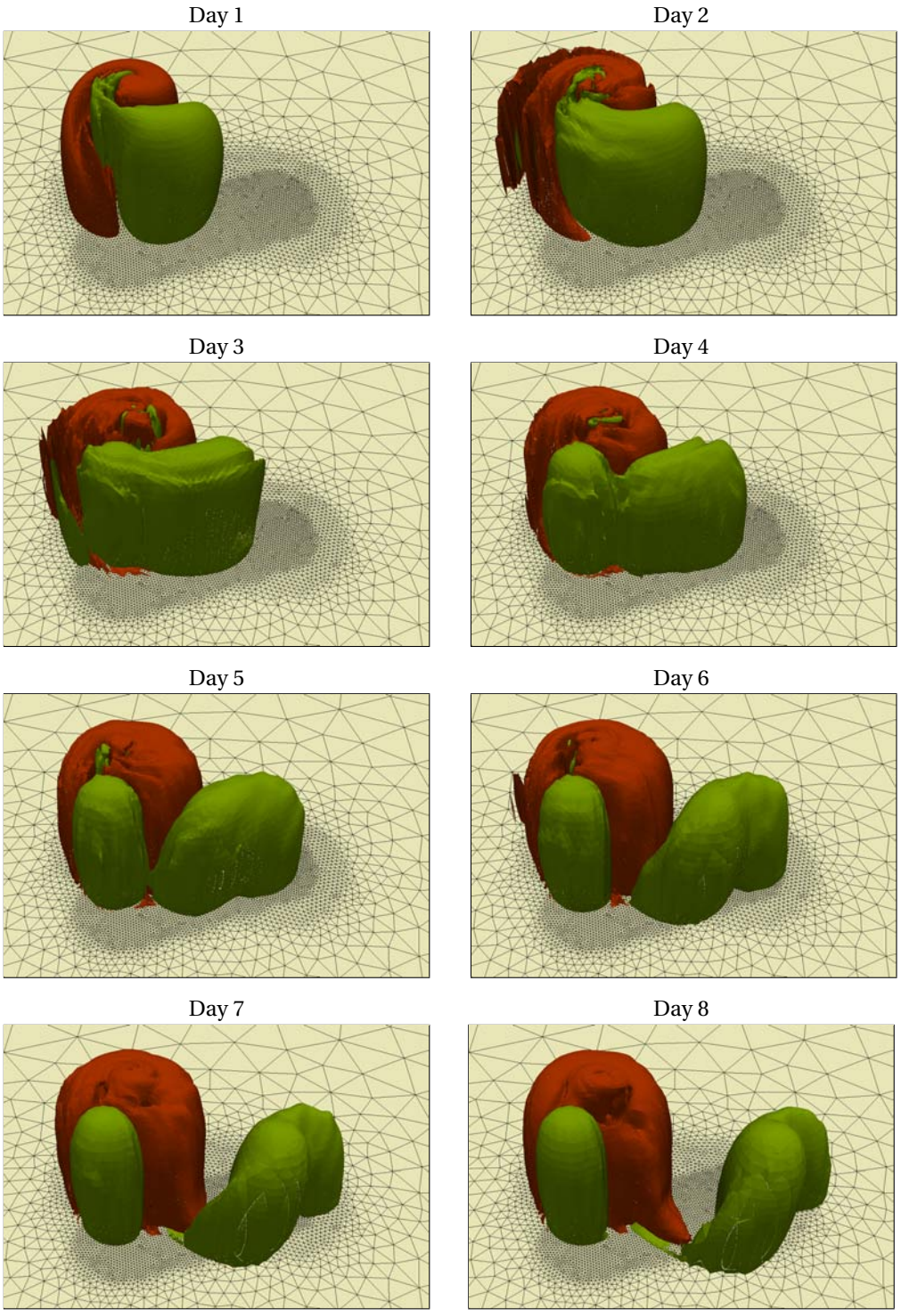

Figure 5.4: Time evolution of the isosurfaces of the density perturbation. Isovalues of density perturbation of $-0.001 kg\ m^{-3}$ are in green. Isovalues of density perturbation of $0.001 kg m^{-3}$ are in red. The two-dimensional mesh is given on the sea bottom.

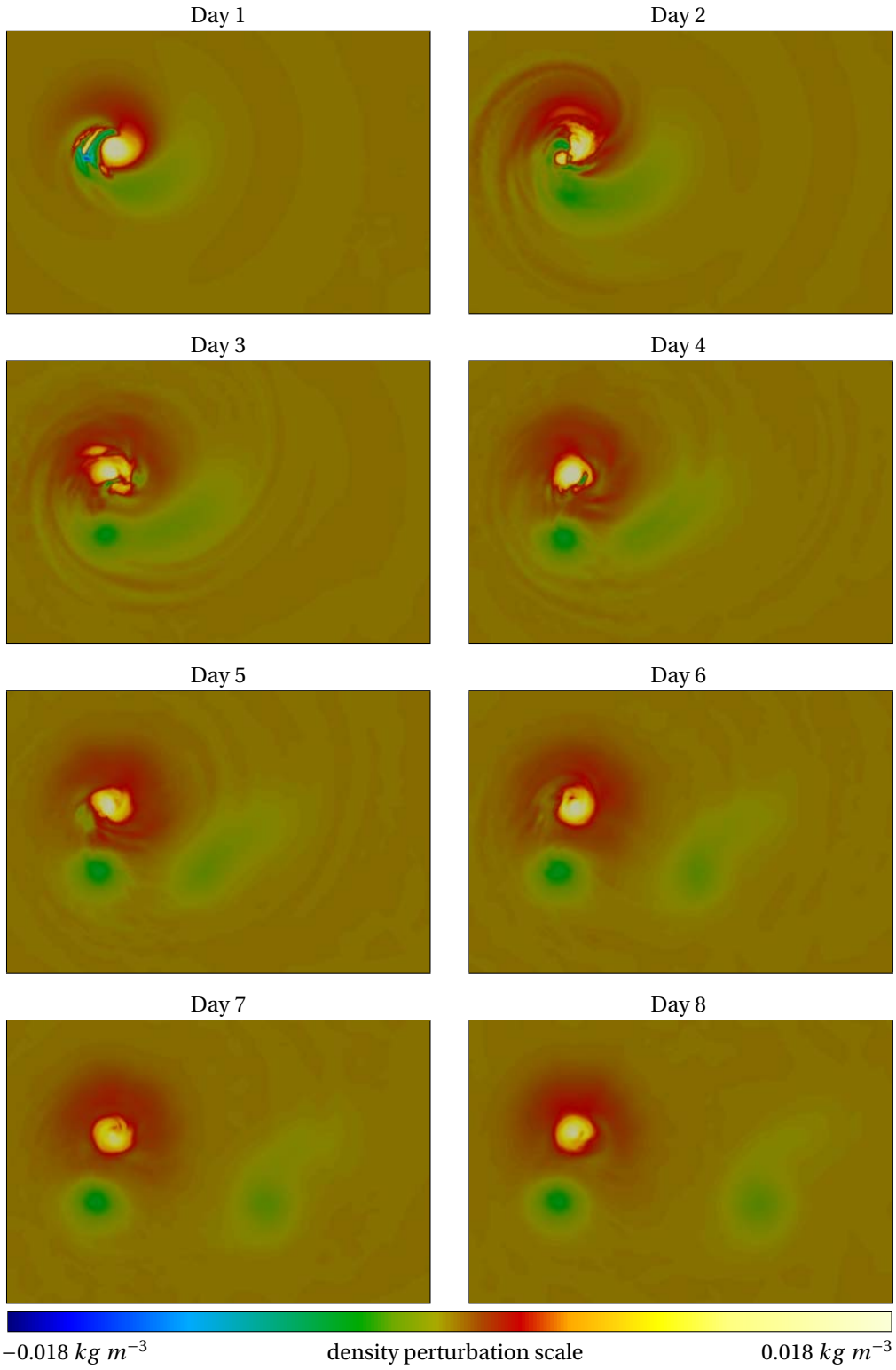

Figure 5.5: Density perturbation for a horizontal cut at 400 m depth.

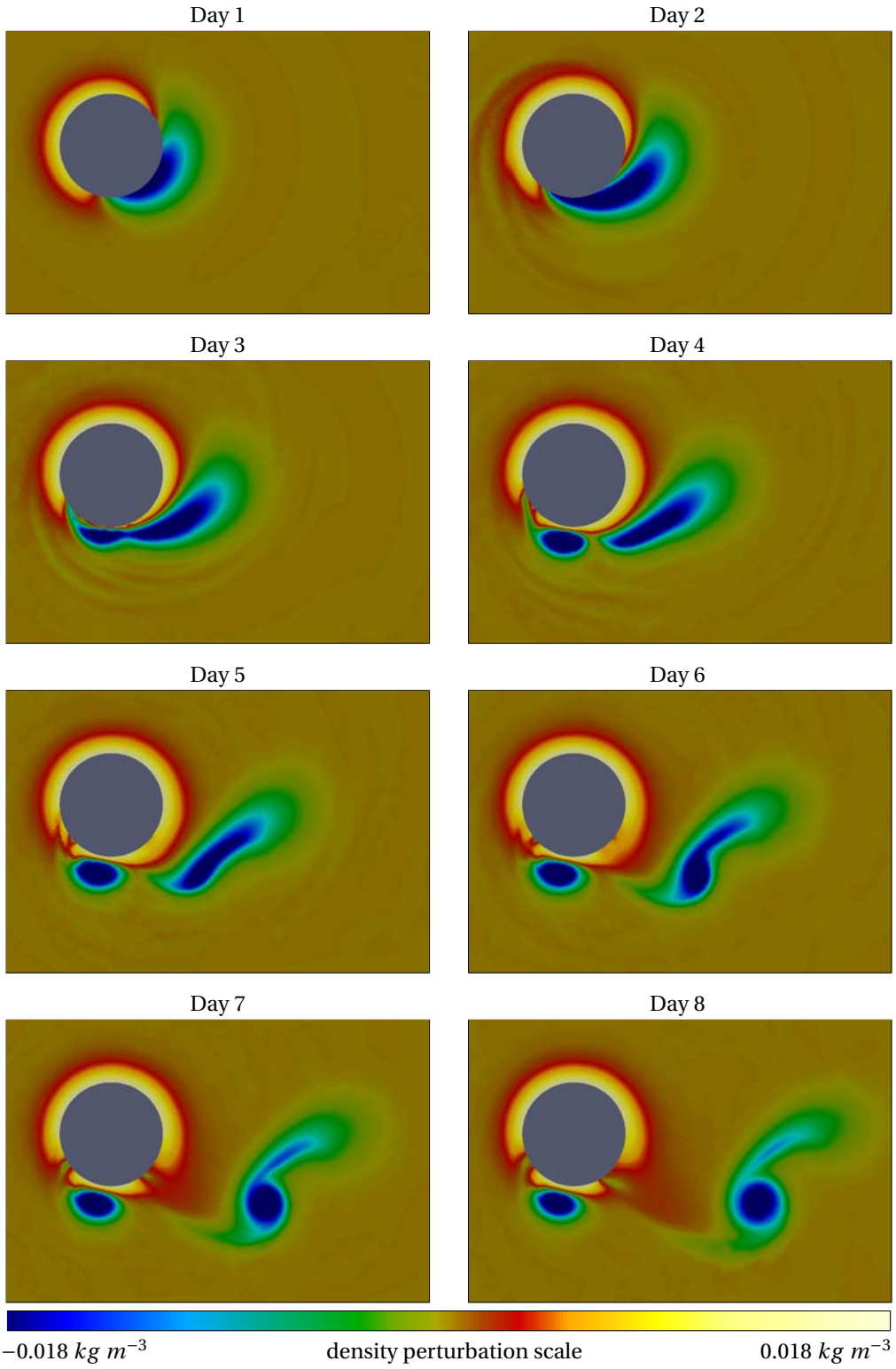

Figure 5.6: Density perturbation for a horizontal cut at 4000 m depth.

- Ford et al. (2004a) use a finite-element non-hydrostatic model, with rigid-lid approximation and Laplacian dissipation.

The problem is not exactly the same as we introduce the full Coriolis term on the sphere, while the f-plane approximation is considered in those previous calculations. However, this should not induce significant flow discrepancy, as we focus on the small scale, where the variations of the Coriolis parameter are negligible compared to other effects, such as the influence of the bathymetry.

For the early stages of the flow, our model exhibits numerous wave phenomena. In Figures 5.7 and 5.8, we show a detailed comparison with the results obtained by Chapman and Haidvogel (1992). Both simulations produce a quite similar behavior during the first two days. However, our calculation exhibits significant internal spiral waves that do not appear in Chapman and Haidvogel (1992) and Ford et al. (2004a). This observation could be explained by the rather smaller dissipation introduced by our numerical scheme. Those waves could also be due to an interaction with the free-surface, while Chapman and Haidvogel (1992) and Ford et al. (2004a) use the rigid lid approximation. In Figures 5.9 and 5.10, we observe that the counterclockwise eddy is stretched and breaks up, one part being trapped near the seamount while the other is shedded. In our computation, the break up of the eddy happens much faster. The trapped eddy is much larger, and the shedded eddy tends to become much more circular. This difference can be explained easily: Ford et al. (2004a) and Chapman and Haidvogel (1992) carry out their computation in a box domain, with lateral walls. Indeed, these walls are too close to the seamount for their influence to be negligible. Figure 5.11 sketches the elevation deviation after 3 and 7 days, along with black lines located where the lateral walls are found in Ford et al. (2004a). It can be seen that the flow clearly varies along those boundaries. When those boundaries are present, the counterclockwise vortex cannot develop laterally, and this prevents its breakup.

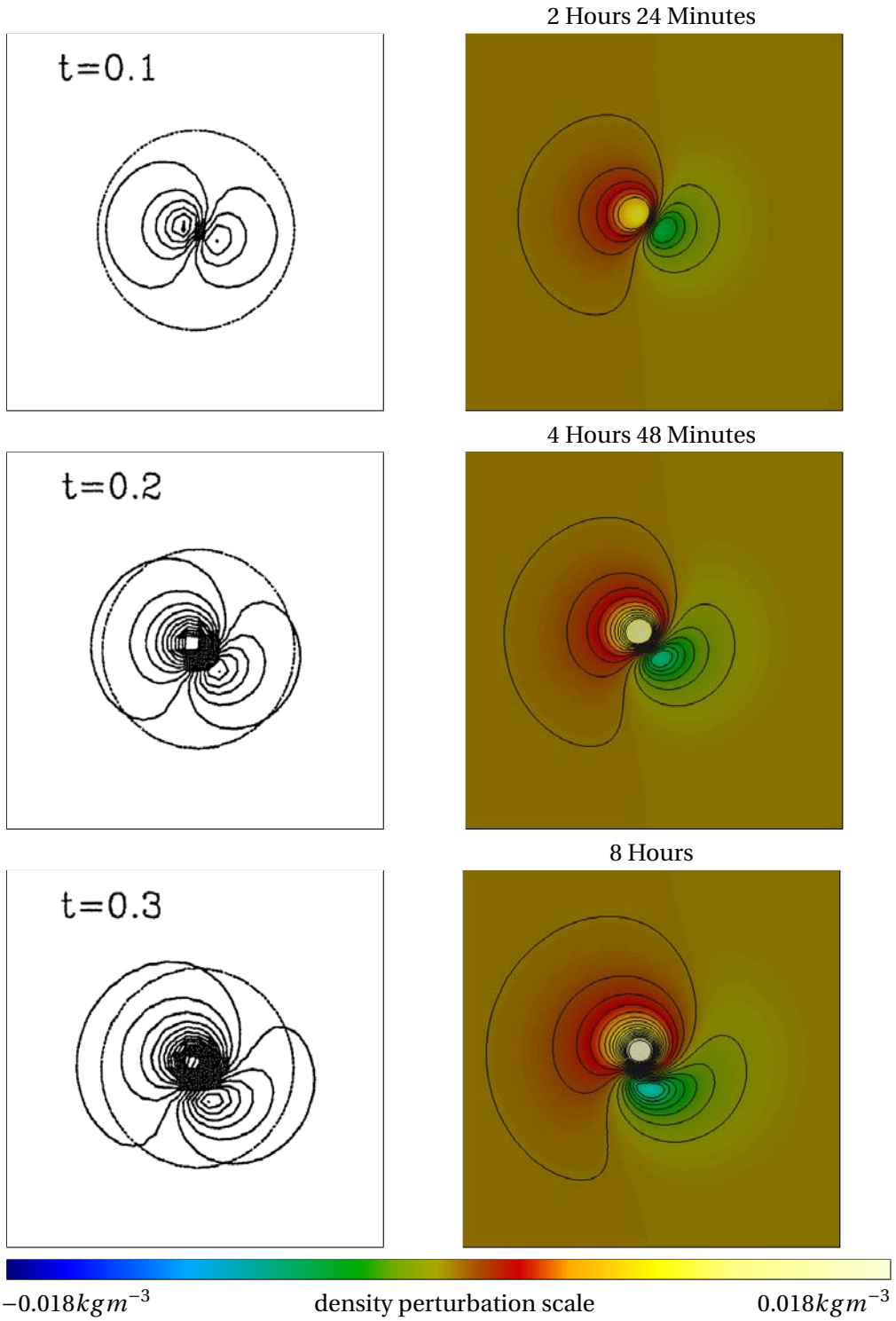

Figure 5.7: Comparison of density perturbation field at 400 m depth with results obtained by Chapman and Haidvogel (1992), during the start-up of the calculations. The dashed circle in the reference data is the 4000 m isobath. For t = 0.1, isolines range from -0.0039 to 0.0051. For t = 0.2, isolines range from -0.0059 to 0.0101. For t = 0.3, isolines range from -0.0069 to 0.0161. Isolines interval is 0.001 $kg\ m^{-3}$. The same values are used for both models.

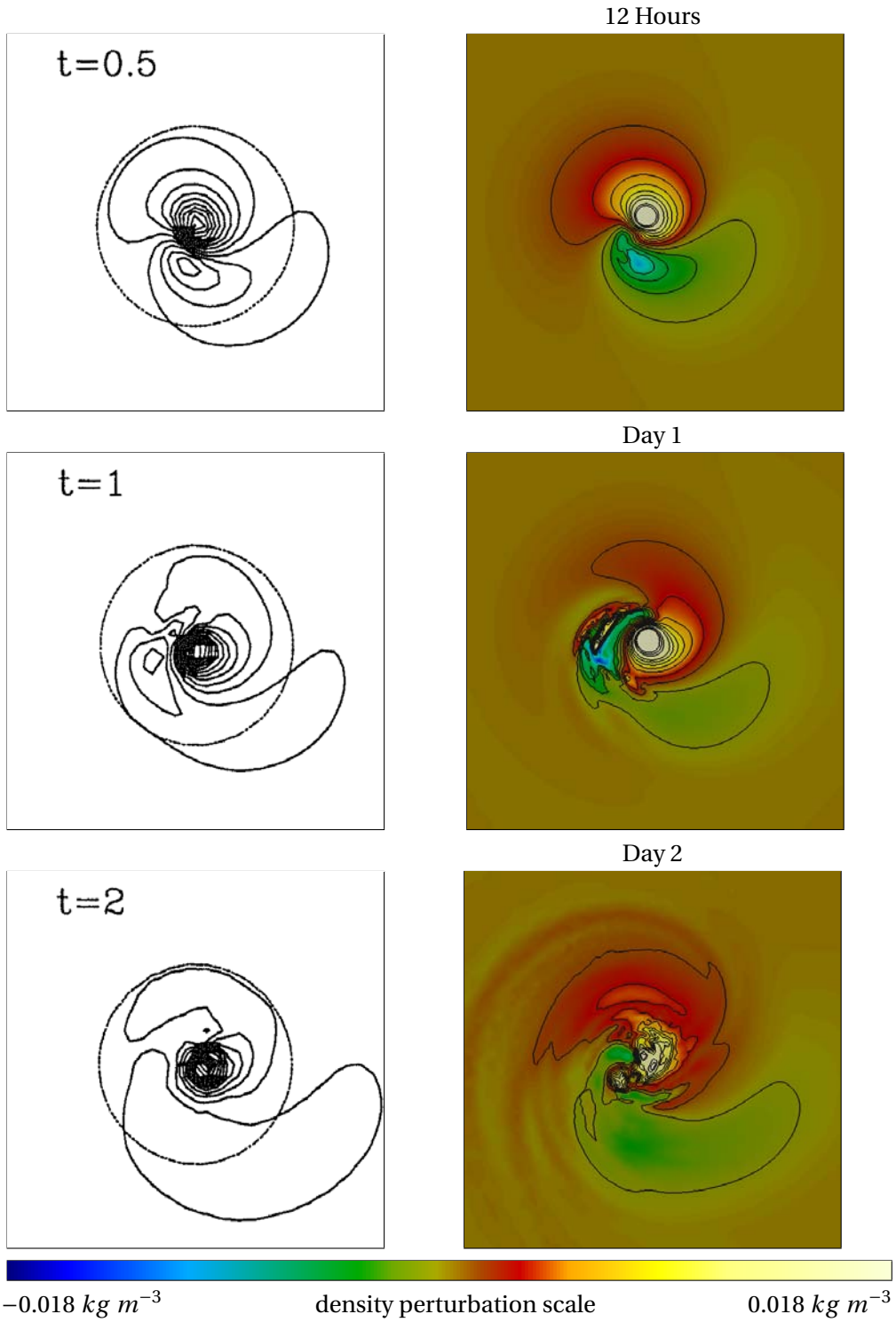

Figure 5.8: Comparison of density perturbation field at 400 m depth with results obtained by Chapman and Haidvogel (1992) during the two first days. The dashed circle in the reference data is the 4000 m isobath. For t = 0.5, isolines range from -0.0069 to 0.0191. For t = 1.0, isolines range from -0.0049 to 0.0211. For t = 2.0, isolines range from -0.0009 to 0.0231. Isolines interval is 0.002 $kg\ m^{-3}$. The same values are used for both models.

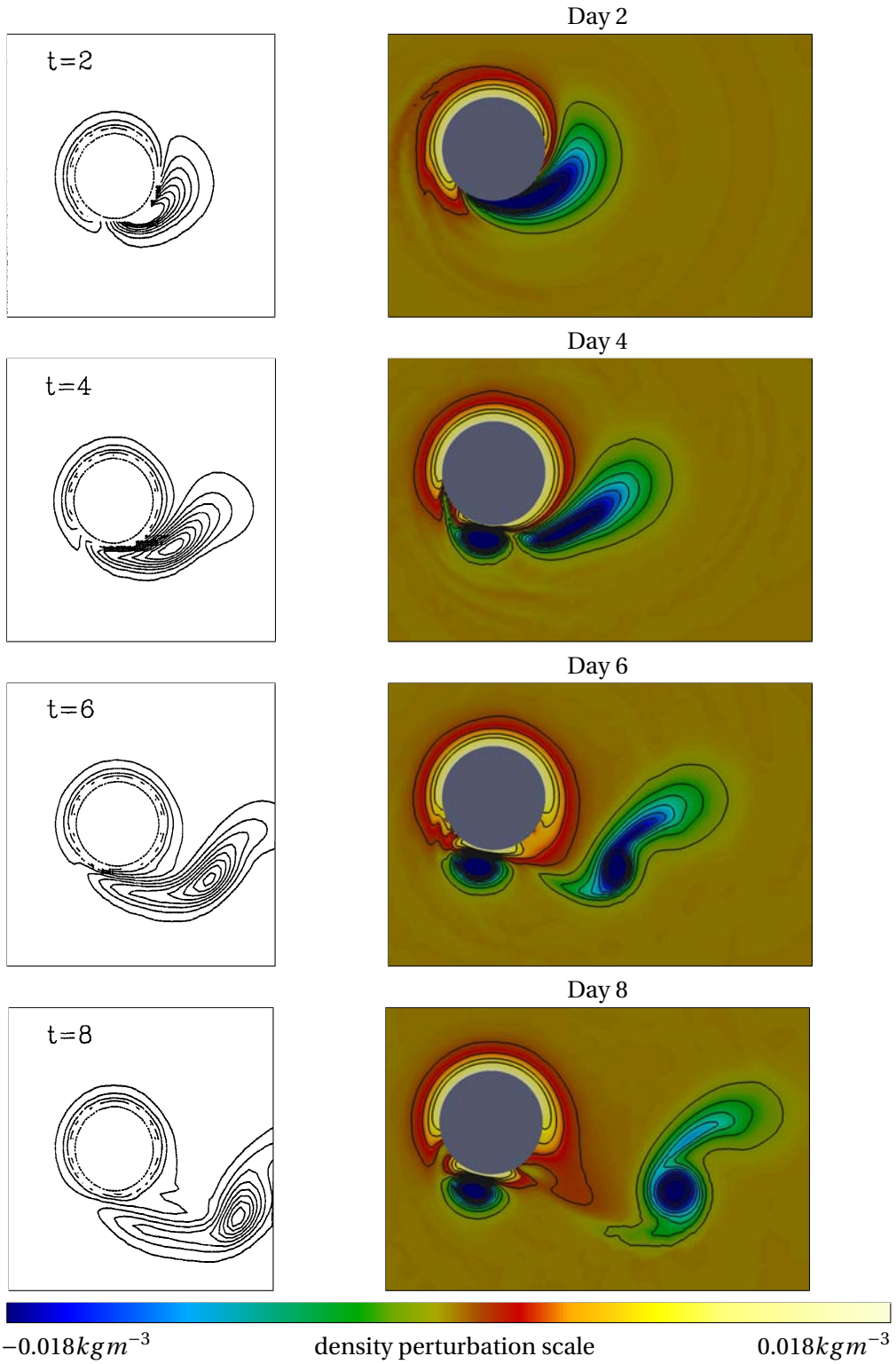

Figure 5.9: Comparison of density perturbation field at 4000 m depth with results obtained by Chapman and Haidvogel (1992) during the eight first days. Isolevels are the same for both models, ranging from -0.0212 to 0.0088 with a interval of 0.0025 $kg\ m^{-3}$.

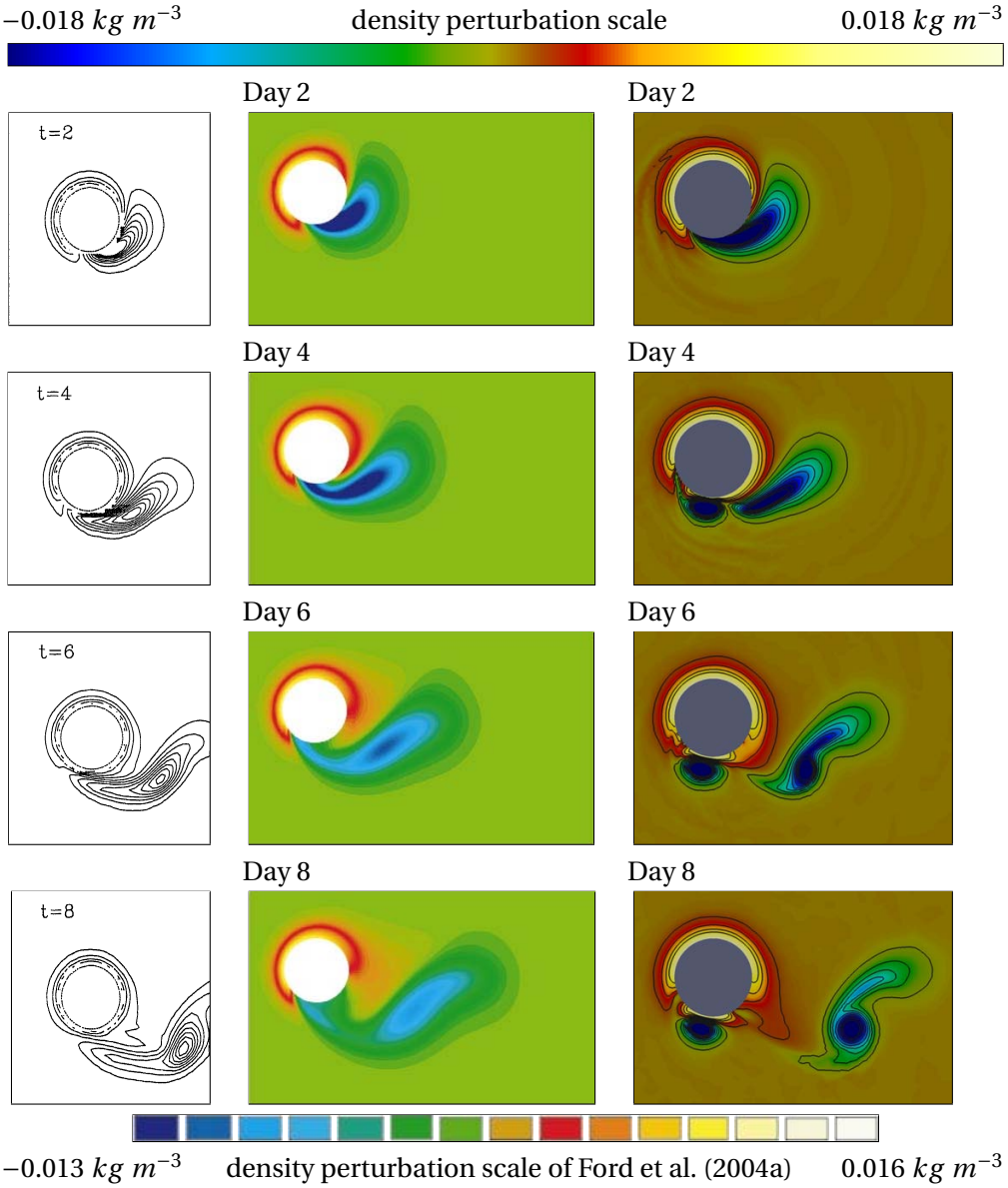

Figure 5.10: Comparison of density perturbation field at 4000 m depth with results of Chapman and Haidvogel (1992) (left) and of Ford et al. (2004a) (middle) during the first eight days. Isolevels are the same for the left and right sides, and range from -0.0212 to 0.0088 with a interval of 0.0025 $kg\ m^{-3}$.

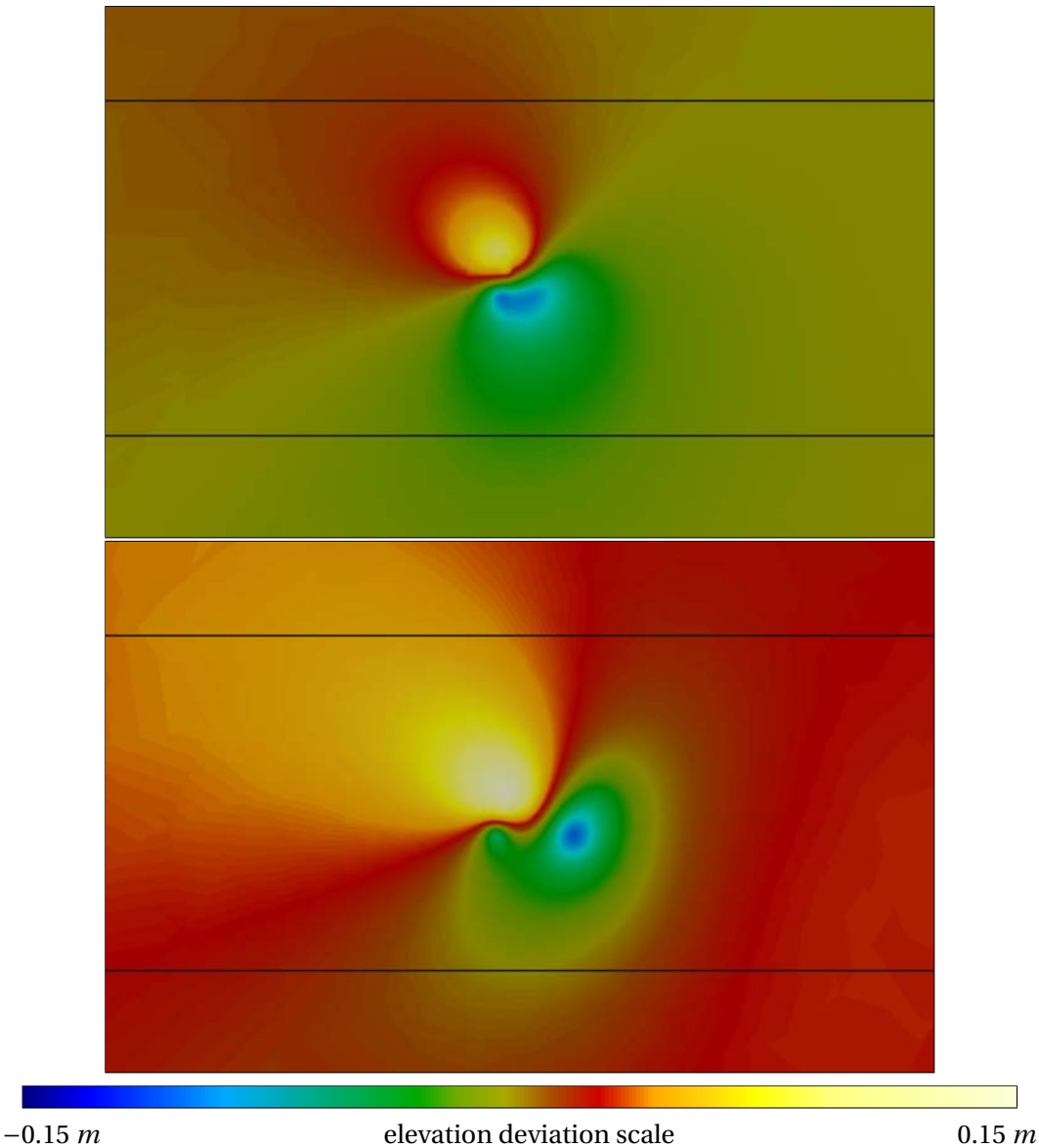

Figure 5.11: Sea surface elevation deviation after three days (top) and seven days (bottom).. The black lines denotes the location of lateral boundary in Ford et al. (2004a). It can be observed that the flow significantly varies outside of the domain denoted by the black lines.

5.6 Conclusions

An implicit-explicit time discretization for the three-dimensional free-surface baroclinic marine model described in Blaise et al. (2010a) is proposed. The major contribution consists in the definition of a new implicit mode-splitting procedure with compatible barotropic and baroclinic problems. To achieve this, the two-dimensional barotropic problem is discretely obtained from the three-dimensional baroclinic problem. Compatibility between the two modes is enforced in a weak way by introducing Lagrange multipliers. The transports in the two- and three-dimensional problems are constrained by explicitly incorporating this compatibility constraint in the three-dimensional horizontal momentum equation. Combined with implicit-explicit Runge-Kutta (IMEX) methods, such an approach sounds very attractive. The order of accuracy can be selected as required. On the one hand, we take advantage of the stability of the implicit method that will damp the unresolved or poorly resolved modes. On the other hand, we could also benefit from the Total Variation Diminishing property of the explicit part of some methods.

Revisiting the benchmark flow over an isolated seamount of Blaise et al. (2010a), we simulate the complex spiral wave dynamics that previous calculations were not able to capture, either because of the rigid-lid assumption or their numerical methods. Thanks to the unstructured nature of the mesh, the resolution is refined in the lee of the seamount, enabling a detailed representation of the wave dynamics in this region. Further, vortex shedding is observed. The early stages of the simulation compare well with the two previous calculations.

For such an implicit/explicit approach to be interesting, the discrete operators for the dynamics handled implicitly must be significantly stiffer than those for the explicit dynamics. Indeed, the time-step allowed by the IMEX scheme must be significantly larger than the time-step of a purely explicit discretization. It is definitely the case when the vertical mixing parameters are deduced from a turbulence closure. For the simulation of the internal waves in the lee of a moderately tall seamount, it is not really the case as the stratification is rather strong. The internal waves are fast, and the vertical viscosity is still reasonable. The time steps are only 20 times larger than the explicit time step, and are much more expensive, as local linear systems are solved. In our opinion, the way to faster computations is twofold. On one hand, the computation of the discrete terms can still be improved, by recasting most of the operations into efficient matrix-matrix products computed with highly optimized linear algebra subroutines. It is the classical optimization procedure of a numerical model. On the other hand, the time-stepping strategy can itself be improved. Indeed, most ocean models have resorted to a mode splitting approach to avoid solving three-dimensional linear systems. It may be necessary to go beyond this paradigm and investigate a full implicit approach. To be efficient, it must be scalable. Multigrid methods have the potential to provide scalable solutions to large-scale discrete problems. Further such multigrid methods do not need the matrix of the linear system to be assembled, significantly reducing the memory footprint of the algorithm. However, the design of an efficient multigrid algorithm is in itself a whole domain of research and goes much beyond the scope of this work.

CHAPTER 6

CONCLUSION AND PERSPECTIVES

This thesis has been conducted under the auspices of the SLIM project. The goal of this project is to build an efficient and accurate model for the ocean general circulation, using finite element methods on unstructured meshes.

In Chapter 2, we have provided a detailed description of the weak formulation and Riemann solvers used to deduce a finite element discretization of the shallow water equations where stabilization is induced by interface terms. Further, we have carried out an evaluation of five finite element pairs using this formulation for various flow regimes. This work clearly discards the $P_1^{NC} - P_1$ pair, that provides accurate results if and only if diffusion is dominant.

The previous three-dimensional version of SLIM, developed by Laurent White (White et al., 2008a,b), was based on this $P_1^{NC} - P_1$ pair. Therefore, a complete rewriting of the software was needed, to integrate flexibility in the choice of the interpolation and in the choice of the time-stepping scheme, for the model to be parallel, to integrate iterative solvers and to operate on the sphere.

In the last two chapters of this manuscript, we have presented a prototype three-dimensional baroclinic model based on the discontinuous Galerkin method. The three-dimensional mesh is made up of prisms and is obtained by extruding a two-dimensional triangular surface mesh. The model solves the hydrostatic primitive equations relying on an implicit mode splitting procedure and implicit/explicit Runge-Kutta time integration. The interface terms are deduced using a Lax-Friedrichs approximate Riemann solver taking into account internal waves dynamics. We have provided the first stages of a validation using benchmark problems. These benchmarks consider flows over an isolated Gaussian seamount on the sphere. The complexity of the dynamics is accurately represented.

This model operates naturally in spherical geometry, thanks to the algorithm described in Chapter 3, based on local coordinate systems. This algorithm is now used in the latest version of FEOM, the finite element ocean model developed in Bremerhaven.

SLIM: a multi-purpose modeling tool

In parallel with the development of the three-dimensional component of the model, I have participated in the development of a two-dimensional depth-integrated component, based on the discrete formulation described in Chapter 2. This 2d component includes the shallow water equations and reactive tracer equations, with explicit (Gourgue et al., 2009) and implicit (Kärnä et al., 2010) wetting and drying algorithms. It features diagonally implicit Runge-Kutta iterators, using a Newton-Raphson method with the Jacobian computed with finite differences. This 2d component is implicitly coupled to a 1d river network solver (de Brye et al., 2010). This model is used in our research group for three main domains of interest:

- The Great Barrier Reef, off Queensland (Australia), where the ecosystems are changing fast. For instance, Lambrechts et al. (2010) performed a study of sediment dynamics using SLIM, and Munday et al. (2009) studied the impact of climate change on coral reef connectivity. Figure 6.1 shows that the displacement of the bifurcation point of the South-Equatorial Current due to climate change can dramatically change the propagation of passive tracers such as larvae.

- The Scheldt Estuary, modeled with its tidal river system upstream and the Northwestern European continental shelf downstream, down to the shelf break. The model has been validated for this domain (de Brye et al., 2010), optimal design of sampling strategy has been formulated (de Brauwere et al., 2009) and residence time computations have been carried out (Blaise et al., 2010b). Figure 6.2 shows the amplitude of the residence time associated with the spring-neap component of the tide.

- The Mahakam river system, located in Borneo Island, East Kalimantan Province, Indonesia. This tropical land-sea continuum includes peat swamps, lakes, the river itself, with its tributaries, the delta and the Makassar Strait. Figure 6.3 illustrates a typical mesh used for preliminary computations.

This two-dimensional model can use all the finite element pairs described in Chapter 2. Among these pairs, $P_1^{DG} - P_1^{DG}$ is not the best in terms of accuracy, the Coriolis term inducing a lack of convergence, as explained in Chapter 2. However, the discontinuous approach is compelling and mostly resorted to for practical applications of SLIM. From the implicit point of view, DG problems are easier to solve with iterative solvers than mixed formulation using $P_1^{NC} - P_1$ or $P_1^{DG} - P_2$. From the explicit point of view, the elements are only coupled by fluxes, enabling easy to implement flux or solution limiting strategies.

For now, the most constraining drawback is the relative slowness of the model. SLIM users want to compute long term simulations, and the faster the better. Therefore, we are now working on ways to increase the model efficiency.

Perspectives for two-dimensional modeling

As explained above, the most useful finite element pair for the shallow water equations is $P_1^{DG} - P_1^{DG}$. The discontinuous approach as many advantages. From my personal experience, iterative solvers are more efficient than for other discretization, limiting strategies

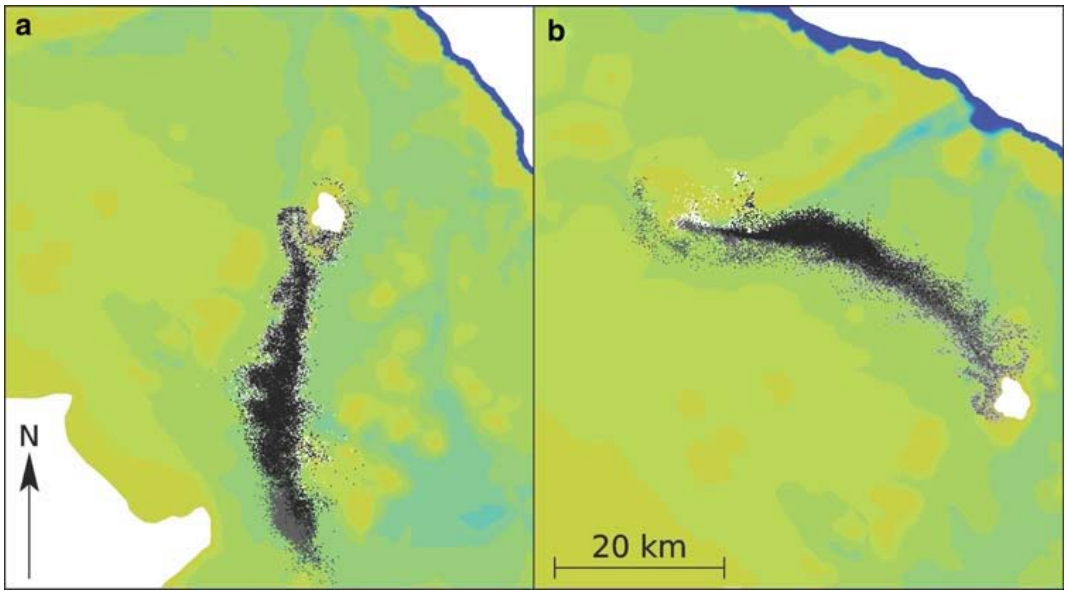

Figure 6.1: Simulated advection of passive particles around Lizard Island , Great Barrier Reef, Northeastern Australia, as computed by SLIM. Panel (a) and (b) compares two computation where the bifurcation point of the South Equatorial Current, forcing the mean flow in this region, is either in its position of December 1995, or shifted by 2 °to the South. Picture from Munday et al. (2009).

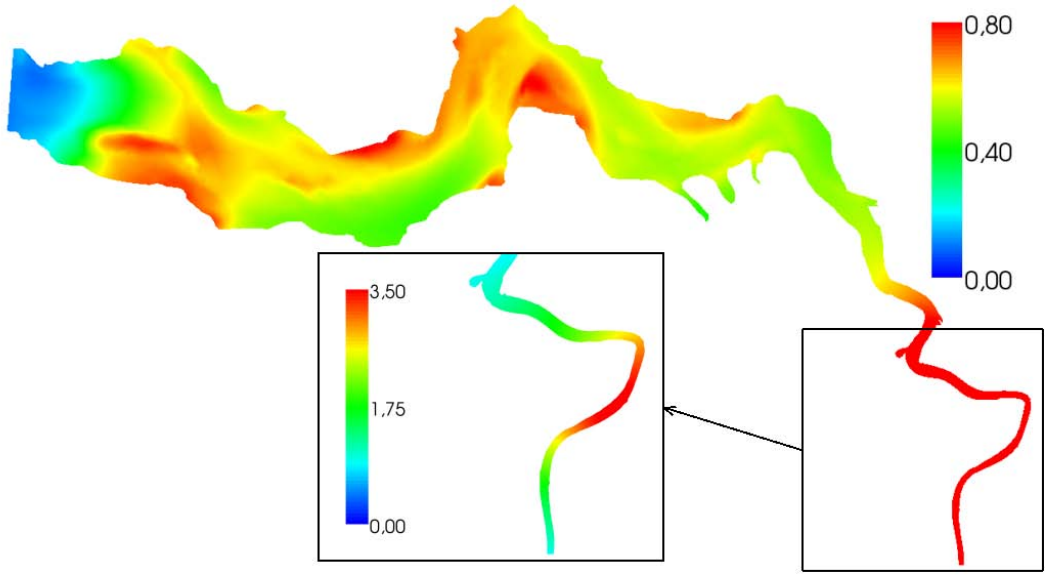

Figure 6.2: Amplitude of the residence time variations associated with the M_{SF} (spring-neap) component of the tide. Figure from Blaise et al. (2010b).

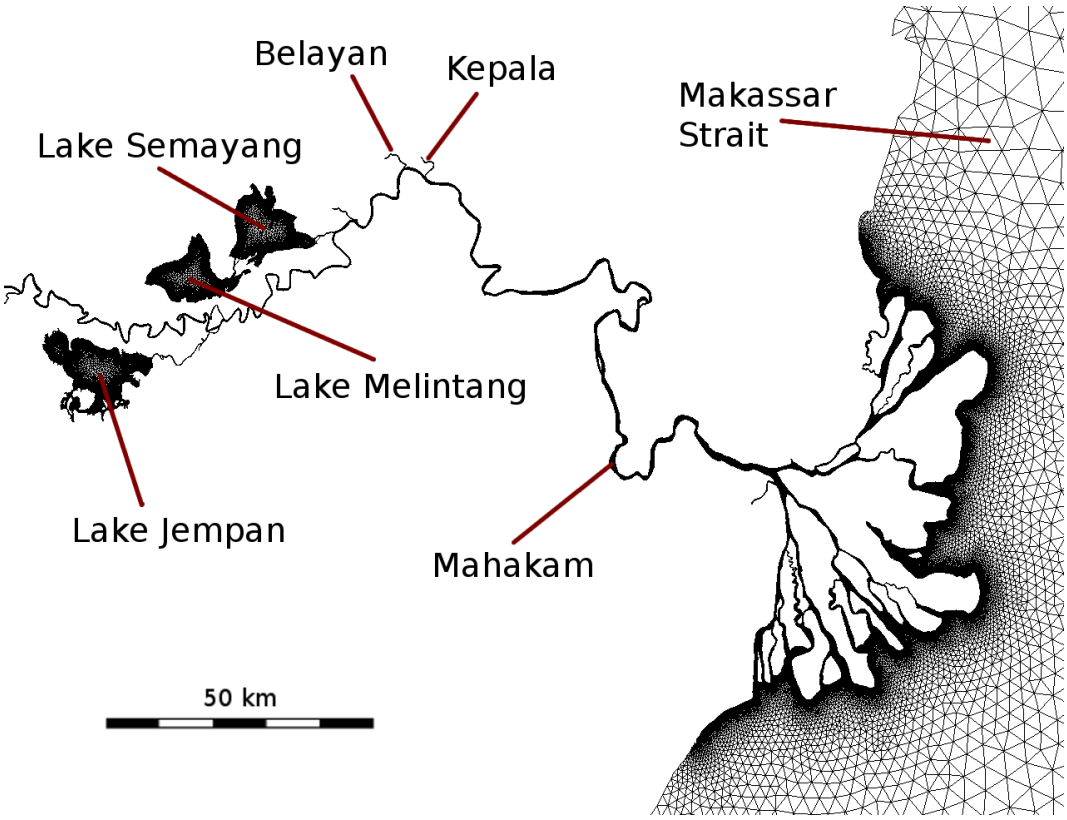

Figure 6.3: Mesh of the Mahakam river system, courtesy of Sébastien Schellen.

are similar as for finite volume methods and p- and h-adaptivity can be integrated naturally (Burbeau and Sagaut, 2005; Remacle et al., 2003, 2006; Bernard et al., 2007).

I see two main goals in the future development of the 2d shallow water model in SLIM. First, the quality of the solution must be increased. Second, the efficiency, i.e. the speed, of the model must be increased.

A better space discretization

The study of Chapter 2 did not include variable bathymetry. It appears that discontinuous Galerkin discretizations of the shallow water equations exhibit significant inter-element jumps when the gradient of the bathymetry is important. Indeed, this set of equations contains source terms that are not balanced by interface terms. In the conservative formulation, where the variables are total height and transports, the discretization provide a smooth solution for total height, in the sense that the jumps are small compared to the variation of the field inside an element. However, for geophysical flows, where the gradient of the bathymetry is much larger than the gradient of the sea-surface elevation, there is no warranty that the elevation field will be smooth. However, the gradient of this elevation field is a source term in the momentum equation. A similar behavior is observed when considering the non-conservative formulation described in Chapter 2. A possible solution to circumvent this issue would be to rely on Riemann solvers adapted

to equations with source terms, such as the one described in Murillo and García-Navarro (2010).

Discontinuous Galerkin methods are especially compelling when high order shape functions are used. However, typical solution limiting strategies are designed for linear shape functions, satisfying the pleasant property that the extrema of the solution occurs at the nodes. If an efficient limiting strategy is designed for second order shape functions, as it is the case for structured finite volume methods (Colella and Woodward, 1984), then a DG discretization using such second order shape functions would be extremely efficient and accurate.

Wetting drying procedures are mandatory for coastal and estuarine modeling. Such methods have been developed for P_1^{DG} discretizations combined with either explicit (Gourgue et al., 2009; Bunya et al., 2009) or implicit (Kärnä et al., 2010) time-stepping schemes. These methods should be further improved, to increase their robustness and accuracy.

A faster implementation

In the current implementation of SLIM, the focus has been put on implicit time-stepping strategies. Such an approach enables time steps as large as thirty minutes for modeling of zones influenced by tides such as the Scheldt estuary, where elements are as small as a few hundred meters, while classical explicit discretizations would induce time steps as small as a fraction of a second. The drawbacks of such an approach is twofold. On the one hand, the parallel scalability of the model strongly depends on the strategy for solving the linear systems arising from the Newton-Raphson linearization. For now, incomplete factorization combined with additive-Schwartz domain decomposition method is used as preconditioner for a GMRES iterative solver. Convergence to the solution is ensured as soon as the time step is not incredibly large. However, the parallel scaling is not optimal, and is strongly related to the efficiency of the communication between processors. On the other hand, limiting strategies becomes overcomplicated, and properties such as monotonicity cannot be ensured in a simple manner. Therefore, the explicit approach cannot be discarded definitely.

Recently, multirate Runge-Kutta time-stepping strategies have been proposed (Constantinescu and Sandu, 2007; Schlegel et al., 2009). Using such methods, the computational domain is partitioned, each partition progressing in time with its own time step $2^n \Delta t$. Buffer layers are needed to allow communication between zones with different time-steps. These methods allow two kinds of benefits. First, the scheme is robust to ill-shaped elements. Indeed, for explicit computations on unstructured meshes of complicated geometries, the time step is usually constrained by a few ill-shaped elements, while most of the elements allow much bigger time steps. This constraint is removed with multirate time-stepping schemes. Second, the scheme is optimally suited for multiscale problems, where several zones of interest are considered, with various corresponding timescales.

Coworkers have shown that discontinuous Galerkin methods can be implemented in such a way that most of the operations can be realized using highly optimized BLAS3 matrix-matrix products (Lambrechts and Remacle, 2010). Such an optimized implementation allows for a speed-up factor as high as three, for $P_1^{DG} - P_1^{DG}$ explicit computations of the shallow water equations, compared with usual implementation with loops. Higher speed-ups are observed for discretizations where there are more degrees of freedom per element, i.e. for quadrilateral elements, 3d elements or higher order elements.

A preliminary study shows that using a multirate Runge-Kutta time-stepping strategy, combined with a BLAS optimized implementation of discontinuous Galerkin methods, explicit computations of tidal flows in the Great Barrier Reef are only three times slower than the best implicit solution available within SLIM, running on a single processor. Explicit methods have an optimal scaling on parallel computers. Such a property is hard to obtain with implicit methods. Therefore, for computationally more expensive problems, the explicit approach can win.

Perspectives for three-dimensional modeling

Which time-stepping procedure ?

While designing our 3d model, we chose to discretize implicitly as many operators as possible. It appears that this is not the best approach. Indeed, the overhead of an implicit vertical dynamics is not always balanced with an significant increase in the stable time-step, especially if internal wave propagation is the constraining process. The Lagrange multipliers approach for coupling barotropic and baroclinic modes is elegant but when only vertical diffusion and Coriolis are treated implicitly, its overhead compared to the "compute and correct afterwards" approach is significant. Indeed, solving a symmetric linear system arising from the discretization of a diffusion operator and solving a saddle-point linear system arising from a Lagrange multipliers problem does not have the same cost. Further, if the two-dimensional baroclinic mode is solved implicitly, it must be done in a scalable way. Otherwise, for fine two-dimensional meshes with few layers, the computation of the 2d mode will become the limiting aspect of the algorithm. Such a scalable algorithm is available if the 2d problem is similar to an Helmholtz problem as in Dukowicz and Smith (1994), but not yet for the whole 2d shallow water system.

I see two ways to obtain a consistent and fast algorithm for free-surface large scale ocean modeling. Either the 3d component is treated completely explicitly, and the "correct afterwards" approach can be consistent, but the time step will be constrained by vertical diffusion, and such a solution will be unaffordable when vertical diffusion is significant (unless operator splitting is resorted to for this operator), or the whole coupled 2d and 3d system is advanced implicitly using a multigrid approach aware of the anisotropy of the problem. Such a multigrid algorithm requires the design of adapted coarsening strategies and the use of smoothers taking into account the physics of the problem. The main advantage of a multigrid algorithm compared to other implicit methods is that the Jacobian matrix of the system is never needed, as opposed to standard ILU Newton-Krylov methods, where the matrix is needed for preconditioning. Therefore, limiting tricks can be applied in a more or less straightforward manner.

A better discretization

To naturally incorporate surface water fluxes due to precipitation or evaporation, the computational domain must evolve following the free-surface, as explained in White et al. (2008b). Such a scheme must be adapted to work with multistage time stepping schemes such as the Runge-Kutta integrators we have presented.

A main concern is about internally supercritical flows. For large scale oceanography, the barotropic mode is always subcritical. It is not the case for the three-dimensional mode. Indeed, in many cases, steep density gradients are observed, due to interaction

of the ocean system with sea-ice, or caused by inflow of freshwater. Such configurations may induce dam-break like problems for the internal waves. Such phenomena will not be handled efficiently by the scheme described in Chapter 4. As for all supercritical flows, a specific limiting strategy is needed, that will reduce the accuracy of the scheme to first order. The limiting strategies are well known on structured grids. Such limiters must be studied for discontinuous Galerkin discretizations. Indeed, the standard solution limiter, that limits uniformly the slope of an element to avoid overshoots compared to the averages of neighboring cells, may not be applied as it. Indeed, ocean flows are stratified, and this stratification should not be destroyed by the limiter.

Lateral boundary conditions implementation are also a main issue. In its inviscid limit, the hydrostatic system of equations is ill-posed for any set of boundary conditions of local type (Rousseau et al., 2004). Impermeability condition generates a viscous boundary layer for horizontal velocity, as well as for vertical velocity. This boundary layer is never resolved, and induces significantly larger vertical velocities than anywhere else in the domain. We chose to discretize implicitly vertical advection with this problem in mind. In most models, this boundary layer problem is overcome thanks to limiting. A better solution should be deduced.

More physics

Once a robust model is obtained, physically relevant problems can be considered. Therefore, relevant parameterizations must be added, such as a turbulence model for vertical eddy viscosity. Parameterizations for mesoscale eddies are also needed. Isopycnal diffusion and Gent-McWilliams stirring are now viewed as standard models. Griffies et al. (1998) proposed an isoneutral diffusion scheme for finite difference models, based on a functional formalism. Indeed, finite element are naturally based on such a functional formalism. We show in appendix C that the natural discretization of the isopycnal diffusion operator with continuous finite elements is naturally variance diminishing and guarantees a vanishing isoneutral flux of the density, if a linear equation of state is used. The latter property cannot be ensured using interior penalty methods for discontinuous finite elements. Indeed, the isoneutral direction cannot be defined at inter-element interfaces, where the density is discontinuous. A possible way would be to apply diffusion operators on the continuous component of the tracer fields, with a consistent definition of restriction and prolongation operators, that can be used to obtain the continuous or the discontinuous representation from the other.

The ocean system is essentially a forced system. It is forced by momentum fluxes (i.e. wind), energy and mass fluxes at sea-surface. In polar regions, there is a strong interaction between the ocean and the covering sea-ice layer. Indeed, energy fluxes are strongly decreased, the albedo of the sea-ice being much larger than the albedo of sea water. Mass and salt fluxes generate unstable water columns, leading to convective adjustment. These zones are especially important for climate modeling, as much of the ocean deep water is formed in a few polar zones. A climate model couples at least an atmosphere component, an ocean component, and a sea-ice component. It is therefore mandatory to couple the sea-ice module developed by Lietaer et al. (2008) with a robust baroclinic model.

For coastal applications, wetting and drying procedures are mandatory. For instance, in the Scheldt Estuary, over a tidal cycle, sand banks are alternatively submerged and emerged. Such zones cannot be excluded of the domain, because at high water, a signif-

icant amount of water flows over them. These wetting and drying procedures are usually developed for the two-dimensional shallow water equations (Gourgue et al., 2009; Bunya et al., 2009; Kärnä et al., 2010). However, in the regions of freshwater influence (ROFI), a three-dimensional model is required to model the effects of density gradients. Therefore, wetting and drying algorithms must be adapted for a 3d discretization. A solution could be to coarsen dynamically the vertical discretization so that where drying occurs, the 3d model reduces to a classical 2d shallow water model, and usual techniques can be applied.

Long term perspectives

As I have explained above, many improvements are needed to be able to solve a realistic problem. On the one hand, more physics must be added in the model, that for now only deals with highly idealized benchmarks. On the other hand, the numerical tools must be improved, to obtain a stable and accurate solution of the considered problems, with a method as fast as possible.

We will not be able to deal with realistic problems without a fast solver, and this solver won't be useful if realistic problems are not tackled.

The two-dimensional version of SLIM is already operational and used for scientifically relevant applications. The three-dimensional problem involves much more complicated dynamics. For instance, supercritical features must be handled in a stable manner and implementation of boundary conditions is far from being straightforward.

In my opinion, two versions of the model should be developed concurrently. The first one should rely on a low order discretization, i.e. linear shape functions, and focus on robustness and efficiency. Limiting strategies, even if decreasing the accuracy of the scheme in the regions where the flow is smooth, must be considered to ensure that the model always produces a result. In a first time, this model should rely on an essentially explicit time integration procedures, where only vertical diffusion would be treated implicitly, for instance using an operator splitting approach. Such an explicit limited model would be able to handle complicated flows in a robust manner, even if not always accurate. To increase the stable time step, a simple implicit mode splitting procedure, using the solve and correct afterwards approach could be implemented, relying for instance on pseudo-time stepping to solve the two-dimensional mode.

The second version of the model would be focused on novelty in the numerical methods. In particular, high order implicit discretizations should be considered. p- and non-nested h-multigrid methods should be the preferred linear solver/preconditioner. Such a state of the art model won't be able to solve practical applications as is. Indeed, for a high order model to be efficient, there must not exist noise neither in the solution nor in the forcings and bathymetry. This means that on the one hand subgrid scale parametrizations must completely filter subgrid scale phenomena, i.e. the user cannot rely on the model to be robust to unresolved features. On the other hand, the forcings and bathymetry must be smoothed beforehand, so that they do not introduce spurious noise at the subgrid size level, which is much smaller than the element size for high order methods.

Unstructured grid marine models will become mainstream when they will be able to deal with problems that are out of scope of current mainstream structured models. For instance, it is well known that continental shelves play a crucial role in the carbon cycle. Structured models can hardly incorporate these shelf seas in the same compu-

tational framework as the general circulation module. Unstructured grid models have this potential. We must proof that our models are able to tackle such problems to convince the ocean modeling community that it is worth paying the price to take the step to unstructured modeling.

It will take years to reach such an objective, but such methods will sooner or later induce a revolution in marine modeling, with a new generation of researchers using a new generation of models.

Appendices

APPENDIX A

SUPPLEMENTARY MATERIAL FOR CHAPTER 3

A.1 Scaling of second kind Christoffel symbols

Consider a sphere of radius r. For each flat triangle, we define a local cartesian basis $\mathbf{e}_\xi$, $\mathbf{e}_\eta$, $\mathbf{e}_\zeta$, with $\mathbf{e}_\xi$ and $\mathbf{e}_\eta$ parallel to the plane of the triangle. To make the derivation of metric terms easier, the origin of this cartesian basis is the center of the sphere. There exists an isomorphism $\mathbf{x}(\boldsymbol{\xi})$ transforming the flat triangle into the spherical triangle (as illustrated in figure A.1):

$$\mathbf{x}(\boldsymbol{\xi}) = \frac{r}{\|\boldsymbol{\xi}\|}\boldsymbol{\xi}. \tag{A.1}$$

Using this isomorphism, we can deduce the covariant basis of the spherical triangle:

$$\begin{aligned}
\mathbf{g}_\xi &= \frac{\partial \mathbf{x}(\boldsymbol{\xi})}{\partial \xi} = \frac{r}{\|\boldsymbol{\xi}\|}\left(\mathbf{e}_\xi - \xi\frac{\boldsymbol{\xi}}{\|\boldsymbol{\xi}\|^2}\right),\\
\mathbf{g}_\eta &= \frac{\partial \mathbf{x}(\boldsymbol{\xi})}{\partial \eta} = \frac{r}{\|\boldsymbol{\xi}\|}\left(\mathbf{e}_\eta - \eta\frac{\boldsymbol{\xi}}{\|\boldsymbol{\xi}\|^2}\right),\\
\mathbf{g}_\zeta &= \frac{\boldsymbol{\xi}}{\|\boldsymbol{\xi}\|}.
\end{aligned}$$

In the case of a curved surface embedded into the three-dimensional space, the second kind Christoffel symbols $\Gamma^\gamma_{\alpha\beta}$ (with α, β, and γ being ξ or η) can be computed from:

$$\frac{\partial \mathbf{g}_\alpha}{\partial \beta} = \sum_{\gamma=\xi,\eta} \Gamma^\gamma_{\alpha\beta}\mathbf{g}_\gamma + n_{\alpha\beta}\mathbf{g}_\zeta, \tag{A.2}$$

where $n_{\alpha\beta}$ are coefficient that need not to be computed, as they are related to the component normal to the surface. For our specific application, this leads to:

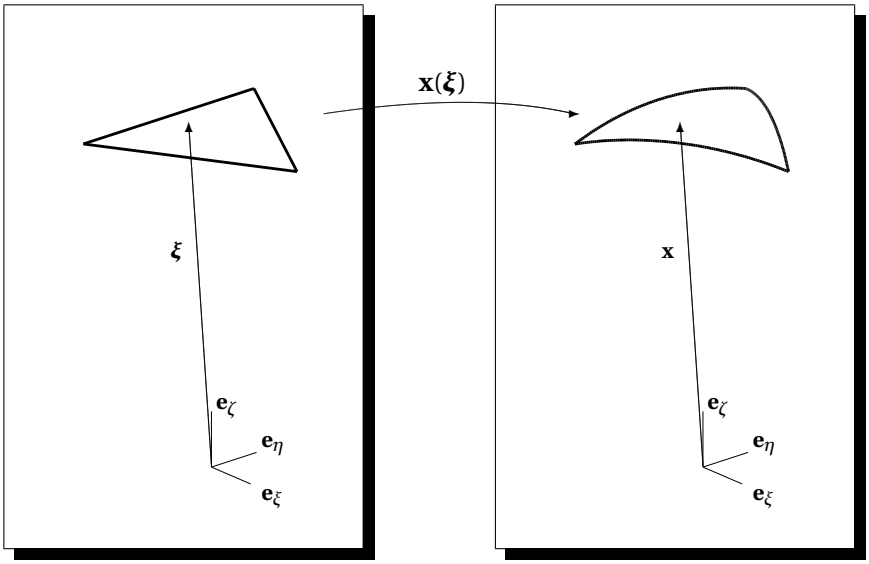

Figure A.1: The isomorphism turning a flat triangle into a spherical one.

$$\Gamma^{\xi}_{\xi\xi} = -2\frac{\xi}{\|\boldsymbol{\xi}\|^2}, \qquad \Gamma^{\xi}_{\xi\eta} = \Gamma^{\xi}_{\eta\xi} = \frac{\eta}{\|\boldsymbol{\xi}\|^2}, \qquad \Gamma^{\xi}_{\eta\eta} = 0,$$
$$\Gamma^{\eta}_{\xi\xi} = 0, \qquad \Gamma^{\eta}_{\xi\eta} = \Gamma^{\eta}_{\eta\xi} = -\frac{\xi}{\|\boldsymbol{\xi}\|^2}, \qquad \Gamma^{\eta}_{\eta\eta} = -2\frac{\eta}{\|\boldsymbol{\xi}\|^2}.$$

Therefore, the estimation of the order of magnitude for these symbols is straightforward:

$$\begin{aligned} &\xi \in [0;h], \\ &\|\boldsymbol{\xi}\| = \sqrt{(r')^2+\xi^2} \approx r, \\ &\Gamma^{\gamma}_{\alpha\beta} \approx \frac{h}{r^2}, \end{aligned}$$

for α, β and γ being ξ or η. Of course, the asymptotic assumption $h \ll r$ is always valid in ocean modeling.

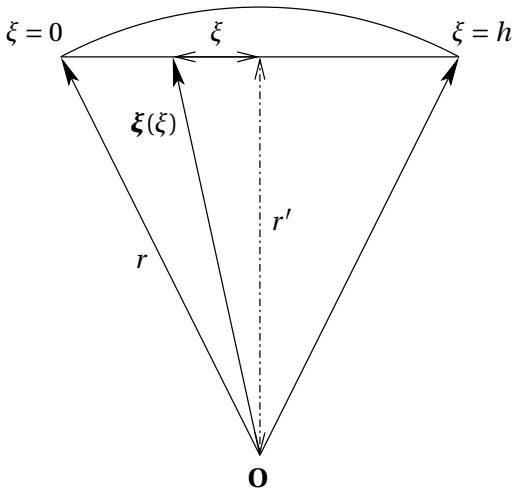

Figure A.2: A one-dimensional illustration of the different terms involved in the calculation of Christoffel symbols.

APPENDIX B

SUPPLEMENTARY MATERIAL FOR CHAPTER 5

B.1 Time-stepping algorithms of FEOM

To get rid of the a posteriori correction step of the three-dimensional velocities, the barotropic mode could be time-stepped implicitly, using the same time-step as the baroclinic mode. No correction step is needed, when all three-dimensional terms are advanced explicitly in time. In this case, the calculation could be both compatible and consistent. However, if some terms in the three-dimensional momentum equation are advanced implicitly in time, such an approach assumes that those implicit terms have no influence on the barotropic mode (Wang, 2007, p29, last paragraph), and the solution is not naturally compatible anymore. An efficient strategy to discretize implicitly the free-surface equation is to solve a smaller system corresponding to the Schur complement of the system. The finite element ocean model FEOM uses a similar approach but performs directly the equivalent algebra in the continuous framework (Wang, 2007).

Let us consider first that all terms in the three-dimensional mode are time-stepped explicitly The semi-discrete implicit form of the linearized free-surface equation (5.4) is

$$\frac{\eta^{n+1}-\eta^n}{\Delta_t} + \nabla_h \cdot \int_{-h}^{0} \boldsymbol{u}^{n+1}\, dz = 0. \tag{B.1}$$

As in the horizontal momentum equation, only the elevation gradient is implicitly integrated, the new velocity $\boldsymbol{u}^{n+1}$ is obtained by:

$$\frac{\boldsymbol{u}^{n+1}-\boldsymbol{u}^n}{\Delta_t} = -g\nabla_h \eta^{n+1} + \boldsymbol{f}^{\text{expl}}, \tag{B.2}$$

where $\boldsymbol{f}^{\text{expl}}$ includes explicit terms. This expression can be substituted into equation (B.1) to obtain an implicit two-dimensional free-surface problem:

$$\frac{\eta^{n+1}-\eta^n}{\Delta_t} + \nabla_h \cdot \int_{-h}^{0} \left[\boldsymbol{u}^n + \Delta_t\left(-g\nabla_h \eta^{n+1} + \boldsymbol{f}^{\text{expl}}\right)\right] dz = 0. \tag{B.3}$$

The time marching procedure of FEOM consists then in calculating η^{n+1} by solving the two-dimensional equation (B.3) and then deriving $\boldsymbol{u}^{n+1}$ with equation (B.2).

Now, let us consider an implicit integration for the vertical diffusion in order to reduce time step limitations. An intermediate velocity $\boldsymbol{u}^*$ is obtained by solving:

$$\frac{\boldsymbol{u}^* - \boldsymbol{u}^n}{\Delta_t} - \frac{\partial}{\partial z}\left(\nu_v \frac{\partial \boldsymbol{u}^*}{\partial z}\right) = -g\nabla_h(\eta^n) + \boldsymbol{f}^{\text{expl}}. \tag{B.4}$$

Then, η^{n+1} is calculated by solving the two-dimensional problem:

$$\frac{\eta^{n+1} - \eta^n}{\Delta_t} + \nabla_h \cdot \int_{-h}^{0} \left[\boldsymbol{u}^* - \Delta_t\, g\nabla_h\left(\eta^{n+1} - \eta^n\right)\right] dz = 0. \tag{B.5}$$

Finally, the new velocity $\boldsymbol{u}^{n+1}$, is obtained by solving the correction problem:

$$\frac{\boldsymbol{u}^{n+1} - \boldsymbol{u}^*}{\Delta_t} = -g\nabla_h(\eta^{n+1} - \eta^n), \tag{B.6}$$

The two-dimensional problem (B.5) is also obtained by substituting the new velocity from the correction step into equation (B.1). Implicit vertical viscosity is neglected in the correction step, meaning that this term is computed using $\boldsymbol{u}^*$ rather than $\boldsymbol{u}^{n+1}$. That was needed to be able to perform the substitution and obtain (B.5), but it renders the method incompatible and inconsistent a priori. The method of substitution is similar to the Schur complement approach used by Dukowicz and Smith (1994), but the substitution is performed in the continuous space rather than at the discrete level. In the continuous world, the inverse of the mass matrix $M_{\boldsymbol{u}}^{-1}$ does not appear in what corresponds to the Schur complement. The discrete system for the elevation reads:

$$\left[M_\eta - \Delta_t L\right] X_\eta = f_\eta - \Delta_t DF_{\boldsymbol{u}},$$

where L is the discrete Laplacian matrix and Δ_t is the time step.

APPENDIX C

PROPERTIES OF THE ISOPYCNAL DIFFUSION OPERATOR FOR CONTINUOUS FINITE ELEMENTS

Abstract

Griffies et al. (1998) proposed a scheme for isoneutral diffusion that respect both the variance diminishing properties and vanishing isoneutral flux of the density. We show here that both properties are naturally satisfied by the classical finite element discretization of the isopycnal diffusion as defined by Redi (1982).

C.1 Variance diminishing property is guaranteed

The finite element semi-discrete formulation is the following:

$$\int \psi_i \frac{\partial c}{\partial t}\, d\Omega = -\int \nabla\psi_i \cdot \boldsymbol{\kappa} \cdot \nabla c \, d\Omega \quad \forall\ i, \tag{C.1}$$

with $\int \quad d\Omega$ representing the integral over the whole domain, ψ_i the usual test function and c the discrete tracer field, $\boldsymbol{\kappa}$ the diffusivity tensor, that is diagonal in a frame of reference aligned with the isopycnal.

The diffusivity is defined by the Redi tensor (Redi, 1982) as:

$$\boldsymbol{\kappa} = \frac{A_H}{\rho_x^2+\rho_y^2+\rho_z^2} \begin{pmatrix} \rho_z^2+\rho_y^2+\epsilon\rho_x^2 & (\epsilon-1)\rho_x\rho_y & (\epsilon-1)\rho_x\rho_z \\ (\epsilon-1)\rho_x\rho_y & \rho_z^2+\rho_x^2+\epsilon\rho_y^2 & (\epsilon-1)\rho_y\rho_z \\ (\epsilon-1)\rho_x\rho_z & (\epsilon-1)\rho_y\rho_z & \rho_x^2+\rho_y^2+\epsilon\rho_z^2 \end{pmatrix}, \tag{C.2}$$

where ρ_x, ρ_y and ρ_z are shortcuts for $\frac{\partial\rho}{\partial x}$, $\frac{\partial\rho}{\partial y}$ and $\frac{\partial\rho}{\partial z}$, A_H is the value of isopycnal diffusivity and ϵ is so that ϵA_H is the diapycnal diffusivity.

The discrete tracer field is related to the nodal values C_i using the following relation:

$$c = \sum_i C_i \psi_i. \tag{C.3}$$

To ensure variance diminishing property, as the integral of the tracer is conserved, the formulation must discretely satisfy the following property:

$$\frac{d}{dt}\int c^2 \, d\Omega \leq 0, \tag{C.4}$$

$$\Leftrightarrow \int \frac{\partial c^2}{\partial t} \, d\Omega \leq 0, \tag{C.5}$$

$$\Leftrightarrow \int 2c\frac{\partial c}{\partial t} \, d\Omega \leq 0, \tag{C.6}$$

$$\Leftrightarrow \int c\frac{\partial c}{\partial t} \, d\Omega \leq 0. \tag{C.7}$$

The left-hand-side can be computed using definition C.3:

$$\begin{aligned}
\int c\frac{\partial c}{\partial t} \, d\Omega &= \int \sum_i \left[C_i \psi_i\right] \frac{\partial c}{\partial t} \, d\Omega && \text{(C.8)}\\
&= \sum_i \left[C_i \int \psi_i \frac{\partial c}{\partial t} \, d\Omega \right] && \text{(C.9)}\\
&= -\sum_i \left[C_i \int \nabla\psi_i \cdot \boldsymbol{\kappa} \cdot \nabla c \, d\Omega \right] && \text{(C.10)}\\
&= -\int \sum_i \left[C_i \nabla\psi_i\right] \cdot \boldsymbol{\kappa} \cdot \nabla c \, d\Omega && \text{(C.11)}\\
&= -\int \nabla c \cdot \boldsymbol{\kappa} \cdot \nabla c \, d\Omega && \text{(C.12)}
\end{aligned}$$

The right-hand-side term of equation (C.12) is less or equal to zero for the Redi diffusion tensor, because the Redi tensor is positive semidefinite.

Therefore, the natural finite element discretization of the isopycnal diffusion operator satisfies the diminishing variance property.

C.2 Vanishing isoneutral flux of the density is guaranteed

Finite element methods use the exact operator on a finite dimensional discretization of the field, while finite difference methods use approximation of the operators at grid points. We will now show that using the finite element method for the isopycnal diffusion operator, we satisfy the vanishing isoneutral flux of density.

Let us recall equation C.1:

$$\int \psi_i \frac{\partial c}{\partial t} \, d\Omega = -\int \nabla\psi_i \cdot \boldsymbol{\kappa} \cdot \nabla c \, d\Omega \quad \forall \; i.$$

If the tracer c is the density used to deduce the Redi diffusivity tensor $\boldsymbol{\kappa}$, the isopycnal diffusion should not modify the density field at all. This property is naturally satisfied by finite element formulation. Indeed, the isopycnal diffusion flux

$$\boldsymbol{\kappa} \cdot \nabla c$$

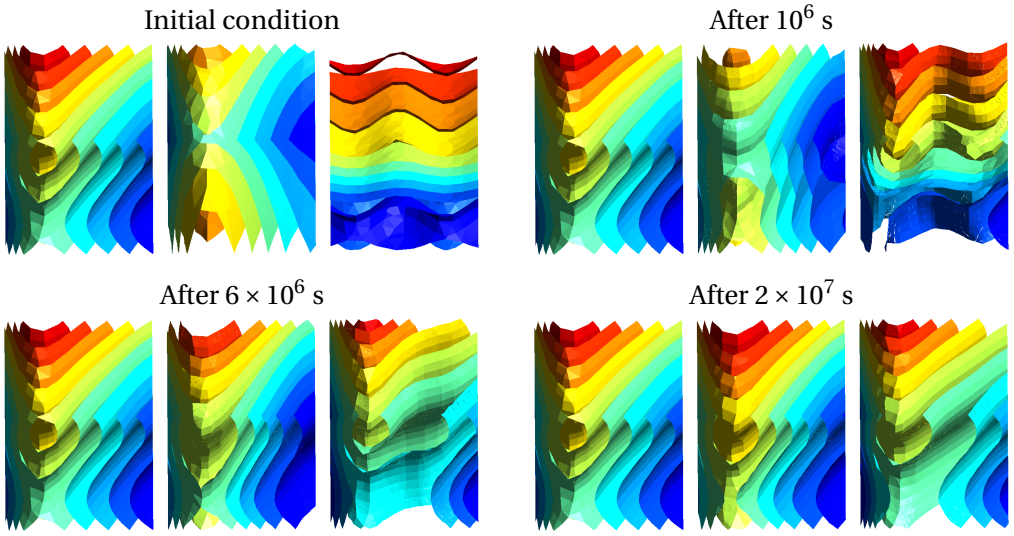

Figure C.1: Illustration of the vanishing isoneutral fluxes on a toy problem. Left panels: density, center panels: salinity, right panels: temperature. Salinity and temperature evolve according to an isopycnal diffusion equation, where the Redi tensor is computed using the density field. The density field is simply the sum of salinity and temperature fields. The domain is 1000km×1000km×1000m, the isopycnal diffusion is $10^4 m^2 s^{-1}$ and no diapycnal diffusion is used.

can be expressed in a frame of reference aligned with the isopycnal as:

$$\begin{bmatrix} \kappa_i & 0 & 0 \\ 0 & \kappa_i & 0 \\ 0 & 0 & 0 \end{bmatrix} \begin{bmatrix} \frac{\partial c}{\partial i_0} \\ \frac{\partial c}{\partial i_1} \\ \frac{\partial c}{\partial d} \end{bmatrix}, \tag{C.13}$$

where i_0 and i_1 are local isopycnal axes and d is the local diapycnal axis. By definition of the isopycnal and diapycnal, $\frac{\partial c}{\partial i_0}$ and $\frac{\partial c}{\partial i_1}$ are exactly nil, and therefore the product is zero. This is true for any continuous finite element interpolation.

As the diffusion equation is linear, solving the isopycnal diffusion equation for both temperature and salinity and deducing the density as a diagnostic is exactly equivalent as iterating the isopycnal diffusion on the density itself, for linear equation of state. We have shown just above that the finite element discretization of the isopycnal diffusion preserve the field used to deduce the Redi tensor. Therefore, if a linear equation of state is used, temperature and salinity can be diffused strongly while preserving density at rounding errors. This is highlighted in Figure C.1 on a toy example problem. A square box domain is considered. Complex initial conditions are given for temperature and salinity. The density is deduced from temperature and salinity using a linear equation of state. Both temperature and salinity evolve due to isopycnal diffusion (there is no diapycnal diffusion), while the density, deduced from these varying temperature and salinity, is held constant in time to rounding errors.

REFERENCES

A. Adcroft, C. Hill, and J. Marshall. Representation of topography by shaved cells in a height coordinate ocean model. *Monthly Weather Review*, 95:2293–2315, 1997. doi: 10.1175/1520-0493(1997)125<2293:ROTBSC>2.0.CO;2. Cited on pages 2, 69, 94, 98.

A. Adcroft, J.-M. Campin, C. Hill, and J. Marshall. Implementation of an atmosphere-ocean general circulation model on the expanded spherical cube. *Monthly Weather Review*, 134:2845–2863, 2004. doi: 10.1175/MWR2823.1. Cited on pages 2, 35.

V. Aizinger and C. Dawson. A discontinuous Galerkin method for two-dimensional flow and transport in shallow water. *Advances in Water Resources*, 25:67–84, 2002. doi: 10.1016/S0309-1708(01)00019-7. Cited on pages 4, 12, 53.

V. Aizinger and C. Dawson. The local discontinuous galerkin method for three-dimensional shallow water flow. *Computer Methods in Applied Mechanics and Engineering*, 196:734–746, 2007. doi: 10.1016/j.cma.2006.04.010. Cited on pages 4, 53.

A. Arakawa and V.R. Lamb. Computational design of the basic dynamical processes of the UCLA general circulation model. In J. Chang, editor, *Methods in Computational Physics*, pages 173–265. Academic Press, 1977. Cited on pages 52.

D. N. Arnold, F. Brezzi, B. Cockburn, and L. D. Marini. Unified analysis of discontinuous Galerkin methods for elliptic problems. *SIAM Journal on Numerical Analysis*, 39:1749–1779, 2002. doi: 10.1137/S0036142901384162. Cited on pages 12, 27, 61.

U. M. Ascher, S. J. Ruuth, and B. T. Wetton. Implicit-explicit methods for time-dependent partial differential equations. *SIAM Journal on Numerical Analysis*, 32:797–823, 1995. doi: 10.1137/0732037. Cited on pages 91.

U. M. Ascher, S. J. Ruuth, and R. J. Spiteri. Implicit-explicit Runge-Kutta methods for time-dependent partial differential equations. *Applied Numerical Mathematics*, 25: 151–167, 1997. doi: 10.1016/S0168-9274(97)00056-1. Cited on pages 40, 91, 93.

F. Bassi, A. Crivellini, D. A. Di Pietro, and S. Rebay. An artificial compressiblility flux for the discontinuous Galerkin solution of the incompressible Navier-Stokes equations. *Journal of Computational Physics*, 218:794–815, 2006. doi: 10.1016/j.jcp.2006.03.006. Cited on pages 27.

P.-E. Bernard, N. Chevaugeon, V. Legat, E. Deleersnijder, and J.-F. Remacle. High-order h-adaptive discontinuous Galerkin methods for ocean modelling. *Ocean Dynamics*, 57:109–121, 2007.
doi: 10.1007/s10236-006-0093-y. Cited on pages 12, 20, 112.

P.-E. Bernard, J.-F. Remacle, and V. Legat. Boundary discretization for high order discontinuous Galerkin computations of tidal flows around shallow water islands. *International Journal for Numerical Methods in Fluids*, 2008a.
doi: 10.1002/fld.1831. Cited on pages 12, 17, 53.

P.-E. Bernard, J.-F. Remacle, and V. Legat. Modal analysis on unstructured meshes of the dispersion properties of the $P_1^{NC} - P_1$ pair. *Ocean Modelling*, 2008b.
doi: 10.1016/j.ocemod.2008.03.005. Cited on pages 13, 27, 52.

P.-E. Bernard, J.-F. Remacle, R. Comblen, V. Legat, and K. Hillewaert. High-order discontinuous Galerkin schemes on general 2d manifolds applied to the shallow water equations. *Journal of Computational Physics*, 228:6514–6535, 2009.
doi: 10.1016/j.jcp.2009.05.046. Cited on pages 8, 33.

S. Blaise, E. Deleersnijder, L. White, and J.-F. Remacle. Influence of the turbulence closure scheme on the finite-element simulation of the upwelling in the wake of a shallow-water island. *Continental Shelf Research*, 27:2329–2345, 2007.
doi: 10.1016/j.csr.2007.06.003. Cited on pages 6.

S. Blaise, R. Comblen, V. Legat, J.-F. Remacle, E. Deleersnijder, and J. Lambrechts. A discontinuous finite element baroclinic marine model on unstructured prismatic meshes. Part I: space discretization. *Ocean Dynamics (submitted)*, 2010a. Cited on pages 84, 85, 88, 94, 96, 108.

S. Blaise, B. de Brye, A. de Brauwere, E. Deleersnijder, E. J. M. Delhez, and R. Comblen. Capturing the residence time boundary layer - application to the Scheldt Estuary. *Ocean Dynamics (in press)*, 2010b.
doi: 10.1007/s10236-010-0272-8. Cited on pages 110, 111.

S. Blaise, B. de Brye, A. de Brauwere, E. Deleersnijder, E. J. M. Delhez, and R. Comblen. Capturing the residence time boundary layer - application to the Scheldt Estuary. *Ocean Dynamics*, 60:535–554, 2010c.
doi: 10.1007/s10236-010-0272-8. Cited on pages 53.

R. Bleck. On the use of hybrid vertical coordinates in numerical weather prediction models. *Monthly Weather Review*, 106:1233–1244, 1978.
doi: 10.1175/1520-0493(1978)106<1233:OTUOHV>2.0.CO;2. Cited on pages 2.

A. F. Blumberg and G. L. Mellor. A description of three-dimensional coastal ocean circulation model. In N. S. Heaps, editor, *Three Dimensional Coastal Ocean Model*, pages 1–16. American Geophysical Union, 1987. Cited on pages 2, 34, 82.

S. W. Bova and G. F. Carey. An entropy variable form and applications for the two-dimensional shallow water equations. *International Journal For Numerical Methods In Fluids*, 23:29–46, 1996.
doi: 10.1002/(SICI)1097-0363(19960715)23:1<29::AID-FLD411>3.0.CO;2-U. Cited on pages 12.

F. Brezzi and M. Fortin. *Mixed and Hybrid Finite Element Methods*. Number 15 in Springer Series in Computational Mathematics. Springer-Verlag, 1991. Cited on pages 23.

A. N. Brooks and T. J. R. Hughes. Streamline upwind/Petrov-Galerkin formulations for convection dominated flows with particular emphasis on the incompressible Navies-Stokes equations. *Computer Methods in Applied Mechanics and Engineering*, 32:199–259, 1982.
doi: 10.1016/0045-7825(82)90071-8. Cited on pages 3.

K. Bryan. A numerical method for the study of the circulation of the world ocean. *Journal of Computational Physics*, 4:347–376, 1969.
doi: 10.1016/0021-9991(69)90004-7. Cited on pages 2, 52, 82, 94.

S. Bunya, E. J. Kubatko, J. J. Westerink, and C. Dawson. A wetting and drying treatment for the runge-kutta discontinuous galerkin solution to the shallow water equations. *Computer Methods in Applied Mechanics and Engineering*, 198(17-20):1548 – 1562, 2009.
doi: 10.1016/j.cma.2009.01.008. Cited on pages 113, 116.

A. Burbeau and P. Sagaut. A dynamic p-adaptive discontinuous Galerkin method for viscous flow with shocks. *Computer and Fluids*, 34:401–417, 2005.
doi: 10.1016/j.compfluid.2003.04.002. Cited on pages 12, 112.

V. Casulli and R.A. Walters. An unstructured grid, three-dimensional model based on the shallow water equations. *International Journal for Numerical Methods in Fluids*, 32: 331–348, 2000. Cited on pages 52.

V. Casulli and P. Zanolli. Semi-implicit numerical modeling of nonhydrostatic free-surface flows for environmental problems. *Mathematical and Computer Modelling*, 32:331–348, 2000.
doi: 10.1016/S0895-7177(02)00264-9. Cited on pages 4.

D. C. Chapman and D. B. Haidvogel. Formation of Taylor caps over a tall isolated seamount in a stratified ocean. *Geophysical and Astronomical Fluid Dynamics*, 64:31–65, 1992.
doi: 10.1080/03091929208228084. Cited on pages 69, 72, 84, 94, 98, 102, 103, 104, 105, 106.

D. C. Chapman and D. B. Haidvogel. Generation of internal lee waves trapped over a tall isolated seamount. *Geophysical and Astronomical Fluid Dynamics*, 69:33–54, 1993.
doi: 10.1080/03091929308203573. Cited on pages 69, 94.

C. Chen, H. Liu, and R. C. Beardsley. An unstructured grid, finite-volume, three-dimensional, primitive equations ocean model: Applications to coastal ocean and estuaries. *Journal of Atmospheric and Oceanic Technology*, 20:159–186, 2003.
doi: 10.1175/1520-0426(2003)020<0159:AUGFVT>2.0.CO;2. Cited on pages 4, 52.

N. Chevaugeon, J. Xin, P. Hu, X. Li, D. Cler, J. E. Flaherty, and M. S. Shephard. Discontinuous Galerkin methods applied to shock and blast problems. *Journal of Scientific Computing*, 22-23:227–243, 2005.
doi: 10.1007/s10915-004-4138-4. Cited on pages 12.

N. Chevaugeon, K. Hillewaert, X. Gallez, P. Ploumhans, and J.-F. Remacle. Optimal numerical parametrization of discontinuous Galerkin method applied to wave propagation problems. *Journal of Computational Physics*, 223:188–207, 2007.
doi: 10.1016/j.jcp.2006.09.005. Cited on pages 73, 96.

B. Cockburn and C. Shu. The local discontinuous Galerkin finite element method for time-dependent convection-diffusion systems. *SIAM Journal on Numerical Analysis*, 35:2440–2463, 1998a.
doi: 10.1137/S0036142997316712. Cited on pages 12, 62.

B. Cockburn and C.-W. Shu. The Runge-Kutta discontinuous Galerkin method for conservation laws V - multidimensional systems. *Journal of Computational Physics*, 141: 191–224, 1998b.
doi: 10.1006/jcph.1998.5892. Cited on pages 12.

B. Cockburn and C.-W. Shu. Runge-Kutta discontinuous Galerkin methods for convection-dominated problems. *Journal of Scientific Computing*, 16:173–261, september 2001.
doi: 10.1023/A:1012873910884. Cited on pages 91.

B. Cockburn, G. Kanschat, D. Schötzau, and C. Schwab. Local discontinuous Galerkin methods for the Stokes system. *SIAM Journal on Numerical Analysis*, 40:319–343, 2002.
doi: 10.1137/S0036142900380121. Cited on pages 31.

P. Colella and P. R. Woodward. The piecewise parabolic method (PPM) for gas-dynamical simulations. *Journal of Computational Physics*, 54:174–201, 1984.
doi: 10.1016/0021-9991(84)90143-8. Cited on pages 113.

R. Comblen, S. Legrand, E. Deleersnijder, and V. Legat. A finite element method for solving the shallow water equations on the sphere. *Ocean Modelling*, 28:12–23, 2009.
doi: 10.1016/j.ocemod.2008.05.004. Cited on pages 31, 58.

R. Comblen, S. Blaise, V. Legat, J.-F. Remacle, E. Deleersnijder, and J. Lambrechts. A discontinuous finite element baroclinic marine model on unstructured prismatic meshes. Part II: implicit/explicit time discretization. *Ocean Dynamics (submitted)*, 2010a. Cited on pages 51.

R. Comblen, J. Lambrechts, J.-F. Remacle, and V. Legat. Practical evaluation of five part-discontinuous finite element pairs for the non-conservative shallow water equations. *International Journal for Numerical Methods in Fluids*, 73:701–724, 2010b.
doi: 10.1002/fld.2094. Cited on pages 52, 55, 60, 61.

E. M. Constantinescu and A. Sandu. Multirate timestepping methods for hyperbolic conservation laws. *Journal of Scientific Computing*, 33:239–278, 2007.
doi: 10.1007/s10915-007-9151-y. Cited on pages 113.

J. Côté. A Lagrange multiplier approach for the metric terms of semi-Lagrangian models on the sphere. *Quarterly Journal of the Royal Meteorological Society*, 114:1347–1352, 1988.
doi: 10.1002/qj.49711448310. Cited on pages 35.

C. J. Cotter, D. A. Ham, and C. C. Pain. A mixed discontinuous/continuous finite element pair for shallow-water ocean modelling. *Ocean Modelling*, 26:86–90, 2009a. doi: 10.1016/j.ocemod.2008.09.002. Cited on pages 13, 52.

C. J. Cotter, D. A. Ham, C. C. Pain, and S. Sebastian Reich. LBB stability of a mixed Galerkin finite element pair for fluid flow simulations. *Journal of Computational Physics*, 228:336–348, 2009b. doi: 10.1016/j.jcp.2008.09.014. Cited on pages 13, 52.

A. C. Coward, P. D. Killworth, and J. R. Blundell. Tests of a two-grid world ocean model. *Journal of Geophysical Research*, 99:725–735, 1994. doi: 10.1029/94JC01893. Cited on pages 35.

B. Cushman-Roisin. *Introduction to Geophysical Fluid Dynamics*. Prenctice Hall, 1994. ISBN 0-13-353301-8. Cited on pages 98.

S. Danilov, G. Kivman, and J. Schröter. A finite-element ocean model: principles and evaluation. *Ocean Modelling*, 6:125–150, 2004. doi: 10.1016/S1463-5003(02)00063-X. Cited on pages 6.

S. Danilov, G. Kivman, and J. Schröter. Evaluation of an eddy-permitting finite-element ocean model in the north atlantic. *Ocean Modelling*, 10:35–49, 2005. doi: 10.1016/j.ocemod.2004.07.006. Cited on pages 6.

S. Danilov, Q. Wang, M. Losch, D. Sidorenko, and J. Schröter. Modeling ocean circulation on unstructured meshes: comparison of two horizontal discretizations. *Ocean Dynamics*, 58:365–374, 2008. doi: 10.1007/s10236-008-0138-5. Cited on pages 6.

C. Dawson and V. Aizinger. A discontinuous galerkin method for three-dimensional shallow water equations. *Journal of Scientific Computing*, 22-23:245–267, 2005. doi: 10.1007/s10915-004-4139-3. Cited on pages 4, 53.

A. de Brauwere, F. D. Ridder, O. Gourgue, J. Lambrechts, R. Comblen, R. Pintelon, J. Passerat, P. Servais, M. Elskens, W. Baeyens, T. Kärnä, B. de Brye, and E. Deleersnijder. Design of a sampling stategy to optimally calibrate a reactive transport model: Exploring the potential for Escherichia coli in the Scheldt Estuary. *Environmental Modelling & Software*, 24:969–981, 2009. doi: 10.1016/j.envsoft.2009.02.004. Cited on pages 110.

B. de Brye, A. de Brauwere, O. Gourgue, T. Kärnä, J. Lambrechts, R. Comblen, and E. Deleersnijder. A finite-element, multi-scale model of the Scheldt tributaries, river, estuary and ROFI. *Coastal Engineering*, 57:850–863, 2010. doi: 10.1016/j.coastaleng.2010.04.001. Cited on pages 110.

E. Deleersnijder. Numerical mass conservation in a free-surface sigma coordinate marine mode with mode splitting. *Journal of Marine Systems*, 4:365–370, 1993. doi: 10.1016/0924-7963(93)90021-D. Cited on pages 82.

E. Deleersnijder and J.-M. Beckers. On the use of the sigma-coordinate in regions of large bathymetric variations. *Journal of Marine Systems*, 3:381–390, 1992. doi: 10.1016/0924-7963(92)90011-V. Cited on pages 54.

E. Deleersnijder and J.-M. Campin. On the computation of the barotropic mode of a free-surface world ocean model. *Annales Geophysicae*, 13:675–688, 1995.
doi: 10.1007/s00585-995-0675-x. Cited on pages 34.

E. Deleersnijder and P. F. J. Lermusiaux. Multi-scale modeling; nested-grid and unstructured-mesh approaches. *Ocean Dynamics (special issue)*, 58:335–498, 2008. Cited on pages 52.

E. Deleersnijder, J.-P. Van Ypersele, and J.-M. Campin. An orthogonal curvilinear coordinate system for a world ocean model. *Ocean Modelling (Newsletter)*, 100:7–10, 1993. Cited on pages 35.

D. A. Di Pietro. Analysis of discontinuous Galerkin approximation of the Stokes problem based on an artificial compressibility flux. *International Journal for Numerical Methods in Fluids*, 55:793–813, 2007.
doi: 10.1002/fld.1495. Cited on pages 27.

J. Donea and A. Huerta. *Finite Element Methods for Flow Problem*. Wiley, 2003. Cited on pages 12.

J. K. Dukowicz and R. D. Smith. Implicit free-surface method for the Bryan-Cox-Semtner ocean model. *Journal of Geophysical Research*, 99:7991–8014, April 1994.
doi: 10.1029/93JC03455. Cited on pages 2, 83, 114, 126.

J. K. Dukowicz, R. D. Smith, and R. C. Malone. A reformulation and implementation of the Bryan-Cox-Semtner ocean model on the connection machine. *Journal of Atmospheric and Oceanic Technology*, 10:195–208, 1993.
doi: 10.1175/1520-0426(1993)010<0195:ARAIOT>2.0.CO;2. Cited on pages 82.

M. Eby and G. Holloway. Grid transformation for incorporating the Arctic in a global ocean model. *Climate Dynamics*, 10:241–247, 1994.
doi: 10.1007/BF00208991. Cited on pages 35.

T. Ezer. Entrainment, diapycnal mixing and transport in three-dimensional bottom gravity current simulations using the Mellor-Yamada turbulence closure. *Ocean Modelling*, 9:151–168, 2005.
doi: 10.1016/j.ocemod.2004.06.001. Cited on pages 84.

T. Ezer. Topographic influence on overflow dynamics: Idealized numerical simulations of the Faroe Bank Channel overflow. *Journal of Geophysical Research*, 111, 2006.
doi: 10.1029/2005JC003195. Cited on pages 84.

T. Ezer and G. L. Mellor. A generalized coordinate ocean model and a comparison of the bottom boundary layer dynamics in terrain-following and in z-level grids. *Ocean Modelling*, 6:379–403, 2004.
doi: 10.1016/S1463-5003(03)00026-X. Cited on pages 84.

R. Ford, C.C. Pain, M. Piggott, A. Goddard, C.R. de Oliveira, and A. Umpleby. A non-hydrostatic finite element model for three-dimensional stratified oceanic flows, Part II: Model validation. *Monthly Weather Review*, 132:2832–2844, 2004a.
doi: 10.1175/MWR2825.1. Cited on pages 69, 71, 84, 94, 95, 96, 102, 106, 107.

R. Ford, C.C. Pain, M. Piggott, A. Goddard, C.R. de Oliveira, and A. Umpleby. A non-hydrostatic finite element model for three-dimensional stratified oceanic flows, Part I: Model formulation. *Monthly Weather Review*, 132:2816–2831, 2004b.
doi: 10.1175/MWR2824.1. Cited on pages 6, 52.

O. B. Fringer, M. Gerritsen, and R. L. Street. An unstructured-grid, finite-volume, nonhydrostatic, parallel coastal ocean simulator. *Ocean Modelling*, 14:139–173, 2006.
doi: 10.1016/j.ocemod.2006.03.006. Cited on pages 4, 52.

A. J. Gadd. A split-explicit integration scheme for numerical weather prediction. *Quarterly Journal of the Royal Meteorological Society*, 104:569–582, 1978.
doi: 10.1002/qj.49710444103. Cited on pages 34.

P. R. Gent and J. C. McWilliams. Isopycnal mixing in ocean circulation models. *Journal of Physical Oceanography*, 20:150–155, 1990.
doi: 10.1175/1520-0485(1990)020<0150:IMIOCM>2.0.CO;2. Cited on pages 2.

P. R. Gent, J. Willebrand, T. J. McDougall, and J. C. McWilliams. Parameterizing eddy-induced tracer transports in ocean circulation models. *Journal of Physical Oceanography*, 25:463–474, 1995.
doi: 10.1175/1520-0485(1995)025<0463:PEITTI>2.0.CO;2. Cited on pages 2.

C. Geuzaine and J.-F. Remacle. Gmsh: a three-dimensional finite element mesh generator with buit-in pre- and post-processing facilities. *International Journal for Numerical Methods in Engineering*, 79:1309–1331, 2009.
doi: 10.1002/nme.2579. Cited on pages 4, 5, 20.

F. X. Giraldo. Lagrange-Galerkin methods on spherical geodesic grids : The shallow water equations. *Journal of Computational Physics*, 160:336–368, 2000.
doi: 10.1006/jcph.2000.6469. Cited on pages 35.

F. X. Giraldo. High-order triangle-based discontinuous Galerkin methods for hyperbolic equations on a rotating sphere. *Journal of Computational Physics*, 214:447–465, 2006.
doi: 10.1016/j.jcp.2005.09.029. Cited on pages 12, 35, 53.

F. X. Giraldo and T. Warburton. A nodal triangle-based spectral element method for the shallow water equations on the sphere. *Journal of Computational Physics*, 207:129–150, 2005.
doi: 10.1016/j.jcp.2005.01.004. Cited on pages 35.

F. X. Giraldo, J. S. Hesthaven, and T. Warburton. Nodal high-order discontinuous Galerkin methods for the spherical shallow water equations. *Journal of Computational Physics*, 181:499–525, 2002.
doi: 10.1006/jcph.2002.7139. Cited on pages 35.

F. X. Giraldo, J. B. Perot, and P. F. Fischer. A spectral element semi-lagrangian (SESL) method for the spherical shallow water equations. *Journal of Computational Physics*, 190:623–650, 2003.
doi: 10.1016/S0021-9991(03)00300-0. Cited on pages 35, 83.

G. Gorman, M. Piggott, C. Pain, R. de Oliveira, A. Umpleby, and A. Goddard. Optimisation based bathymetry approximation through constrained unstructured mesh adaptivity. *Ocean Modelling*, 12:436–452, 2006.
doi: 10.1016/j.ocemod.2005.09.004. Cited on pages 4.

G. Gorman, M. Piggott, and C. Pain. Shoreline approximation for unstructured mesh generation. *Computers and Geosciences*, 33:666–677, 2007.
doi: 10.1016/j.cageo.2006.09.007. Cited on pages 4.

O. Gourgue, R. Comblen, J. Lambrechts, T. K. V. Legat, and E. Deleersnijder. A flux-limiting wetting-drying method for finite-element shallow-water models, with application to the Scheldt Estuary. *Advances in Water Resources*, 32:1726–1739, 2009.
doi: 10.1016/j.advwatres.2009.09.005. Cited on pages 110, 113, 116.

P. M. Gresho and R. L. Sani. *Incompressible Flow and the Finite Element Method - Isothermal Laminar Flow*. Wiley, 2000. ISBN 0-471-96789-0. Cited on pages 40.

S. Griffies. *Fundamentals of ocean climate models*. Princeton University Press, 2004. Cited on pages 2, 12, 56, 63.

S. M. Griffies, A. Gnanadesikan, R. C. Pacanowski, V. D. Larichev, J. K. Dukowicz, and R. D. Smith. Isoneutral diffusion in a z-coordinate ocean model. *Journal of Physical Oceanography*, 28:805–830, 1998.
doi: 10.1175/1520-0485(1998)028<0805:IDIAZC>2.0.CO;2. Cited on pages 115, 127.

S. M. Griffies, C. Böning, F. O. Bryan, E. P. Chassignet, R. Gerdes, H. Hasumi, A. Hirst, A.-M. Treguier, and D. Webb. Developments in ocean climate modeling. *Ocean Modelling*, 2:123–192, 2000.
doi: 10.1016/S1463-5003(00)00014-7. Cited on pages 2, 52, 82.

S. M. Griffies, A. J. Adcroft, H. Banks, C. W. Böning, E. P. Chassignet, G. Danabasoglu, S. Danilov, E. Deleersnijder, H. Drange, M. England, B. Fox-Kemper, R. Gerdes, A. Gnanadesikan, R. J. Greatbach, R. W. Hallberg, E. Hanert, M. J. Harrison, S. A. Legg, C. M. Little, G. Madec, S. Marsland, M. Nikurashin, A. Piran, H. L. Simmons, J. Schröter, B. L. S. A.-M. Treguier, J. R. Toggweiler, H. Tsujino, G. K. Vallis, and L. White. Problems and prospects in large-scale ocean circulation models. *OceanObs'09*, 2009. URL `http://www.oceanobs09.net/blog/?p=88`. Cited on pages 2, 52.

B. E. Griffith and C. S. Peskin. On the order of accuracy of the immersed boundary method: Higher order convergence rates for sufficiently smooth problems. *Journal of Computational Physics*, 208:75–105, 2005.
doi: 10.1016/j.jcp.2005.02.011. Cited on pages 3.

R. Hallberg. Stable split time stepping schemes for large-scale ocean modeling. *Journal of Computational Physics*, 135:54–56, 1997.
doi: 10.1006/jcph.1997.5734. Cited on pages 34, 82.

D. A. Ham, J. Pietrzak, and G. S. Stelling. A scalable unstructured grid 3-dimensional finite volume mode for the shallow water equations. *Ocean Modelling*, 10:153–169, 2005.
doi: 10.1016/j.ocemod.2004.08.004. Cited on pages 4, 52.

E. Hanert and V. Legat. How to save a bad element with weak boundary conditions. *Computer & Fluids*, 35:477–484, 2006.
doi: 10.1016/j.compfluid.2005.02.005. Cited on pages 40.

E. Hanert, D. L. Roux, V. Legat, and E. Deleersnijder. Advection schemes for unstructured grid ocean modelling. *Ocean Modelling*, 7:39–58, 2004.
doi: 10.1016/S1463-5003(03)00029-5. Cited on pages 40, 41.

E. Hanert, D. Y. L. Roux, V. Legat, and E. Deleersnijder. An efficient Eulerian finite element method for the shallow water equations. *Ocean Modelling*, 10:115–136, 2005.
doi: 10.1016/j.ocemod.2004.06.006. Cited on pages 6, 7, 13, 27, 31, 40, 52.

E. Hanert, R. A. Walters, D. Y. Le Roux, and J. D. Pietrzak. A tale of two elements: P_1NC-P_1 and RT_0. *Ocean Modelling*, 2008.
doi: 10.1016/j.ocemod.2008.07.002. Cited on pages 13, 27.

R. L. Haney. On the pressure gradient force over steep topography in sigma coordinate ocean models. *Journal of Physical Oceanography*, 21:610–619, 1991.
doi: 10.1175/1520-0485(1991)021<0610:OTPGFO>2.0.CO;2. Cited on pages 54.

R. Hartmann and P. Houston. Adaptive discontinuous Galerkin finite element methods for the compressible Euler equations. *Journal of Computational Physics*, 183:508–532, 2002.
doi: 10.1006/jcph.2002.7206. Cited on pages 12.

G. Hauke. A symmetric form for computing transient shallow water flows. *Computer Methods in Applied Mechanics and Engineering*, 163:111–122, 1998.
doi: 10.1016/S0045-7825(98)00007-3. Cited on pages 12.

G. Hauke. A stabilized finite element method for the Saint-Venant equations with application to irrigation. *International Journal For Numerical Methods In Fluids*, 38:963–984, 2002.
doi: 10.1002/fld.250. Cited on pages 12.

B. Haurwitz. The motion of atmospheric disturbances on the spherical earth. *Journal of Marine Research*, 3:254–267, 1940. Cited on pages 44.

R. Heikes and D. A. Randall. Numerical integration of the shallow-water equations on a twisted icosahedral grid. part i: Basic design and results of tests. *Monthly Weather Review*, 123:1862–1880, 1995.
doi: 10.1175/1520-0493(1995)123<1862:NIOTSW>2.0.CO;2. Cited on pages 35.

R. L. Higdon. A two-level time-stepping method for layered ocean circulation models. *Journal of Computational Physics*, 177:59–94, 2002.
doi: 10.1006/jcph.2002.7003. Cited on pages 34.

R. L. Higdon and R. A. de Szoeke. Barotropic-baroclinic time splitting for ocean circulation modeling. *Journal of Computational Physics*, 135:30–53, 1997.
doi: 10.1006/jcph.1997.5733. Cited on pages 34, 82.

B.-L. Hua and F. Thomasset. A noise-free finite element scheme for the two-layer shallow water equations. *Tellus*, 36A:157–165, 1984.
doi: 10.1111/j.1600-0870.1984.tb00235.x. Cited on pages 13, 52.

T. J. Hughes. *The Finite Element Method - Linear Static and Dynamic Finite Element Analysis*. Dover, 2000. Cited on pages 38.

T. J. R. Hughes and M. Mallet. A new finite element formulation for computational fluid dynamics: III. the generalized streamline operator for multidimensional advective-diffusive systems. *Computer Methods in Applied Mechanics and Engineering*, 58:305–328, 1986.
doi: 10.1016/0045-7825(86)90152-0. Cited on pages 3.

H. E. Huppert and K. Bryan. Topographically generated eddies. *Deep-Sea Research*, 23: 655–679, 1976.
doi: 10.1016/S0011-7471(76)80013-7. Cited on pages 69, 94.

R. Jakob-Chien, J. J. Hack, and D. L. Williamson. Spectral transform solutions to the shallow water test set. *Journal of Computational Physics*, 119:164–287, 1995.
doi: 10.1006/jcph.1995.1125. Cited on pages 43.

E. R. Johnson. Starting flow for an obstable moving transversely in a rapidly rotating fluid. *Journal of Fluid Mechanics*, 149:71–88, 1984.
doi: doi:10.1017/S0022112084002548. Cited on pages 98.

T. Kärnä, B. de Brye, O. Gourgue, J. Lambrechts, R. Comblen, V. Legat, and E. Deleersnijder. A fully implicit wetting-drying method for DG-FEM shallow water model. *Computer Methods in Applied Mechanics and Engineering (in press)*, 2010.
doi: 10.1016/j.cma.2010.07.001. Cited on pages 110, 113, 116.

P. D. Killworth, D. Stainforth, D. J. Webb, and S. M. Paterson. The development of a free-surface Bryan-Cox-Semtner ocean model. *Journal of Physical Oceanography*, 21:1333–1348, september 1991.
doi: 10.1175/1520-0485(1991)021<1333:TDOAFS>2.0.CO;2. Cited on pages 2, 34, 82.

E. J. Kubatko, J. J. Westerink, and C. Dawson. hp discontinuous Galerkin methods for advection dominated problems in shallow water flows. *Computational Methods in Applied Mechanics and Engineering*, 196:437–451, 2006.
doi: 10.1016/j.cma.2006.05.002. Cited on pages 4, 12, 53.

R. J. Labeur and G. N. Wells. Interface stabilised finite element method for moving domains and free surface flows. *Computer Methods in Applied Mechanics and Engineering*, 198(5-8):615 – 630, 2009. ISSN 0045-7825.
doi: 10.1016/j.cma.2008.09.014. Cited on pages 52.

J. Lambrechts and J.-F. Remacle. Efficient assembly of high order continuous and discontinuous finite element operators. *in Preparation*, 2010. Cited on pages 113.

J. Lambrechts, R. Comblen, V. Legat, C. Geuzaine, and J.-F. Remacle. Multiscale mesh generation on the sphere. *Ocean Dynamics*, 58(5):461–473, 2008.
doi: 10.1007/s10236-008-0148-3. Cited on pages 4, 5.

J. Lambrechts, C. Humphrey, L. McKinna, O. Gourgue, K. E. Fabricius, A. J. Mehta, S. Lewis, and E. Wolanski. Importance of wave-induced bed liquefaction in the fine sediment budget of Cleveland Bay, Great Barrier Reef. *Estuarine, Coastal and Shelf*

Science (in press), 2010.
doi: http://dx.doi.org/10.1016/j.ecss.2010.06.009. Cited on pages 110.

D. Lanser, J. G. Blom, and J. G. Verwer. Spatial discretization of the shallow water equations in spherical geometry using Osher's scheme. *Journal of Computational Physics*, 165:542–565, 2000.
doi: 10.1006/jcph.2000.6632. Cited on pages 35.

Y. Le Bars, F. Lyard, C. Jeandel, and L. Dardengo. The AMANDES tidal model for the Amazon estuary and shelf. *Ocean Modelling*, 31:132–149, 2010.
doi: 10.1016/j.ocemod.2009.11.001. Cited on pages 4.

D. Y. Le Roux. A new triangular finite-element with optimum constraint ratio for compressible fluids. *SIAM Journal on Scientific Computing*, 23:66–80, 2001.
doi: 10.1137/S1064827500367403. Cited on pages 13.

D. Y. Le Roux. Dispersion relation analysis of the $P_1^{NC} - P_1$ finite-element pair in shallow-water models. *SIAM Journal on Scientific Computing*, 27:394–414, 2005.
doi: 10.1137/030602435. Cited on pages 13, 27.

D. Y. Le Roux, A. Staniforth, and C. A. Lin. Finite elements for shallow-water equation ocean model. *Monthly Weather Review*, 126:1931–1951, 1998.
doi: 10.1175/1520-0493(1998)126<1931:FEFSWE>2.0.CO;2. Cited on pages 7, 13, 52.

D. Y. Le Roux, C. A. Lin, and A. Staniforth. A semi-implicit semi-Lagrangian finite-element shallow-water ocean model. *Monthly Weather Review*, 128:1384–1401, 2000.
doi: 10.1175/1520-0493(2000)128<1384:ASISLF>2.0.CO;2. Cited on pages 13.

D. Y. Le Roux, A. Sene, V. Rostand, and E. Hanert. On some spurious mode issues in shallow-water models using a linear algebra approach. *Ocean Modelling*, 10:83–94, 2005.
doi: 10.1016/j.ocemod.2004.07.008. Cited on pages 13, 27, 40.

D. Y. Le Roux, V. Rostand, and B. Pouliot. Analysis of numerically induced oscillations in 2d finite-element shallow-water models part I: inertia-gravity waves. *SIAM Journal on Scientific Computing*, 29:331–360, 2007.
doi: 10.1137/060650106. Cited on pages 27, 52.

D. Y. Le Roux, V. Rostand, and B. Pouliot. Analysis of numerically induced oscillations in 2d finite-element shallow-water models part II: free planetary waves. *SIAM Journal on Scientific Computing*, 30:1971–1991, 2008.
doi: 10.1137/070697872. Cited on pages 27, 52.

J. R. Ledwell, A. J. Watson, and C. S. Law. Evidence for slow mixing across the pycnocline from an open-ocean tracer-release experiment. *Nature*, 364:701–103, 1993.
doi: 10.1038/364701a0. Cited on pages 56, 63.

S. Legg, R. W. Hallberg, and J. B. Girton. Comparison of entrainment in overflows simulated by z-coordinate, isopycnal and non-hydrostatic models. *Ocean Modelling*, 11: 69–97, 2006.
doi: 10.1016/j.ocemod.2004.11.006. Cited on pages 84.

S. Legrand, V. Legat, and E. Deleersnijder. Delaunay mesh generation for an unstructured-grid ocean circulation model. *Ocean Modelling*, 2:17–28, 2000. doi: 10.1016/S1463-5003(00)00005-6. Cited on pages 4.

S. Legrand, E. Deleersnijder, E. Hanert, V. Legat, and E. Wolanski. High-resolution, unstructured meshes for hydrodynamic models of the great barrier reef, australia. *Estuarine, Coastal and Shelf Science*, 68:36–46, 2006. doi: 10.1016/j.ecss.2005.08.017. Cited on pages 4.

S. Legrand, E. Deleersnijder, E. Delhez, and V. Legat. Unstructured, anisotropic mesh generation for the Northwestern European continental shelf, the continental slope and the neighbouring ocean. *Continental Shelf Research*, 27:1344–1356, 2007. doi: 10.1016/j.csr.2007.01.009. Cited on pages 4.

R. J. LeVeque. *Finite Volume Methods for Hyperbolic Problems*. Cambridge Texts in Applied Mathematics. Cambridge University Press, 2002. Cited on pages 19, 61.

O. Lietaer, T. Fichefet, and V. Legat. The effects of resolving the Canadian Arctic Archipelago in a finite element sea ice model. *Ocean Modelling*, 24:140–152, 2008. doi: 10.1016/j.ocemod.2008.06.002. Cited on pages 115.

Y. Liu, M. Vinokur, and Z. J. Wang. Spectral (finite) volume method for conservation laws on unstructured grids V: Extension to three-dimensional systems. *Journal of Computational Physics*, 212:454–472, 2006. doi: 10.1016/j.jcp.2005.06.024. Cited on pages 3.

R. V. Madala. Efficient time integration schemes for atmosphere and ocean models. In D. L. Book, editor, *Finite-difference techniques for vectorized fluid dynamics calculations*. Springer, Heidelberg, 1981. Cited on pages 34.

G. Madec and M. Imbard. A global ocean mesh to overcome the North Pole singularity. *Climate Dynamics*, 12:381–388, 1996. doi: 10.1007/BF00211684. Cited on pages 35.

D. Majewski, D. Liermann, P. Prohl, B. Ritter, M. Buchhold, T. Hanisch, G. Paul, W. Wergen, and J. Baumgardner. The operational global icosahedral-hexagonal gridpont model gme : Description and high-resolution tests. *Monthly Weather Review*, 130:319–338, 2002. doi: 10.1175/1520-0493(2002)130<0319:TOGIHG>2.0.CO;2. Cited on pages 35.

J.C. Marshall, A.J. Adcroft, C.N. Hill, L. Perelman, and C. Heisey. A finite-volume, incompressible Navier Stokes model for studies of the ocean on parallel computers. *Journal of Geophysical Research*, 102:5753–5766, 1997. doi: 10.1029/96JC02775. Cited on pages 2, 83.

G. L. Mellor and A. F. Blumberg. Modeling vertical and horizontal diffusivities with the sigma coordinate system. *Monthly Weather Review*, 8:1379–1383, 1985. doi: 10.1175/1520-0493(1985)113<1379:MVAHDW>2.0.CO;2. Cited on pages 63.

G.L. Mellor and T. Yamada. Development of a turbulence closure model for geophysical fluids problems. *Review of Geophysics and Space Physics*, 20:851–875, 1982. doi: 10.1029/RG020i004p00851. Cited on pages 2.

F. Mesinger and A. Arakawa. *Numerical Methods used in Atmospheric Models*. GARP Publications Series No. 17. WMO - ICSU, August 1976. Cited on pages 12.

R. Mittal and G. Iaccarino. Immersed boundary methods. *Annual Review of Fluid Mechanics*, 37:239–261, 2005.
doi: 10.1146/annurev.fluid.37.061903.175743. Cited on pages 3.

P. Munday, J. Leis, J. Lough, C. Paris, M. Kingsford, M. Berumen, and J. Lambrechts. Climate change and coral reef connectivity. *Coral Reefs*, 28:379–395, 2009.
doi: 10.1007/s00338-008-0461-9. Cited on pages 110, 111.

J. Murillo and P. García-Navarro. Weak solutions for partial differential equations with source terms: application to the shallow water equations. *Journal of Computational Physics (in press)*, 2010.
doi: 10.1016/j.jcp.2010.02.016. Cited on pages 113.

R. J. Murray. Explicit generation of orthogonal grids for ocean models. *Journal of Computational Physics*, 126:251–273, 1996.
doi: 10.1006/jcph.1996.0136. Cited on pages 35.

R. J. Murray and C. J. C. Reason. Fourier filtering and coefficient tapering at the North Pole in OGCMs. *Ocean Modelling*, 4:1–25, 2002.
doi: 10.1016/S1463-5003(01)00009-9. Cited on pages 34.

R. D. Nair, S. J. Thomas, and R. D. Loft. A discontinuous Galerkin global shallow water model. *Monthly Weather Review*, 133:876–888, 2005.
doi: 10.1175/MWR2903.1. Cited on pages 12, 35, 53.

D. Nechaev, J. Schröter, and M. Yaremchuk. A diagnostic stabilized finite-element ocean circulation model. *Ocean Modelling*, 5:37–63, 2003.
doi: 10.1016/S1463-5003(02)00013-6. Cited on pages 6.

T. M. Özgökmen and E. P. Chassignet. Dynamics of two-dimensional turbulent bottom gravity currents. *Journal of Physical Oceanography*, 32:1460–1478, 2002.
doi: 10.1175/1520-0485(2002)032<1460:DOTDTB>2.0.CO;2. Cited on pages 84.

R. C. Pacanowski and S. G. H. Philander. Parametrization of vertical mixing in numerical models of tropical oceans. *Journal of Physical Oceanography*, 11:1443–1451, 1981.
doi: 10.1175/1520-0485(1981)011<1443:POVMIN>2.0.CO;2. Cited on pages 2.

J. Pedlosky. *Geophysical Fluid Dynamics, second edition*. Springer-Verlag, Heidelberg, 1987. Cited on pages 24, 25.

J. Pedlosky. *Waves in the Ocean and Atmosphere*. Springer, 2003. Cited on pages 73.

M. D. Piggott, G. J. Gorman, C. C. Pain, P. A. Allison, A. S. Candy, B. T. Martin, and M. R. Wells. A new computational framework for multi-scale ocean modelling basid on adapting unstructured meshes. *International Journal For Numerical Methods In Fluids*, 56:1003–1015, 2008.
doi: 10.1002/fld.1663. Cited on pages 4, 52.

A. Priestley. The Taylor-Galerkin method for the shallow-water equations on the sphere. *Monthly Weather Review*, 120:3003–3015, 1992.
doi: 10.1175/1520-0493(1992)120<3003:TTMFTS>2.0.CO;2. Cited on pages 35.

M. H. Redi. Oceanic isopycnal mixing by coordinate rotation. *Journal of Physical Oceanography*, 12:1154–1158, 1982.
doi: 10.1175/1520-0485(1982)012<1154:OIMBCR>2.0.CO;2. Cited on pages 2, 56, 127.

J.-F. Remacle, J. E. Flaherty, and M. S. Shephard. An adaptive discontinuous Galerkin technique with an orthogonal basis applied to compressible flow problems. *SIAM review*, 45:53–72, 2003.
doi: 10.1137/S00361445023830. Cited on pages 112.

J.-F. Remacle, S. S. Frazão, X. Li, and M. S. Shephard. An adaptive discretization of shallow-water equations based on discontinuous Galerkin methods. *International Journal for Numerical Methods in Fluids*, 52:903–923, 2006.
doi: 10.1002/fld.1204. Cited on pages 12, 112.

F. L. B. Ribeiro, A. C. Galeão, and L. Landau. Edge-based finite element method or shallow water equations. *International Journal For Numerical Methods In Fluids*, 36:659–685, 2001.
doi: 10.1002/fld.151. Cited on pages 12.

P. Rípodas, A. Gassmann, J. Förstner, D. Majewski, M. Giorgetta, P. Korn, L. Kornblueh, H. Wan, G. Zängl, L. Bonaventura, and T. Heinze. Icosahedral Shallow Water Model (ICOSWM): results of shallow water test cases and sensitivity to model parameters. *GeoscientiC Model Development*, 2:231–251, 2009.
doi: 10.5194/gmd-2-231-2009. Cited on pages 44.

B. Riviere. *Discontinuous Galerkin Methods for Solving Elliptic and Parabolic Equations: Theory and Implementation*, volume 35 of *Frontiers in Mathematics*. SIAM, 2008. ISBN 978-0-898716-56-6. Cited on pages 12, 18, 31, 62.

J. L. Roberts, P. Heil, R. J. Murray, D. S. Holloway, and N. L. Bindoff. Pole relocation for an orthogonal grid: an analytic method. *Ocean Modelling*, 12:16–31, 2006.
doi: 10.1016/j.ocemod.2005.03.004. Cited on pages 35.

C. Ronchi, R. Iacono, and P. S. Paolucci. The cubed sphere : a new method for the solution of partial differential equations in spherical geometry. *Journal of Computational Physics*, 124:93–114, 1996.
doi: 10.1006/jcph.1996.0047. Cited on pages 35.

J. A. Rossmanith. A wave propagation method for hyperbolic systems on the sphere. *Journal of Computational Physics*, 213:629–658, 2006.
doi: 10.1016/j.jcp.2005.08.027. Cited on pages 35.

V. Rostand and D. Le Roux. Raviart-thomas and brezzi-douglas-marini finite element approximations of the shallow-water equations. *International Journal of Numerical Methods in Fluids*, 57:951–976, 2008.
doi: 10.1002/fld.1668. Cited on pages 52.

V. Rostand, D. Le Roux, and G. Carey. Kernel analysis of the discretized finite difference and finite element shallow-water models. *SIAM Journal of Scientific Computing*, 31: 531–556, 2008.
doi: 10.1137/070695198. Cited on pages 52.

A. Rousseau, R. Temam, and J. Tribbia. Boundary layers in an ocean related system. *Journal of Scientific Computing*, 21:405–432, 2004.
doi: 10.1007/s10915-004-4096-x. Cited on pages 54, 115.

R. Sadourny, A. Arakawa, and Y. Mintz. Integration of the nondivergent barotropic vorticity equation with and icosahedral-hexagonal grid for the sphere. *Monthly Weather Review*, 96:351–356, 1968.
doi: 10.1175/1520-0493(1968)096<0351:IOTNBV>2.0.CO;2. Cited on pages 35.

M. Schlegel, O. Knoth, M. Arnold, and R. Wolke. Multirate Runge-Kutta schemes for advection equations. *Journal of Computational and Applied Mathematics*, 226:345–357, 2009.
doi: 10.1016/j.cam.2008.08.009. Cited on pages 113.

D. Schwanenberg and M. Harms. Discontinuous Galerkin finite-element method for transcritical two-dimensional shallow water flows. *Journal of Hydraulic Engineering*, 130:412–421, 2004.
doi: 10.1061/(ASCE)0733-9429(2004)130:5(412). Cited on pages 12.

K. Shahbazi. An explicit expression for the penalty parameter of the interior penalty method. *Journal of Computational Physics*, 205:401–407, 2005.
doi: 10.1016/j.jcp.2004.11.017. Cited on pages 18, 62.

R. K. Smith and D. G. Dritschel. Revisiting the Rossby-Haurwitz wave test case with contour advection. *Journal of Computational Physics*, 217:473–484, 2006.
doi: 10.1016/j.jcp.2006.01.011. Cited on pages 36, 46, 47, 49.

A. St-Cyr, C. Jablonowski, J. M. Dennis, H. M. Tufo, and S. J. Thomas. A comparison of two shallow water models with non-conforming adaptive grids. *Monthly Weather Review*, 136:1898–1922, 2008.
doi: 10.1175/2007MWR2108.1. Cited on pages 35.

G. R. Stuhne and W. R. Peltier. New icosahedral grid-point discretizations of the shallow water equations on the sphere. *Journal of Computational Physics*, 148:23–58, 1999.
doi: 10.1006/jcph.1998.6119. Cited on pages 35.

G. R. Stuhne and W. R. Peltier. A robust unstructured grid discretization for 3-dimensional hydrostatic flows in spherical geometry: A new numerical structure for ocean general circulation modeling. *Journal of Computational Physics*, 213:704–729, 2006.
doi: 10.1016/j.jcp.2005.08.031. Cited on pages 35, 52.

Y. Sun, Z. J. Wand, and Y. Liu. Spectral (finite) volume method for conservation laws on unstructured grids VI: Extension to viscous flow. *Journal of Computational Physics*, 215:41–58, 2006.
doi: 10.1016/j.jcp.2005.10.019. Cited on pages 3.

P. N. Swarztrauber. Spectral transform methods for solving the shallow-water equations on the sphere. *Monthly Weather Review*, 124:730–744, 1996.
doi: 10.1175/1520-0493(1996)124<0730:STMFST>2.0.CO;2. Cited on pages 34.

P. N. Swarztrauber, D. L. Williamson, and J. B. Drake. The Cartesian method for solving partial differential equations in spherical geometry. *Dynamics of Atmospheres and Oceans*, 27:679–706, 1997.
doi: 10.1016/S0377-0265(97)00038-9. Cited on pages 35.

M. Taylor, J. Tribbia, and M. Iskandarani. The spectral element method for the shallow water equations on the sphere. *Journal of Computational Physics*, 130:92–108, 1997.
doi: 10.1006/jcph.1996.5554. Cited on pages 35.

J. Thuburn. Multidimensional flux-limited advection schemes. *Journal of Computational Physics*, 123:74–83, 1996.
doi: 10.1006/jcph.1996.0006. Cited on pages 2.

J. Thuburn. A PV-based shallow-water model on a hexagonal-icosahedral grid. *Monthly Weather Review*, 125:2328–2347, 1997.
doi: 10.1175/1520-0493(1997)125<2328:APBSWM>2.0.CO;2. Cited on pages 35.

J. Thuburn and Y. Li. Numerical simulations of Rossby-Haurwitz waves. *Tellus*, 52A:181–189, 2000.
doi: 10.1034/j.1600-0870.2000.00107.x. Cited on pages 44, 46.

R. Timmermann, S. Danilov, J. Schröter, C. Böning, D. Sidorenko, and K. Rollenhagen. Ocean circulation and sea ice distribution in a finite element global sea ice-ocean model. *Ocean Modelling*, 27(3-4):114 – 129, 2009. ISSN 1463-5003.
doi: 10.1016/j.ocemod.2008.10.009. Cited on pages 52.

H. Tomita, M. Tsugawa, M. Satoh, and K. Goto. Shallow water model on a modified icosahedral geodesic grid by using spring dynamics. *Journal of Computational Physics*, 174: 579–613, 2001.
doi: 10.1006/jcph.2001.6897. Cited on pages 35.

E. Toro. *Riemann Solvers and Numerical Methods for Fluid Dynamics, a Practical Introduction*. Springer, Berlin, 1997. Cited on pages 3, 61.

Y.-H. Tseng and D. E. Dietrich. Entrainment and transport in idealized three-dimensional gravity current simulation. *Journal Of Atmospheric and Oceanic Technology*, 23:1249–1269, 2006.
doi: 10.1175/JTECH1915.1. Cited on pages 84.

J. Verron and C. Le Provost. A numerical study of quasi-geostrophic flow over isolated topography. *Journal of Fluid Mechanics*, 154:231–252, 1985.
doi: 10.1017/S0022112085001501. Cited on pages 96, 98.

R.A. Walters. Design considerations for a finite element coastal ocean model. *Ocean Modelling*, 15:90–100, 2006.
doi: 10.1016/j.ocemod.2005.11.002. Cited on pages 4.

Q. Wang. *The Finite Element Ocean Model and its aspect of vertical discretization*. PhD thesis, Bremen University, 2007. Cited on pages 83, 89, 125.

Q. Wang, S. Danilov, and J. Schröter. Comparison of overflow simulations on different vertical grids using the finite element ocean circulation model. *Ocean Modelling*, 20: 313–335, 2008a.
doi: 10.1016/j.ocemod.2007.10.005. Cited on pages 6, 52, 69, 84.

Q. Wang, S. Danilov, and J. Schröter. Finite element ocean circulation model based on triangular prismatic elements, with application in studying the effect of topography representation. *Journal of Geophysical Research*, 113, 2008b.
doi: 10.1029/2007JC004482. Cited on pages 6, 52, 54, 69, 83, 94.

Z. J. Wang. Spectral (finite) volume method for conservation laws on unstructured grids. basic formulation. *Journal of Computational Physics*, 178:210–251, 2002.
doi: 10.1006/jcph.2002.7041. Cited on pages 3.

Z. J. Wang and Y. Liu. Spectral (finite) volume method for conservation laws on unstructured grids: II. extension to two-dimensional scalar equation. *Journal of Computational Physics*, 179:665–697, 2002.
doi: 10.1006/jcph.2002.7082. Cited on pages 3.

Z. J. Wang and Y. Liu. Spectral (finite) volume method for conservation laws on unstructured grids III: one dimensional systems and partition optimization. *Journal of Scientific Computing*, 20:137–157, 2004.
doi: 10.1023/A:1025896119548. Cited on pages 3.

Z. J. Wang, L. Zhang, and Y. Liu. Spectral (finite) volume method for conservation laws on unstructured grids IV: extension to two-dimensional systems. *Journal of Computational Physics*, 194:716–741, 2004.
doi: 10.1016/j.jcp.2003.09.012. Cited on pages 3.

D. Webb, B. de Cuevas, and A. Coward. The first main run of the OCCAM global ocean model. Internal document no. 34, Southampton Oceanography Centre, 1998. Cited on pages 35.

L. White, E. Deleersnijder, and V. Legat. A three-dimensional unstructured mesh finite element shallow-water model, with application to the flows around an island and in a wind-driven elongated basin. *Ocean Modelling*, 22:26–47, 2008a.
doi: 10.1016/j.ocemod.2008.01.001. Cited on pages 4, 7, 49, 109.

L. White, V. Legat, and E. Deleersnijder. Tracer conservation for three-dimensional, finite-element, free-surface, ocean modeling on moving prismatic meshes. *Monthly Weather Review*, 136:420–442, 2008b.
doi: 10.1175/2007MWR2137.1. Cited on pages 4, 7, 49, 57, 68, 82, 87, 109, 114.

D. L. Williamson, J. B. Drake, J. J. Hack, R. Jakob, and P. N. Swarztrauber. A standard test set for numerical approximations to the shallow water equations in spherical geometry. *Journal of Computational Physics*, 102:211–224, 1992.
doi: 10.1016/S0021-9991(05)80016-6. Cited on pages 34, 36, 41, 69, 95.

M. Zhang and C.-W. Shu. An analysis of and a comparison between the discontinuous Galerkin and the spectral finite volume method. *Computer and Fluids*, 34:581–592, 2005.
doi: 10.1016/j.compfluid.2003.05.006. Cited on pages 3.